Analyse et modélisation de l'impact des décharges électrostatiques et des agressions électromagnétiques sur les microcommutateurs

Jinyu Jason Ruan

▶ To cite this version:

Jinyu Jason Ruan. Analyse et modélisation de l'impact des décharges électrostatiques et des agressions électromagnétiques sur les microcommutateurs. Networking and Internet Architecture [cs.NI]. Université Paul Sabatier - Toulouse III, 2010. English. NNT : . tel-00512333

HAL Id: tel-00512333
https://theses.hal.science/tel-00512333

Submitted on 30 Aug 2010

HAL is a multi-disciplinary open access archive for the deposit and dissemination of scientific research documents, whether they are published or not. The documents may come from teaching and research institutions in France or abroad, or from public or private research centers.

L'archive ouverte pluridisciplinaire **HAL**, est destinée au dépôt et à la diffusion de documents scientifiques de niveau recherche, publiés ou non, émanant des établissements d'enseignement et de recherche français ou étrangers, des laboratoires publics ou privés.

THÈSE

En vue de l'obtention du

DOCTORAT DE L'UNIVERSITÉ DE TOULOUSE

Délivré par *l'Université Toulouse III - Paul Sabatier*
Discipline ou spécialité : *Micro-ondes, Electromagnétisme et Optoélectronique*

Présentée et soutenue par *Jinyu Jason RUAN*
Le *2 juillet 2010*

Titre : *Analyse et modélisation de l'impact des décharges électrostatiques et des agressions électromagnétiques sur les microcommutateurs microondes (MEMS RF)*

Title: *Investigation and modeling of the impact of electrostatic discharges on capacitive RF MEMS switches*

JURY

Président:	Pr. Nicolas NOLHIER
Directeurs de thèse:	Pr. Robert PLANA Pr. Nicolas NOLHIER
Rapporteurs:	Pr. Ingrid DE WOLF Pr. Pierre BLONDY
Examinateurs:	Pr. Manos TENTZERIS Dr. Olivier VENDIER
Invités :	Pr. George PAPAIOANNOU Dr. Fabio COCCETTI

Ecole doctorale : *GEET*
Unité de recherche : *MINC & ISGE*
Directeur(s) de Thèse : *Prof. Robert PLANA & Prof. Nicolas NOLHIER*
Rapporteurs : *Prof. Ingrid de WOLF & Prof. Pierre BLONDY*

Thèse

pour obtenir le grade de

DOCTEUR DE L'UNIVERSITÉ DE TOULOUSE
délivré par l'**Université Toulouse III - Paul Sabatier**

Ecole Doctorale: Génie Electrique, Electronique, Télécommunications
Discipline: Micro-ondes, Electromagnétisme et Optoélectronique

présentée et soutenue

par

Jinyu Jason RUAN

date: 2 juillet 2010

Titre: Analyse et modélisation de l'impact des décharges électrostatiques et des agressions électromagnétiques sur les microcommutateurs microondes (MEMS RF)

Title: Investigation and modeling of the impact of electrostatic discharges on capacitive RF MEMS switches

Directeurs de thèse:
Prof. Robert PLANA and Prof. Nicolas NOLHIER

JURY

Président:
Pr. Nicolas NOLHIER

Directeurs de thèse:
Pr. Robert PLANA
Pr. Nicolas NOLHIER

Rapporteurs:
Pr. Ingrid DE WOLF
Pr. Pierre BLONDY

Examinateurs:
Pr. Manos TENTZERIS
Dr. Olivier VENDIER

Invités:
Pr. George PAPAIOANNOU
Dr. Fabio COCCETTI

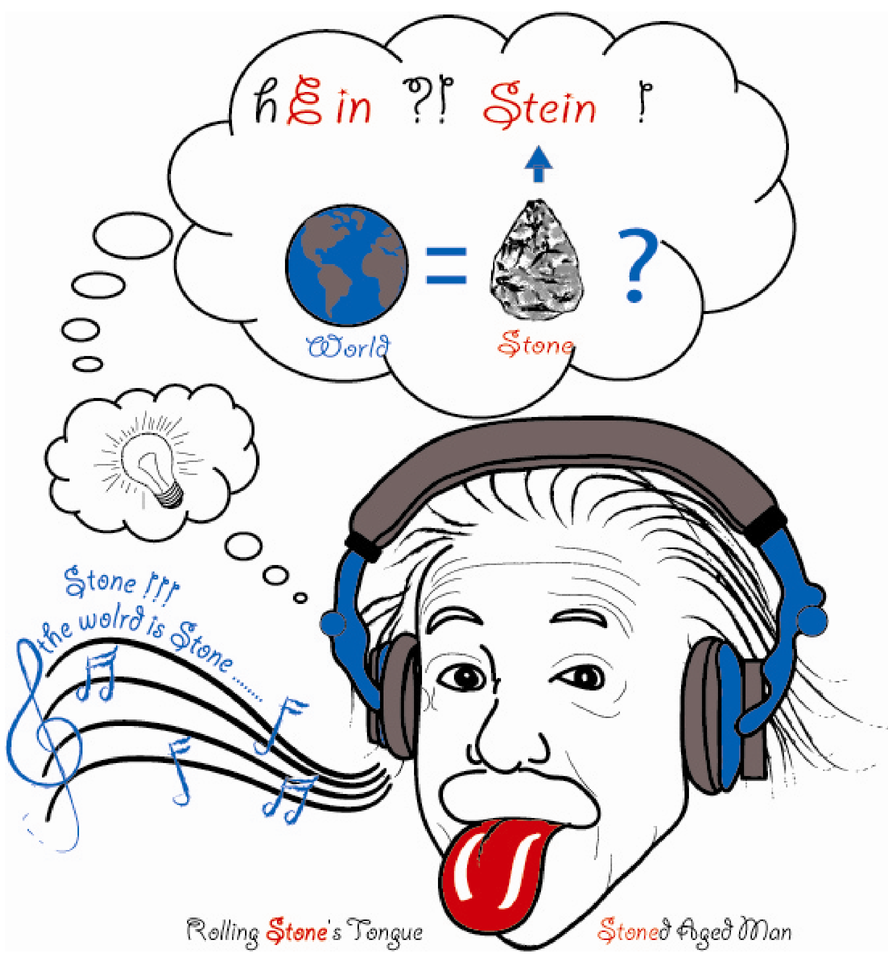

"Theorie ist wenn man weiß wie es geht und es nicht funktioniert. Praxis ist wenn es funktioniert und niemand weiß warum. Realität ist wenn nichts funktioniert und niemand weiß warum."

UNIVERSITE TOULOUSE III

Résumé

Paul Sabatier
UFR Micro-Ondes, Electromagntisme et Optolectronique

Doctorat

par Jinyu Jason Ruan

Les futures architectures des systèmes de communication présenteront une forte complexité due à des besoins de reconfiguration à la fois en termes de fréquence, de puissance émise et/ou reçue, de puissance consommée et de fiabilité.
Une solution consiste à utiliser les MEMS RF pour obtenir ces fonctionnalités augmentées. Ces composants seront soumis à des agressions à la fois électrostatiques et/ou électromagnétiques dont il est important d'analyser et de comprendre leur impact. D'autre part la tenue en puissance de ces composants est un paramètre qualitatif de leur robustesse. Étant donné qu'ils présentent également des intérêts pour les applications spatiales, il est important de comprendre leur sensibilité face au rayonnement.
Le sujet de thèse vise à analyser l'impact de ces agressions sur les paramètres fonctionnels (tensions d'actionnements, vitesse de fonctionnement, pertes d'insertion et isolation) à partir du développement d'une plateforme appropriée ainsi qu'une analyse fine des mécanismes de dégradation apparaissant suite aux stress appliqués ; tension continu, décharges électrostatiques (de type HBM ou TLP), puissance RF et rayonnement.
Ces stress seront appliqués sur des composants aux architectures différentes (types de diélectrique différentes, épaisseur membrane, géométrie des dispositifs, topologie des zones d'actionnement) afin de déterminer si certaines architectures et ou filières technologiques sont plus résistantes que d'autres.
Enfin, afin de valider ces travaux, il sera conçu un design plus complexe présentant des résistances aux ESD/EMI améliorées et un circuit de vieillissement de ces composants sera également proposé.
Ce projet de thèse rentre dans le cadre d'un réseau d'excellence AMICOM sur les microsystèmes RF où la fiabilité a été identifiée comme étant un des enjeux majeurs pour leur intégration et commercialisation.

UNIVERSITY TOULOUSE III

Abstract

Paul Sabatier
Departement of Microwave, Electromagnetic and Optoelectronic

Doctor

by Jinyu Jason Ruan

Future architectures of communication systems will be more and more complex due to the need for reconfigurability in terms of frequency, emitted and received power, power consumption and reliability.
One interesting and very promising technology comes under the name of RF MEMS. In general MEMS component replaces and outperforms its counterparts. These structures will be yielded to electrostatic and/or electromagnetic strains that it is necessary to investigate and to understand the effects. Besides, power handling of those devices is one of the parameters that qualify its robustness. Since they have shown interesting functionalities for space applications, its sensitivity to radiation needs to be understood.
The motivation of the thesis aims at analysing the impact of those strains in the functional parameters (actuation voltages, switching times, insertion losses, isolation), using an appropriate reliability bench test. Clever analyses of the failure mechanisms that occur after stresses such as DC stress, ESD discharge, RF power qualification and radiation, have been performed.
The stresses will be applied on various structures with various architectures and designs, in order to determine the robustness and the reliability of each technology. Finally, the validation and the new findings of these works present one design integrating ESD protection and an accelerated stress test circuit is also proposed. This thesis was being part of the framework of the European Network of Excellence AMICOM on RF Micro-systems where reliability has been defined to be a major challenge to its integration and its commercialization.

Remerciements

Il était une fois, alors que j'étais étudiant en Master de Recherche Systèmes de communications hautes fréquences, dirigé par Mme. Odile PICON, professeur à l'Université Paris-Est et en phase de terminer mon stage de fin d'étude au sein de l'équipe ESYCOM basée à l'école d'ingénieur ESIEE, j'ai pris goût pour le travail de la recherche grâce à cette formation et ce stage de fin d'étude sous la tutelle de Mr. Jean-Luc POLLEUX, maitre de conférences à l'Université Paris-Est. Ma première reconnaissance lui est dédiée tout naturellement, pour sa patience, ses qualités pédagogiques et ses disponibilités et pour sa recommandation auprès de Mr. Robert PLANA, professeur à l'Université Paul Sabatier de Toulouse, qui m'a encadré par la suite.
L'année de formation à Paris s'est très bien passée en compagnie de mes camarades de classe de Master ; Martha, Jaime, Luis et Nadia, avec qui j'ai partagé des moments aussi bien studieux que culturels.

C'était exactement le mercredi 27 septembre 2006, que j'ai sauté au plafond après l'entretien téléphonique avec Robert. Ma page parisienne tourna ce jour là et mon aventure de recherche commença le 01 octobre 2006 à Toulouse. Je tiens à exprimer ma reconnaissance à Robert pour la confiance qu'il m'a témoignée pour ce sujet de thèse, et par la même occasion pour mon accueil au sein de son groupe de recherche MINC (Micro et Nano systèmes pour les Communications sans fils) au LAAS (Laboratoire d'Analyse et d'Architecture des Systèmes). Un groupe qui n'a pas cessé de montrer un dynamisme croissant et son caractère très international est très appréciable.
Peu de temps plus tard, je rencontrai mon co-directeur Mr. Nicolas NOLHIER également professeur à l'Université Paul Sabatier de Toulouse du groupe de recherche ISGE (Intégration de Systèmes de Gestion de l'Energie) dirigé par Mme. Marise BAFLEUR, directeur de recherche de 2ème classe. Je les remercie tous deux pour mon accueil au sein du groupe de travail ESD (David, Fabrice, Nicolas-2, Nicolas-3, Sandra, Antoine, Johan, Franck, Mariane), où les réunions de discussion ont fructifié les idées des uns et des autres.
Toute ma gratitude va également à Mr. Georges PAPAIOANNOU, professeur à l'Université des Athènes, pour son expertise en physique des composants, ses conseils, sa pédagogie, ses disponibilités, son écoute et ses qualités humaines. Puis à Mr. Fabio COCCETTI, docteur de l'Université de München, ingénieur à

NovaMEMS et cadre scientifique du groupe MINC, pour ses avis pluridisciplinaires et ses encouragements.
J'ai donc évolué dans une ambiance à la fois très conviviale et internationale, où la production scientifique n'était pas négligeable. Jusqu'au jour où c'était important pour moi de dactylographier noir sur blanc mes résultats de recherche et de commencer à rédiger ces pages.

Vous pouvez imaginer combien je suis honoré d'avoir un jury de grande qualité. Un très grand merci à mes deux rapporteurs de thèse, Mme. Ingrid DE WOLF, professeur de l'Université de Louvain et chercheur à l'IMEC et Mr. Pierre BLONDY, professeur de l'Université de Limoges et chercheur à Xlim. J'adresse pareillement mes remerciements à Mr. Manos TENTZERIS, professeur à Georgia Tech, Atlanta et à Mr. Olivier VENDIER, docteur de Georgia Tech et ingénieur à Thales Alenia Space, Toulouse, d'avoir accepté d'être examinateurs de ce jury de thèse.

Mon expérience de thèse au LAAS était très enrichissante, tant au niveau scientifique qu'au niveau social, car on pouvait facilement partager le vécu des uns et des autres venus de partout le monde, dans les bureaux du groupe, à la cantine ou encore durant une pause café. En conséquence je commence à remercier notre secrétaire de groupe Brigitte, pour sa serviabilité, sa gentillesse, son instinct maternel et ses histoires de voyage. Puis mes collègues de bureau ; Fadi, Badreddine et leurs épouses respectives Nadine, Nafissa, ainsi que Ali et Sami... Leurs récits et contes sur le Liban, l'Algérie et le Maroc m'ont encore plus ouvert les yeux sur la différence culturelle et m'ont donné envi de voyager et leurs spécialités culinaires sont très raffinées et délicieuses.

Ensuite dans l'ordre des bureaux ; je voudrais remercier Sébastien, alias le corse pour ses blagues les unes plus drôles que les autres mais aussi pour son sérieux en tant que scientifique (et sa compagne Béatrice), Hicham pour ses cerises, Abdoulaye pour ses récits du Mali, Georgios pour les pauses café et les séances de tennis de table, Ahmed Ali, Heba et Nour pour leur gentillesse et les milles encouragements et les chroniques de l'Egypte, Mariano pour les cafés italiens, Nuria pour son soutien de l'équipe de Barcelona, Alex pour son expertise en matière électromagnétisme, Thomas pour les discussions sur diverses sujets, Daniela pour sa bonne humeur et ses connaissances sur les plats roumains raffinés,

Hervé pour ses qualités de grand professeur, Dimitri pour les encouragements, Guillaume pour ses jeux de mots, Vincent pour m'avoir fait découvrir l'escalade, Julien pour bien gérer tous les doctorants, Michael pour m'avoir fait découvrir le Feuerzangenbowle, une boisson traditionnelle allemande, Mehdi pour les séances de billard, Usama pour les explications des coutumes égyptiennes, Sylvia pour ses Tiramisus réalisés en suivant la recette originale italienne, Giancarlo pour ses explications des gestes italiens, Euloge pour les contes congolais, l'histoire de Tati et Oko par exemple, Franck pour ses blagues transmises par radar et ses histoires de l'armée, Michal pour sa bonne humeur polonaise, Patrick pour son professionnalisme technologique, Christina pour ses travaux de développement de process et la fabrication des dispositifs. Les autres personnes du groupe et les stagiaires ne sont pas tombés dans l'oublie.
J'aimerais également citer et remercier ceux qui ne sont plus au labo tels que Mai pour ses sourires et par la même occasion Gaëtan, Hikmat et Micheline pour leur sympathie, Fabienne pour les encouragements, David pour son humour (avec Elise et leurs enfants), Jean-François et Yesmith pour leur crêpes, Christine et Romain pour les apéros, Mona pour sa vitalité et ses rires, Chloé pour son naturel...

Les mercis vont également à l'équipe 2I, Laurent, Alexandre, Nicolas-2, Sandrine pour leur support et leur disponibilité et leur écoute, et tout particulièrement Tonio pour sa curiosité, ses compétences, ses connaissances historiques, sa serviabilité, sa recette de Crostata et aussi pour m'avoir fait découvrir la Sardaigne.
En termes d'activités sportives, je voudrais remercier les grimpeurs d'escalaas, Guilhem, David, Gustavo, Ariane ..., et aussi les basketteurs hispanophones du samedi matin.
Je remercie bien sûr les personnes des autres services, Rodrigo, Camille ... et aussi ceux que j'ai oubliés.

Je ne pourrais pas finir ces pages sans une parenthèse personnelle, dans laquelle j'aimerais remercier mes colocataires ; Marie la cheftaine des brebis pour ses champagnes, Jérôme l'instituteur souvent tête en l'air et adorable pour ses qualités de jardinier et Lena pour sa touche d'innocence. Grâce à eux j'ai l'impression de vivre dans une maison de vacance toute l'année. Les amis de Toulouse reçoivent aussi les mercis ; Charli, Bidouille, AnSo, Marie et Nico, Marie-Paule, Nath, Julien, Nolwenn, Bud, Bibain, Caro, Elsa, Thatiana, Faf, Ludo, Mélo,... Les anciens colocataires me sont aussi très chers, je pense à Nico qui m'a gentiment

accueilli ma première nuit à Toulouse, avec Aurel et Lilou bien sûr, Caroline la danseuse contemporaine franco-suisse, Sara la danseuse franco-italiano-espagnole et je n'oublie pas les amis de la colocation de Bellefontaine, Gwen pour ses chansonnettes, Lucas, Sophie de la colocation de rue de Metz, Erwann, Freddy, Revax, Steph, Lize, Adrien, Zabeth,Patrick,... Je finis par Mélissa et Julien, mes premiers colocataires de la maison actuelle.

En ce qui concerne mes centres d'intérêts, je remercie mon club de billard Black Ball Spirit ; Fabien, Henry, Sylvie, Bénédicte, Alexandro, Franck, Yassine, Christopher,... Et tout particulièrement un grand merci à Henry et Monique et le petit Florian pour leur familiarité avec moi. Grâce à leurs soutiens, conseils et expériences, j'ai pu participer aux finales du secteur Sud-ouest N1 dans la discipline Billard US, où j'ai terminé 14ème, totalement satisfait.

J'en viens à mon club d'escalade que j'ai rencontré sur les berges de la Garonne au cours de ces années de thèse. C'était une belle rencontre. Je remercie Pauline, une grimpeuse exceptionnelle avec un grand coeur et une âme écolo et un sens de la famille appréciable pour le covoiturage et l'immense éventail de sujets de conversation, Julien pour sa sympathie et ses connaissances de la montagne et de l'Ariège, Etienne prince des cocktails pour son sens d'animateur encourageant, Hervé pour ses qualités de magnétiseur, Sylvain et Mathieu pour leur fine cuisine, Franck, Véronique et Tobey pour leur accompagnement et l'organisation des sorties falaises, Marion pour les vidéos et photos de grimpe, Yann pour les madeleines et les cookies et ses cataclope cataclope cataclope, Jérôme pour les photos également, Cédric pour ses ouvertures de bloc dans la salle, Naboss et Delphine et les nouveaux et d'autres grimpeurs de Toulouse,... En somme, résultat des entrainements j'ai pu finir la 7a de la salle à la dernière séance et les moments de grimpe de toute la saison restent à jamais gravés dans ma mémoire.

Evidemment j'ai une pensée pour ma famille pour laquelle je dédicace ce manuscrit; particulièrement ma soeur Jinyu Shannon à qui je dois toute ma reconnaissance pour sa gentillesse, son courage, son sens de la famille, son rôle de grande soeur et plus encore, mes parents Chun Jiao et Qi Ming pour leur courage, leur éducation, leur fierté envers moi, leur amour et le fait d'avoir cru en moi et de m'avoir entendu et aussi ma famille de coeur ou bien de lait ; France, Laurent, Edouard, Léa, Elina pour m'avoir adopté comme fils et pour leurs encouragements et soutiens dans mes

études. Je mets le point final en remerciant mes amis d'enfance, Atat, la famille Allheilly, la famille d'Arthur, Hero & Feng Ming et leurs enfants, Robert & Julie et leur enfant, Mary & Tifi et leurs enfants, et tous les autres amis du Suriname et de la Guyane française, pays de mon enfance et de mon coeur.

Contents

Abstract (FR) vii

Abstract (EN) viii

Remerciements ix

List of Figures xix

List of Tables xxiii

Abbreviations xxv

Symbols xxvii

Introduction 1
General introduction 1
Objectives of this thesis 2
Structure of this thesis 3

1 Background 5
1.1 The micro- nano- world 5
1.2 MicroElectroMechanical Systems 6
1.2.1 Definition 6
1.2.2 Materials and fabrication 7
1.2.2.1 Materials 7
1.2.2.2 Bulk micromachining 7
1.2.2.3 Surface micromachining 8
1.2.2.4 High aspect ratio processes 9
1.2.2.5 Wafer bonding 9
1.2.3 Products 9
1.3 RF-MEMS technology 10
1.3.1 RF-MEMS switches 12
1.3.1.1 The designs 12
1.3.1.2 RF performances 13
1.3.2 Applications of RF-MEMS switches 16
1.3.2.1 Single Pole Double Throw 17

1.3.2.2 Phase shifter 17
1.3.2.3 Tunable filter 18
1.3.2.4 Tunable dual behaviour resonator 19
1.3.2.5 Tunable matching network 19
1.3.3 Industry and market roadmap 20
1.3.3.1 Potential applications 21
1.3.3.2 Major companies 22
1.3.3.3 Total volume needs 23
1.3.4 Status of the fabrication technology and the reliability . . . 27
1.3.4.1 Present fabrication technologies of RF MEMS . . . 27
1.3.4.2 Reliability of RF MEMS 27

2 Failure mechanisms in capacitive switches 31
2.1 Failure modes and failure mechanisms 31
2.2 Capacitive RF-MEMS switch theory 34
2.2.1 Principle of operation 34
2.2.2 Switching time 37
2.2.3 Switching ratio 39
2.2.4 Microwave characteristics 39
2.2.5 Theory of dielectric charging 42
2.2.5.1 The model 42
2.2.5.2 Dielectric polarization 44
2.2.5.3 Charge injection mechanisms 46
2.3 Focussed reliability concerns 49
2.3.1 Dielectric charging in capacitive switches 50
2.3.2 ESD/EOS specificities in MEMS 51
2.3.2.1 ESD Testing standards 52
2.3.2.2 Human Body Model (HBM) 53
2.3.2.3 Transmission Line Pulsing (TLP) 54
2.3.3 Operational power handling considerations 54
2.3.4 Radiation effects 56
2.3.4.1 Space radiation environment 57
2.3.4.2 Radiation effect on materials 58
2.3.4.3 RF-MEMS switches sensitivity to radiations 59

3 Experimentations: methodology, equipment and results 63
3.1 Hold-down charging studies on AlN devices and comparison 64
3.1.1 DUT 64
3.1.2 Testing methodology and equipment 65
3.1.2.1 The in-house RF-MEMS characterisation set-up . . 65
3.1.2.2 Microwave measurements 66
3.1.2.3 Extraction of capacitance values from S-parameters 67
3.1.2.4 Switching times 69

3.1.2.5 Transmission parameter S_{21} as a function of control voltage . . . 69
3.1.2.6 Hold-down charging . . . 70
3.1.3 Results and discussion . . . 71
3.2 ESD investigations in RF MEMS capacitive switches . . . 78
3.2.1 DUT . . . 78
3.2.2 Testing methodology and equipment . . . 79
3.2.2.1 TLP . . . 79
3.2.2.2 HBM . . . 80
3.2.2.3 Capacitance-based charging monitoring without pull-down of the switch . . . 81
3.2.2.4 Charging mechanisms hypothesis . . . 83
3.2.3 Results and discussion . . . 84
3.2.3.1 Breakdown phenomena in RF MEMS . . . 84
3.2.3.2 Charging studies . . . 89
3.2.3.3 Inhomogeneous dielectric charging . . . 92
3.2.3.4 Pulse induced accelerated stress test analyses . . . 95
3.3 RF power handling characterizations . . . 103
3.3.1 DUT . . . 103
3.3.2 Power handling setup . . . 104
3.3.3 Results . . . 104
3.4 Radiation effects in capacitive switches . . . 106
3.4.1 Experiment . . . 106
3.4.2 Results and discussion . . . 107
3.4.2.1 Radiation introduced vacancies . . . 107
3.4.2.2 Effect in MIM capacitors . . . 108
3.4.2.3 Effect in MEMS switches . . . 109

Conclusion **111**

Outlook **113**

List of Papers **127**

Appendices **131**

A Designs and Simulations **133**
A.1 MEMS designs for RF applications . . . 133
A.1.1 Electro-Mechanical considerations . . . 134
A.1.2 Electro-Magnetic analysis . . . 135
A.1.3 Technology process . . . 136
A.1.4 Displacement characterizations . . . 137
A.2 MEMS protecting RF-MEMS . . . 139

B Accelerated Stress Test Circuit **141**

List of Figures

1 The first integrated circuit. 1
2 Vacuum tubes. 1

1.1 Xenon atoms on a nickel surface 5
1.2 The first MEMS: a gold resonating MOS gate structure 6
1.3 Fully integrated MEMS oscillators on CMOS 6
1.4 Bulk micromachining 8
1.5 Surface micromachining 9
1.6 PIN diode and GaAs FET switch I-V graphs. 13
1.7 Typical S parameters of RF MEMS switches 14
1.8 A K-band Single Pole Double Throw Circuit 17
1.9 A 60 GHz Phase shifter 17
1.10 V-band Tunable Band Pass Filter 18
1.11 W- to V-band tunable resonator 19
1.12 Tunable matching network 19
1.13 The RF MEMS switch hype curve. 20
1.14 Companies in production of RF-MEMS. 23
1.15 The RF MEMS switch total market. 24

2.1 The ‘bathtub curve’ for reliability development. 32
2.2 The failure driven qualification methodology. 33
2.3 Principle of operation of a capacitive RF MEMS switch 34
2.4 A measured C(V) curve of a capacitive RF-MEMS switch with its applied voltage waveform in the inset. 35
2.5 Measured S-parameters of a 35 GHz capacitive RF-MEMS switch in both up-state and down-state configuration. 40
2.6 Simplified charging model of a capacitive switch, by analogy to the parallel plate model. 42
2.7 Charging mechanisms in RF-MEMS capacitive switches 44
2.8 Dipolar or orientational polarization illustration. 45
2.9 Space charge and interfacial polarization illustration. 46
2.10 Energy level diagram illustrating an inelastic trap assisted tunneling process. 47
2.11 Energy level diagram illustrating the Poole-Frenkel conduction mechanism. 48
2.12 Operating parameters vs. device’s operation time. 49

2.13 An example of the shift of the C(V) characteristics, measured for a constant voltage stress of around 30 min under 40V biasing. 50
2.14 Log-log plot of the dielectric charging dependence on the stress time. 50
2.15 A microscope image of a capacitive switch submitted to several HBM pulses (no apparent failure is visible). 52
2.16 A microscope image of a breakdown caused by EOS in a capacitive switch. 52
2.17 Short circuit current of common ESD-stress models. 53
2.18 The equivalent circuit used to test the discharge sensitivity of a device based on human body model. 53
2.19 The equivalent electric circuit of the Transmission Line Pulsing set-up. 54
2.20 Hot-switching operation time and power handling capacity comparison of MEMS switches from worldwide publications. 56
2.21 The space radiation environment near the earth. 57
2.22 Space radiation environment inside and outside spacecraft. 57

3.1 Topology of the AlN-based capacitive RF-MEMS switches. 64
3.2 Diagram of test equipment setup for RF MEMS reliability monitoring. 65
3.3 Timing charts of microwave and switching measurements. 66
3.4 Measured S-parameters of the DUT. 67
3.5 The *ABCD* parameters of the equivalent 2-port circuit. 67
3.6 The extracted capacitance values. 68
3.7 The switching times. 69
3.8 Timing charts of control and detected signals. 69
3.9 Transmission parameter S_{21} vs. control voltage. 69
3.10 Timing charts of hold-down measurements. 70
3.11 Hold-down charging in AlN-based switches. 71
3.12 Empirical comparison of different insulating materials. 77
3.13 Tested devices. 78
3.14 S-parameters of (a) SW2 and (b) SW3 structures. 79
3.15 Block diagram of ESD set-ups including capacitance monitoring (a) TLP and (b) HBM. 79
3.16 Simple experimental apparatus employed here to measure mechanical variation of the movable membrane. 80
3.17 Principle of C(V) characteristic below the pull-down point. 81
3.18 Typical C(V) characteristic of the capacitive switch measured in the non-contact state voltage span. 82
3.19 The PIC test bench combine with a capacitance meter. 83
3.20 Charging mechanisms hypothesis in capacitive switch. 83
3.21 TLP Current-Voltage failure signature of SW1 switches. 84
3.22 $S_{21}(V)$ graph of SW1 affected by soft failures. 84
3.23 Microscope picture of a partially damaged switch. 85
3.24 Microscope picture of a completely destroyed switch. 85
3.25 Breakdown voltage in air at 1 atm versus gap. 86
3.26 Light emission obtained during breakdown on SW1. 87

3.27 Light emission obtained during breakdown on SW2. 87
3.28 Electric field distribution using static 2D and 3D simulation with a DC voltage of 420V at the CPW access. 88
3.29 Current waveform responses in function of HBM failure signature. . 88
3.30 Optical checking (a) after the total stress is applied, (b) a zoom of the dielectric area after removing the bridge. 89
3.31 The shift of $V_{capamin}$ as a function of positive TLP pulses, for MF-SiN and LF-SiN structures. 90
3.32 The shift of $V_{capamin}$ as a function of the magnitude of one positive HBM pulse. 90
3.33 Capacitance over time of devices submitted to one positive HBM pulse of $50V$ 91
3.34 Non-contact C(V) curve for device which has been stressed at 50V for short pulse of $10ms$. 93
3.35 Surface potential distribution of a stressed device. 93
3.36 The shift of $V_{capamin}$ as a function of number of cycles. 96
3.37 The shift of $V_{capamin}$ as a function of the down-state duration $t_{down,s}$. 96
3.38 The shift of $V_{capamin}$ as a function of HBM stress electric field. . . . 97
3.39 The shift of $V_{capamin}$ as a function number of HBM pulses at different electric-fields. 97
3.40 The shift of $V_{capamin}$ as a function of the down-state time. 98
3.41 Comparison between $\Delta V_c(N_c)$ and $\Delta V_s(E_s)$. 98
3.42 The slopes as a function of the temperature. 99
3.43 The shift of $V_{capamin}$ as a function of stress voltage from $25°C$ to $55°C$. 99
3.44 Arrhenius model fit. 100
3.45 Capacitance transient response measured after the applied stresses during 1 hour. 100
3.46 Devices for power applications. 103
3.47 Measurement setup for high power testing at 10GHz. 104
3.48 Distribution of Si and N vacancy introduction rates (V) for a MIM capacitor. 107
3.49 TSDC spectra and stored charge of MIM capacitor obtained before and after each successive irradiation experiment. 107
3.50 Arrhenius plots of TSDC currents obtained before and after each successive irradiation experiment for (a) $-20V$ and (b) $+20V$. . . . 108
3.51 Dependence of stored charge on radiation fluence for (◦) positive and (•) negative bias on top electrode. 109
3.52 Dependence of (◦) change capacitance at zero bias and (•) bias for capacitance minimum vs. radiation fluence. 109

A.1 Different topologies of SPST switches. 133
A.2 Measured and simulated C(V) characteristics. 135
A.3 Measured and simulated S parameters characteristics. 135
A.5 Pictures of the fabricated structures. 137

A.6 Optical profilometer data of the fabricated BDG3 switch. 138
A.7 Prototypes including ESD protection. 139
A.8 Profilometer image and cross sections of BDG1 with the protection structure. 140

B.1 Electrical schematic of the AST circuit for MEMS. 141
B.2 The AST-MEMS circuit. 142
4.3 Le marché total du commutateur MEMS RF [45]. 149
4.4 Principle de fonctionnement d'un switch MEMS RF capacitif (a) à l'état haut (non actionné) et (b) à l'état bas (actionné). 151
4.5 Courbe C(V) complète du μ-commutateur MEMS RF capacitif. . . 152
4.6 Caractéristiques typiques du chargement du diélectrique et de la défaillance. 152
4.7 Modèle de chargement simplifié du μ-commutateur capacitf. 153
4.8 Chronogramme des signaux de commande et de la réponse du $\mu -$ commutateur. 156
4.9 Comparaison empirique de différents matériaux diélectriques. 158
4.10 Courbes courant-tension TLP comme signature de défaillance. . . . 159
4.11 Une courbe typique de $S_{21}(V)$ dans le cas d'un commutateur affecté par des défaillances mineures. 159
4.12 Observations au microscope (a) après une série de décharge, (b) un agrandissement du diélectrique après avoir enlevé la membrane. . . 160
4.13 La dérive de $V_{capamin}$ en fonction d'impulsions positives TLP, pour les structures MF-SiN et LF-SiN. 161
4.14 La dérive de $V_{capamin}$ en fonction d'une impulsion positive HBM pour des valeurs de tension allant de 30 à 100V, pour les structures MF-SiN et LF-SiN. 162
4.15 La dérive de $V_{capamin}$ en fonction du nombre de cycles (avec l'equivalence de la densité de charge en surface). 163
4.16 La dérive de $V_{capamin}$ en fonction du temps d'actionnement $t_{down,s}$. . 163
4.17 La dérive de $V_{capamin}$ en fonction du champ électrique du stress HBM. 164
4.18 La dérive de $V_{capamin}$ en fonction du nombre d'impulsions HBM pour différents champs électriques. 164
4.19 La dérive de $V_{capamin}$ en fonction du temps d'actionnement. 164
4.20 Comparaison entre $\Delta V_c(N_c)$ et $\Delta V_s(E_s)$. 164
4.21 La dérive de $V_{capamin}$ en fonction du champ électrique à des températures de $25°C$ à $55°C$. 165
4.22 Le fit utilisant la loi d'Arrhenius. 165

List of Tables

1.1 Overview of functional materials used in MEMS 7
1.2 MEMS structures and applications 10
1.3 RF-MEMS devices, circuits and applications 11
1.4 Main RF-MEMS switch designs 12
1.5 Performance comparison of switches based on RF-MEMS, FET and PIN diodes 15
1.6 Main application fields of RF-MEMS switches 16
1.7 Potential application fields of RF MEMS switches. 22
1.8 Total volume needs of RF MEMS switches 2006 - 2011. 24
1.9 Fabrication technologies overview. 25
1.10a Reliability summary of RF MEMS metal-contact switches. 28
1.10b Reliability summary of RF MEMS capacitive switches and switched-capacitors. 29

2.1 Total dose levels for Earth orbits. 58
2.2 Overview of radiation effects on materials. 59
2.3 Overview of radiation effects on RF MEMS switches. 61

3.1 An overview of dielectric materials used in capacitive RF-MEMS. . 102
3.2 Comparative summary of RF MEMS power switch performance. . . 105

A.1 Physical dimensions of SPST switches shown in Fig.A.1. 134

4.2 Tableau comparatif de performance RF entre commutateurs MEMS-RF, FET et diodes PIN [4, 5, 8, 24, 39]. 147
4.3 Les principaux champs d'application des micro-commutateurs MEMS RF. 148

Abbreviations

AF	**A**cceleration **F**actors
ATE	**A**utomatic **T**est **E**quipment
BAW	**B**ulk **A**coutic **W**ave
CMOS	**C**omplementary **M**etal-**O**xide- **S**emiconductor
CPW	**C**o**P**lanar **W**aveguide
DARPA	**D**efense **A**dvanced **R**esearch **P**rojects **A**gency
DBR	**D**ual **B**ehavior **R**esonator
DLP	**D**igital **L**ight **P**rocessing
DMD	**D**igital **M**icro-mirror **D**evice
DMTL	**D**istributed **M**EMS **T**ransmission **L**ine
DRIE	**D**eep **R**eactive **I**on **E**tching
EOS	**E**lectrical **O**ver**s**tress
ESD	**E**lectro**S**tatic **D**ischarge
FA	**F**aluire **A**nalysis
FBAR	**F**ilm **B**ulk **A**coustic-Wave **R**esonator
FET	**F**ield **E**ffect **T**ransistor (switch)
FMEA	**F**ailure **M**odes and **E**ffects **A**nalysis
GaAs	**Ga**llium **A**r**s**enide
HARMT	**H**igh **A**spect **R**atio **M**icrostructure **T**echnology
HBM	**H**uman **B**ody **M**odel
IC	**I**ntegrated **C**ircuit
IL	**I**nsertion **L**oss
LIGA	Roentgen-**LI**thography **G**alvanik **A**bformung
LTCC	**L**ow **T**emperature **C**ofired **C**eramic

MEMS	**M**icro **E**lectro **M**echanical **S**ystems
MMIC	**M**onolithic **M**icrowave **I**ntegrated **C**ircuits
MOS	**M**etal **O**xide **S**emiconductor
MPW	**M**ulti **P**roject **W**afer
MST	**M**icro **S**ystems **T**echnology
MTTF	**M**ean **T**ime **T**o **F**ailure
PA	**P**ower **A**mplifier
PF	**P**oole-**F**renkel
PIN	**P**ositive **I**ntrinsic **N**egative (diode)
RF-MEMS	**R**adio **F**requency- **M**icro **E**lectro **M**echanical **S**ystems
RIE	**R**eactive **I**on **E**tching
SCREAM	**S**ingle **C**rystal **R**eactive **E**tch **A**nd **M**etal
SMR	**S**olide **M**ounted **R**esonator
SOI	**S**ilicon **O**n **I**nsulator (substrate)
SoS	**S**ilicon **on** **S**apphire
TAT	**T**rapped **A**ssisted **T**unneling
TBPF	**T**unable **B**and**P**ass **F**ilter
TLP	**T**ransmission **L**ine **P**ulsing
TSDC	**T**hermally **S**timulated **D**epolarization **C**urrent
TTF	**T**ime **T**o **F**ailure
ULSI	**U**ltra **L**arge **S**cale **I**ntegration
WLAN	**W**ireless **L**ocal **A**rea **N**etwork
WPAN	**W**ireless **P**ersonal **A**rea **N**etwork

Symbols

A	Capacitance area	μm^2
b	Damping coefficient	
C	Capacitance value	pF
C_{down}	Down-state capacitance value	pF
C_{meas}	Measured down-state capacitance value	pF
C_{th}	Theoretical down-state capacitance value	pF
C_{up}	Up-state capacitance value	pF
C_0	The minimum of capacitance	pF
d	Distance between electrodes	μm
E_a	Activation energy	eV
E_{mech}	The Young's modulus	N/mm^2
E_e	Distance-dependent electrostatic energy accumulated by the capacitor	$N \cdot m$
E_r	Restoring energy of the membrane	$N \cdot m$
E_{eff}	Effective electric field intensity	V/m
f_0	Series resonant frequency	Hz
F	Radiation fluence	m^{-2}
F_e	Electrostatic force	N
F_c	Sum of attractive and repulsive nuclear contact forces	N
J	Current density	$A.m^{-2}$
J_{PF}	Poole-Frenkel current density	$A.m^{-2}$
J_S	Schottky current density	$A.m^{-2}$
J_{TAT}	Trap Assisted Tunneling current density	$A.m^{-2}$
k	Spring or force constant	N/m

k_s	Stress-stiffening spring constant	N/m
k_B	Boltzmann's constant	eV/K
K	Temperature acceleration factor	
K_0	Constant of the Arrhenius model	
K_1	Amplitude coefficient of the Arrhenius model	
m	Mass of the beam	g
P	Polarization	$q/Area$
$P_{\sum}$	Total polarization	$q/Area$
P_D	Dipolar polarization	$q/Area$
P_{SC-i}	Intrinsic space charge polarization	$q/Area$
P_{SC-e}	Extrinsic space charge polarization	$q/Area$
Q	Amount of charge	C
R_{sw}	Ratio between down-state and up-state capacitance	
R_Q	Rate of charging	
S_{21}	Transmission coefficient	dB
t_{down}	Time the switch remains in the down-state	s
t_s	Switching time	s
t_{50}	Median time-to-failure (electromigration)	s
V	Voltage	V
$V_{capamin}$	Voltage corresponding to the minimum of capacitance	V
V_{down}	Pull-down voltage	V
$V_{down-eq}$	Equivalent pull-down voltage (power handling calculation)	V
V_{off}	Offset voltage corresponding to the mean value of V_{shift}	V
V_{shift}	Offset voltage due to charging	V
V_{up}	Release-up voltage	V
V_{up-eq}	Equivalent release-up voltage (power handling calculation)	V
z	Displacement	μm
z_d	Insulator layer thickness	nm
Z_0	Characteristic impedance	Ω
ε_r	The relative dielectric constant of the insulator material	

$\Delta C(t)$	Capacitance transient component	pF
$\Delta\omega$	Bandwidth	Hz
$\Delta P(t)$	Time-dependent polarization	$q/Area$
ΔV_c	Shift of threshold voltages due to cycling	V
ΔV_s	Shift of threshold voltages due to pulse stress	V
ν	The Poisson's ratio for the bridge material	
ω_m	Mechanical resonant angular frequency	$rad \cdot s^{-1}$
σ_{mech}	Mechanical stress in the beam	Pa
σ_p	Parasitic charge density	C/m^2
σ_Σ	Total surface charge density	C/m^2
ρ	The trapped charge density	C/m^2

To my sister and my parents...

Where there's a will, there's a way

British proverb

Introduction

General introduction

In our information age, the micro- nano- world belongs to everyday life. The beginning starts with, the first integrated circuit (Fig.1) successfully demonstrated by *Jack Kilby* in 1958, which has revolutionized the world of electronics. Since then down-scaling has increased in scope from vacuum tube technology (Fig.2) to Ultra-Large Scale Integration (ULSI). Today we are able to integrate more than one hundred-thousand components on a single square centimeter chip.

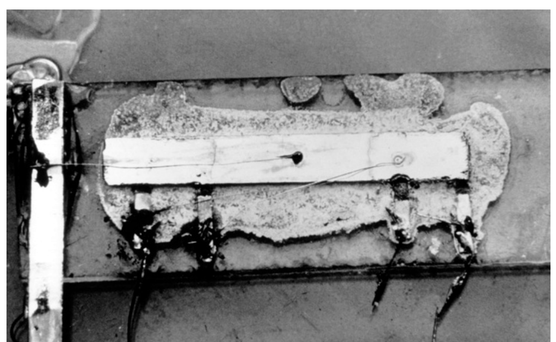

FIGURE 1: The first integrated circuit.

FIGURE 2: Vacuum tubes technology.

Microelectronic technology started with a few spots and wires on a chip of semiconductor, and has already grew into computers on chips. The significant successes of microelectronics is based on its ability for integration, miniaturization, multifunctionality and high volume production. In this microworld conquest Microelectromechanical systems (MEMS) appears to be a very good conqueror. They are very tiny systems that integrate functionalities from different physical domains into one device. It is an extreme interdisciplinary field that combines design, engineering and manufacturing expertise from diverse technical areas including integrated-circuit (IC), fabrication technology, materials science,

mechanical, electrical, chemistry and chemical engineering, as well as fluidics and optics.

Objectives of this thesis

In the pass years, communications were exclusively dedicated to military and governmental uses. Nowadays the electromagnetic spectrum available for telecommunication is quite broadband and civilian use constitutes a huge and important market. In order to adapt the evolution in the allocated frequencies, radical change in terms of flexibility and efficiency in architectures and systems is required. It is than obvious that general communication systems will need tunable and switching components that must be smaller, more secure, perform more functionalities and at the same time consume less power and have a very low noise behaviour.

"The RF chip has to work properly anywhere, anytime and has to be as cheap as possible"
Robert Plana [1]

One very interesting and promising candidate, coming from the concept of micro-electro-mechanics is the Wireless MEMS, more famously called as RF-MEMS switch. Those devices have been demonstrated to gather performances such as; low insertion loss and high isolation, high linearity, high power handling and high Q factor, and low power consumption with respect to other microwave switching technologies [2–5]. Mass production techniques from already existing semiconductor industry can be used, which allows mass production and reduces unit prices.

However their restricted widespread integration is mainly due to the limited reliability data (i.e. operation time of RF-MEMS devices should be greater than 10 years). As a result, the reliability of RF-MEMS is still attracting many research interests. In order to be integrated into mainstream RF applications, they must demonstrate their reliability. One of the main challenges in this field is to identify and understand the failure modes so that accelerated stress tests can be developed. In this frame, this thesis focuses on the topic of reliability of RF-MEMS switches through:

- Charging,
- Electrostatic discharge,
- Power handling,

- Radiation.

Obviously, from infinitely large to infinitesimally small, reliability aspects considered in this work require rather disparate disciplines and paradigms (e.g. material science, fabrication processing, mechanical engineering, physics, design and modeling engineering, simulations etc...). Therefore discussions with all the necessary experts was useful, appreciable and it has contributed to the writing of this manuscript.

Structure of this thesis

This manuscript deals with the reliability field of RF-MEMS. It is a interdisciplinary field involving the areas of integrated circuit fabrication technology, mechanical and materials science, engineering of microscopic mechanisms, and RF and microwave electronics engineering. Therefore the document starts with an overview of the motivation and the activities in the field, from the micro- nano- world vision to the expected market forecast and the present status and trend (Chapter 1). The second part of this document integrates fundamentals physics related to the focussed reliability research topics, in order to provide references for further study of the related topics (Chapter 2). The effect of packaging on reliability is not discussed in this thesis. Furthermore, the scientific work of this thesis is based on, experimental results validating hypotheses on the failure behaviour and the failure mechanisms of the structures. Because standard reliability testing is not possible until a common set of reliability requirements is developed (Chapter 3). Finally the manuscript ends with common conclusions and gives a brief outlook over the possible continuation of the work described in this thesis.

Why cannot we write the entire 24 volumes of the Encyclopaedia Britannica on the head of a pin?

Richard P. Feynman
1918-1988, American physicist
in "There is *Plenty* of Room at the Bottom"

Chapter 1

Background

1.1 The micro- nano- world

Almost 50 years ago a american scientist named Richard P. Feynman predicted the future, the future of nanotechnology. It was 1959, only 2 years after the first satellite *Sputnik 1* was lunched and 2 years earlier the first man *Yuri Gagarin* space walked. In that time, nobody had really seen an atom with a microscope. His talk "There is *Plenty* of Room at the Bottom" [6] given on December 29th 1959 at the annual meeting of the American Physical Society at the California Institute of Technology, will become a roadmap for nanotechnology. Feynman predicted how technology may make things smaller and smaller. Forty years after, in 1989 Don Eigler and his research group moved individual atoms. They used 35 atoms to spell out IBM (Fig. 1.1). Today we are using nanotechnology and making things smaller and smaller. The world of objects that are smaller than a wavelength of visible light "the micro- nano- world" belongs to everyday life.

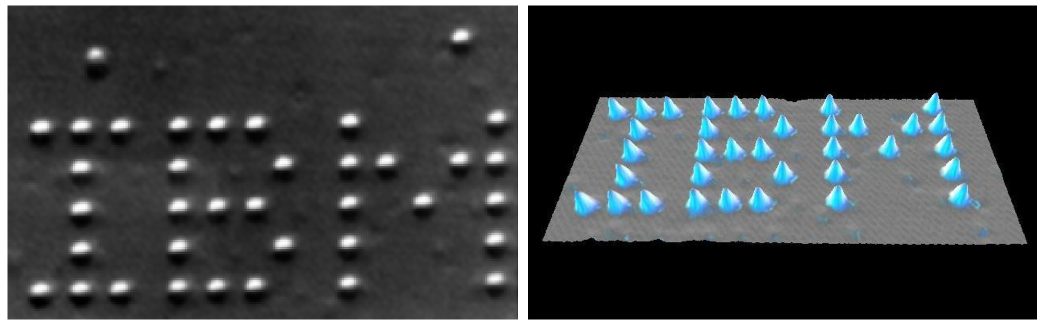

FIGURE 1.1: Xenon atoms on a nickel surface

1.2 MicroElectroMechanical Systems

1.2.1 Definition

The world of MEMS is so small that it is not imperceptible to the human eye. A world where volume effects such as gravity and inertia are no longer important, but atomic forces and surface science such as electrostatics and wetting dominate. "MEMS" also referred to as micromachines in Japan or Micro Systems Technology (MST) in Europe, are very tiny systems (its size is comparable than a grain of pollen) that integrated microstructures combining electrical and mechanical properties. These systems have the ability to sense, control and actuate in order to interact with physical, chemical surroundings such as motion, sound, light, radio waves, gases, liquids, thermic radiation etc. A whole new class of micro-products performing tasks on the microscale and generating effects on the macroscale has emerged. MEMS is one of the most exciting and huge evolution in microelectronics, a "smart matter" in a small world with big opportunities.

In 1967, less than 10 years after the invention of the IC (Fig.1), H. C. Nathanson used microelectronic fabrication processes to make the first MEMS device [7], which was a gold resonating MOS gate structure (Fig.1.2). Since this demonstration, the progress in this field never stops. Nowadays, MEMS technology has reached the maturity as silicon resonating market threatens the quartz crystal one. In fact, Discera, SiTime and Silicon Clocks are already manufacturing silicon MEMS oscillators , and Toyocom (Seiko Epson) produces micromachined quartz MEMS oscillators. This is a nice representation of MEMS on CMOS integration.

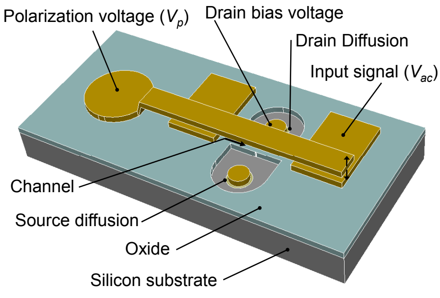

FIGURE 1.2: The first MEMS: a gold resonating MOS gate structure

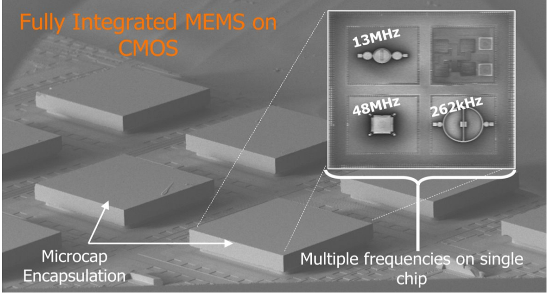

FIGURE 1.3: Fully integrated MEMS oscillators on CMOS (*Courtesy of Silicon Clocks Inc.*)

Substrates	Ceramics	Metals
Silicon/SOI	Silicon dioxide (SiO_2)	Gold (Au)
Quartz	Silicon nitride (Si_3N_4)	Aluminium (Al)
Glass	Alumina (Al_2O_3)	Nickel (Ni)
Gallium arsenide	Aluminium nitride (AlN)	Chromium (Cr)
Polymide flexible	Titanium dioxide (TiO_2)	Titanium (Ti)
	Tantalum pentoxide (Ta_2O_5)	Tungsten (W)
	Hafnium oxide (HfO_2)	Platinum (Pt)
	Barium strontium titanate (BST)	Silver (Ag)
	Zinc oxide (ZnO)	Tantalum silicide ($TaSi_2$)
	Lead zirconate titanate (PZT)	
	Polysilicon	

Table 1.1: Overview of functional materials used in MEMS

1.2.2 Materials and fabrication

In a sense, MEMS technology is an "turn old into new" technology because significant parts of the technology has been adopted from IC know-how (the use of silicon wafer, thin films of materials, photolithography technique etc.). Since there is a wide variety of materials having physical properties suitable for MEMS devices, this section does not attempt to present a comprehensive review of all of them but a short introduction to the basic fundamentals of materials and technologies is absolutely necessary to design, model, fabricate and characterize MEMS.

1.2.2.1 Materials

Depending on the function and the operating environment of MEMS devices, the selection criteria of the materials will change (Section 1.6 in [8], Chapter 3 in [9]). For instance, if we consider MEMS mechanical resonators and switches, we want materials that have high quality factor and low electrical resistivity to reduce insertion loses and chargingless material as insulator. Table 1.1 gives an overview of functional materials used in MEMS. These three main classes of materials are used to structure most of the MEMS devices using basic fabrication techniques such as deposition, patterning (by photolithography) and etching.

1.2.2.2 Bulk micromachining

In 1979, K. E. Petersen reported "Micromechanical Membrane Switches on Silicon" [10] showing the potentialities of the micromachining technology. One of the broad

categories of MEMS technologies is bulk micromachining. As it is shown in Fig.1.4, it consists in using etching techniques (anisotropic or isotropic wet etching and deep-reactive ion etching (D-RIE), sputter and vapour phase etching) to selectively etch away unwanted parts and create suspended structures. These techniques allow the fabrication of a multitude of micromachined sensors, actuators, and mechanical structures ([11],Chapter 3 in [12],Section 1.3.1 in [8], Section 1.2.1 in [9]).

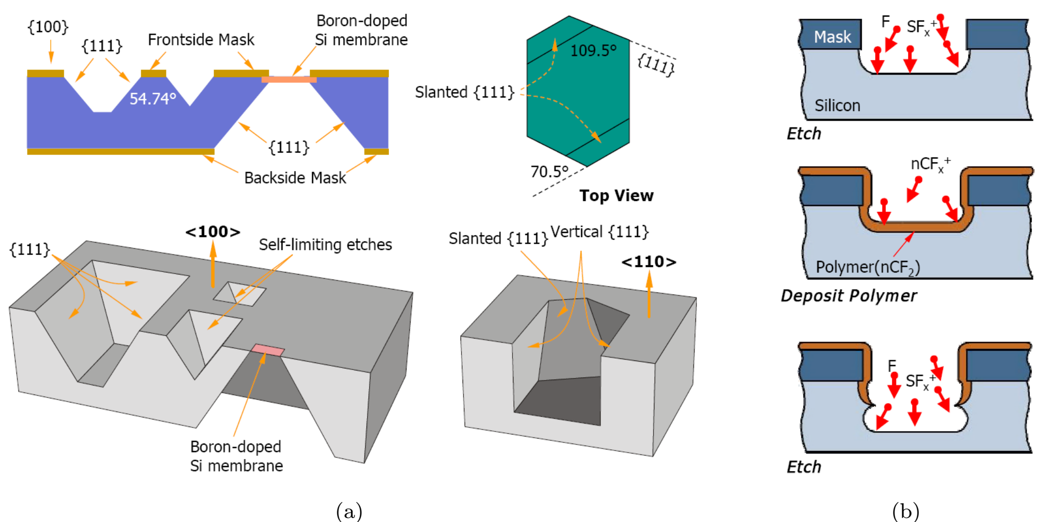

FIGURE 1.4: Bulk micromachining (a) anisotropic wet etching (b) deep reactive ion etching (*Courtesy of DARPA*)

1.2.2.3 Surface micromachining

The recent emergence of higher resolution results in adopting surface micromachining approaches. Contrary to bulk micromachining, here devices are fabricated by structuring layer-by-layer (Chapter 3 in [12], Section 1.3.2 in [8], Section 1.2.2 in [9]). The Fig.1.5 depicts typical steps used in the surface micromachining process. The sequence is often composed by; depositing thin films on a wafer, patterning by photolithography and then etching the patterns into the films. The use of sacrificial and structural materials makes mechanical elements to move and fulfil its function.

E. Garcia and J. Sniegowshi from Sandia National Lab. have shown a whole series of microengines fabricated using surface micromachining process [13].

1.2.2.4 High aspect ratio processes

The depth of etching can be increase using high aspect ratio microstructure technology (HARMT) such as LIGA, DRIE and SCREAM, to name a few. LIGA is a German acronym of Roentgen-**LI**thography
Galvanik **A**bformung, describing the process sequence; X-ray lithography, electrodeposition and moulding [14, 15]. SCREAM process stands for **S**ingle **C**rystal silicon **R**eactive **E**tch and **M**etal and use submicron optical lithography to defines MEM devices with a single mask [16, 17]. In HAR silicon micromachining the thickness can be from 10 to 100μm whereas it is only around 2μm in basic micromachining processes. HARMT gives the possibility to fabricate a wider array of mechanical elements.

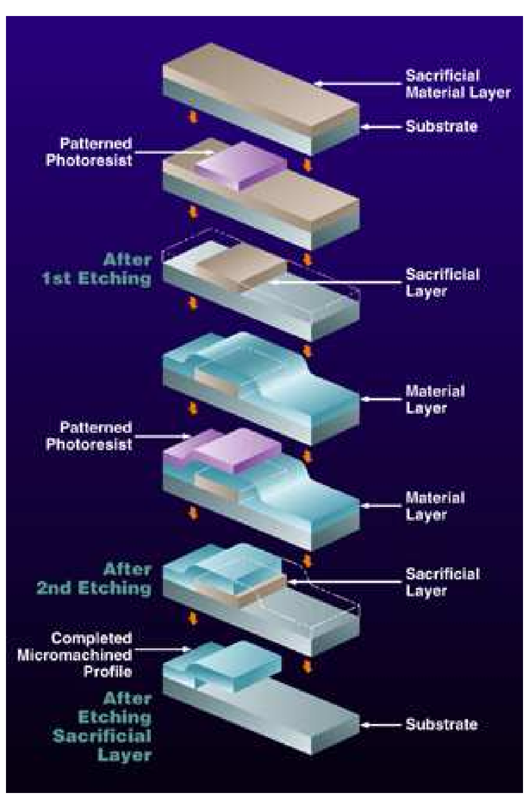

FIGURE 1.5: Surface micromachining [18]

1.2.2.5 Wafer bonding

Originated from the development of silicon-on-insulator (SOI) wafers, bonding techniques (anodic bonding,intermediate-layer assisted bonding and direct bonding) can combine silicon and bulk micromachining for building complex 3D microstructures in a monolithic format. The principle deals with the creation of atomic bonds between two wafers either directly or through a thin film (Section 1.3.4 in [19] and section 1.3.3 in [8]). As a result, further advanced MEMS structures in the field of pressure sensors, accelerometers and resonant structures can be developed and assembled.

1.2.3 Products

It is remarkable how using relatively easy processes, we can create unlimited structures, just “our ideas limited”. MEMS keep creating new capabilities, extending its functionalities, by the way its field of application. Table 1.2 tends to

<table>
<tr><th>Sensor/Actuator/Structure</th><th>Functions/Physical surroundings</th><th>Categories</th><th>Field of application (commercial/military)</th></tr>
<tr><td>Pressure sensors
Accelerometers
Gyroscopes
Comb drivers
Piezo-resistors
Micro resonant strain gage
Temperature sensors</td><td>Mechanical deformation
Thermal expansion
Inertial
Vibration</td><td>Mechanical MEMS</td><td rowspan="8">Biomedical
Automotive
Robotics
Consumer electronics
Multimedia
Telecommunication
Mobile phone
Watch industry
Earthquake Detection
Gas Shutoff
Shock and Tilt Sensing
Biochemical warfare detection
Inertial systems for guidance and navigation
Equipment for Soldiers
Aeronautics
Aerospace</td></tr>
<tr><td>Blood pressure sensors
Biocapsules
Bioneedles
Micro-pumps
Micro-valves
Micro-resevoirs
Micro-actuators
Bio-potential electrodes
Chemosensor</td><td>Lab on chip
Drug delivery
Neural probes
Breating rate
Heart rate
Sense organs</td><td>Bio-
Fluidic-
Chemical-
MEMS</td></tr>
<tr><td>Interferometric modulator display
MEMS Polychromator
Micromirrors
Digital MEMS shutter</td><td>Optical modulation
Digital Light Processing
Light deflection and control</td><td>MOEMS
MEMS Display</td></tr>
<tr><td>Inkjet printers pins nozzles
Microphones</td><td>Acousticwave</td><td>Multimedia MEMS</td></tr>
<tr><td>MEMS Actuator array
Thermal MEMS</td><td>Data storage</td><td>MEMS Memory</td></tr>
<tr><td>Micro- fuel cells/reactors
Micro- heat engines/coolers</td><td></td><td>Power MEMS</td></tr>
<tr><td>RF switches/varactors/oscilators
single and multi-throw switches
Phase shifters
Tunable filters/matching networks
Switch matrices</td><td>Microwave</td><td>RF MEMS</td></tr>
</table>

TABLE 1.2: MEMS structures and applications

summarize a part of it. Most of them are fully commercialized and MEMS success stories have been achieved by pressure sensors,accelerometers, inkjet print heads and DLP mirror array. One single look at the call of paper of IEEE-MEMS 2010 conference is enough to realize that the area of activity in the development and application of MEMS is extremly wide.

1.3 RF-MEMS technology

The first radio frequency - microelectromechanical systems (RF-MEMS) were developed under one of DARPA programs. It was in 1991, L. E. Larson [20] presented an MEMS switch and an varactor, specifically designed up to 45GHz. In spite of the immaturity of the RF-MEMS technology at that time, two cutting-edge designs have been demonstrated; one was an ohmic switch coming from Rockwell Science Center [21] and the second one was capacitive contact switch from Texas Instruments [22]. Since then RF-MEMS start to evolute and technologically progress. The fact that RF-MEMS technology suits well to the strong demand for flexibility, complexity, lightweight and low power consumption of advanced

wired and wireless systems, triggers many interest from research institutes and universities [1–4, 23–26]. From 1995 (considered as the RF-MEMS technology trigger point) up to now, a huge number of publications presenting new RF-MEMS concepts follow one after the other but only by the end of the 1990s the research included device reliability issues [27–29]. In fact, the scope of the reliability topic in RF-MEMS goes together with the apparition of MEMS with contacting/touching parts (metal to metal, metal to insulator, metal to substrate or insulator to substrate). From then on new physics of failure and failure mechanisms appears out of this energy transfer [30]. RF-MEMS technology is composed fundamentally by building blocks listed in Table 1.3. Finally performance enhancements and manufacturing cost reduction are evident characteristics of this technology and it is finding its way into next generation timing, wired and wireless applications.

RF-MEMS building blocks (a-b,c)	RF-MEMS circuits	RF-MEMS applications
High-Q μ-mechanical resonators and oscillators (1-125MHz,2.5GHz) MEMS high-Q inductors (1.1-8GHz) BAW resonators** (0.5-11GHz) Tunable capacitros(0.1-100GHz,220GHz) Cavity resonators(40-100GHz,15GHz) MEMS switches(0.1-100GHz,220GHz) Other microwave and milimeter-wave components	Single and multi-throw circuits Phase shifters Tunable filters Tunable matching networks Timing oscillators Switch matrices Programmable attenuators Reconfigurable antennas	Mobile handsets Consumer electronics and Information Technology Wireless network systems (WLAN/WPAN) Base stations Microwave communications RF test and ATE equipment Automotive radar and antennas Satellite transponders Phased arrays* Tactical radio*

* military
** include FBAR and SMR devices
$^{a-b}$operative frequency range
^{c}upper or lower limit (need more development efforts)

TABLE 1.3: RF-MEMS devices, circuits and applications

Performance of RF MEMS switches is truly spectacular when compared to PIN diode or FET switches

Gabriel M. Rebeiz [4]

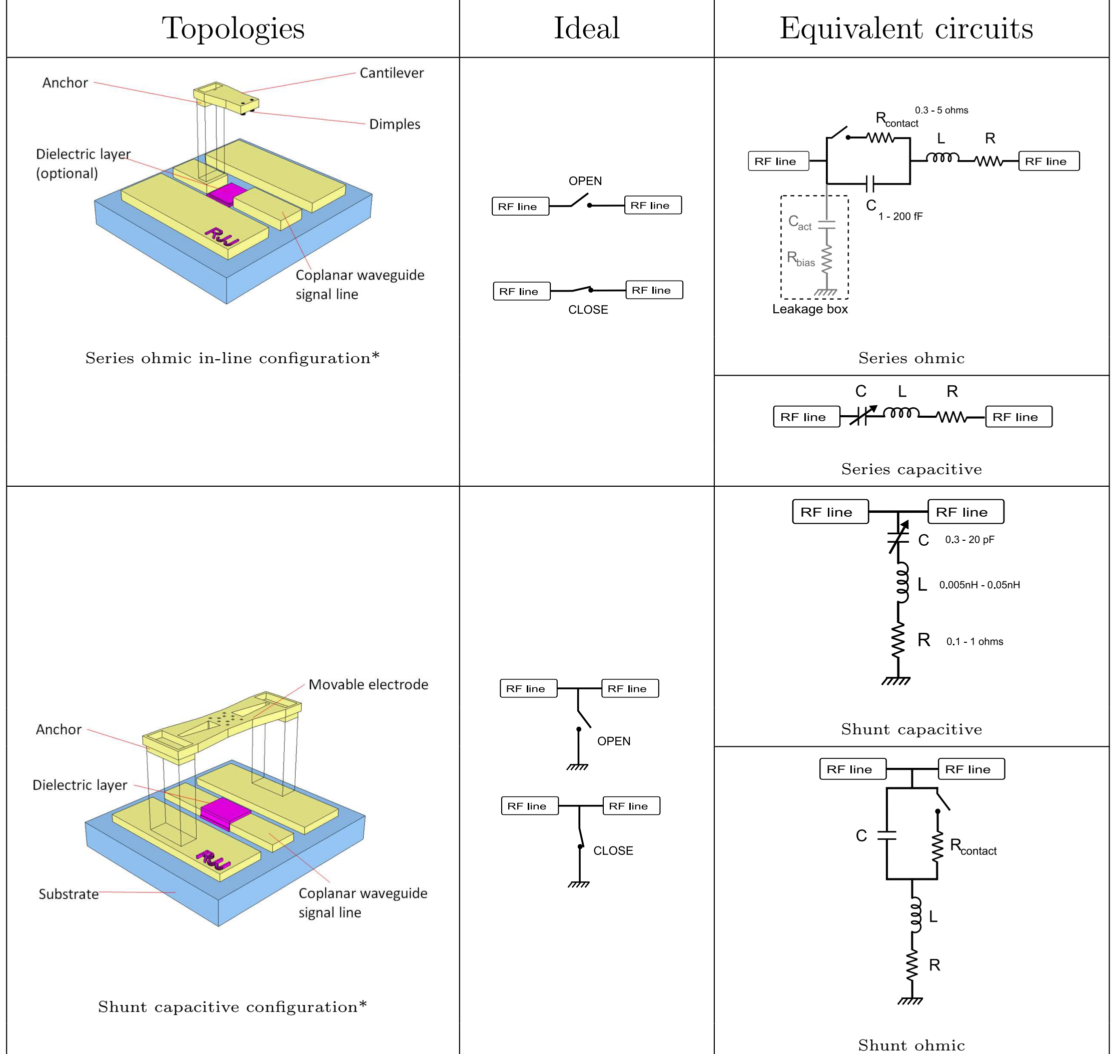

* topologies that works better

TABLE 1.4: Main RF-MEMS switch designs

1.3.1 RF-MEMS switches

1.3.1.1 The designs

RF-MEMS switches are basically used to make a short circuit or an open circuit in the RF transmission line. They can be designed to work at electrical operating frequency from 0.1 up to > 200GHz [31]. Their mechanical displacement can be generated from field forces (electrostatic and magnetic) or molecular forces (piezoelectric, electro-thermal, bi-metallic) and ranged typically from 0.1 to 3μm. The two main topologies are catalogued in Table 1.4 – serial and shunt switches, with their ideal and "*realistic*" equivalent models. Based on these two categories, a huge variety of designs has been demonstrated by optimizing the mechanical

structure (cantilever, fixed-fixed beam, two-pull down electrodes, lateral anchors, U-shape membrane ...) as well as the aforementioned actuation mechanisms in order to achieve fast switching, low actuation voltage operation (also called *control, command or pull-in* voltage) or high power handling.

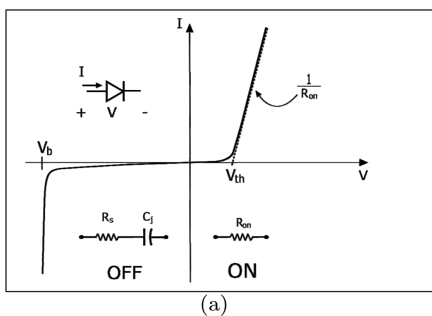

(a)

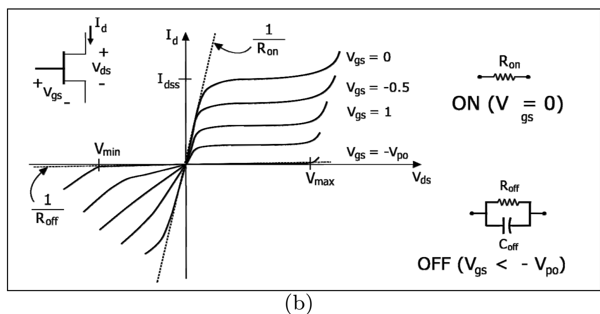

(b)

FIGURE 1.6: Typical I-V graphs of PIN diode and GaAs FET switch, with their microwave equivalent circuit (a) PIN diode (b) GaAs FET device (in the low impedance and high impedance states).

Note: Microelectronic RF switching technologies

▶ **PIN Diode** is a diode with a intrinsic semiconductor region inserted in between two p-type and n-type doped regions. As shown in Figure 1.6(a), when forward biased (on-state) the device exhibits a very low resistive impedance and when reverse biased (off-state) it gives a high-frequency resistance in parallel with a low capacitance. PIN diodes are useful as RF switches (phase shifters), attenuators, and photodetectors.

▶ **FET Switch** is a semiconductor device considered as a type of transistor. Its specific characteristics is the use of an electric field to control the shape and hence the conductivity of a channel of one type of charge carrier in a semiconductor material. Figure 1.6(b) shows that to work like a switch, the FET is DC biased at zero drain-source voltage ($V_{ds} = 0V$), and the gate is biased either zero bias in its low impedance state (on-state) or pinch-off in its high impedance state (off-state) *i.e.* when a negative voltage with respect to the channel is applied. FET switches are often used in digital electronics (Boolean operations), power controls, audio amplifiers and RF switching blocks.

1.3.1.2 RF performances

Comparing microelectronic RF switching technologies, RF MEMS switches offer a substantially higher performance than its electronic counterparts; PIN diode and FET switches. The parameters taken for the comparison are : power consumption, losses, isolation, linearity, manufacturing and final product cost, speed, power handling and control voltage. The comparison survey of the properties is listed out in Table 1.5.

⊕ Electrostatic actuation requires 15-80 V but does not consume any current,

leading to a very low power dissipation [4]. For instance, in a phased array antenna, to perform a 2D scanning, there's over 4000 phase shifters, where each 4 bits phase shifter integrates around 14 elements. If each diode consumes 10mA@0.6V DC current, then the 2D scanning will needs 178W instead of only 0.01W if it is done using RF-MEMS switches.

⊕ RF-MEMS switches are made up of suspended membrane, therefore in series switches the air gaps provide very low off-state capacitance (2-4 fF) resulting in very high isolation at 0.1 - 40 GHz [4]. By the same way, the insertion loss in RF-MEMS switches is less than 0.1 dB up to > 40 GHz. Typical scattering parameters of series ohmic and shunt capacitive configurations is shown in Fig.1.7.

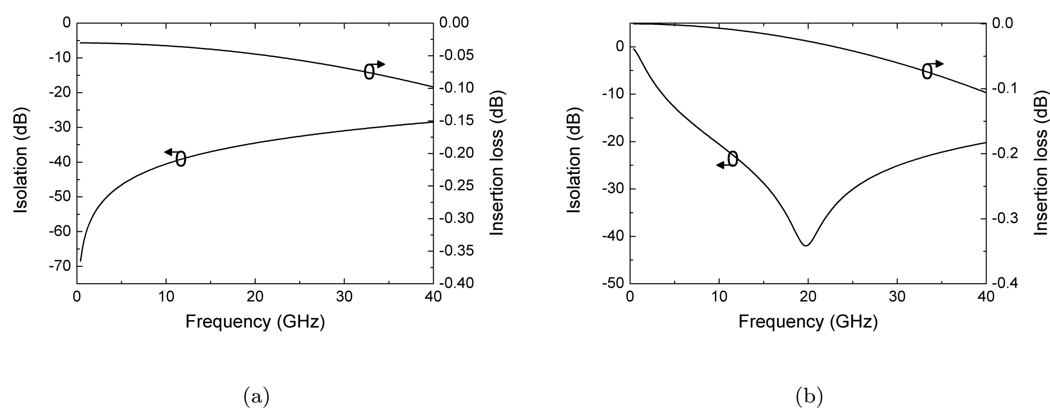

(a) (b)

FIGURE 1.7: Typical S parameters of RF MEMS switches (a) series ohmic and (b) shunt capacitive

⊕ In terms of linearity, RF-MEMS switches does not suffer from nonlinear I-V relationship compared to semiconductor switches. It results in very low intermodulation products.

Since RF-MEMS technology processes are done, using surface or bulk micromachining techniques, with low cost materials and less process steps (Section. 1.2.2), its manufacturing cost amounts to very low. Unfortunately, its final product cost increase with the cost of packaging and the high-voltage drive chip.

⊕ Another very interesting parameter is its ability for integration. Thanks to its relatively easy fabrication processes, RF-MEMS switches can be manufactured with MMIC processes on any substrate material including silicon, GaAs, glass (Pyrex), alumina and also low-temperature cofired ceramic (LTCC).

⊘ The switching time of RF-MEMS switches usually ranges from 1 to > 20 μs, which is too long compared to its counterparts one (especially for

Parameter	Unit	RF-MEMS	FET switch	PIN diode
Size	mm^2	<0.1	~ 1	0.1
Control voltage	V	3 – 80	1 – 10	3 – 5
Control current	μA	<10	<10	3K – 10K
Current handling	mA	~ 200	~ 200	> 20
Power consumption	mW	~ 0.001 – 0.05	1 – 5	1 – 5
Power handling	W	<4	<10	<10
Insertion loss	dB	0.1 up to 120 GHz	0.4 – 2 up to 10 GHz	0.3 – 1.0 up to 10 GHz
Isolation	dB	> 30 up to 100 GHz	15 – 25 up to 10 GHz	20 – 35 up to 10 GHz
Switching time	ns	> 300	1 – 100	1 – 100
Bandwidth	GHz	10 - 30*/ <100**	n/a	0.02–2
Cutoff frequency	THz	20 – 80	0.5 – 2	1 – 4
Third-order intercept point	dBm	> 60	40 – 60	30 – 45
Up-state capacitance	fF	1 – 10 fF**	70 – 140	18 – 80
Series resistance	Ω	<1	4 – 6	2 – 4
Capacitance ratio	–	40 – 500*	–	10
Lifetime	Cycles	$> {}^{a}10^{13}$ or $> {}^{b}10^{7}$	$> 10^9$	$> 10^9$
Final cost	$	8 – 20	0.3 – 6	0.9 – 8

* shunt capacitive
** series ohmic
[a] cold switching
[b] hot switching

TABLE 1.5: Performance comparison of switches based on RF-MEMS, FET and PIN diodes [4, 5, 8, 24, 39] and updates.

telecommunication and radar applications). However it is possible to create sub-microsecond switching RF-MEMS devices [32, 33] in compensation for high control voltage.

⊖ In general, RF-MEMS switches can operate and handle in the range of 0.02–0.8W in power. Fortunately several promising designs have been shown handling up to 4 and 8W [34–38].

⊖ The fact that the actuation voltage of reliable electrostatic RF-MEMS switches is often very high, requires additionnal voltage up converter chip when integrated in portable systems.

Finally, the two main issues of RF-MEMS switches is the packaging and the reliability. They need to be packaged in inert atmospheres (nitrogen, argon, hydrogen, helium) and (quasi-)hermetic seals. Currently, packaging cost is still a part important of the final product and the package itself can affect the reliability of the device. The reliability of mature RF-MEMS devices can reach a few billion cycles. However electronic systems require more than 10 years reliability and long-term test has not yet been addressed. Reliability "*in the large sense of the word*" and accelerated lifetime test in RF-MEMS will be the main concern of this manuscript.

RF-MEMS circuits	Application fields				
	Phased array antennas*	Satellite transponders	Automatic Test Equipments	Base stations	Mobile telephony
Single and multi-throw switches	x	x	x	x	x
Phase shifters	x	-	-	-	-
Tunable filters	x	x	-	x	x
Tunable matching networks	x	x	-	x	x
Timing oscillators	-	-	-	-	x
Switch matrices	-	x	-	-	-

^{x} might be implemented in

* military, aeronautic, automotive radars

Table 1.6: Main application fields of RF-MEMS switches

1.3.2 Applications of RF-MEMS switches

RF-MEMS technology is entering into the next generation timing and wireless applications. This technology has opportunities in analogue and digital applications, such as in satellite and fibre-optic communication systems, in cellular phones and other wireless equipment, in automatic test equipment, and for other diverse civilian and military uses. This concept enables superior reconfigurable functions, using in particular;

• Switching networks/Switch matrices/Switched filter banks for satellite and wireless communication systems.

• Phase shifters/Phased array antennas for satellite based radars, missile systems, long range radars and automotive radars.

• High-performance switches/Programmable attenuators for instrumentation systems.

Table 1.6 shows the possibilities of RF-MEMS circuits that may be implemented into the system level. The very interesting performances of RF MEMS switches (both metal-contact and capacitive) have triggered a thousand and one inventiveness of many designers to build cutting-edge switching circuits in the frequency range of 0.1 to >120 GHz. In terms of illustration, instead of presenting state of art components, this section shows examples of several RF-MEMS circuits designs from LAAS-CNRS.

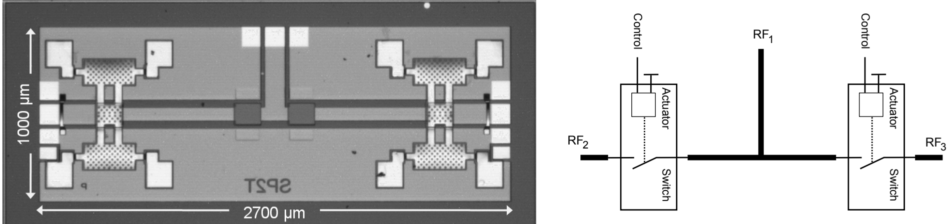

FIGURE 1.8: A K-band Single Pole Double Throw Circuit (*designed by V. Puyal*)

1.3.2.1 Single Pole Double Throw

Single-pole N-throw (SPNT) switches are often used in N×N switching matrices and filter or amplifier selection. The basic one is the SPDT (single-pole double-throw) routing switch. The one shown in Figure 1.8 is build with K-band shunt switches. It consists of a tee with a RF-MEMS at each of the output(RF_2 and RF_3). The switches are placed at a distance of a quarter guided wavelength from the tee junction so that when one switch is actuated, the virtual RF short is assimilated as an open at the junction and the signal is routed away toward the other RF path. RF-MEMS based SPNT becomes very attractive over their solid state counterparts, mainly prompted by the power consumption and the linearity. They result in much smaller and lighter systems as well, which is for instance essential for satellite applications.

1.3.2.2 Phase shifter

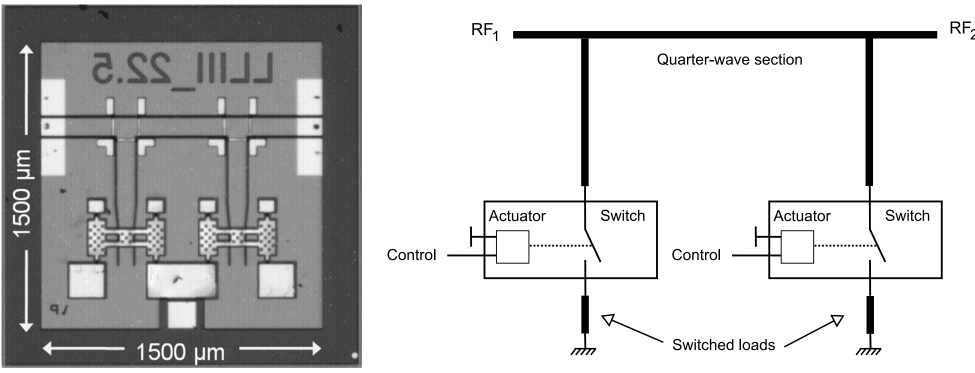

FIGURE 1.9: A 60 GHz Loaded-line Phase shifter (*designed by V. Puyal*)

RF-MEMS based phase shifters exist in several configurations namely switched line , loaded-line, reflection and high-pass/low-pass. This example deals with a 1-bit V-band loaded-line (22.5 degree) phase shifter [40] (Figure 1.9). The two loads induce a perturbation in the phase of the signal when switched into the

circuit, while they have only a small effect on the amplitude of the signal. The amplitude perturbation can be minimized and equalized using a quarter-wavelength spacing between the reactive loads. In terms of phase versus frequency response, this kind of phase shifter is usually flatter than the switched line phase shifter, but less flat than the high-pass/low-pass phase shifter. Only one control signal is required for this loaded-line phase shifter, since the loads can be biased simultaneously. The implementation of phase shifter in phased array antennas allows the development of passive reflect array at X- to W-band frequencies. The cost is also another factor because reflect arrays are much less expensive than standard phased arrays.

1.3.2.3 Tunable filter

Tunable filters are key elements used in advanced transceiver architectures. Bandpass filter is used for its good selectivity and sensitivity and bandstop filter is used to eliminate undesired signals such as spurious responses or cross-talk interferences (in transceiver configuration). From design to characterisation, both aforementioned tunable filters have been presented in [41]. It consists of using CPW quarter wavelength stubs and MEMS switches : two cantilever shunt switches. The example shown in Figure 1.10 is the TBPF topology. The stubs have different geometrical lengths, which are translated into two zeros in the transmission coefficient and it results in a bandpass behaviour. Adding a MEMS switch at the end of the stubs will makes the filter tunable.

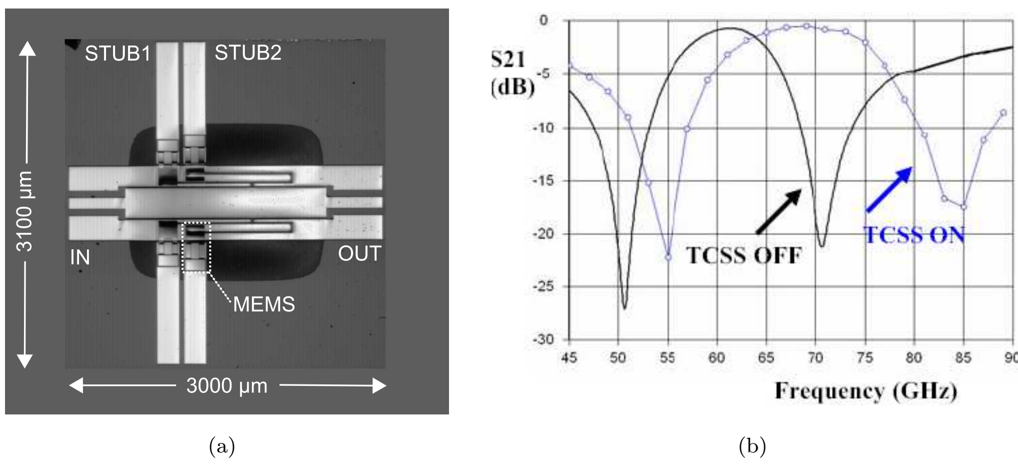

(a) (b)

FIGURE 1.10: V-band Tunable Band Pass Filter (a) fabricated device and (b) simulated transmission coefficient [41]

1.3.2.4 Tunable dual behaviour resonator

Another interesting tuning element is the dual behaviour resonator (DBR) because it allows the control of two attenuated bands on either side of one bandpass [42]. In fact the DBR topology consists of two different open-ended stubs which bring a transmission zero on either side of a pass-band. MEMS switches can be used to change the length of the inter-stubs line in order to tune the center frequency and keep a correct matching level. Figure 1.11 shows a DBR resonator which was realized in thin film microstrip technology implemented in Si-BCB substrate.

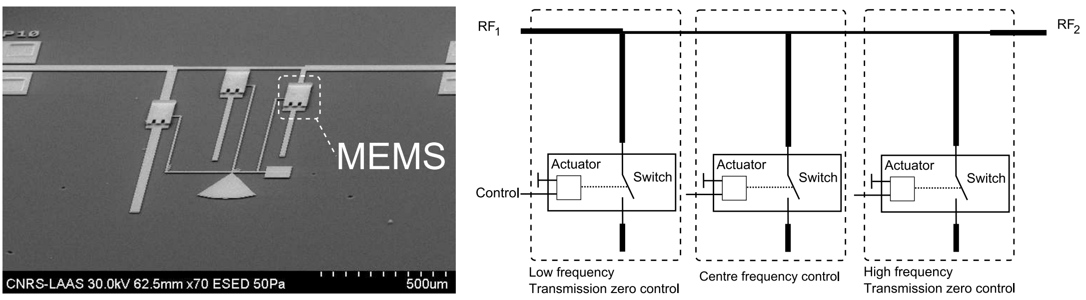

FIGURE 1.11: W- to V-band tunable resonator [43]

1.3.2.5 Tunable matching network

Tunable matching network is interesting to be used in real-time adaptable RF front-ends, in order to maintain low loss and high linearity. Implementing RF-MEMS within such a system will minimize degradation to the overall amplifier performance. The design shown in Figure 1.12 illustrate impedance tuner based on the distributed MEMS transmission line (DMTL). The main idea is to maintain the matching performance over a broad bandwidth by changing the physical length of the transmission line.

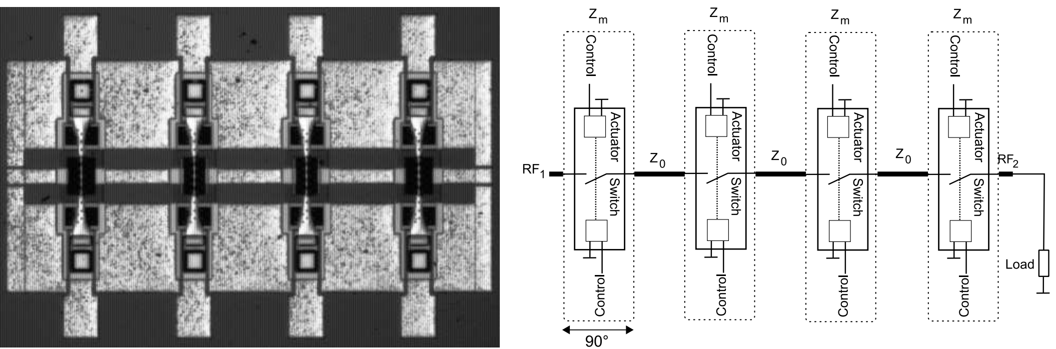

FIGURE 1.12: Tunable matching network

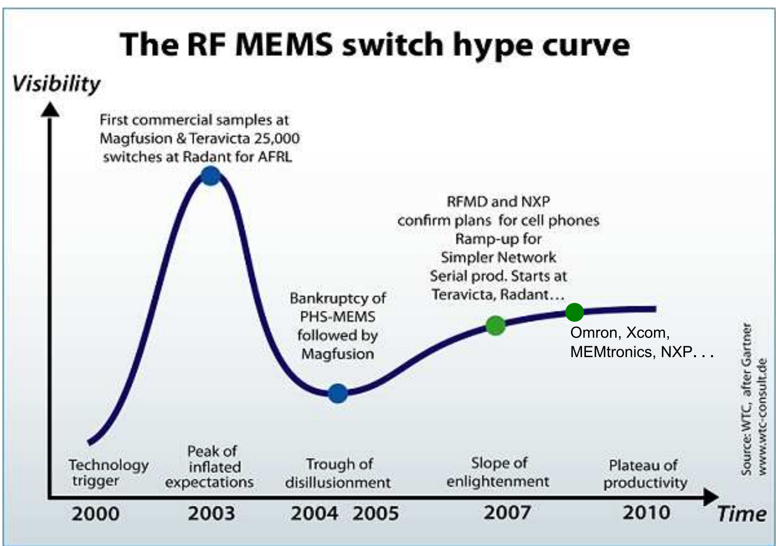

FIGURE 1.13: The RF MEMS switch hype curve [44].

1.3.3 Industry and market roadmap

In this section, a survey has been carried out of several market studies from WTC,Yole Development,ARRRO (Applied Research Roadmaps for RF MEMS Opportunities), iSuppli Corporation and Mancef, in order to state today's market of RF-MEMS switches and foresee the RF MEMS switch volume needs upto 2012. It will let us have a glance to the global economic and market background.

MEMS components have emerged in the mid-1990s under a DARPA's military radar program [10]. RF-MEMS switches came into the spotlight only in the early 2000s. With their remarkable RF performances, RF-MEMS components have created a lot of excitement, but their commercialization is eagerly-awaited. Happily, if we look at the hype curve [1] of RF MEMS (Figure 1.13), it shows that RF MEMS switches will reach the "Plateau of productivity" soon, as the industry and technology are both maturing. The first commercial micromachined RF device was the FBAR duplexer from Agilent Technologies. It is a set of piezoelectric filters that separate incoming and outgoing signals in the frequency range of 800 MHz and 1900 MHz. But it may not be complex enough to be considered as a "true" MEMS. In the meantime, other RF MEMS products have become commercially available, including switches (Omron, Radant, XCOM Wireless, Wispry...), inductors and micro-mechanical resonators (Discera, SiTime, Silicon Clocks). In order to be consistent, all roadmap studies:

1. The hype curve was first proposed by Gartner, an analyst/research house based in U.S. as a way to place technologies in their particular stage of evolution

• considered the stand-alone device and not global systems that include MEMS devices,
• volumes and prices are for the lowest level packaged MEMS device,
• and consisted of in-depth interviews with around 100 key industry experts in the field of MEMS technology.
The market forecasts have been done by paying attention to (1.3.3.1) the potential applications of RF MEMS switches, (1.3.3.2) major companies in production and also (1.3.3.3) the total volume needs upto 2011.

1.3.3.1 Potential applications

RF MEMS switches are in development for a very wide spectrum of applications. For the market analysis it can be fragmented into six major application fields (Table 1.7);
• ***Automated Test Equipment*** (ATE) for semiconductors is the first commercial application for RF MEMS switches. Here the use of RF MEMS switch is to replace conventional relays without changing the whole system and therefore the implementation of MEMS is quick and easy. While its integration into RF instrumentation equipment is expected at the earliest in 2009, mostly due to power handling issues.
• ***Cell phone*** industry was very interested to use RF MEMS technology to develop T/R switch, multiband filters, filter banks, impedance matching networks, and so on. But reliability and packaging difficulties, represented by the "trough of disillusionment" phase in Figure 1.13, created a lot of disappointment. Nevertheless, NXP, RFMD and WiSpry still believe and develop impedance matching networks for the power amplifier (PA) or MEMS-based reconfigurable antenna module, which offer the best prospects for RF MEMS switches in this market.
• ***Automotive applications*** such as RF MEMS based long range radar or phase shifter technology for phased array, have no envisioned opportunities for RF MEMS in the 2006-2012 time frame. The market is dominated by SiGe technology (3rd generation of 77 GHz ACC systems / Precrash systems).
• ***Satellite applications*** tend to evolute towards higher frequencies and increase the integration with greater functionality. Consequently, there's is a need for complex redundancy scheme, large microwave routing network and reconfigurable antennas. RF-MEMS switches fit well to the specific space application needs.

	Application	Frequency	Reliability	Product configuration
ATE	RF instruments	DC - 40 GHz	0.1 to 10 billion cycles	SP2T
	ATE commutation boards	DC - 10 GHz	0.1 to 10 billion cycles	SP4T
	Others	DC - 10 GHz ...	0.1 to 10 billion cycles	SP2T, SP4T, ...
Cell phone	Reconfigurable architecture	0.6 - 6 GHz	0.1 to 10 M cycles	SP4T, SPxT
Auto motive	Long range radars	77GHz	1 to 10 billion cycles	Phase shifters
Satellites	Redundant circuits	12 - 40 GHz	1 M cycles but 18 years guaranty	SP2T Monolithically integrated
	Reconfigurable commutation matrix	12 - 40 GHz	1 M cycles but 18 years guaranty	Matrix
	Steering Antenna	12 - 40 GHz	100 M cycles	Phase shifter
Military	Telecommunications	20 - 50 GHz	0.1 to 10 billion cycles with 15 years operation warranty	SPxT
	Radars	MHz, 10GHz, upto 94 GHz bands	1 to 10 billion cycles with 15 years operation warranty	Phase shifter
Telecom Infrastructure	BTS redundant circuits	0.6 - 6 GHz	0.1 to 10 billion cycles	SP2T
	Multiband BTS	0.6 - 6 GHz	0.1 to 10 billion cycles	SPxT
	Automation of the last copper mile network maintenance	0.6 - 6 GHz	0.1 to 1M cycles	Matrix 16×

Table 1.7: Potential application fields of RF MEMS switches [44].

• ***Military applications*** have historically driven the development of RF MEMS switches in the US and still does. The volume application in this field will be phased array antennas for communication (multiband radio, data communications and satellite communication across the board) and radar (low frequency imaging, tracking radar and missile seekers and radiometry applications).

• ***Telecom infrastructure***, e.g. base station products required to serve the various markets, bands and standards. Hence base station manufacturers are confronted with the need to offer a broad selection of products in order to support the technology migration strategies of operators. Therefore, a reconfigurable base station system that can serve multiple bands is necessary. In this reconfigurable sense, RF MEMS switches are good candidates.

1.3.3.2 Major companies

Funding of RF-MEMS switch start-ups started in 2001 with Teravicta, Magfusion and MEMX. Since then, more than 60 industrial companies have been worldwide referenced including MEMS start-ups, IC manufacturers, manufacturers of passive

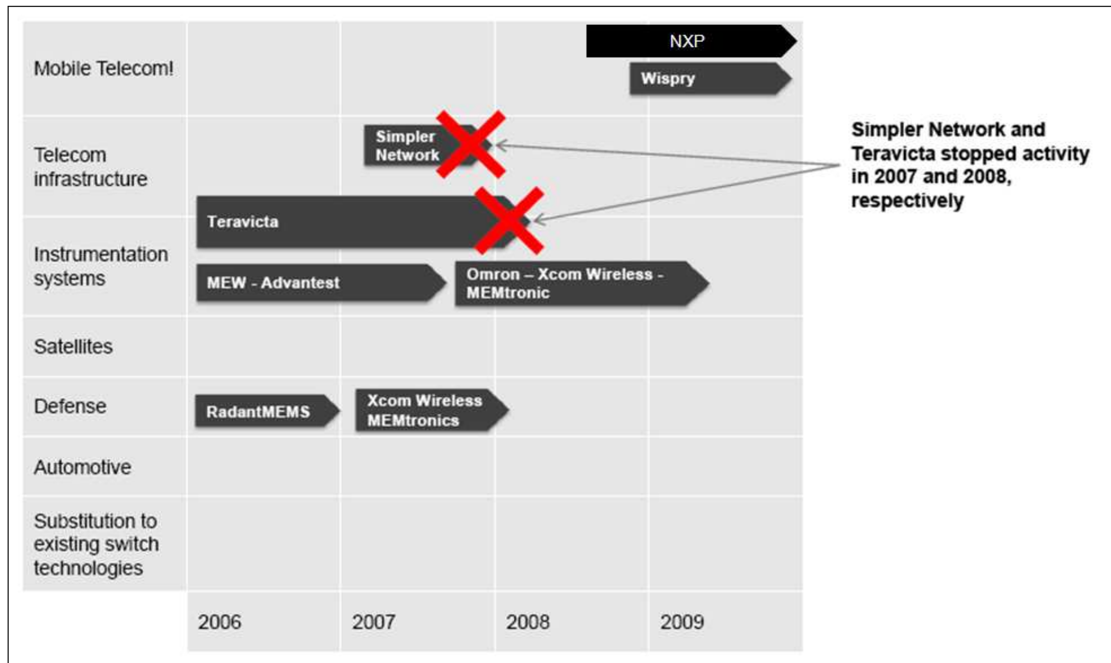

FIGURE 1.14: Companies in production of RF-MEMS [45].

RF devices and integrators. These companies where mainly targeting industrial and high volume applications. Alternatively specific development from WiSpry and NXP focuses on RF MEMS switches for radio handset applications. Then came the "trough of disillusionment" period (2002-2005) where unsatisfied announcements of commercial samples reduced the trust in RF MEMS switch products. Fortunately, RF MEMS switches have left this period for the much more enjoyable "slope of enlightenment". The table of the major commercialisation leaders worldwide after this period and the areas they are involved in is given in Figure 1.14. Despite the stop of two activities in 2007 and 2008 (Teravicta, SimplerNetwork), several additional companies are in volume production: Omron, XcomWireless, MEMtronics, Wispry. This dynamic around the RF MEMS switch shows that the opportunities for suppliers will be in the field of; single components for ATE, phase shifters or tunable filters for base station or defense and aerospace, and modules for wireless handsets.

1.3.3.3 Total volume needs

One of the most interesting parts of the market analysis of RF-MEMS is probably the anticipation of the volume needs of RF-MEMS (Table 1.8). In fact the RF-MEMS switch market, which is the reflection of the volume needs (Figure 1.15), reached a close-to-insignificant $6 million in 2006. Hopefully, the global RF MEMS

	2006	2007	2008	2009	2010	2011
Telecom infrastructure	0	0	0,000	0,06	4,9	25
Telecom handsets	0	0	4,1	92	339	754
RF Relay Substitution	0	0	0,000	0,0	0,2	1
Automotive	0	0	0	0	0	0
Defense	0,001	0,004	0,010	0,022	0,045	0,072
Space	0	0	0	0	0,0000	0,0001
Instrumentation	0,032	0,15	0,05	0,19	0,4	0,7

in Million units

TABLE 1.8: Total volume needs of RF MEMS switches 2006 - 2011 [45].

switch market is expected to show a 80% CAGR [2] on the 2009-2011 period. It will represent a $475 million in 2011, mainly dependant on high volume needs applications such as handset applications and Telecom infrastructure. The other volume needs of RF MEMS switches for medium to low volume applications will increase after 2011, when it will reach the right price point. Nevertheless, attention should be also paid to alternative and new competing technologies such as SoS FET or ferroelectric devices (like shown in automotive radar and roof antennas).

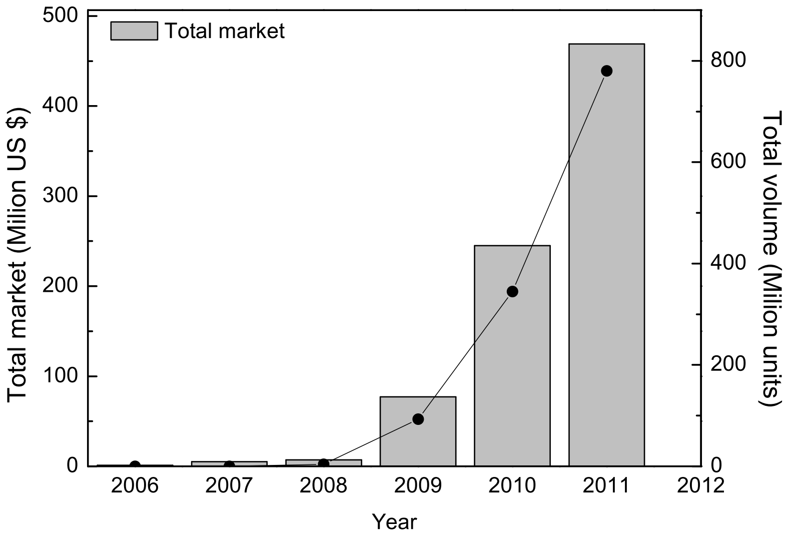

FIGURE 1.15: The RF MEMS switch total market [45].

2. ***Compound Annual Growth Rate*** is a business and investing specific term for the year-over-year growth rate calculation of an investment over a specified period of time

Process	Switch type	Characteristics	Material or dielectric	Maturity
ISIT MPW	Capacitive switch, MEMS capacitors	Actuation voltage ~ 40V, wide band, S_{21} <-25 dB @ Ku band, IL= ~ 0.8dB @ Ku band, low mechanical resonance frequency, cost efficient.	AlN, Si_3N_4 or Ta_2O_5	H
IRST MPW	Serie and shunt type, clamped beams, cantilever beams	$V_{pull-down}$ = ~20V-26V, $V_{return-up}$ = ~16V-24V, IL= -0.5 dB @ 20 GHz, S_{21} >-25 dB @ 20 GHz, CMOS compatible, cost efficient	LTO (SiO_2)	H
VTT MPW	Switches, Varactors, MEMS capacitors	CMOS compatible, 200 GHz RF MEMS circuit @ G-band, $V_{pull-down}$ = 4V-5V, upstate Q_{mems} @ 170 GHz = 90, downstate Q_{mems} @ 170 GHz = 28	PECVD Si_3N_4	H
WATERLOO MPW	Capacitive contact cantilever with dimples	IL < 0.3 - 0.4 dB and S_{21} = -25 dB @ C-band, DC contact switch or dielectric-less device (feasible)	SiO2	H
CEA-LETI Metal membrane capacitive electrostatic switch fabrication process	Capacitive switch	$V_{pull-down}$= 30 - 40V, IL < 0.5dB, S_{21} = -20 dB @ 20 GHz, tested upto 25×10^{10} cycles without failure, low complexity	SiO_2 or Si_3N_4	H
CEA-LETI Nitride membrane ohmic electrostatic switch fabrication process	DC-contact nitride-membrane switch	IL = 0.15dB @ 5 GHz, 0.3 dB @ 30 GHz, S_{21} = -36 dB @ 5 GHz and 20 dB @ 30 GHz, t_{switch}= 0.5-2 μs, Cycling: 25×10^{10} cycles	SiN membrane	H
CEA-LETI Piezoelectric process	Piezoelectric actuated capacitive switch		Piezo material : AlN	L
XLIM fabrication process for fast switching capacitive RF MEMS	Fast switching capacitive switch	t_{switch}=150-400ηs, 14 billion cycles, poor capacitance ratio 2.3, high actuation voltage due to the stiffness, Q_{mems}=100 @ 10 GHz and Q_{mems}=50 @20 GHz are expected	Al_20_3	L
LAAS	Capacitive switch, MIM capacitors	t_{switch}10-20μs, $V_{pull-down}$ = 18-30V, $\frac{C_{on}}{C_{off}}$= 20-40, IL 1dB @ 10 GHz, S_{21} = -30 - -40 dB @ 10 GHz	SiNx	L
LAAS Si-BCB process	Contact switch	t_{switch} <0.5μs, $V_{pull-down}$ = 60-70V, IL 1.9 dB @ 60 GHz, S_{21} <-14 dB @ upto 110 GHz, tested upto 3M cycles without failure	Au	L

Switch type are the different kind of possibilities using the design rules proposed by the manufacturer.
Characteristics recap the performances or drawbacks of the devices.
Material or dielectric (capacitive switches) shows the dielectric material used in capacitive switches and other original materials if used.
Maturity show the reproducibility of the process, for instance MPW and industrial runs have high (H) maturity due to their stable process flow, in the other hand, for low (L) maturity, we have reported information from published papers showing expected results if the process is improve.

TABLE 1.9: Fabrication technologies overview.

Process	Switch type	Characteristics	Material or dielectric	Maturity
LG fully wafer-level packaged RF MEMS piezoelectric actuators process	Original design of piezoelectric capacitive switch with DC contact	IL = 0.63 dB and S_{21}= -26.4 dB @5 GHz, $V_{pull-down}$ = 5V. The measured packaged loss = 0.2dB and return loss = 33.6 dB @ 5 GHz	PZT	?
KTH Microsystem Technology Lab.	Mechanically SPDT metal-contact	$V_{pull-down}$=39 - 89V is use only for trigger between 3 stable states, S_{21}=-43 dB @ 1 GHz and -22dB @ 10 GHz, total IL including T-junction = 0.31 dB @ 1 GHz and 0.68 dB @ 10 GHz, low complexity.	Dielectric-less, Au	H
University of ULm	Bi-stable micro actuator	V_{switch} = 12V (déflection ∼10μm) , consuming energy of 700mJ, large switching forces, in the range of hundreds of μN	Nano-diamond on $Al_2 0_3$ substrate	L
Toshiba fabrication process of piezoelectric tunable MEMS capacitors	Piezoelectric tunable MEMS capacitors	$V_{actuation}$ = 3V and its self resonance frequency = 18GHz. No reliability results are reported in the paper	AlN, SiN	?
EADS	Cantilever	Low complexity, cost efficient, particularity : air gap ∼17μm, $V_{pull-down}$=40V - 80V, IL= -0.3dB @ 22 GHz - 40 GHz, S_{21} = -15 dB @ 22 GHz (for cantilever with L = 500μm),operation up to 120řC, 10^9 switching cycles	plasma oxide	H
Radant	Ohmic cantilever switch (wafer caped)	More than 10^{10} cycles, IL 0.4 dB and S_{21}= -20dB @ 10 GHz (for 2-contact switch, $R_{contact}$ = 2Ω) and 0.2 dB and -27dB @ 2 GHz (for 8-contact switch $R_{contact}$ =3Ω), wafer scale package has exceeded 30 billion cycles	All metal surface-micromachining	H
Teravicta	SPDT RF MEMS switch	100 million cycle, 70sec switching time, 0.1dB of insertion loss @ 1GHz, 35dB return loss @ 1GHz, -30 dB S_{21} = @1GHz, switch up to 30W RF power, compatible CMOS	Bulk metal	H
		K band, DC to 35 GHz, IL 0.4dB @ 20GHz, more than 20 dB return loss @ 20GHz, isolation -20dB@20GHz	Bulk metal	H
NXP (PASSI^{TM})	MEMS Tunable capacitors	Tuning ratio of 4.5, quality factor 100 < Q < 300 @ 0.5-4 GHz, need a hermetic package, cost efficient process	$Al_2 0_3$	H
Baolab (PolyMUMPS technology from MEMSCAP)	Micro-relays (SPDT)	Low voltage contact micro-relay (below 5V)	Dielectric-less	H
Mitsubishi Electric Corporation	RF passives / metalized air cavity	Air gap = 30μm, IL = 2dB, RL=21 @ 12GHz for 90° hybrid cavity, Manufacturing cost efficient, high applicability	SiN membrane	H
Omron	Surface-mounted SPDT contact switch	Miniature, S_{21}=-30 dB@10 GHz band, IL = 1 dB @10 GHz band, 100M cycles reliability guaranteed, power consumption of 10 μW.	Oxide, Al, oxide	H

Continuation of Table 1.9.

1.3.4 Status of the fabrication technology and the reliability

1.3.4.1 Present fabrication technologies of RF MEMS

RF MEMS switches are still an emerging technology. They outperform other microwave switching technologies but improvement in term of reliability is crucial. As aforementionned, RF MEMS switches also need to continuously improve their performances faced with alternative technologies. Therefore, the fabrication process should be well known in detail (in companies and even research laboratories). Table 1.9 summarize a few protagonists involved in the fabrication of RF MEMS devices; on multi-project wafer, in academic process and in industry. It is classified by *switch type*, *original characteristics of the component*, *materials* and *maturity* of the fabrication know-how. Many aspects dealing with the fabrication process reliability of MEMS switches are still not well understood and are currently under investigation. To name a few, the effect of temperature on the planarity of low stress films, the effect of packaging procedures on the performances, the effect of gases or organic materials. Nevertheless, the global maturity reported in Table 1.9 and the trend of the future RF-MEMS market (Figure 1.15) show that several of these problems will be solved in the coming years.

1.3.4.2 Reliability of RF MEMS

Since the end of the 1990s, every publication dealing with RF MEMS switches has a discussion on reliability. In fact, it is a major challenge for the successful application of RF MEMS switches, they must demonstrate the ability to switch reliably over billions of cycles. The high packaging cost, the most expensive step in the production will limit the price of commercialization. Moreover, power handling capabilities (>1W) is still a major issue for long-term reliability of RF-MEMS switches. For DC-contact switches, the main failure mechanisms comes from the metal contact area damage and it results in a increase the contact resistance of the switch, while for capacitive switches, the predominant failure mechanism is due to stiction between the dielectric layer and the metal layer due to the large contact and also the charge injection and charge trapping in the dielectric layer. In these contexts, much work remains to be done in the development of modeling and design methodologies for the multi-physics multi-domain devices characteristic, and their proper methodology and reliability assessments. This

thesis will focus on the following reliability aspects: ***charging mechanism*** within or surrounding the device, ***power handling***, ***radiation related effects*** and ***electrostatic discharge (ESD) events*** that impair the reliability of micro-gap devices. Another significant part of this study deals with ***accelerated testing*** in capacitive RF-MEMS switches using short impulse signals. Finally to foster optimistic opinion on reliability in RF MEMS switches, extremely reliable switches have been fabricated after 12 years of research and funding. Tables 1.10a and 1.10b summarize the recent reliability results for DC- contact switches and capacitive shunt switches respectively.

TABLE 1.10A: Reliability summary of RF MEMS metal-contact switches [46].

	RADANT (Emperor)	**RFMD**	**XCOM**	**OMRON**
Actuator type	Cantilever	Cantilever	Cantilever	Bridge
Actuator material	Au	Au	Au	Silicon
Substrate	Silicon	SOI (on CMOS)	Silicon	Silicon
Actuation voltage (V)	90	90	90	10-20
Unipolar/bipolar actuation	Unipolar	Unipolar	Unipolar	Unipolar
Switching speed (μs)	10	5	30	300
Metal contact $R_{on}(\Omega)$, C_{off} (fF)	4, 25 (2-contact) 2, 50 (8-contact)	1, 15	1-2, 4	0.5, 5
Package type	Hermetic wafer cap	Hermetic dielectric cap	Ceramic hermetic cap	Wafer package ,glass frit
Reliability (# of switches tested)	>200B[a] at 20 dBm (>100) >1,000B[a] at 20 dBm (>6) >10B[a] at 30 dBm (>50) >100B[a] at 30 dBm (>5) >10B[a] at 40 dBm (>10) >200B[a] at 40 dBm (2)	100-1,000M at 10 dBm	100M at 1 mA	10M at 10 mA (>100)
Cycle frequency (kHz)	20[b]	5	<1	0.5[b]

[a] All reliability tests stopped before switch failure
[b] All switching waveforms have -50% duty cyle

Kan poul lévé lasou dizé, a manjé li ka sasé

French Guiana's Creole proverb

TABLE 1.10B: Reliability summary of RF MEMS capacitive switches and switched-capacitors [46].

	MIT-LL (Emperor)	**Raytheon (Emperor)**	**MEMtronics**	**WISpry**	**UCSD**	**USCD**	**Xlim (Limoges)**
Actuator type	Cantilever	Bridge	Bridge	Cantilever	Cantilever	Bridge	Cantilever
Actuator material	Al	Al	Al	Al	Au	Au	Au
Substrate	Silcion	Silicon, Alumina, GaAs, Quartz	Quartz, Glass	Silicon (on CMOS)	Fused silica	Fused silica	Fused silica
Actuation voltage (V)	55-65	30-40	25-40	35 (3 V on chip)	30-40	30-40	60
Unipolar/bipolar actuation	Alterning	Unipolar	Both	Unipolar	Unipolar	Bipolar	Unipolar
Switching speed (μs)	20	5	10	<100	0.8^e,50^f	1	10-20
Capacitance ratio	150:1	50:1	10:1-20:1	10:1-20:1	5-7:1	4-5:1	9:1
Package type	Hermetic wafer cap	Hermetic wafer cap	Wafer level Liquid	Thin-film semihermetic wafer cap	Unpackage^c	Unpackage^c	Unpackage^d
Reliability^{a,b} (# of switches tested)	>600B at 0 dBm (6)	>200B at 20 dBm (2) >150B at 20 dBm (4) >100B at 10 dBm (5)	>100B at 20 dBm	N/A	2B at 30 dBm (1)^e 100B at 30 dBm(1)^f	>20B at 20 dBm (5) >5B at 27 dBm (5)	>1B at 10 dBm (>5) >20B at 10 dBm >2B a t33 dBm
Cycle frequency (kHz)	5	5	20-40	N/A	50^e, 15^f	50	N/A

[a] All tests stopped before switch failure
[b] All reliability tests done at 10-35 GHz when dBm is quoted
[c] Tests done in lab ambient environment
[d] Tests done in vacuum chamber backfilled with N_2
[e] UCSD Mini-high Cr design
[f] UCSD High-Q design

Discover through the eyes of a child and do it with the hands of an expert

Chapter 2

Failure mechanisms in capacitive switches

This chapter provides an overview of the state of the art for the main failure modes and underlying failure mechanisms in RF-MEMS switches reliability. The specific issues of capacitive RF-MEMS switch caused by stiction due to surface forces and electric charge are discussed. It covers some basic physics related to dielectric charging, power handling, radiation, electrostatic discharge in capacitive switches. The effect of packaging on reliability is not discussed in this thesis.

2.1 Failure modes and failure mechanisms

Definitions

The IEEE defines 'reliability' as the probability that a system or device will perform its required functions under stated conditions for a specified period of time. Usually this definition can be interpreted as; *required functions* correspond to the expected satisfactory operation, *stated conditions* concern the overall environment conditions (mechanical, thermal, environmental and electrical conditions) and finally *stated period of time* means that we require a definite operation time, which is ruled by the dedicated application. The mass production of RF-MEMS switches is more challenging than expected, due to its 'reliability'. Unfortunately, reliability concerns is often the last step that is considered in a new technology development. The first steps are dominated by the race for

performances i.e. design for performance, functionality and feasibility studies. Whereas reliability should be taken into account at each stage from design to packaging. Worded differently, very close interaction should be taken place between designers, processing engineers, packaging specialist and simulation, test and reliability engineers. As a result, it will shifts the *bathtub curve*[1](Figure 2.1) lower by taking into account the effect of design, processing, packaging and also environment [47]. There are two main approaches to assess the reliability of a

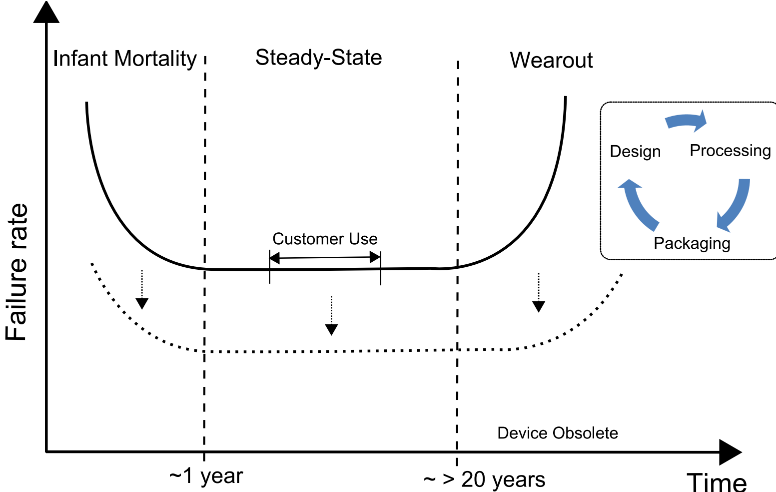

FIGURE 2.1: The 'bathtub curve' for reliability development.

novel technology. The coventional approach is by applying standard reliability test procedures given in MIL-handbooks[2] or IEC-standards[3], also called 'stress test driven qualification methodology'. However in the frame of MEMS devices, certainly in the case of RF-MEMS switches, those standards are not applicable [47]. Therefore the 'failure driven qualification methodology' seems to be more appropriate between the functionalities of the component and the qualification procedures. In this case, a detailed, well known and well understood database of failure modes and failure mechanisms need to be indexed (Figure 2.2). Typically Failure Modes and Effects Analysis (FMEA)[4] can be done in order to brainstorm potential failure modes. The methodology consists of, in a first time, defining the expected failure mechanisms that can happen. Then stresses are performed in order to identify failures and build the database. Once the MEMS-specific failure

1. In reliability engineering, the bathtub curve curve is generated by mapping the rate of early "infant mortality" failures when first introduced, the rate of random failures with constant failure rate during its "useful life", and finally the rate of "wear out" failures as the product exceeds its design operation time.

2. http://www.mil-standards.com/

3. http://www.iec.ch/

4. http://www.amsup.com/fmea/index.htm

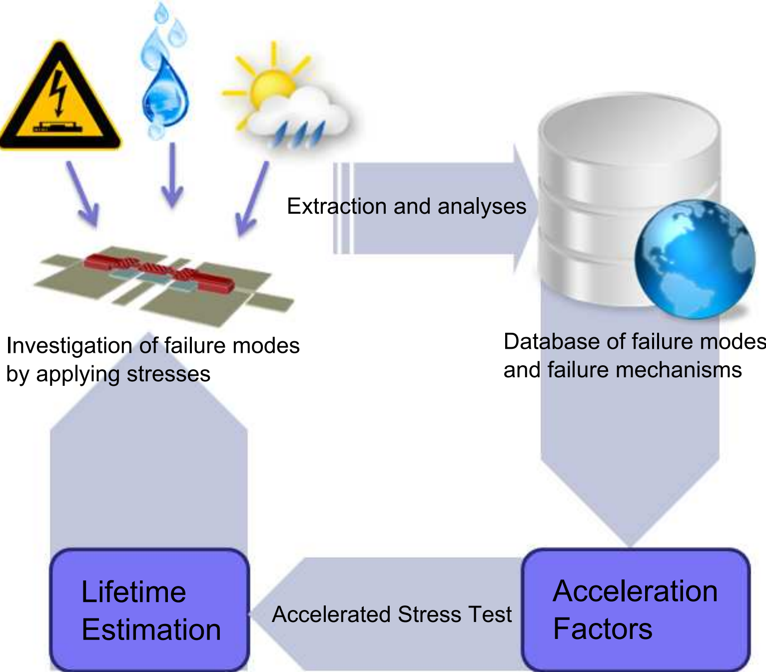

FIGURE 2.2: The failure driven qualification methodology.

mechanisms are detected and well understood, accelerated stress tests can then be defined. So Acceleration Factors (AF) are estimated using experimental data and it is used to estimate time compression and thereby the operation time of the device under test.

$$Test_time = \frac{Operation_time}{AF} \tag{2.1}$$

Confusion is often made on the terminology used in failure analysis and therefore a clarification on the definition of the several terms is given. This relies on the terminology defined in the frame of AMICOM project [48];

- ***Failure analysis :*** *When a failure occurs, i.e. the device does not perform anymore according to the specifications during functional or reliability testing or in the field, an investigation is normally carried out to determine the cause.* FA involves brainstorming potential "failure modes", identifying associated root causes (by electrical testing, fail-site isolation, de-processing, defect characterization), assigning levels of risk and following through with corrective actions.
- ***Failure mode*** *or apparent failure : defines what is first identified i.e. measured or observed as deviating or failing, i.e. the symptoms.* In the case of an capacitive RF-MEMS switch, typically it is a shift in the capacitance-voltage measurement which induce a change in the S-parameters.
- ***Failure defect*** *or signature : is what is observed after the failure mode is seen*

(it is possible that non failure defect is seen. For instance not permanent or sticking of the switch, deformation of the membrane, cracks, etc.

- ***Failure mechanism:*** *is the physics and/or chemistry causing the failure.* Examples are, dielectric charging of the insulator, electromigration, creep of the membrane, fatigue, corrosion, etc.
- ***Failure cause:*** *is causing the failure mechanism and is in general design, processing, packaging or monitoring related.* For instance electric field charge, air-gap breakdown, radiation, electron emission, humidity causing capillary stiction, etc.

The boundaries between these definitions can be easily blurred, therefore we will try to keep these words in this manuscript. This distinction is important because often the failure mode is reported when something is wrong, while the problem can only be accurately addressed by investigating the failure mechanism [49].

2.2 Capacitive RF-MEMS switch theory

2.2.1 Principle of operation

The capacitive RF-MEMS switch basically consists of a movable metallic bridge, anchored on the ground traces of a ground-signal-ground coplanar waveguide (CPW) line (Fig.4.4(a)). The line located below the bridge can be used as an actuation electrode. It is coated by a thin insulating layer to avoid short-circuiting upon bridge deflection (contact between the electrodes i.e. the movable membrane and the CPW line). Its simplest model, when the movable bridge is in the up-state, is the parallel plate configuration. The capacitance in this case is proportional to

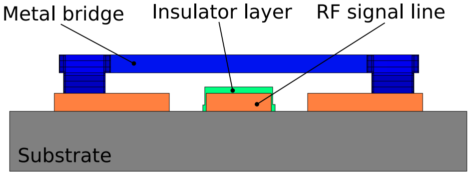

(a) Low capacitance value, RF signal passes.

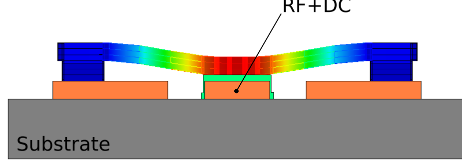

(b) High capacitance value, RF signal blocked.

FIGURE 2.3: Principle of operation of a capacitive RF MEMS switch (a) in the upstate and (b) in the downstate.

the reciprocal gap between the two metallic electrodes:

$$C = \frac{\varepsilon_0 \cdot A}{d} \tag{2.2}$$

where A is the active capacitive area, d is the distance between the plates and ε_0 is the permittivity of vacuum.
Take into account the insulator layer thickness, it will be :

$$\boxed{C_{up} = \frac{\varepsilon_0 \cdot A}{d + (\frac{z_d}{\varepsilon_r})}} \tag{2.3}$$

where z_d and ε_r are the thickness and relative dielectric constant of the dielectric layer.

In this up-state configuration, the capacitance between bridge and signal line is small and the RF signal can pass. By applying a voltage (also known as command, control or polarization voltage) between the bridge and the RF signal line causes an electrostatic attraction which pulls the membrane to the down-state (Fig. 4.4(b)). This results in a large capacitance formed by the metal/insulator/metal stack, blocking the RF signal and that can be calculated using:

$$\boxed{C_{down} = \frac{\varepsilon_0 \cdot \varepsilon_r \cdot A}{z_d}} \tag{2.4}$$

Figure 2.4 shows a typical and complete C(V) curve measured using a triangle voltage waveform of 100 Hz. When increasing the voltage, the membrane stays up

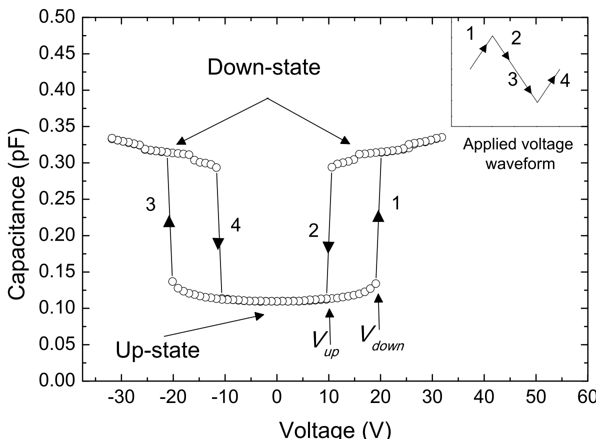

FIGURE 2.4: A measured C(V) curve of a capacitive RF-MEMS switch with its applied voltage waveform in the inset.

and the capacitance remains low until the applied voltage becomes larger than the pull-down (pull-in, actuation) voltage V_{down} and the membrane will mechanically contact the insulator surface, resulting in an increase of the capacitance (1 and 3). Upon decreasing the voltage the membrane returns up when the applied voltage is lower than the restore-up (pull-out) voltage V_{up} (2 and 4).
The calculation of V_{down} and V_{up} can be done by taking into account the distance-dependent electrostatic energy accumulated by the capacitor E_e and the restoring energy of the membrane E_r. If we keep using a parallel-plate capacitor model, their functions can be written as:

$$E_e = \frac{1}{2} \cdot C \cdot V^2 \tag{2.5}$$

where V is the voltage applied between the membrane and the signal line and C is the distance-dependent capacitance value.

$$E_r = \frac{1}{2} \cdot k \cdot (z - d)^2 \tag{2.6}$$

where k is the spring or force constant of the membrane and $z - d$ is the displacement due to electrostatic attraction.

At the particular pull-down point, which is determine to be at $z = \frac{2}{3} \cdot d$, the electrostatic force becomes greater than the increase in the restoring force, resulting in a unstable state which brings the membrane in contact with the insulator layer [5]. In this situation, the energies are equal and its derivative equals to zero, so we can write:

$$z^3 - d \cdot z^2 + \frac{\varepsilon_0 \cdot A \cdot V^2}{k} = 0 \tag{2.7}$$

$$3 \cdot z^2 - 2 \cdot d \cdot z = 0 \Rightarrow z = \frac{2}{3} \cdot d \tag{2.8}$$

The pull-down voltage V_{down} is then calculated by re-injecting $z = \frac{2}{3} \cdot d$ into Eq. 2.7 (without including the insulator layer contribution):

$$\boxed{V_{down} = V\left(\frac{2}{3} \cdot d\right) = \pm\sqrt{\frac{8}{27} \cdot \frac{k}{\varepsilon_0 \cdot A} \cdot d^3}} \tag{2.9}$$

The restore-up voltage V_{up} can be estimated by assuming that the contact involves

two hard and flat surfaces. The fringing capacitance has been neglected here. In this configuration, the initial distance between the two surfaces does not correspond to an equilibrium, but to the thickness of the insulator layer z_d. Therefore the voltage needs to be reduced to let the mobile membrane get back to its equilibrium position. The energies considered in this configuration can be written as:

$$E_e = \frac{1}{2} \cdot \frac{\varepsilon_0 \cdot \varepsilon_r \cdot A}{z_d^2} \cdot V^2 \tag{2.10}$$

$$E_r = \frac{1}{2} \cdot k \cdot (d - z_d)^2 \tag{2.11}$$

Finally, the restore-up voltage is obtained when the sum of these energies equals to zero and considering that $z_d \ll d$:

$$\boxed{V_{up} = 2z_d \cdot \sqrt{\frac{2 \cdot d \cdot k}{\varepsilon_r \cdot \varepsilon_0 \cdot A}}} \tag{2.12}$$

Every electrical and mechanical variation in the device can be monitored using this complete C(V) characteristic. For instance, if charging occurs, the curve will shift either to the positive side or to the negative side. And if the membrane is collapses the C(V) curve will be a flat line.

2.2.2 Switching time

One more electro-mechanical parameter which is important to know in a RF-MEMS switch is its switching time. The dynamic equation of switch is derived using Newton's second law of motion and given by [5]:

$$m\frac{\mathrm{d}^2 z}{\mathrm{d}t^2} + b\frac{\mathrm{d}z}{\mathrm{d}t} + k \cdot z + k_s \cdot z^3 = F_e + F_c \tag{2.13}$$

where m is the mass of the beam, z is the displacement from the up-state position, $b = \dfrac{k}{\omega_0 \cdot Q}$ is the damping coefficient, $k = k' + k''$ the spring constant, is the sum of the bending spring and residual-stress spring constants and k_s is the stress-stiffening spring constant (only applicable to the fixed-fixed beam case and it can be neglected for small displacement) and F_e is the electrostatic pull-down force, F_c represents the attractive and the repulsive nuclear contact forces.

The effective spring constant k depends on the geometrical dimensions of the

metal beam and on the Young's modulus of the material used, k is given by:

$$k = k' + k'' = 32 \cdot E_{mech} \cdot \mathrm{w} \cdot \left(\frac{z_b}{l}\right)^3 \cdot k'_{a-a} + 8 \cdot \sigma_{mech} \cdot (1-\nu) \cdot \mathrm{w} \cdot \left(\frac{z_b}{l}\right) \cdot k''_{a-a} \quad (2.14)$$

where E_{mech} is the Young's modulus, ν is the Poisson's ratio for the bridge material, σ_{mech} is the mechanical stress in the fixed-fixed beam (not to be confused with the interface charge density σ_i), l, w and z_b are the length, the width and thickness of the beam, respectively and k'_{a-a},k''_{a-a} are constants depending on the position x of the attractive area of the device:

$$k'_{a-a} = \frac{1}{8 \cdot \left(\frac{x}{l}\right)^3 - 20 \cdot \left(\frac{x}{l}\right)^2 + 14 \cdot \left(\frac{x}{l}\right) - 1} \quad (2.15)$$

$$k''_{a-a} = \frac{1}{3 - 2 \cdot \left(\frac{x}{l}\right)} \quad (2.16)$$

Several approximations are adopted in order to have a closed-form of the switching time equation and to have a simplified analytical model to explain dynamic behaviour of the switch;

- $z = d$
- The voltage of the switch is constant
- The damping coefficient is very small and constant ($b \simeq 0$)
- A high quality factor ($Q \geq 2$ for a gold membrane)
- Perfect hard and flat surfaces

So the simplified-dynamic equation can be written as:

$$m\frac{\mathrm{d}^2 z}{\mathrm{d}t^2} + k \cdot z = -\frac{1}{2}\frac{\varepsilon_0 \cdot A \cdot V^2}{d^2} \quad (2.17)$$

The solution of this equation gives:

$$\boxed{t_s \simeq 3.67\frac{V_{down}}{V_{applied} \cdot \omega_m} \text{ or } t_s \simeq \frac{9 \cdot V_{down}^2}{4 \cdot \omega_m \cdot Q \cdot V_{applied}^2} \text{ (if } V_{applied} \gg V_{down})} \quad (2.18)$$

where t_s is the switching time, $V_{applied}$ is the applied voltage and ω_m is the "mechanical" resonant angular frequency.

It has been demonstrated [5] that the best trade-off between switching response and the magnitude of the applied voltage of a device is obtained for $V_{applied} \simeq 1.3 - 1.4V_{down}$.

To do likewise, the calculation of the release time is slightly different. It is mostly affected by the effect of restoring and contact forces and the damping coefficient whereas $F_e = 0$.

2.2.3 Switching ratio

The switching (or capacitance) ratio is also one of the figures of merit characterizing switches. It is calculated as the down-state (also known as close or on-state) capacitance C_{down} divided by the up-state (also known as open or off-state) capacitance C_{up}. The higher is this ratio the more useful the device is for RF applications.For infinite hard surfaces and a perfect contact, it is given by:

$$\boxed{R_{sw} = \frac{C_{down}}{C_{up}} = \frac{\dfrac{\varepsilon_0 \cdot \varepsilon_r \cdot A}{z_d}}{\dfrac{\varepsilon_0 \cdot A}{d + (\dfrac{z_d}{\varepsilon_r})}} = \frac{\varepsilon_r \cdot d}{z_d} + 1} \tag{2.19}$$

It can be noticed that the switching ratio depends mainly on the quality of the dielectric material and also the distance between the two electrode, whose are both mainly governed by the fabrication process. This also means that nano-scale air gaps are present in the contacting state due to the surfaces roughness and $z_{d_{eff}} = z_d + \varepsilon_r d$, which decreases this ratio.

2.2.4 Microwave characteristics

The electro-mechanical behaviour of the switch is directly linked to its microwave characteristics. Fig.2.5 shows all the scattering parameters summarizing the microwave characteristics of a capacitive RF-MEMS switch. This example is used in this section in order to illustrate *the series-resonant frequency, the isolation parameter, insertion and return losses and the bandwidth.* The simplest equivalent circuit that described a shunt capacitive switch is modelled by two short sections of RF-line and a lumped CLR model of the bridge with the bistable capacitor (see in Table.1.4 of section 1.3.1).
The impedance of the lumped CLR model is given by:

$$Z_s = R_s + j\omega L + \frac{1}{j\omega C} \tag{2.20}$$

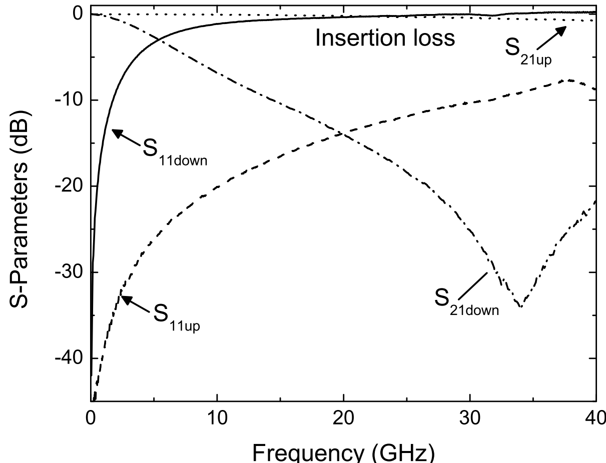

FIGURE 2.5: Measured S-parameters of a 35 GHz capacitive RF-MEMS switch in both up-state and down-state configuration.

So the LC "electrical" series-resonant frequency of the model is:

$$\boxed{f_0 = \frac{1}{2\pi}\frac{1}{\sqrt{L \cdot C}}} \tag{2.21}$$

The transmission parameter S_{21} (dB) of this resonant circuit is given by :

$$|S_{21}| = \sqrt{\frac{1+\alpha^2}{\alpha^2 + (1+\beta)^2}} \tag{2.22}$$

with,

$\alpha = \frac{1}{R} \cdot \sqrt{\frac{L}{C} \cdot \left(X - \frac{1}{X}\right)}$

$\beta = \frac{Z_0}{2 \cdot R}$

$X = \frac{\omega}{\omega_0}$ The normalised pulsation of the structure

The maximum isolation level is obtained at the resonant frequency. It corresponds to the situation when the electrical down-state resonant frequency of the switch is around the frequency of the transmitted RF signal. This is given by:

$$\text{IS}\,(dB) = -20 \cdot log\left(\frac{Z_0}{2 \cdot R}\right) \tag{2.23}$$

Based on Eq.2.22, the analytical expression of insertion loss around the resonant angular frequency ω_0 is given by (assuming that there's no ohmic losses in the

line):

$$\text{IL}\,(dB) = -10 \cdot log \left[1 + \frac{1}{R_{sw}^2} \cdot \left(\frac{Z_0}{2 \cdot R}\right)^2 \cdot \left(\frac{\triangle\omega}{\omega_0}\right)^2\right] \tag{2.24}$$

where R_{sw} is the capacitance ratio calculated from Eq.2.19, Z_0 the characteristic impedance of the line, R the equivalent resistance value of the membrane and $\Delta\omega$ is the bandwidth of the structure at the resonant angular frequency ω_0. According to this expression, higher is the capacitance ratio, lower the insertion loss will be. Besides, if the bandwidth $\Delta\omega$ is low the sensitivity of the transmission parameter S_{21} is thereby increased with respect to technological dispersions. Consequently, a trade-off needs to be done and it will be easier if the capacitance ratio is important.

Impedance matching is a critical element in all high-frequency design. When load is mismatched in a transmission line, not all the available power is delivered resulting in unwanted reflections within the circuit. This loss is the return loss (RL) and is defined as:

$$\text{RL}\,(dB) = -20 \cdot log \left|\frac{-j\omega \cdot C_{up} \cdot Z_0}{2 + j\omega \cdot C_{up} \cdot Z_0}\right| \tag{2.25}$$

The switch should be matched to minimize (within acceptable limits) its impact on the performance of the complete circuit.

The 3-dB bandwidth [5] of a capacitive shunt switch is given by:

$$\frac{\Delta\omega}{\omega_0} = R \cdot \sqrt{\frac{C_{down}}{L}} \tag{2.26}$$

Having a high bandwidth will ensure a better isolation for a given frequency range and with respect to the technological dispersion, the performances will be less sensitive. Indeed, the resonant frequency is related to the down-state capacitance value C_{down}, which is very sensitive to the quality of the contact between the membrane and the dielectric surface. A low bandwidth will be very dependent on the reproducibility of this contact, even more if targeting low actuation voltage devices. High bandwidth value can be obtained with high resistance, high capacitance and low inductance.

5. The 3-dB bandwidth is where the transmission coefficient S_{21} falls off from its highest peak by three dB

2.2.5 Theory of dielectric charging

One may think that electrostatic is well known and well understood since Poisson, Gauss and Maxwell described the phenomenon. But nowadays, materials make the complexity and the current developments of what we can call "modern"-electrostatic. In the case of electrostatic devices such as capacitive switches, dielectric charging is the most challenging issue that affect its reliability. The main reason is that in the down state (i.e. when the membrane is in contact with the dielectric surface), there is a high electric field across this insulator layer. This can cause charging on the dielectric and can results in a change of the electrical behaviour of the structure and may severely limit its functionalities.
This section will first recall the necessary knowledge on the basics of dielectric charging in MEMS.

2.2.5.1 The model

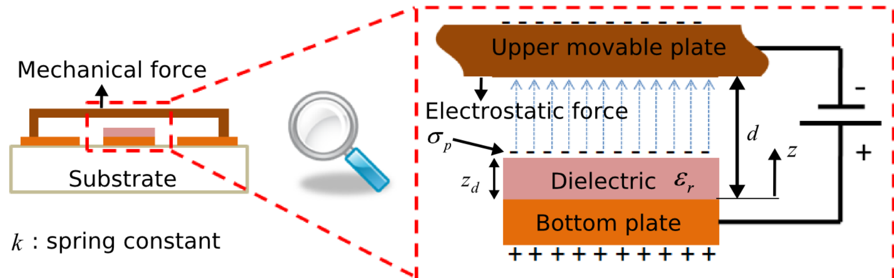

FIGURE 2.6: Simplified charging model of a capacitive switch, by analogy to the parallel plate model.

The investigation starts with the use of the simplified charging model shown in Fig.2.6. Although charging in insulating materials has been reported since the 1800s, in the field of MEMS, the first model was proposed in 1998 by J. Wibbeler et al. [50]. They derived the relationship between the accumulated charge and its effects on a switch characteristic (in a gaseous and high-voltage conditions). From then on one more extended model is presented by W. M. van Spengen et al. [51] and X. Rottenberg et al. [52]. We will adopt these approaches and interpret it to our experimental results. This model defines very well the influence of dielectric parasitic surface charge density σ_p (arising from the environment conditions or from voluntary applied stresses) on the acting electrostatic force between the two

plates within the active section of dA, which is given by:

$$F_e = \int_{(A)} \mathrm{d}F = \frac{\mathrm{d}C}{\mathrm{d}z} \cdot \int_{(A)} \frac{(V - V_{shift})^2}{2} \mathrm{d}A \tag{2.27}$$

with,

$C = \dfrac{1}{\dfrac{d-z}{\varepsilon_0 \varepsilon_{air}} + \dfrac{z_d}{\varepsilon_0 \varepsilon_r}}$ The capacitance per unit area

$V_{shift} = -\sigma_p \cdot \dfrac{z_d}{\varepsilon_0 \varepsilon_r}$ The offset voltage leading to a shift of the C(V) characteristic

Keeping in mind that the fields in the dielectric and the air gap are considered to be homogeneous in this model.

When a voltage V is applied across the two electrodes the resulting electric field will polarize the insulating film and the charged movable membrane will be attracted by the fixed bottom electrode. This voltage is written as:

$$V = -\int_0^{d-z} \vec{E}_e \cdot \mathrm{d}\vec{l}, \tag{2.28}$$

where d is the distance between electrodes, z is the displacement and d$\vec{l}$ is the integral factor.
Since the electric displacement is constant within the distance d, the parasitic charge density will be given by:

$$\sigma_p = -\frac{\varepsilon_0 \cdot V + z_d \cdot P}{\varepsilon_r (z - d)} \tag{2.29}$$

where P is the dielectric polarization.

An extended function of the dielectric polarization has been proposed by G. Papaioannou [53] in agreement with experimental results. Keeping this simple model, the dielectric bulk and surface charges are included in the macroscopic dipole moment per unit volume P. During charge injection all the mechanisms occur simultaneously, so the macroscopic polarization is given by:

$$P_{\sum} = P_D + P_{SC-i} - P_{SC-e} \tag{2.30}$$

where $P_{\sum}$ is the total polarization, P_D is the dipolar, P_{SC-i} is the intrinsic space

charge polarization of intrinsic origin arising from free charge displacement inside the dielectric when an electric field is applied and P_{SC-e} is the space charge polarisation of extrinsic origin and comes from the fact that in the down-state charge injection takes place.

Charges may be injected through asperities due to the roughness of both surfaces, the metallic membrane and the insulating material surfaces, or by field emission. The injected charges will initially decrease the local polarization of the active section dA. The sign of this polarization will change according to the amount of injected charge. In other words, the dielectric surface can contain charges of opposite polarity or the charge density may strongly fluctuate. In this case the capacitance transient component will be proportional to the time-dependent polarization and it is given by:

$$\Delta C(t) \simeq \Delta P(t) \tag{2.31}$$

In the next chapter (Chapter.3), a more detailed discussion will be given on the analyses of the shape and polarity of $\Delta C(t)$, will reveal the dominating polarization/charging mechanism and the dependence of the charging on external stresses such as constant voltage, bipolar signal, RF power, high voltage pulse (electrostatic discharge) or temperature.

2.2.5.2 Dielectric polarization

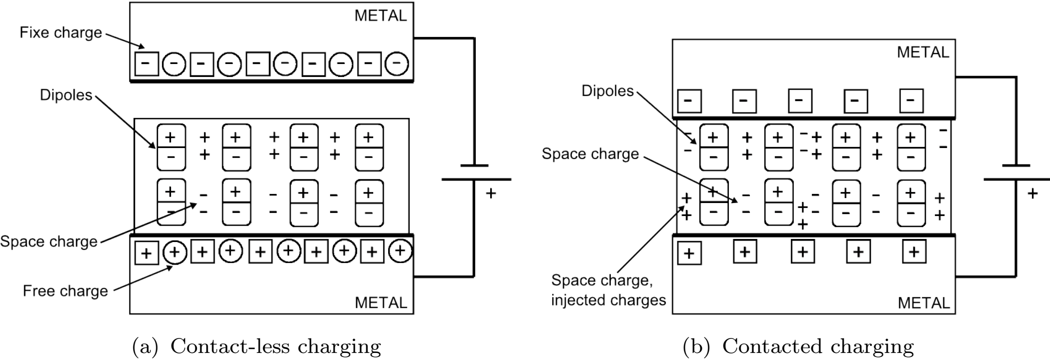

(a) Contact-less charging (b) Contacted charging

FIGURE 2.7: Charging mechanisms in RF-MEMS capacitive switches.

Based on work done by G. Papaioannou et al. [53], which states that at room temperature the dominant mechanism is the space charge polarization of extrinsic origin P_{SC-e} (injected charges) and at higher temperatures ($380°K$) the

dipolar and space charge due to intrinsic origin dominate. Since the experiments done in this thesis do not exceeded $330°K$, charging mechanisms assessed here are coming from the extrinsic origin. Fig.2.7 shows the summary of these charging mechanisms. In the contact-less situation the time-varying electric field can interact with the dielectric material under two processes; both the dipolar (reorientation of defects having an electric dipole moment) and the space charge polarization, arising from redistribution of pre-existing and or field generated charge carriers. In the contacting situation, the mechanism originates from charges injected into the dielectric through various mechanisms that will be described in the next paragraph. The total time dependent polarization's function is given by Eq.2.30.

Dipolar or orientational polarization

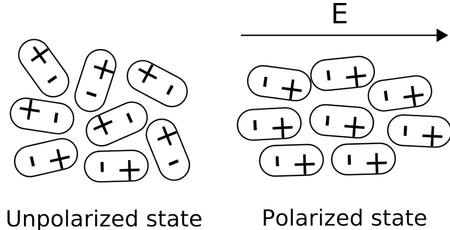

FIGURE 2.8: Dipolar or orientational polarization illustration.

Dielectric materials have a distribution of dipoles that are illustrated in Fig.2.8. In the unpolarized state these materials are charge neutral i.e. each dipole contains an equal amount of positive and negative charges. In the presence of an electric field E, the permanent dipoles will orient to align the permanent dipole moment along the direction of E. It is obvious that this orientation involves the energy required to overcome the frictional resistance of the medium, so this process is strongly time and temperature dependent.

Space charge and interfacial polarization

The aforementioned orientational polarization is due to the bound positive and negative charges within the atom or the molecule itself. Space charge polarization (volume effect) and interfacial polarization (surface effect) are associated with mobile and trapped charges. Since the common material used in capacitive switches are often amorphous or consisted of traps, charges carriers may be injected

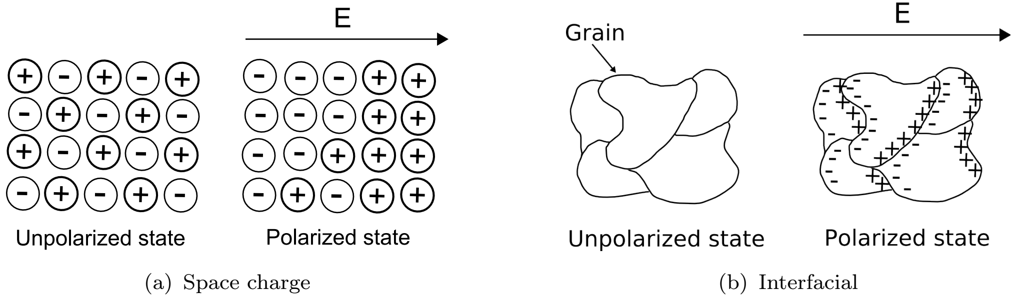

(a) Space charge (b) Interfacial

FIGURE 2.9: Space charge or interfacial polarization illustration.

from electrical contacts or from a high electric field stress and it can be trapped in the bulk or at the interfaces. A change in conductivity may occur at boundaries, imperfections such as cracks and defects lead to accumulation of charges. The accumulated space charges will affect the field distribution, as a result it will modify the average dielectric constant of the inhomogeneous material.
In MEMS switches, we can distinguish two possible ways in which space charge polarization may result [53];
• Intrinsic space charge polarization involves hetero-charges already existing and or generated from the field as charge carriers
• Extrinsic space charge polarization deals with homo-charges created in the dielectric due to high electric field stress or ionic charge carriers that may arise from contact injection mechanisms, surrounding atmosphere or discharges.

2.2.5.3 Charge injection mechanisms

The conduction mechanisms are divided in two categories [54]; the steady state which does not contribute to charging because quantity of charges entering the top surface is the same as the one exiting from the bottom surface. Hence the divergence $\bigtriangledown \cdot D$ is equal to zero, where D is the electric flux density. The transient current (the second category) contributes to charging. In capacitive RF-MEMS switches the insulating film is usually a few hundred nm thick and the electric field used across the structure is very high ($0.6 - 3 \times 10^6$ V/cm). This leads to conduction mechanisms that are dominated by transport via traps and by charge injection and tunelling. In order to describe the charge injection mechanisms in MEMS we can take advantage of the leakage current models from MIM capacitor proposed by Ramprasad [55]. By analysing leakage current transients, the dielectric charging

can be monitored and then related to MEMS reliability [56, 57] whereas the direct relation between DC leakage current and dielectric charging has not been brought out yet [58]. The main electronic processes that have been identified to take place in MEMS switches are; the *Trap Assisted Tunneling* (TAT) and the *Poole-Frenkel* (PF) conductions.

Trap Assisted Tunneling **(TAT)**

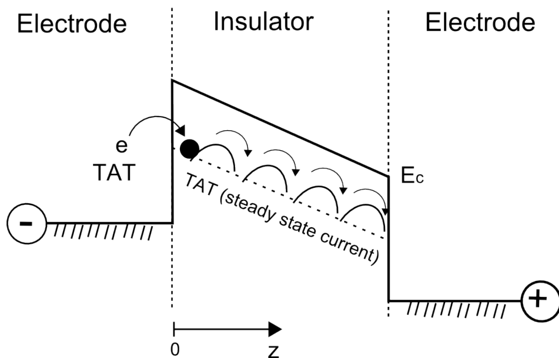

FIGURE 2.10: Energy level diagram illustrating an inelastic trap assisted tunneling process.

Defects in the dielectric layer give rise to tunneling processes based on two or more steps. It has been widely investigated in thin dielectric films used in MOS capacitors and memory devices. There's numerous models reported that describe trap-assisted tunneling (Chang et al., Ielmini et al., Ramprasad et al., Ricco et al., Houng et al.). The energy band diagram of the model is shown in Fig.2.10. A simple model applicable to MEMS switches according to its operating electric field range and which relates tunneling current density with the trap energy level is given by:

$$J_{TAT} \approxeq \exp\left\{-\frac{4\sqrt{2 \cdot q \cdot m_e}}{3\hbar E}\Phi_t^{3/2}\right\} \tag{2.32}$$

where q is the electronic charge, m_e is the effective mass of the electron, E is the electric field across the dielectric, $\hbar = 6.626068 \times 10^{-34} m^2 kg/s$ Planck's constant and Φ_t is determined with the slope of the "ln$J$ vs $1/E$" (TAT) plot.

Poole-Frenkel effect **(PF)**

The Poole-Frenkel effect is the thermal emission of charge carriers from Coulombic traps in the bulk of a insulating or semiconducting material [59]. The Fig.2.11 shows the energy level diagram of such a trap. Under large electric field, the electron may get out of its localized state and move to the conduction band. This Frenkel's model assumes that the potentials do not overlap, which is valid only

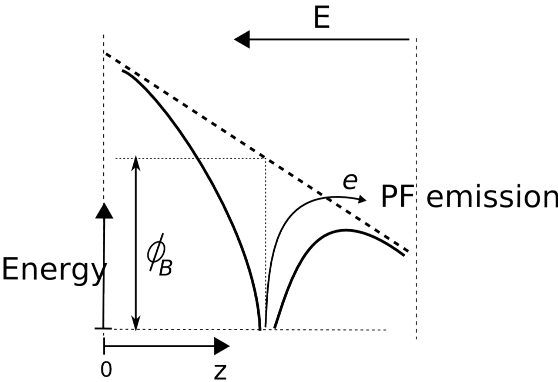

FIGURE 2.11: Energy level diagram illustrating the Poole-Frenkel conduction mechanism.

if the impurity density is low. In amorphous material, the current due to Poole-Frenkel emission is given by:

$$J_{PF} \approxeq E \cdot \exp\left\{\left(-\frac{q}{k_B \cdot T}\right)\left(\Phi_t - \sqrt{\frac{q \cdot E}{\pi \cdot \varepsilon_r}}\right)\right\} \tag{2.33}$$

where E is the electric field across the dielectric, $k_B = 1.3806503 \times 10^{-23} m^2 s^{-2} K^{-1}$ is the Boltzmann's constant, Φ_t is determined with the slope of the "ln$J$ vs $1/E$" (TAT) plot and ε_r is the permittivity of the dielectric.

This general model has been validated experimentally by S. Mellé et al. [60]. The analyses have been made assuming that at high electric field and for low dielectric thickness, the PF conduction is dominating in the total current density. In addition, the roughness of the dielectric and the moving electrode has been included in this experiments by taking into account the measured capacitance values in the calculation of the intrinsic effective electric-field parameter (see more details in Section 3.1.3).

2.3 Focussed reliability concerns

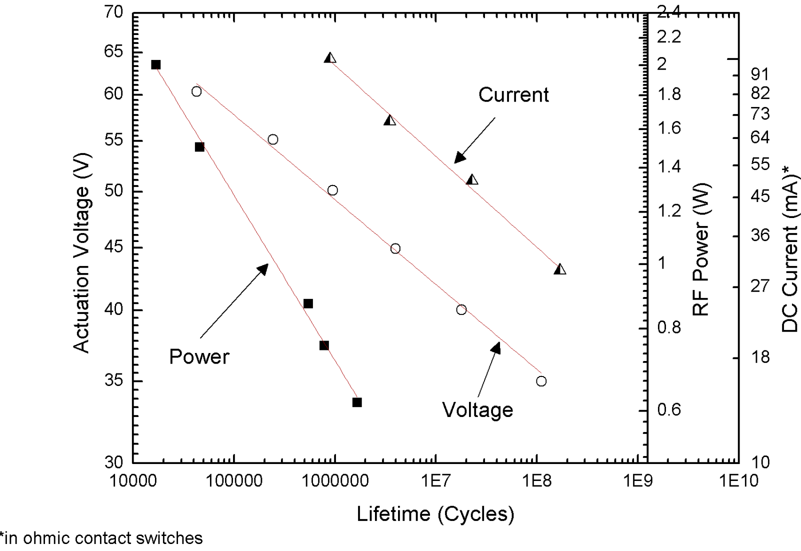

FIGURE 2.12: Operating parameters vs. device's operation time.

In this section, several failure modes will be addressed and their failure mechanisms will be investigated. First of all, it should be point out that RF MEMS switches are not subject to structural mechanical failure of the beam i.e. the beams don't crack or break even after billions of cycles. A great demonstrator of this mechanical performance is the Digital Micromirror Device (DMD) from Texas Instruments [61], where its expected performance level has shown, in some cases to exceed its reliability goals (3 trillion mirror cycles $\sim$ 100 years of normal use device's operation time). The primary failures in RF-MEMS switches are based in materials choice and the geometry (for power operation range below $< 100mW$); in series ohmic switches an increase of the contact resistance takes place and in shunt capacitive switches the main failure mechanism is dielectric charging.
The current figure of MEMS switches reliability is illustrated in Fig.2.12. It shows the applied stresses (i.e. actuation voltage, RF power and DC current) as a function of the device's operating time derived from experimental results. There is no definite rule of the failure rate, but the distribution function that best fits the present data and the most commonly used one is the Weibull distribution [6] function. So it is clearly shown that all the stresses feature a power law relation

6. The Weibull distribution is one of the most widely used lifetime distributions in reliability engineering. It is a versatile distribution that can take on the characteristics of other types of distributions, based on the value of the shape parameter named β. According to this parameter ($\beta < 1$, $\beta = 1$ or $\beta > 1$) the three states of the bathtub curve (Fig.2.1) can be well described.

with the operating time and this behaviour has been also noticed by looking at the capacitance ratio R_{sw}. It is a fact, but it has not been well investigated that lower is R_{sw} longer is the operating time. Unfortunately, this means that the product is still in the *infant mortality* region of the bathtub curve (Fig.2.1) and that improvements are needed in the overall field covering factors such as material choice, processing, environmental factors and operating parameters. All the reliability aspects presented in the following sections will be more detailed in Chapter.3.

2.3.1 Dielectric charging in capacitive switches

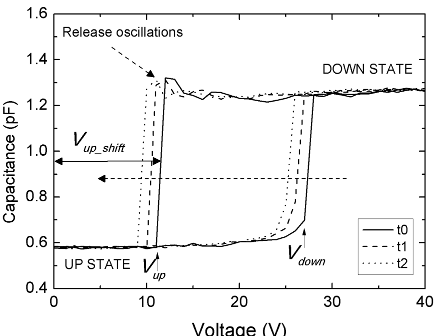

FIGURE 2.13: An example of the shift of the C(V) characteristics, measured for a constant voltage stress of around 30 min under 40V biasing.

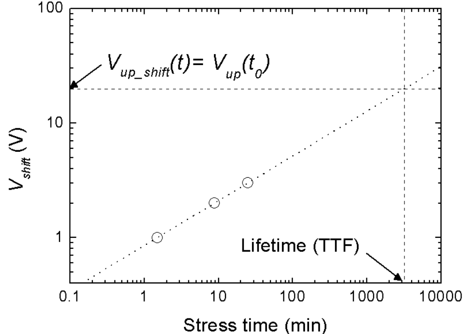

FIGURE 2.14: Log-log plot of the dielectric charging dependence on the stress time.

The worldwide most investigated topic in RF-MEMS capacitive switches is dielectric charging. The main effect of dielectric charging is that it results in a shift of the C(V) characteristics as depicted in Fig.2.13. It is clearly shown that the effect of this offset impacts the pull-down (V_{down}) and the pull-up (V_{up}) voltages. In the time scale of operation of the MEMS device, the charging is proportional to the macroscopic polarization $P_{\sum}$ (Eq.2.30).

$$\langle V_{shift} \rangle \infty \frac{\langle P_{\sum} \rangle \cdot z_d^2 + \varepsilon_0 \cdot V \cdot z_d}{\varepsilon_r^2 \cdot \varepsilon_0 \cdot (z - d)} \tag{2.34}$$

It follows a power law as shown in Fig.2.14. The straight line in the log-log plot indicates the C(V) curve offset dependence with respect to the charging of the insulating material. Since the reliability of capacitive structures lies in this charging factor, estimation and assessment are closely related to it. In [22] they

have shown an exponential relationship [7] between the number of cycles on the peak actuation voltage. Higher is the actuation voltage peak shorter will be the device's operation time. Hence a large amount of injected charge can lead to the worst case where switches remain in the down-state when no voltage is applied i.e. the movable membrane is stuck to the dielectric ($V_{shift} = V_{up}(t_0)$). As an example in Fig.2.14 the time to failure (TTF) of the switch could be extrapolated as 3200 min, which is the total time the switch can remain in the down-state.
In this sense, hold-down charging tests on AlN-based switches have been performed. Most of the electrical characterisations have been performed using capacitance-based techniques to identify and monitor relevant parameters like offset voltages V_{shift}, up and down state capacitance C_{up},C_{down}, and hysteresis parameters like pull-down and pull-up voltages V_{down},V_{up}. The results are discussed in the next chapter in Section 3.1.

2.3.2 ESD/EOS specificities in MEMS

Electro-Static Discharge (ESD) is a disruptive electric current transfer between two objects at different electrical potentials caused by direct contact or induced by an electrostatic field. It results in hard failures or in some cases latent defects. A latent defect is a failure that has not been noticed in the final qualification procedure but let the device in a weakened state. Fig.2.15 shows an example of this effect while the device has been submitted to several Human Body Model (HBM) discharges and no apparent failure has been seen by optical analysis. A more underlying failure analysis (by removing the upper membrane) has shown electrical breakdown in the dielectric layer.
Electrical Overstress (EOS) is a phenomenon where a device is subjected to excess current, resulting in catastrophic breakdown. EOS is usually more destructive than ESD because it last longer and often until breakdown. Therefore it is easier to find and evaluate. A microscope picture derived from a breakdown caused by EOS is shown in Fig.2.16. Failure modes after an ESD event can include anomalies in dielectrics, insulation or metallization.
ESD and EOS damage of MEMS in general has been identified as a new failure mode [62]. Despite the fact that there has been only little focus on the ESD sensitivity of MEMS devices, to date we assist to a growing interest concerning

7. The exponential relation can be considered as a special case of Weibull where $\beta = 1$ and it describes the flat portion of bathtub curve

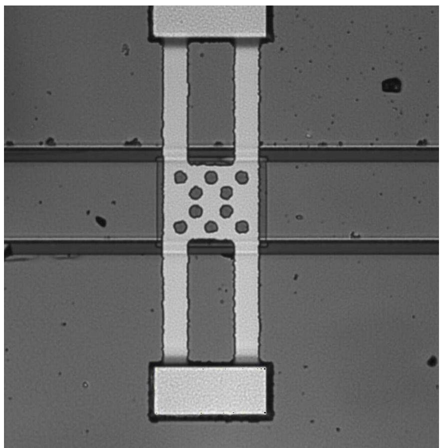

FIGURE 2.15: A microscope image of a capacitive switch submitted to several HBM pulses (no apparent failure is visible).

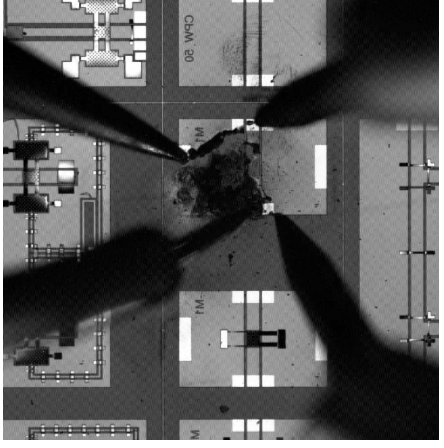

FIGURE 2.16: A microscope image of a breakdown caused by EOS in a capacitive switch.

ESD effects in RF-MEMS components as they interface with environment where static charge can be present. Few publications in the literature on the ESD sensitivity of RF-MEMS switches exist [63–66] and further investigation is necessary to provide a better understanding of the involved physics of failure. The Section 3.2 in Chapter 3 will be dedicate to the susceptibility of the parallel plate structure to ESD. For instance, if the voltage spike is large enough, it could induce sticking by bringing the plates into contact.

2.3.2.1 ESD Testing standards

In integrated circuits, the ESD testing and qualification is performed using a variety of ESD models and methods. The device level ESD testing techniques are as follows:

- Human Body Model (HBM);
- Machine Model (MM);
- Charge Device Model (CDM);
- Charge Cable Model (CCM);
- Cable Discharge Model (CDM);
- Transmission Line Pulsing (TLP);
- Very-Fast Transmission Line Pulsing (VF-TLP);
- Human Metal Model (HMM) [8].

8. The HMM standard test method is published by the ESD Association in 2009 and it defines a new test method for evaluating components using the IEC-61000-4-2 waveform.

A summary of short-circuit currents of several ESD testing standards is depicted in Fig.2.17. According to HBM, MM and CDM, electrostatic stress tests cover already a large spectrum of real-world electrostatic discharge situations in order to quantify ESD sensitivity of IC protections.
In this work the two ESD models that have been used are HBM and TLP, because they are commonly used to characterize active ESD protection structures for ICs. Besides their energy ranges are similar and therefore correlation can be made between 100ns TLP and 500ns HBM while their waveforms are different.

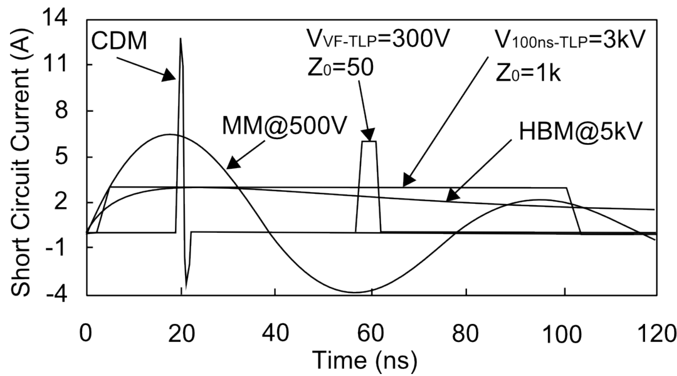

FIGURE 2.17: Short circuit current of common ESD-stress models.

2.3.2.2 Human Body Model (HBM)

The HBM ESD model is a simulation of the discharge which might occur when a initially charged human source touches an electronic device using a finger. The most widely used test model is defined in the United States military standard MIL-STD883G. The equivalent electric circuit of this model is shown in Fig.2.18. In this standard the charged human body is modeled by a 100 pF capacitor in series with a 1500Ω discharging resistance. The characteristic rise time is 10ns and the decay time is given by $\tau_{HBM} = R_{HBM} \times C_{HBM}$.

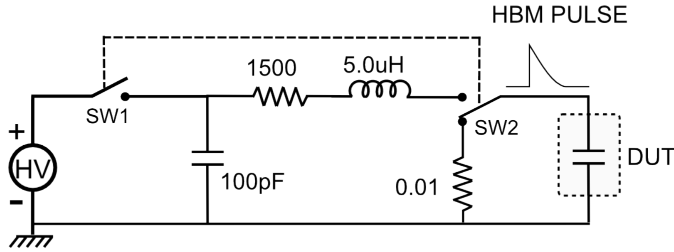

FIGURE 2.18: The equivalent circuit used to test the discharge sensitivity of a device based on human body model.

2.3.2.3 Transmission Line Pulsing (TLP)

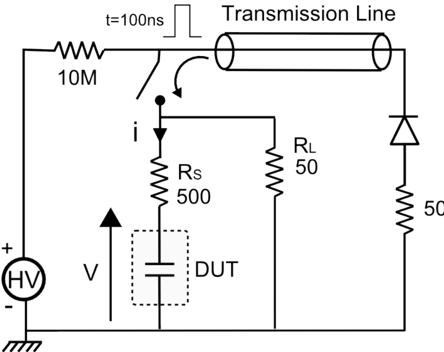

FIGURE 2.19: The equivalent electric circuit of the Transmission Line Pulsing set-up.

The TLP ESD testing technique was introduced by Maloney and Khurana in 1985 [67] as a electrical analysis tool to test on-chip single ESD protection structures. It has been well used by semiconductor and circuit engineers as a means to reduce the design cycle time by observing the pulsed I-V characteristic response. It provides the dynamic electrical characteristics of each ESD protection design at high pulse currents without heating and thereby decrease the probability of infant failures. The equivalent circuit of the in-house TLP system used at LAAS is shown in Fig.2.19 (typically used for IC's ESD protection characterization). The technique consists in charging of a transmission line cable using a voltage source then the TLP system discharges the pulse into the DUT. The characteristic time i.e. the pulse width is a function of the length of the transmission line and the propagation velocity $\tau_{TLP} = 2 \times L_{TLP}/\nu$ ($1ns$ of rise time and $100ns$ pulse width).

2.3.3 Operational power handling considerations

The power handling capability for RF-MEMS switches is one of the most important parameters in high power ($P > 1W$) applications such as front-end emission parts, redundancy circuits, antenna matrices etc. The limiting factors come from:
The conductor parts, transmission line and switch contacts because it is current density dependent due to excessive heat dissipation (heating and temperature rise can induced sticking or microscopic bonding) and hence the onset of electromigration [9]. The electromigration can be estimated by measuring the median time-to-failure (MTF) or t_{50}, which is the time to reach a failure of 50% of all the

9. Electromigration is the transport of mass in metals when stressed at high current densities.

measured samples and it is given by [68]:

$$t_{50} = C \cdot \frac{t_m \cdot w_m}{J^2} \cdot exp\left(\frac{E_a}{kT}\right) \quad (2.35)$$

where C is a constant, t_m is the metal conductor thickness, w_m is the metal conductor width, J is the current density in A/cm^2, E_a is the activation energy in eV, and T is the temperature in Kelvins.

The self-actuation effect, arises from the fact that the input power of the RF signal induced a mechanical force that equals or exceeds the force created by the actuation voltage V_{down} (Eq.2.9) of the movable electrode. The corresponding equivalent DC voltage can be calculated with ($\omega C Z_0 << 1$):

$$V_{up-eq} = \sqrt{2 P_{in} Z_0} \quad (2.36)$$

where P_{in} is the input RF power and Z_0 is the characteristic impedance.

Consequently, this equation allows us to design a switch to withstand a certain power, for instance in we target $10W$ in a 50Ω system, then the pull down voltage of the device shall be $V_{down} > V_{up-eq} = \sqrt{2 \cdot 10 \cdot 50} = 31V$.
When the switched is self-actuated, there is also an equivalent voltage in the down-state $V_{down-eq}$ that maintain the switch in the down position if it is higher than the pull-up voltage V_{up} (Eq.2.12). The equivalent down-state self-actuation voltage is given by:

$$V_{down-eq} = \sqrt{\frac{2 P_{in} Z_0}{1 + 4\omega^2 C_{down}^2 Z_0^2}} \quad (2.37)$$

The capacitive-contact switches have large contact areas and a insulating layer between the electrodes. The ohmic-contact switches have relatively small contact areas and small contact forces and therefore they are more sensitive to the input power levels and heating. Fortunately both capacitive and ohmic contact switches can reach $>$ 100 billion cycles under low power conditions ($< 100mW$) and to billion of cycles under medium to high power conditions ($> 100 - 500mW$). Power handling continues to be an area of MEMS switches that requires improvement while reliable and impressive results has been worldwide demonstrated and they are summarized in Fig.2.20. In the next chapter, a more detail description will be given on the power handling characterisation methodology used to test switches for [38] and [37].

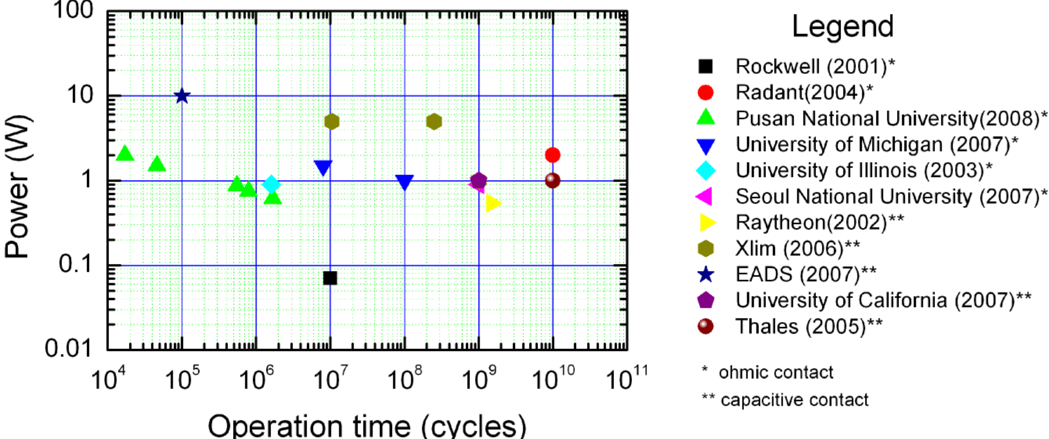

FIGURE 2.20: Hot-switching operation and power handling capacity comparison of MEMS switches from worldwide publications.

2.3.4 Radiation effects

In the early 2000's, it has been reported how MEMS are interesting for use in space applications [69–71], thanks to its ability to enhanced space systems performances by downscaling (i.e. small mass and size, small power consumption and low cost). If all micromachined devices (Table 1.2) can perform all the tasks require in satellite sub-systems such as communication, on-board sensor, power conditioning and storage systems, then lightweight satellites *Picosats* may appear in orbit [70, 71].

The opportunities of RF-MEMS in space are real and quite challenging, in terms of miniaturization and reconfigurability for the development of highly reliable microwave components in space [72]. Therefore, among all the qualification procedures [10] that must be performed for a new microelectronic device, radiation influence on RF-MEMS capacitive switch is here investigated. The main failure mode at high radiation doses is the accumulation of charge in dielectric layers (including ohmic-contact switches having a dielectric material in the control part [73, 74]). The traditional satellite radiation shielding has been proved to be efficient to guarantee electronic device functionalities. However in *Picosats* this efficiency should be verified or in case the radiation cannot totally been suppressed, we need to anticipate the understanding of the failures mechanisms. Therefore the physics

10. Space specifications concerns are radiation, temperature, pressure and vibration. The standardization of those procedures is defined in the United States military standard MIL-STD-883E and it is also defined by the European Cooperation for Space Standardization; ESCC-22900, ESCC-25100.

of how different energetic particles interact with matter, the types of damages are caused and the influence on our device should be well understood.

2.3.4.1 Space radiation environment

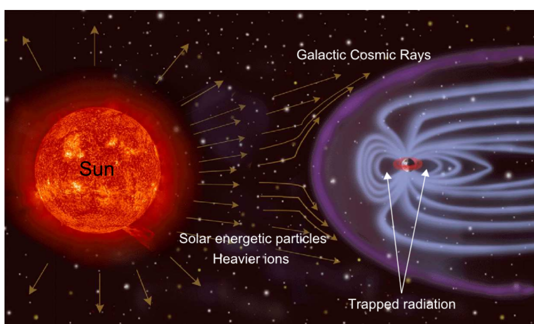

Figure 2.21: The space radiation environment near the earth (picture taken from NASA).

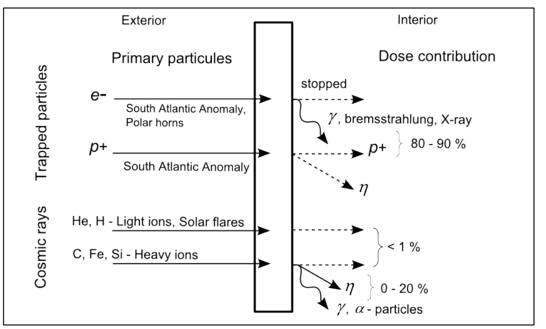

Figure 2.22: Space radiation environment inside and outside spacecraft (illustration reproduced from MIT OCW).

The radiation environment in space is complex and varies with both time and location, and models of particle flux include effects of the Sun, local magnetic fields, and galactic cosmic rays [71]. Fig.2.21 and Fig.2.22 illustrate the main types of radiation encountered near the Earth and inside and outside of a spacecraft in this environment respectively. In consists of the following:

• ***Trapped radiation belts***[11], which is a steady source of radiation. It contains energetic electrons and protons magnetically trapped around the Earth. The energy of the electrons can be up to a few MeV, and for the protons up to several hundred MeV.

• ***Solar energetic particles*** are high-energy protons up to $300MeV$. The proton flux is associated with solar flares, that is why the intensity is variable. For Europa the total dose component of solar flares can be ignored except for peak flux. UV, X-ray and solar cosmic ray burst are produced.

• ***Galactic cosmic rays*** contain low flux of high-energy particles ($1MeV$ to $1GeV$). It can be protons, α particles or even heavy ions.

• ***Secondary radiation*** comes from the interaction between the dose contribution and materials inside the spacecraft. It consists of primarily electron-induced

11. The Van Allen belts are a torus of energetic charged particles near the Earth, which is held in place by Earth's magnetic field.

bremsstrahlung [12], secondary electrons and neutrons.

Orbit	Predominant particles	Dose per year
Low Earth Orbit (LEO)	protons	$\sim 2krad$
Medium Earth Orbit (MEO)	protons and electrons	$\sim 100krad$
Geostationary Earth Orbit (GEO)	electrons	$\sim 10krad$
Geostationary Transfer Orbit (GTO))	protons and electrons	$\sim 50krad$

(nearly all from trapped particles)

TABLE 2.1: Total dose levels for Earth orbits.

The effect of the different types of radiation on devices is defined by the total radiation absorbed dose. It is measured in *rad* (radiation absorbed dose) and its equivalence with the Gray (J/kg) and the erg per gram of material is $1rad = 10^{-2}Gray = 100erg/g$ of irradiated material. The net effect depends on how the excess charge is rearranged before returning to an equilibrium state.
Table 2.1 gives approximate values of energy deposited in a device for different Earth orbits. The deposited energy is time and space dependent of the satellite or spacecraft (as well as on the shielding). Several software (SPENVIS [13], SRIM and TRIM [14] and Space Radiation 5.0 [15]) are available allowing the determination and prediction of the dose of energy and the type of radiation that can trapped (as a function of the trajectory).
In *Picosats*, the shielding will be reviewed and therefore understanding the effect of radiation on MEMS is important[71, 75]. For space missions, they will last at least several years in a radiation environment with dose rates of $\sim 1rad/hour$. Hence, accelerated radiation testing methods is necessary (e.g. $36rad/hour - 36krad/hour$ are commonly used for ^{60}Co, Cobalt-60 gamma rays). However up to now, there is no standard testing procedures established for MEMS, neither for RF-MEMS.

2.3.4.2 Radiation effect on materials

In this section a brief overview of radiation effects on different materials is given and represented in Table 2.2. Usually three degradation mechanisms are distinguished namely ; Single Event Effects (SEE), Ionization and Displacement.

12. Bremsstrahlung, literally “braking radiation” is the electromagnetic radiation produced by the acceleration of a charged particle when it is deflected by another charged particle. It is also refer to the process of producing the radiation.
13. SPENVIS, the Space Environment Information System : http://www.spenvis.oma.be/
14. http://www.srim.org/
15. http://www.spacerad.com/

Radiation	Consequence	Principal radiation damage effects
Electrons Gammas	Ionization : Total Ionizing Dose (TID)	• Polymers: crosslinking, chain scission, embrittlement, outgassing, loss of tensile strength, loss of elongation, destruction of elastomers • Wire and cable: fracture of insulation, loss of dielectric strength, change in dielectric constant, change in impedance • Lubricants: loss of lubricity, change in viscosity, outgassing Thermal control paints: fracture and discoloration • Optics and glasses: darkening, internal charging, fracture, fluorescence • Charge accumulation in dielectrics, possible internal arcing • Ceramics: may cause conductivity, loss of dielectric strength • Semiconductors: charge deposition, single event upsets
Electrons > $0.5MeV$ Protons Neutrons	Displacement: Non Ionizing Energy Loss (NIEL)	• Primary effect is damage to semiconductor devices (junction damage) • Glasses: density change, refractive index change and discoloration • Ceramics: fracture, embrittlement, conductivity, density change Metals: generally immune, but decrease in tensile strength and yield in some • Magnets: possible damage to permanent magnets

Table 2.2: Overview of radiation effects on materials.

SEE is not included in this table because it is the macroscopic manifestation of single ions that should in principle not be problematical for fully mechanical MEMS (without insulator). Moreover its effect on RF-MEMS switches has not been investigated and reported.

• ***Total Ionizing Dose*** effects arise from ionization [16] and it leads to an progressive accumulation of electrically active defects. In dielectrics used in MEMS switches there will be charge accumulation that can be accelerated by the driving electric field. Furthermore the worst case can happen when internal arcing occurs.

• ***Non Ionizing Energy Loss*** or displacement damage arises from a part of the energy loosed from the radiation, which if it is sufficient to transfer the momentum to the atomic nuclei, will generate atomic displacement. Hence the internal structure of materials used in MEMS will be affected and so will be the device's functionalities.

2.3.4.3 RF-MEMS switches sensitivity to radiations

The first data on radiation effect in RF-MEMS switches came from HRL Labs in California [76], where a RF switch has shown to operate dynamically up to a dose

16. Ionization is the conversion of the energy lost from radiation interacting with an matter to electron-hole pairs.

of $1Mrad$. However no longer after, a work done under the NASA Electronics Parts and Packaging program [73] demonstrated that insulators used in switches are affected. Rockwell RF switches were evaluated in the ^{60}Co gamma total dose environment. They have shown that the predominant charging mechanisms is charge injection in the dielectrics and that it can be avoid using a proper design. In fact, the switch responds to radiation is mainly determined by where the charge deposition takes place; ions passing through metal layers would not have a real impact on its performance, but ions passing through the dielectrics will cause charge trapping that will impact the electrostatic force. Since then, year after year a growing interest and attention is given, trying to understand and make the distinction between radiation effects and operation charging effects. The contribution from numerous interesting work in this field is summarize in Table 2.3. The experimental results that will be discussed in this manuscript concerns the effect of $5MeV$ $\alpha-$particle irradiation in RF-MEMS capacitive switches (see Section 3.4 in Chapter 3).

Authors	Year	Source/ Dose	Type of switch or device / Materials	Observations
[76] Schwartz et al.	2000	$1Mrad$	HRL Ohmic-contact switch with $0.5-1\mu m$ of PECVD Si_3N_4	Dynamic test has shown no failure up to $1Mrad$
[73] McClare et al.	2002	^{60}Co 50rad/s, $300krad$	Rockwell ohmic-contact switch with $1-2mmSiO_2$	Charge accumulation in standard switch by secondary electron emission
[77] Papaioannou et al.	2004	$1MeV$ P^+ and α	Si_3N_4, SiO_2 and $Hf0_2$	Charge trapping / A uniform ionization rate for Si_3N_4, SiO_2 and it is in agreement with the electron-hole pair energy $10.8eV$, $17eV$ respectively.
[78] Theonas et al.	2005	From X-rays to γ-rays	MIM devices with Si_3N_4, SiO_2, $Hf0_2$, Al_2O_3, AlN, Ta_2O_5	Materials atomic number, Metal contacts determines the final charge distribution. There a proportionality between photon energy incidence and the sign of the net charge. To reduce the effects of radiation, insulating compounds should contain elements having similar mean atomic number than the metal contacts ones.
[79] Exarchos et al.	2006	$5MeV$ $\alpha-$particles	MIM devices with Si_3N_4 and SiO_2	$5MeV$ $\alpha-$particles irradiation make deep defects from displacement damage and it can be monitor using TSDC and DCT methods.
[80] Crunteanu et al.	2006	^{60}Co $10rad/min$, $100krad$	Al_2O_3-based RF MEMS capacitive switch	Tens of millions of bi-polar operation cycles can be reached but it is still prone to stiction related to dielectric charging.
[81] Ruan et al.	2008	$5MeV$ $\alpha-$particles provided by an Americium (Am) source	MIM and capacitive MEMS with Si_3N_4	Experimental data have shown for both MIM and MEMS devices, an asymmetrical charging due to both different metal work functions and asymmetric trap generation during down state charge injection. The primarily radiation enhance the contribution of space charge polarization to the dielectric charging.
[82] Muldavin et al.	2008	$100-, 500-, 1000-krad(Si0_2)$ X-ray, $1Mrad$ total dose of $10-keV$ X-rays	Fully packaged capacitive switch	The pull-down voltage and pull-up voltage, as well as the S-parameters are slightly affected.
[74] Tazzoli et al.	2009	$2MeV$ protons, 1, 10 and $30Mrad(SiO_2)$ and (10keV x-rays)	Ohmic RF-switch from FBK-IRST	Ionization impacts the actuation voltage and potentially the S-parameters. It is also shown that a device can recovered after 1 month of storage, while being irradiated by $1Mrad$ X-rays.

TABLE 2.3: Overview of radiation effects on RF MEMS switches.

Is it possible to be the last to do something first ?

Chapter 3

Experimentations: methodology, equipment and results

This chapter details the experimental studies that have been carried out during this Ph.D. It is an extension of the discussion started in Chapter 2, Section 2.3. The physical mechanisms involved in the reliability of those structures is still an active area for discussion because it varies greatly from device to device and from one application to the other, due to the numerous factors such as material choice, processing, environmental factors, and operating parameters. Standard testing procedure for RF-MEMS switches do not exist yet. Therefore this chapter will be organised by type and specificity of the experiment. For each experiment we will report:

• The Device Under Test (DUT) i.e. its specificities such as the design, the processing and the materials...

• The detailed testing methodology and equipment.

• The results and discussion.

3.1 Hold-down charging studies on AlN devices and comparison

3.1.1 DUT

The first device that has been tested is an AlN-based microwave capacitive micro-switch and its topology is presented in Fig.3.1. A design from LAAS were used [83] and fabricated by ISIT-FHG within a multi project wafer run [1]. From the bottom up, it starts with a silicon wafer of which resistivity is higher than $3k\Omega \cdot cm^{-1}$ and a thickness of $508\mu m$. A $2\mu m$-thick silicon oxide is grown on it. The coplanar lines are formed from a Ta/Pt/Au/Pt stack which low roughness. The lines outside the switching area and all other interconnections consist of $3\mu m$ thick electroplated gold Au. Then $300nm$ thick sputtered AlN acts as the dielectric between signal line and bridge (dielectric 1). To avoid high voltages in the active parts of the switch two actuation electrodes with an additional PE nitride isolation of 300 nm (dielectric 2) are patterned on the lateral ground planes. Finally, using a Cu sacrificial layer, the membrane is formed of a stack of Au/Ni/Au layers and the total thickness is $0.9\mu m$. Without electrostatic force, the metallic membrane above the dielectric layer of the signal line features $2.4\mu m$ in height. Its RF performances and electromechanical parameters will be described right in the next section.

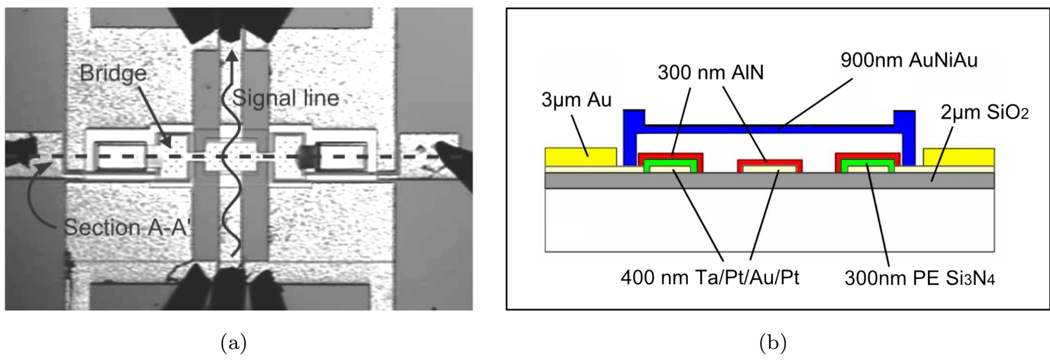

(a) (b)

FIGURE 3.1: Topology of the AlN-based capacitive RF-MEMS switches, (a) microscope picture (b) cross-section A-A' view.

1. http://www.amicom.info/upload/Call_ for_ MPW_ ISiT.pdf

3.1.2 Testing methodology and equipment

3.1.2.1 The in-house RF-MEMS characterisation set-up

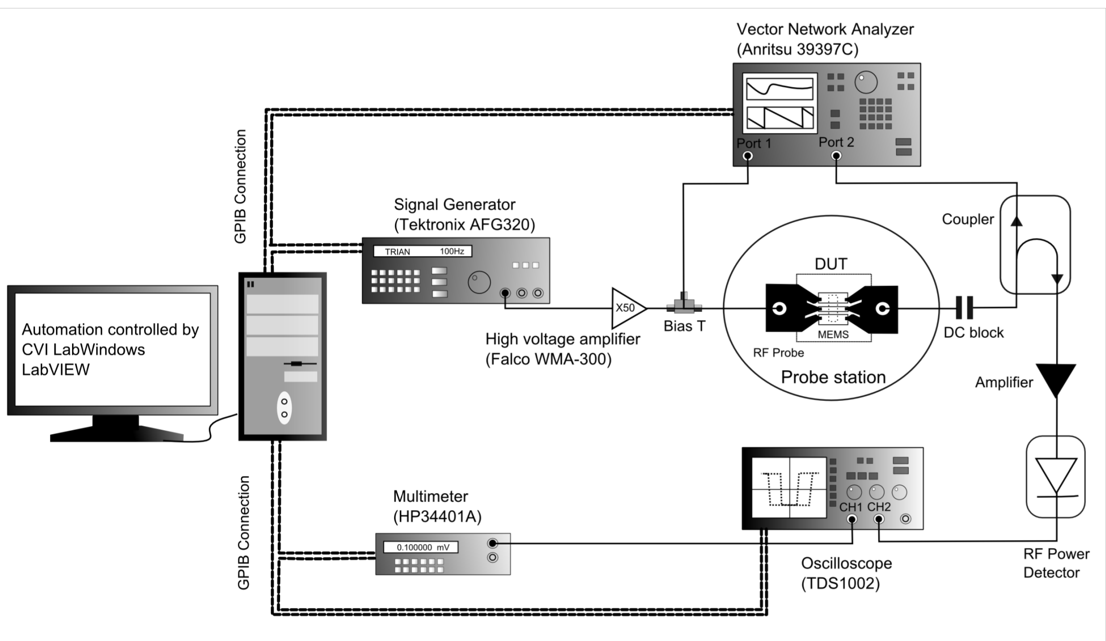

FIGURE 3.2: Diagram of test equipment setup for RF MEMS reliability monitoring.

The performance characterization and reliability testing of the switch has been performed using an in-house set-up (derived from the one presented in [60] it has been improved). This test bench integrates the examination of the microwave, electrostatic, cycling and charging properties of RF MEMS switches. As depicted in Fig.3.2 it consists in using a Vector Network Analyser (VNA) to monitor the microwave characteristics combine with a Arbitrary Signal Generator to applied the DC voltage to drive the electrostatic behaviour of the device through a Bias Tee (the signal is also collected by the channel 1 of the oscilloscope). Then the mechanical changes is monitor through a series of $10dB$ coupler-RF amplifier-RF power detector that have been connected to the channel 2 of the oscilloscope. Finally by setting the oscilloscope in the X-Y mode, we will obtained the operating signature of the structure, which reflects or is correlated to the C-V characteristics (Fig.3.18). The probe station is mounted with a thermal-chuck for which the temperature ranges from $-65°$ to $+200°C$, so thermal cycling and steady- state thermal testing can be done. In addition the station contains a moisture-free cold testing controlled environment enclosure (dry air or nitrogen flux). The automation of the set-up is done with CVI LabWindows or LabVIEW programs. Among the numerous measurements that can be performed, the following will be

detailed:

- Up-state and down-state S-parameters;
- Up-state and down-state capacitance extracted from S-parameters;
- Switching times;
- Transmission parameter S_{21} as a function of control voltage;
- Hold-down charging.

3.1.2.2 Microwave measurements

The VNA used for the microwave measurements is the Anritsu 39397C. The frequency span of this appliance ranges from 0.04 to $40GHz$. First-of-all, a full 2-port on-wafer SOLT calibration is done. The procedure of up-state and down-state S-parameters probing can be executed. It is illustrated in the timing charts shown in Fig.3.3.

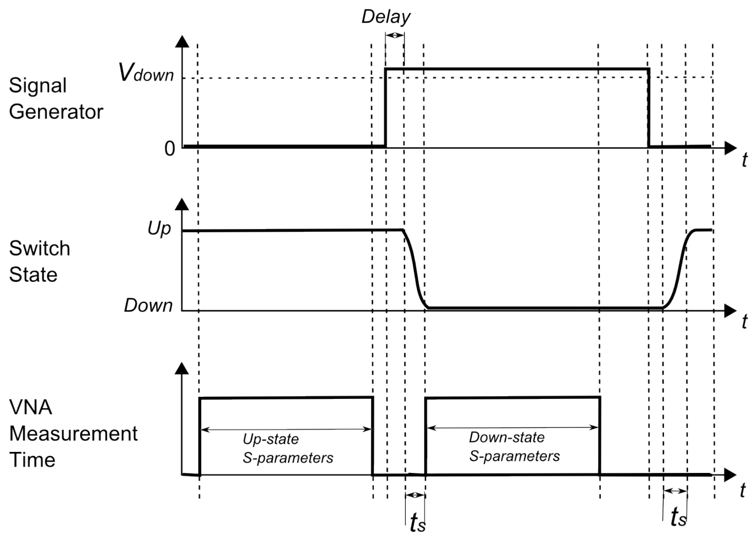

FIGURE 3.3: Timing charts of microwave and switching measurements.

The first S-parameters measurement is done when the membrane is in the up-state (no voltage is applied) and the VNA is in the frequency sweep mode. Right after the data acquisition is made the signal generator is programmed to supply one pulse square signal to the DUT with a magnitude $30 - 40\%$ higher that the pull-down voltage of the switch (note: we can applied a maximum magnitude of $300V$ peak-to-peak). After a short delay the membrane will switch and the switching time can be acquired using both the "CW single frequency sweep" and the "Swept Power Gain Compression" modes of the VNA. It is obvious the data acquisition

time depends on the measurement speed ($1.5ms/point$ in GPIB connection and the maximum points equal 1601) and the average function.

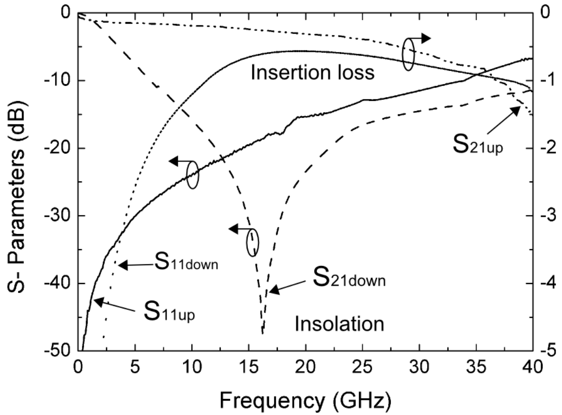

FIGURE 3.4: Measured S-parameters of the DUT.

Fig.3.4 presents the measured S-parameters of the afore-described capacitive switch in its two states. It shows a resonant frequency of $16GHz$ where a isolation greater than $40dB$ is reached and the insertion loss remains below $0.5dB$ until $28GHz$. From the point of view of performances at low GHz frequencies, the use of high constant k dielectric material seems to be more attractive for RF MEMS. However the drawback of high k materials is the high field strength in the case of thin dielectric layer and its sensitivity to electrical breakdown. The calculated capacitance ratio of these switches is about 83, whereas the measured one is about 75. The difference is probably due to the roughness and asperities of the active contact area which reduces the actual contact area.

3.1.2.3 Extraction of capacitance values from S-parameters

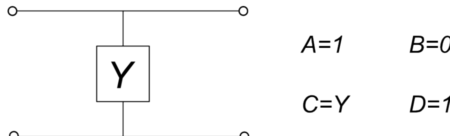

FIGURE 3.5: The *ABCD* parameters of the equivalent 2-port circuit.

The capacitance is not directly measured but it can be extracted from the transmission *ABCD* matrix [84]. The equivalent two-port circuit is shown in Fig.3.5. The conversions between the equivalent 2-port network parameters is given by:

$$A = \frac{(1+S_{11})(1-S_{22})+S_{12}S_{21}}{2S_{21}} \quad (3.1)$$

$$B = Z_0\frac{(1+S_{11})(1+S_{22})-S_{12}S_{21}}{2S_{21}} \quad (3.2)$$

$$C = \frac{1}{Z_0}\frac{(1-S_{11})(1-S_{22})-S_{12}S_{21}}{2S_{21}} \quad (3.3)$$

$$D = \frac{(1-S_{11})(1+S_{22})+S_{12}S_{21}}{2S_{21}} \quad (3.4)$$

So with $Y = G + jC\omega$ and Eq.3.3, the final function that is integrated in the program is written as:

$$C = \frac{Im(Y)}{\omega} = \frac{-2}{Z_0 \cdot \omega \cdot |S_{21}|^2}\left[-Re(S_{11}) \cdot Im(S_{21}) + Im(S_{11}) \cdot Re(S_{21})\right] \quad (3.5)$$

The extracted data is presented in Fig.3.6. The effect of the inductance is clearly shown, therefore the equivalent capacitance values should be extracted at a $< 1GHz$ frequency. The determined capacitance values are $33fF$ and $2.5pF$ for the up-state and down-state respectively. The calculated switching ratio is 75.7. Concerning the accuracy, it has to be pointed out that even if the error rate is less than 10%. This methodology is for sure less accurate than using a good capacitance-meter.

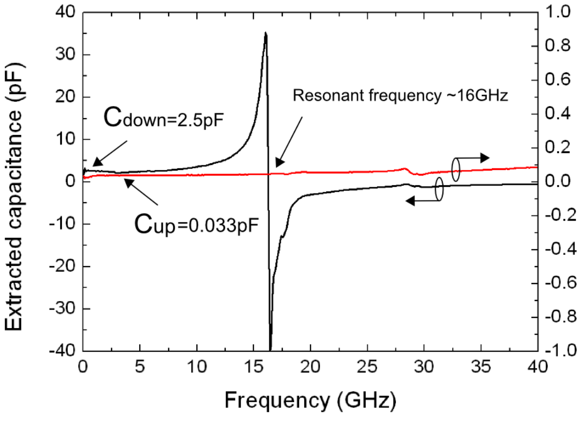

FIGURE 3.6: The extracted capacitance values.

3.1.2.4 Switching times

The switching times are measured by using the VNA in the “CW single frequency sweep” and the “Swept Power Gain Compression” modes. In this configuration the VNA works as a RF source. A bias-tee is used to combine the RF signal with the control signal (one pulse square signal with frequency range of $0.5 - 1kHz$). The mixed signal is then applied to the switch. A part of the modulated signal is split with a $10dB$ coupler, which is then amplified, detected and connected to a oscilloscope. The outcome of this procedure is shown in Fig.3.7 including two insets with shorter time span.

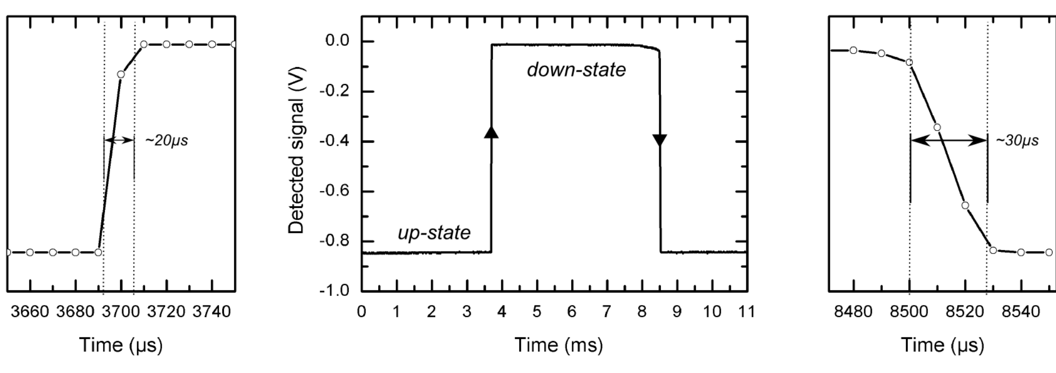

FIGURE 3.7: The switching times.

The results show that the pull-down time (positive edge) is around $20\mu s$ and the release time (negative edge) is around $30\mu s$ ($V_{applied} = 1.3 \times V_{down}$).

3.1.2.5 Transmission parameter S_{21} as a function of control voltage

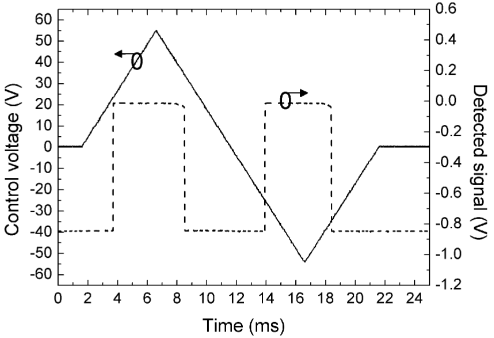

FIGURE 3.8: Timing charts of control and detected signals.

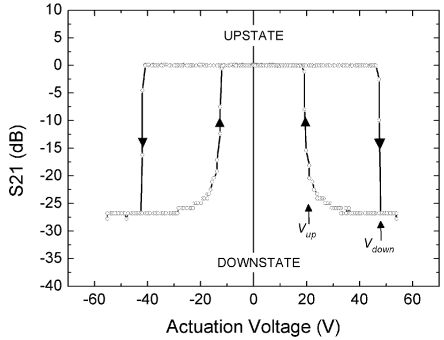

FIGURE 3.9: Transmission parameter S_{21} vs. control voltage.

In this procedure, the transmission parameter S_{21} is not directly measured from the VNA, because the same aforementioned configuration of the VNA is used (i.e CW single frequency sweep mode). So the detected signal comes from the 50Ω-RF detector (Anritsu 75KC50), which has a bandwidth of $0.01 - 40GHz$. The accuracy of the measurement depends on the sensitivity of the detector and it is given in its datasheet [2].

The control and the detected waveforms is shown in Fig.3.8. By plotting the measured data in the X-Y mode we obtained the converted transmission parameter as a function of the control voltage (Fig.3.9). This is typically the electromechanical behaviour of the switch and it can be easily correlated to the C-V characteristics. As depicted, this DUT has a pull-down voltage of around $V_{down} \sim 40 - 45V$ and a pull-off voltage of around $V_{up} \sim 15 - 20V$.

3.1.2.6 Hold-down charging

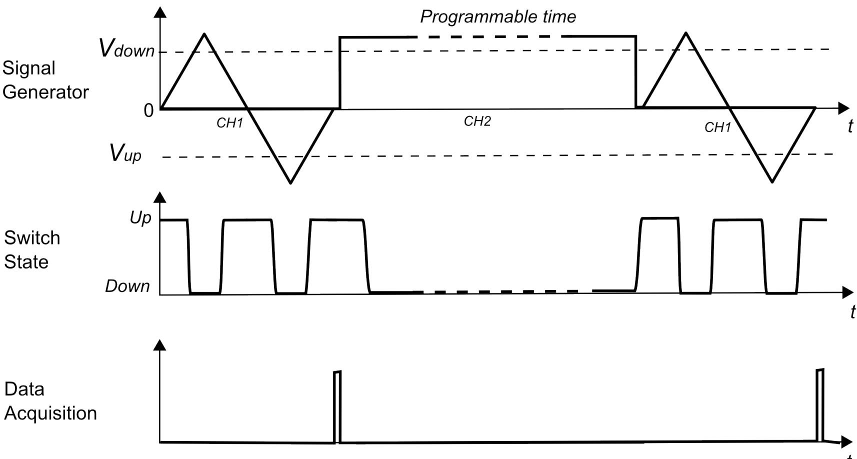

FIGURE 3.10: Timing charts of hold-down measurements.

Hold-down tests asses the ability of the switch to stay in the down-state. For dielectric charging studies it can be considered as an accelerated charging test [85]. Besides as it has been already demonstrated, the operation-time of the device does not depend on the actuation frequency but mainly on the total actuation time [51] (note: it is not a substitute test for cycling, but it gives new benchmarks). Furthermore, for mechanical studies this procedure can be interesting to analyse the device anchors and beam regions in terms of aging (crack propagation, or stress relaxation phenomena).

2. http://www.us.anritsu.com/downloads/files/Microwave_Detectors_70_75Series_54c.pdf

The procedure starts with a first $S_{21}(V)$ measurement, for which the control signal is provided by the channel 1 of the arbitrary signal generator. The hold-down voltage is supplied through channel 2, in order to make the stress signal being programmable in time. Finally the measurement period ends with another $S_{21}(V)$ measurement. By superposing the pre- and post- data acquisition the rate of charging can be evaluated.

3.1.3 Results and discussion

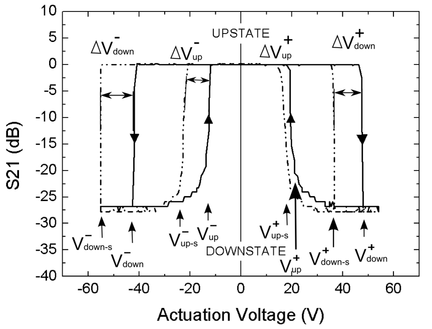

(a) Typical hold-down charging $S_{21}(V)$ graphs.

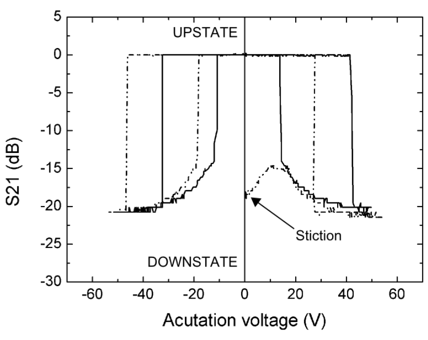

(b) A case where the switch failed to release.

FIGURE 3.11: Hold-down charging in AlN-based switches.

The results obtained by means of the hold-down charging procedure described previously is depicted in Fig.3.11. The transmission parameter S_{21} was recorded while the VNA was in a $10GHz$ single frequency sweep mode. The Fig.3.11(a) was captured before and after the hold-down configuration of $56V$ stress during $3min$. The shift of the threshold voltage (i.e.V_{down} and V_{up}) is relevant with a dielectric charging effect leading to create an internal remaining electric field. This will translate into sticking if the electrostatic force exceeds considerably the restoring force of the membrane and this case is illustrate in Fig.3.11(b).

To continue the work that has been done on Si_3N_4-based switches [60] and contribute to the understanding of different insulating materials susceptible to be charged, AlN-based switches are here tested using the hold-down charging procedure. Usually in capacitive switches, charging is assessed by characterizing the bias voltage dependent capacitance $C(V)$, which exhibits a shift with respect to the initial $V_{applied} = 0$ signature. This shift is mostly due to charge trapping (abundant at the surface) and it could depend on the design, material composition, contamination and environmental conditions. The analytically estimation of the

shift of the voltage is given by solving the one dimension Poisson's equation (considering the simple model of dielectric charging (Fig.2.6)):

$$\frac{\mathrm{d}^2V}{\mathrm{d}z^2} = -\frac{\rho(z)}{\varepsilon_r\varepsilon_0}, \tag{3.6}$$

where V is the electrostatic potential, $\rho(z)$ is the height dependent trapped charge density in the dielectric and it is treated as uniform in the lateral dimensions, so it is shown as a function of only along z direction. The voltage shift caused by insulator trapped charge is given by:

$$\Delta V_{shift} = \frac{1}{\varepsilon_r\varepsilon_0}\int_0^{z_d} z\cdot\rho(z)\mathrm{d}z, \tag{3.7}$$

where $\rho(z)$ is the height dependent trapped charge density related to the total polarization P_Σ (Eq.2.30), z_d, ε_r is the dielectric thickness and constant respectively.

Experimentally, the voltage shift is calculated using the superposition of the initial $S_{21}(V)$ graph and the one measured after the hold-down charging procedure (as shown in Fig.3.11(a)). It is clearly shown that trapped charges modify the charge distribution in the dielectric and hence the electrostatic force and it is translated into a shift in the $S_{21}(V)$ characteristics. If careful attention is paid on the residual charge before and after the stress, the change of charge can then be evaluated. From Fig.3.11(a), the residual charge before stress is defined by:

$$\Delta V_{down} = V^+_{down} + V^-_{down} \tag{3.8}$$

$$\Delta V_{up} = V^+_{up} + V^-_{up}$$

, and the residual charge after the stress is defined by:

$$\Delta V_{down-s} = V^+_{down-s} + V^-_{down-s} \tag{3.9}$$

$$\Delta V_{up-s} = V^+_{up-s} + V^-_{up-s}$$

In an ideal switch, ΔV should be symmetrical independently on the polarity of the bias. In practice it is often not the case. Therefore in order to compare various structures with different materials, average charging values are extracted from the measurements (such as data shown in Fig.3.11(a)). As it is shown in the figure, the

superposition of the initial measurement and the last stress measurement shows different ΔV in the positive and negative bias polarity. In order to calculate the average rate in change of charge all the four branches of threshold voltages are considered (V^+_{down}, V^+_{down-s}, V^-_{down}, V^-_{down-s} for the pull-down and V^+_{up}, V^+_{up-s}, V^-_{up}, V^-_{up-s} for the pull-up) and they are given by:

$$\langle \Delta V_{down} \rangle = \frac{\Delta V_{down} - \Delta V_{down-s}}{2} \tag{3.10}$$

or

$$\langle \Delta V_{up} \rangle = \frac{\Delta V_{up} - \Delta V_{up-s}}{2} \tag{3.11}$$

The offset voltage V_{off} defines the average value of residual charge from both threshold voltages ΔV_{down} and ΔV_{up} extracted from $S_{21}(V)$ graphs, and it is calculated as:

$$\boxed{V_{off} = \frac{\langle \Delta V_{down} \rangle + \langle \Delta V_{up} \rangle}{2}} \tag{3.12}$$

Analytical model

The interpretation of data obtained in this experiment is done through the general case of the analytical model reported in [52]:

$$V = f(z) \pm g(z) = \frac{\mu_\alpha \mu_\beta + \mathrm{cov}_{(\alpha,\beta)}}{\mu_\alpha^2 + \sigma_\alpha^2} \pm \sqrt{\left(\frac{\mu_\alpha \mu_\beta + \mathrm{cov}_{(\alpha,\beta)}}{\mu_\alpha^2 + \sigma_\alpha^2} \right)^2 + \frac{2\varepsilon_0 \cdot k \cdot z/A - (\mu_\beta^2 + \sigma_\beta^2)}{\mu_\alpha^2 + \sigma_\alpha^2}} \tag{3.13}$$

where $f(z)$ is a shift of the reference voltage, $g(z)$ is the mechanical contribution, the symbol $\pm$ is either the positive or negative bias branch of the C(V) characteristic and z is the displacement and μ, σ^2, and cov denote the mean, variance, and covariance respectively, of the $\alpha(x, y, z)$ and charge $\beta(x, y, z)$ distributions:

$$\alpha(x, y, z) = \frac{\varepsilon_0}{(d_0(x, y) - z) - \frac{z_d}{\varepsilon_r}}$$

which is the distribution of capacitance per unite area and:

$$\beta(x, y, z) = \frac{z_d}{\varepsilon_r \varepsilon_0} \Psi_{eq}(x, y) \alpha(x, y)$$

is the distribution of charge density induced at the armature area and $\Psi_{eq}(x, y)$ and z are the equivalent surface charge distribution and the displacement from equilibrium respectively, $d_0(x, y)$ the height of the upper electrode from the surface

of the dielectric along z axis and z_d is the thickness of the dielectric.
Although this equation (Eq.3.13) is valid only for equilibrium (i.e. pull-up state), we can use it in the vicinity of pull-down and pull-up or either in the infinitesimal below pull-down and pull-up state. Under equilibrium, the applied voltage practically has the value of the pull-down and pull-up voltages.

For instance, if we apply Eq.3.8 and Eq.3.9 to Eq.3.13 and assume that during the hold-down procedure the function $f(z)$ and $g(z)$ do not change, then it leads to:

$$\Delta V_{down} = \left[f(z)^{+} + g(z)^{+}\right] + \left[f(z)^{-} - g(z)^{-}\right] = 2 \cdot \left(\frac{\mu_\alpha \mu_\beta + \mathrm{cov}_{(\alpha,\beta)}}{\mu_\alpha^2 + \sigma_\alpha^2}\right) \tag{3.14}$$

$$\Delta V_{down-s} = \left[f(z)_s^{+} + g(z)_s^{+}\right] + \left[f(z)_s^{-} - g(z)_s^{-}\right] = 2 \cdot \left(\frac{\mu_\alpha \mu_\beta + \mathrm{cov}_{(\alpha,\beta)}}{\mu_\alpha^2 + \sigma_\alpha^2}\right)_s$$

Afterwards, by applying Eq.3.10, we will obtain:

$$\langle \Delta V_{down} \rangle \cong \left(\frac{\mu_\alpha \mu_\beta + \mathrm{cov}_{(\alpha,\beta)}}{\mu_\alpha^2 + \sigma_\alpha^2}\right) - \left(\frac{\mu_\alpha \mu_\beta + \mathrm{cov}_{(\alpha,\beta)}}{\mu_\alpha^2 + \sigma_\alpha^2}\right)_s \tag{3.15}$$

, which is the change in net charge (the same calculation can be performed for $\langle \Delta V_{up} \rangle$
Finally applying Eq.3.12 to Eq.3.15 and assuming always that no change occurs during a full C-V measurement, it leads to:

$$V_{off} \cong \left(\frac{\mu_\alpha \mu_\beta + \mathrm{cov}_{(\alpha,\beta)}}{\mu_\alpha^2 + \sigma_\alpha^2}\right) - \left(\frac{\mu_\alpha \mu_\beta + \mathrm{cov}_{(\alpha,\beta)}}{\mu_\alpha^2 + \sigma_\alpha^2}\right)_s \tag{3.16}$$

It means that the shift of the voltages depends directly on the mean value of the background charge distribution μ_β and the variance σ_β. The lesser uniform the charge the higher is its variance σ_β and the larger will be the change in the distribution of the electrostatic field and hence the drift in the actuation parameters of the structure.

The purpose of this study is to compare the charging of the material used in this work (AlN) with other materials, whose properties were reported in the literature. However this parameter may depends on the bulk, surface and interface properties of the material, the quality of the contact, the geometry of the structure or the choice of the metal of the electrodes. A huge amount of parameters that are directly or indirectly related to the charging behaviour of the device. Therefore in

order to make this study, an empirical factor translating the kinetic of charging is used. This empirical factor is defined as the rate of charging R_Q (here it is stated that charging is related to the time the switch last in the down-state [51]):

$$R_Q = \frac{\mathrm{d}V_{off}}{\mathrm{d}t_{down}} \tag{3.17}$$

Experimentally, V_{off} is extracted from C(V) or S21(V) graphs using Eq.3.12 and t_{down} corresponds to the hold-down time in the hold-down charging procedure while for cycling tests, the approximative value of t_{down} is calculated by taking into account the duty cycle and the frequency of the control signal.
The rate of charging factor is in principle an image of the response of the material to charging and it is electric-field-dependent. Moreover the charging factor, as it is analytically discussed above, depends significantly on the roughness [52, 60]. Therefore, to compare materials, it would be more consistent to use the intrinsic electric field of the dielectric proposed in [60]:

$$E_{eff} = \left(\frac{V_{applied}}{z_d}\right) \times \left(\frac{C_{meas}}{C_{th}}\right) \tag{3.18}$$

where $V_{applied}$ is the applied voltage, C_{th} is the theoretical down-state capacitance value calculated from Eq.2.4 and C_{meas} is the measured down-state capacitance value, with:

$$C_{th} = \frac{\varepsilon_0 \cdot \varepsilon_r \cdot A}{z_d}$$

$$C_{meas} = \frac{\varepsilon_0 \cdot \varepsilon_r \cdot A}{z_d + r_a}$$

, and the ratio is given by:

$$\frac{C_{meas}}{C_{th}} = \frac{z_d}{z_d + r_a} = \frac{1}{1 + \dfrac{r_a}{z_d}}$$

, where r_a represents the air gap due to roughness and asperities.

These two expressions (Eq.3.17 and Eq.4.5) together includes implicitly all the physical and electrical parameters such as dielectric properties, the effective intrinsic electric field, the quality of the contact (asperities and roughness of the contacting surfaces which is mainly technology dependent).
From electric conduction fundamentals, the conductivity is a measure of a material's ability to conduct an electric current and it is defined as the ratio

of the current density J to the electric field strength by:

$$J = \sigma \cdot E \tag{3.19}$$

In the case of MEMS switches, the conductivity of dielectrics is affected by the contact between surfaces of the bridge and dielectric (roughness and asperities) and the electric field is inhomogeneous. Those concerns have been taken into account in the calculation of the effective electric field (Eq.4.5). So using Eq.3.17 and Eq.4.5 the apparent conductance of dielectrics can be calculated using:

$$\sigma_{eff} = \frac{R_Q}{E_{eff}} \frac{\varepsilon_0 \varepsilon_r}{z_d} \tag{3.20}$$

where z_d is the thickness of the dielectric.

This parameter is then calculated for experimentally obtained and reported data and it is summarized in Fig.3.12. It shows the apparent effective conductivity of the dielectric as a function of the intrinsic electric field. The extracted E_{eff} values of published papers have been calculated using either values provided by the authors or reported C(V) graphs.
The results obtained from the series of measurements and calculated data of AlN-based structures is shown in Fig.3.12. In terms of comparison it includes also data from previously work on Si_3N_4-based devices [60] and other informations extracted from reported publications showing state-of-art components that have been stressed under a cycling procedure (rough estimations).
How to read this graph ? Higher the extracted point is plotted in the top right hand corner better is the device.
The first remark is that there two groups of points, one group is made from hold-down charging tests and the second one comes from cycling tests. This is due to the electrical accelerated charging effect of hold-down procedure compare to cycling test and the calculation of the rate of charging R_Q in cycling results in very small values (i.e. the mean V_{shift} is very small).
Concerning hold-down charging group of points AlN-structures seem to be less sensitive to charging than Si_3N_4-structures. This reduced charging affinity is probably resulting from a higher structural quality. Which means that PE nitride usually has an amorphous structure that favour the accumulation of traps, whereas sputtered AlN layers are characterised by densely packed columnar grains with an excellent orientation [86]. It is also outlined that AlN-based structures exhibit

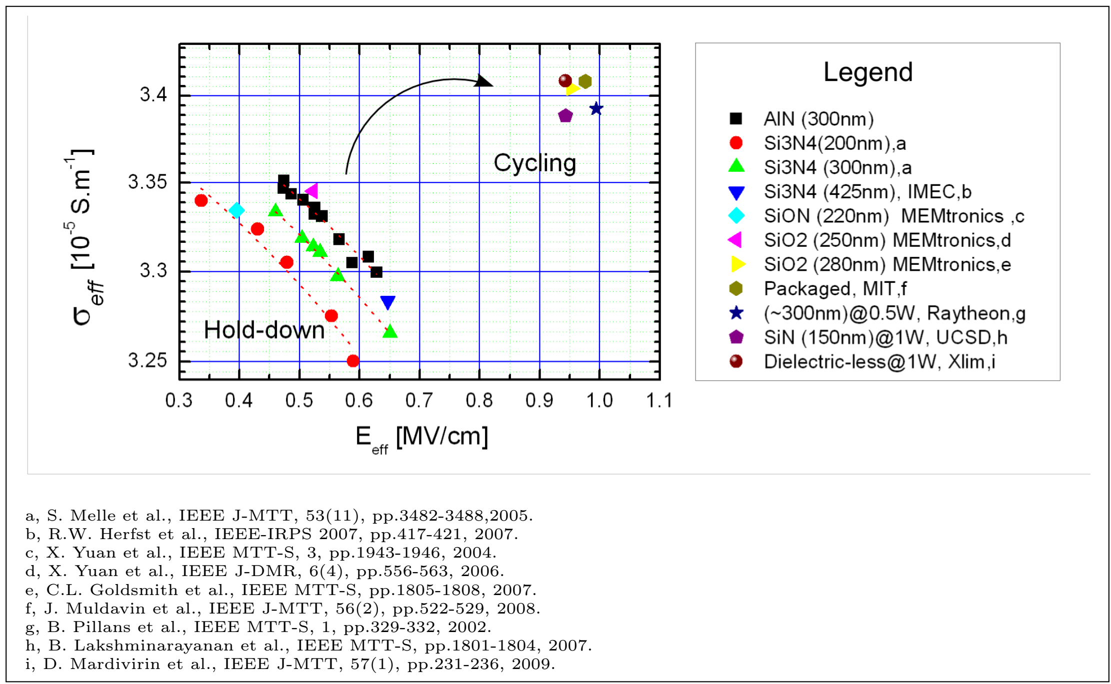

FIGURE 3.12: Empirical comparison of different insulating materials.

similar dielectric charging robustness than SiO_2-based ones with a higher dielectric constant. However, it has been shown that the effect of spontaneous polarization which is related to the defects will affect the $C(V)$ characteristics of the device [87] (it leads to dipole moments related to dislocation or other structural or point defects in polycrystalline AlN).

Finally as a subjective opinion on dielectric charging in switches, if the switch can cross over a few billion cycles, then it will reach easily $>$ 100 billion (as shown by the state-of-art components in Fig.3.12) because the failure mechanisms appear in the time scale before the first billion cycles (as shown in Fig.2.12 the inverse-power law in this time scale and it corresponds also to the "infant mortality" part of the bathtub curve, Fig.2.1).

3.2 ESD investigations in RF MEMS capacitive switches

This section is devoted to describe ESD effects in RF-MEMS capacitive switches. ESD testing is particularly relevant for electrostatically actuated RF MEMS devices, but unfortunately no standard is available yet. Nevertheless several different types of tests exist to examine sensitivity to different types of electrical discharge and breakdown phenomena. TLP and HBM testing results will be presented here.

3.2.1 DUT

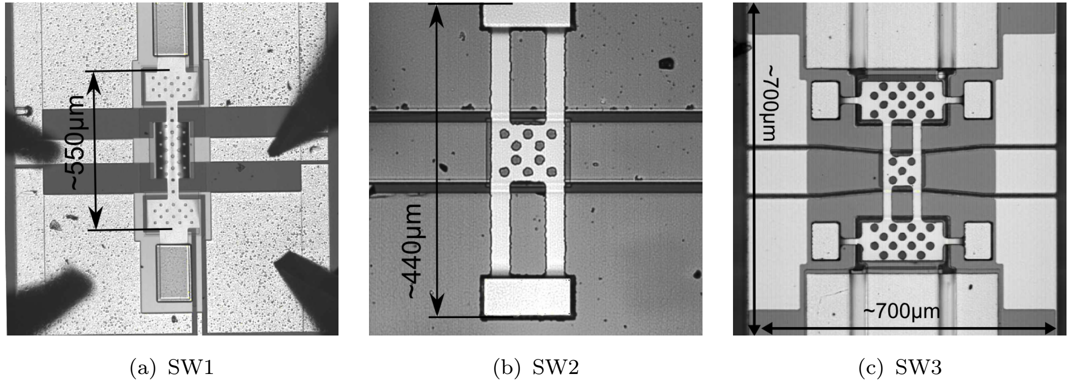

(a) SW1 (b) SW2 (c) SW3

FIGURE 3.13: Tested devices.

The structures that have been tested in those experiments are presented in Fig.3.13. To be easily distinguished, they are identified as SW1, SW2 and SW3. The properties of SW1 have been described in Section 3.1.1. The RF-MEMS technology of SW2 and SW3 is built on high resistivity silicon substrate covered by a Benzo-cyclo-butene (BCB) layer of $10\mu m$ in thickness. The $1.8\mu m$ thick coplanar waveguide line is made of TiAu/Au/multi-layer, formed by liftoff of evaporated gold. The bridge's membrane is made of $2\mu m$ thick electroplated gold. Under the bridge the signal line is covered by $250 \pm 10nm$ of high frequency (HF-) or low frequency (LF-) PECVD Si_2N_4 dielectric layer with a dielectric constant around 6.5 (both types have been tested). Without electrostatic force, the mechanical beam's height over the signal line features $1.9\mu m$. Their microwave characteristics have been verified and it is reported in Fig.3.14. Those designs were initially

developed to be frequency scalable [40]. The actuation voltage of the switches is around $20 - 30V$.

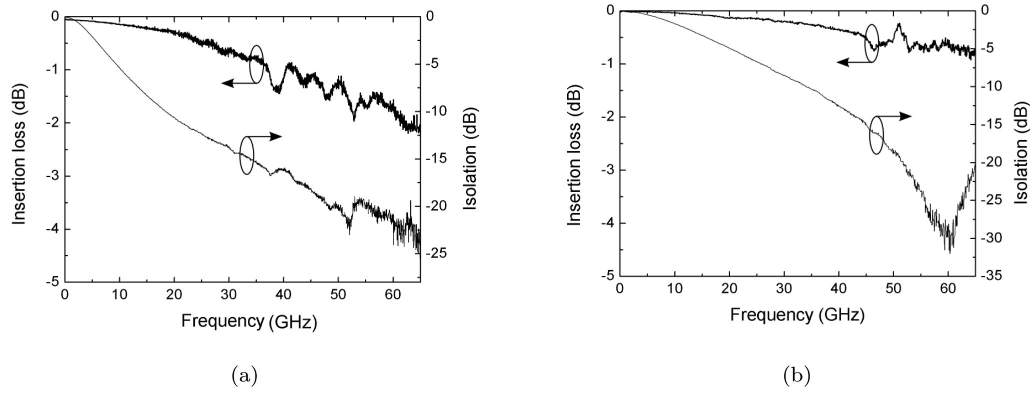

FIGURE 3.14: S-parameters of (a) SW2 and (b) SW3 structures.

3.2.2 Testing methodology and equipment

For ESD evaluation of capacitive RF MEMS, we have used two types of tester (Fig.3.15). The first technique is TLP testing, it is a 50Ω impedance wafer level system, providing rectangular pulse of $100ns$ width with $300ps$ rise time. The second tester is HBM ESD qualification simulator from Hanwa Co., which provides a $500ns$ width double-exponential pulse signal on a short load (with $10ns$ rise time).

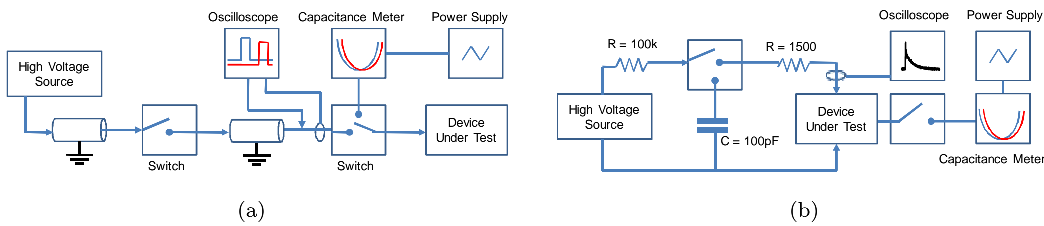

FIGURE 3.15: Block diagram of ESD set-ups including capacitance monitoring (a) TLP and (b) HBM.

3.2.2.1 TLP

The TLP pulses were applied between the signal line and the ground when the membrane is in the up-state configuration. To determine the failure signature,

successive zaps ranging from 10 V to 400 V are applied. It has to be noticed that the actuation voltage of those devices are around 30 V. But, from the device mechanical point of view, the TLP is a very fast transient (100 ns) that cannot induce movement of the membrane (switching time $\simeq 20 - 30\mu s$). This has been verified using a laser spotlight pointing on the membrane, with a photo-detector to readout the reflected ray during the stress (Fig.3.16).

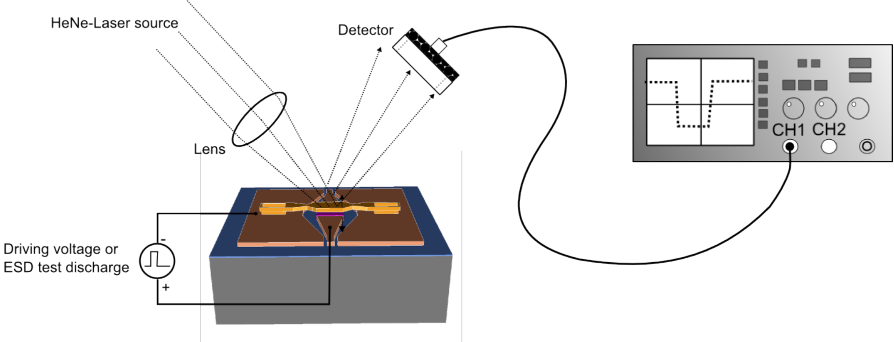

FIGURE 3.16: Simple experimental apparatus employed here to measure mechanical variation of the movable membrane.

3.2.2.2 HBM

The equipment used for HBM effects investigation was a wafer level HBM tester from Hanwa Co., able to monitor voltage and current waveforms during the stress procedure. It is not possible to use the voltage probe in this case for two reasons; on one hand the capacitor of the probe ($8pF$) will affect the measurements ahead the capacitance of the DUT ($0.11pF$ in bridge up-state and $1.5pF$ in down-state). On the other hand the impedance of the DUT is much higher than the voltage probe one, leading to an unrealistic leakage current through the probe discharging the HBM tester capacitance. Therefore, the voltage probe was removed and only current waveform measurements $I(t)$ were performed during the discharge.
The HBM bench use a $100pF$ charged capacitance and $1.5k\Omega$ serial resistance (Fig.3.15(b)), leading to a current transient with $500ns$ decay time. The HBM standards define the shape of a human body discharge into a short circuit. In this particular case the tester behaves like a current generator. In our case, the DUT is equivalent to a capacitor, which means that the tester becomes a voltage generator. It is important to underline that this is exactly what would happen if a real charged human body touch the device. Actually, depending on the precharged voltage the device is equivalent to capacitor or a variable capacitor due to the air

gap of the component (i.e. up-state position is an open circuit and down-state position is a capacitor). So when the $100V$ pre-charged tester is connected to the MEMS, the $100V$ voltage is almost entirely applied to the device due to its very small capacitance compared to the HBM one. This voltage stays for $20ms$ (the time that takes the set-up to short the remaining signal to ground).

3.2.2.3 Capacitance-based charging monitoring without pull-down of the switch

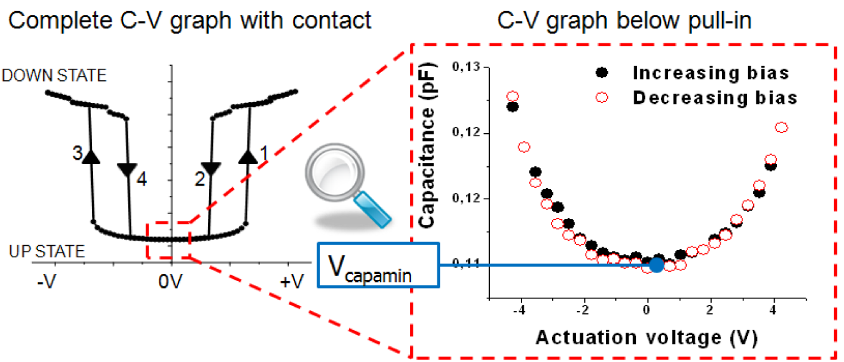

FIGURE 3.17: Principle of C(V) characteristic below the pull-down point.

In order to monitor the charging before and after the ESD stresses, capacitance characteristics have been measured by biasing the device below its pull-down voltage. This precaution is necessary to avoid dielectric charging generated from the test bench. The shift of the voltage corresponding to the capacitance minimum is closely related to the underlying physical mechanisms such as, the kinetic and the amount of trapped charges or residual surface charges. The measurements have been done in ambient environmental conditions (i.e atmospheric pressure, room temperature $25°C$ and 30% of humidity). For charging studies ESD stresses voltage magnitude were used up to 100 V. This value was chosen to be below the electrical breakdown level so to avoid permanent damages of the structure.

Capacitance probes are commonly used for surface charge and surface potential measurements. This principle was first proposed by L. Kelvin in 1898 [88], it is the precursor of the Kelvin probe technique. The simplest model of a capacitor is a two flat and parallel-conductive plates capacitor model. The capacitance of this model will depend on the active surface area (A), the distance between the plates (d) and the medium between them. The function of the capacitance can be expressed as:

$$C = \frac{\varepsilon_r \cdot \varepsilon_0 \cdot A}{d} \tag{3.21}$$

where ε_r is the relative electric permittivity of the material between the electrodes and ε_0 is the electric permittivity of vacuum. The charge on the tested surface can be calculated as:

$$Q = V\frac{\varepsilon_r \cdot \varepsilon_0 \cdot A}{d} \tag{3.22}$$

In the case of the capacitive RF-MEMS switch, if the capacitance is measured in a voltage span where the membrane of the switch is still in the non-contact state, the measured capacitance as a function of the voltage $C(V)$ is a parabola as shown in Fig.3.17. The authors in [50, 52, 89–91] have been also adopted this method previously in their research. However a careful adjusting is necessary between the voltage span and the voltage step in order to measure a more stable capacitance value. The non-linear behavior of the structure as a function of the applied voltage can usually be fitted with the following quadratic expression:

$$C(V) = C_0\left(1 + C_1 \cdot V + C_2 \cdot V^2\right) \tag{3.23}$$

where C_0 is the minimum of capacitance, C_1 the linear coefficient (sensitive to charging) and C_2 is the quadratic coefficient (related to the curvature of the parabola).

When charging occurs in an insulating material, the surface potential will have a value that is related to the amount of charges and the shape of their distribution. The whole parabola can be shifted either to the positive or to the negative side depending on the dielectric material and the bias polarity (Fig.3.18). This shift is proportional to the amount of charge collected by the dielectric and hence to the built in surface potential when stresses are applied to the device (Eq.2.34).
To detect charges, the Pulse Induced Charging (PIC) setup (Fig.3.19) has been used. This setup is inspired by the Kelvin probe principle of operation [88]. In fact

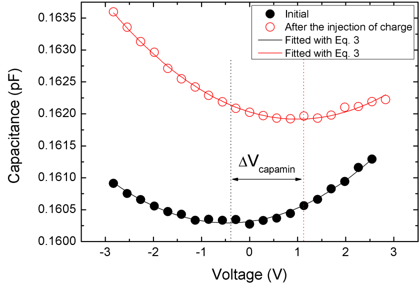

FIGURE 3.18: Typical C(V) characteristic of the capacitive switch measured in the non-contact state voltage span.

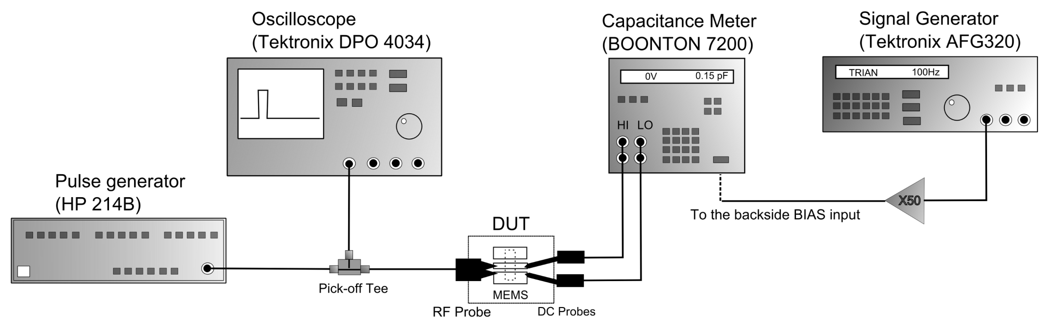

FIGURE 3.19: The PIC test bench combine with a capacitance meter.

non-contact $C(V)$ characteristics are used to measure the change in the amount of surface potential, so the membrane is considered at first as the capacitance probe. Short pulses are then applied in order to bring the membrane in the downstate condition, which favours the charges deposition. A bias voltage is provided by a Tektronix AFG320 signal generator (amplified) to a BOONTON 7200 capacitance meter (internal voltage source can also be used) which can then be used to measure the $C(V)$ characteristics in the non-contact state voltage span. The short pulses are supplied using a HP 214B pulse generator. A pick-off tee has been used to monitor the waveform of the applied pulse. Automation of the setup is performed trough a LabVIEW program and using GPIB connections.

3.2.2.4 Charging mechanisms hypothesis

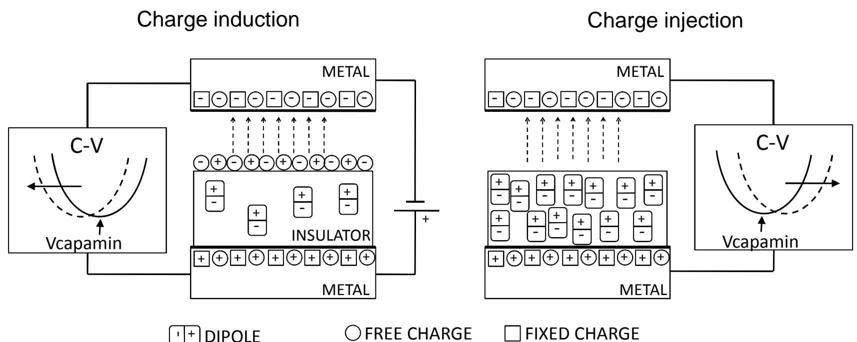

FIGURE 3.20: Charging mechanisms hypothesis in capacitive switch.

Based on the simplified charging model of the capacitive RF-MEMS switches (Fig.2.6 in Chapter 2), when we performed an sweeping of the bias from -4V to +4V (no pull-down occurs), no current flows through the dielectric and any transient current measured in the external circuit will arise from dipolar polarization and

space charge polarization of free charges. This way only the impact of ESD stresses will be analysed. Under high electric field pulses, we expected two charging mechanisms responsible for the polarizability to take place[89] (Fig.3.20):

• The first one is electronic polarization from field-induced charging; The electric field causes translation of symmetrical distribution of the electron clouds of atoms or molecules .

• The second one is orientational polarization from charge injection; The electric field causes the reorientation of the dipoles toward the direction of the field.

In the first case, we expect a drift of $V_{capamin}$ value towards the opposite polarity compare to the applied pulse one, whereas in the second case the shift should be towards the same polarity as the applied pulse's.

3.2.3 Results and discussion

The discussion on the results obtained here will be as followed: Firstly we will presented the breakdown mechanisms in TLP and HBM (3.2.3.1). Then since we want to investigate the charging behaviour due to ESD, we will work in a breakdown free region, so at voltage levels around $\sim 100V$ (3.2.3.2). Using results obtained from the PIC setup, discussion is made on inhomogeneous dielectric charging (3.2.3.3). Finally, it is shown that data from pulse discharges test allow a fast reliability estimation (3.2.3.4).

3.2.3.1 Breakdown phenomena in RF MEMS

Breakdown in TLP testing

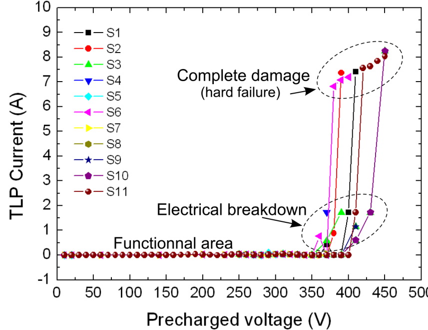

FIGURE 3.21: TLP Current-Voltage failure signature of SW1 switches.

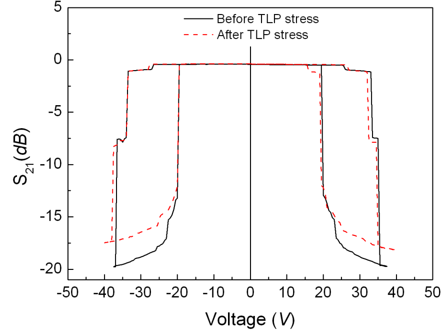

FIGURE 3.22: $S_{21}(V)$ graph of SW1 affected by soft failures.

Fig.3.21 shows typical failure signatures of RF-MEMS capacitive switches. Three different regions are distinguished: an area where the device is still functional after the stress and two failures areas, namely soft failures area, and hard failures area. The functional zone indicates the highest TLP magnitude that the component can withstand and that will not affect its behaviour. Soft failures occur for a voltage around $\sim 400V$. Soft failure defines a device which is still functional after the ESD stress, according to RF-measurements (it still works as a switch and performs its RF function). Fig.3.22 shows the fact that despite some holes occurring in the membrane, there is no modification of the electromechanical behaviour of the device as the pull-down and pull-up voltages remain similar as well as the overall hysteresis cycle. However the off state behaviour is shown on the device's isolation to be clearly affected. Fig.3.23 reports a typical degradation mechanism that has been observed. At high voltage magnitude, some physical degradation is visible through holes in the metallic membrane. It has been found that these holes originate from electric arc occurring under the membrane, due to very high current creating electric arc breakdown channel, resulting in melting of the metal and of the dielectric. We believe that this local degradation is related to a localized breakdown path that explains the holes occurring in the metallic membrane. In the soft failures area of the TLP $I(V)$ graphs in Fig.3.21, each point is linked to an electric arc phenomenon. From these quasi-static measurements, the maximal current that the structure can withstand is $I_{max} = 2A$ (TLP robustness). Finally Fig.3.24 depicts the microscope picture of a structure after the TLP sequence, showing a completely destroyed device (it corresponds to the hard failures area of the TLP $I(V)$ graphs).

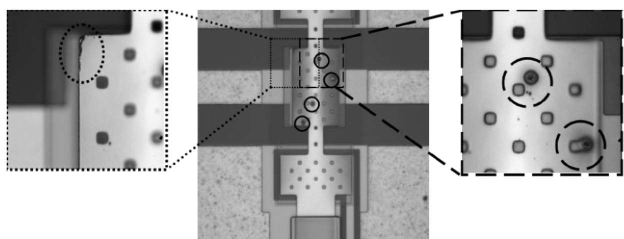

FIGURE 3.23: Microscope picture of a partially damaged switch.

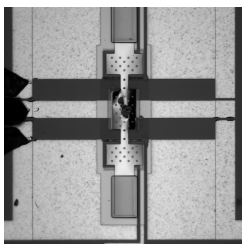

FIGURE 3.24: Microscope picture of a completely destroyed switch.

Note: Electrical breakdown in MEMS air gap switches

The lifetime of capacitive RF MEMS switches can be impacted by parameters such as, the control signal waveform (including amplitude, duty cycle, offset) and the operation environment (i.e. ambient air, vacuum, He, N_2).In addition, in some cases, the electrical discharge can occur between the movable membrane and the bottom electrode, which can be catastrophic in terms of reliability for the device. In fact, the Paschen's law published in 1889 [92] states that the breakdown voltage of a gap is a function of the product of the gas pressure and the gap distance. This law was theoretically demonstrated by Townsend in 1925 [93], confirming that an electric spark occurs if free electrons accelerated by an electric field accumulate enough energy between successive collisions with neutral atoms to ionize them and generate additional ionizations, then resulting in a Townsend avalanche.

Fig.3.25 shows the Paschen's curve for the direct current breakdown voltage of two parallel-plane electrodes in air at $1atm$ as a function of electrode separation. We can observe that for gaps higher than $10\mu m$, electrical breakdown occur when the electric field is around $3V/\mu m$, and the minimum of Paschen is observed at 360 V for electrode separation of $5\mu m$. Nowadays, the air gap in capacitive MEMS is often below $5\mu m$, corresponding to a very high breakdown voltage according to the Paschen's curve, which should provide the RF MEMS a certain voltage overstress immunity. However, Schaffert [94] and Dhariwal [95] demonstrated the field emission phenomenon for gaps between $5nm$ and $5\mu m$, where a "transition" region substitutes for the minimum of Paschen. The modified Paschen is a good guide for taking into account ESD sensitivity in MEMS planar geometry designs. The effect of gas pressure and gas type on the breakdown voltage shall not be overruled [96].

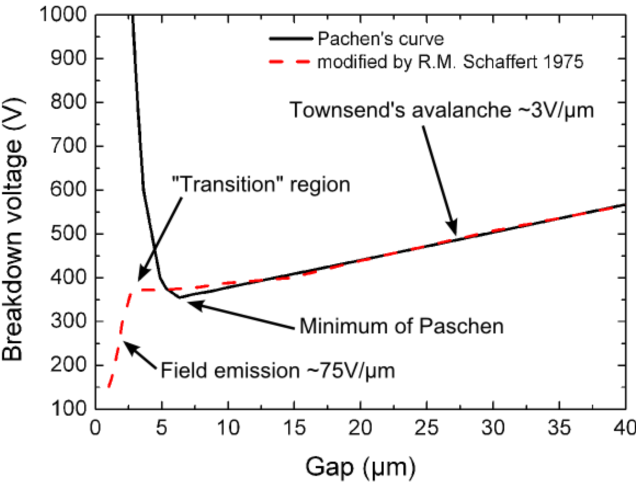

FIGURE 3.25: Breakdown voltage in air at 1 atm versus gap.

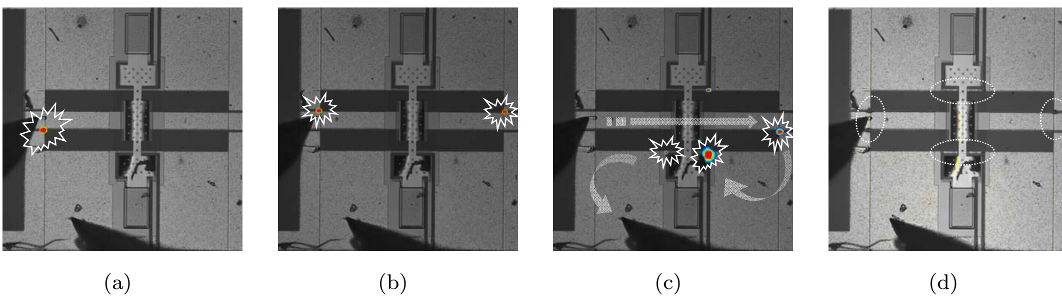

(a) (b) (c) (d)

FIGURE 3.26: Light emission obtained during breakdown on SW1, pulses were generated at (a) $390V_{TLP}$ (b) $400V_{TLP}$ (c) $410V_{TLP}$ and $420V_{TLP}$ (d) visible damages after the stresses.

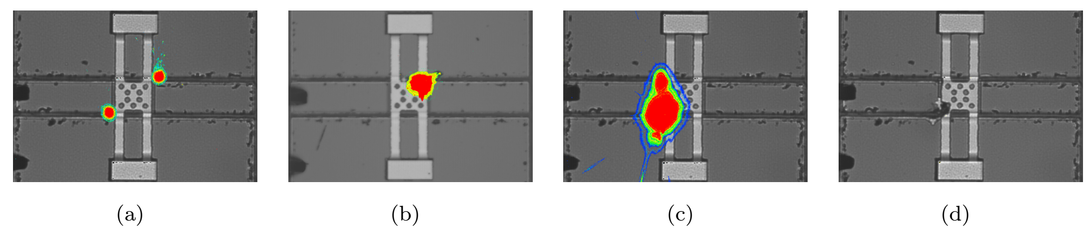

(a) (b) (c) (d)

FIGURE 3.27: Light emission obtained during breakdown on SW2, pulses were generated at (a) $330V_{TLP}$ (b) $450V_{TLP}$ (c) $450V_{TLP}$ (d) visible damages after the stresses.

In order to get deeper insight on this electric-arcing effect, we have conducted optical analysis to detect and localize these failures, using a digital CCD camera (Hamamatsu C4880). When electric arc occurs across the air gap, the resulting photons can be captured using this camera. Fig.3.26 and Fig.3.27 show the light emission acquisition performed on SW1 and SW2 devices. In the case of AlN-structures (SW1), we were wondering why the breakdown starts at the beginning of the CPW line rather than in the active area (the distance between the ground plane and the signal line of the CPW is approximatively $10\mu m$ whereas the distance between the upper membrane and the bottom electrode is $2.5\mu m$). In order to explain this effect, we have conducted 2D (using Silvaco) and 3D static simulations to estimate the electric field profiles. Fig.3.28 presents the electric field distribution in the CPW slot featuring a peak value of $1.9MV \cdot cm^{-1}$ occurring near the metallization. Such high electric field level triggers a spark that yields metallization melting (by edge effect). These two correlated phenomenon are both detected by the CCD sensor. If we calculate the static electric field between the central line and the upper membrane, we find a lower value of $1.75MV \cdot cm^{-1}$. It explain the fact that the hot spot and then the corresponding failure mechanism occurs firstly in the CPW region. It shows how those unwanted disruptive effects are geometry-dependent.

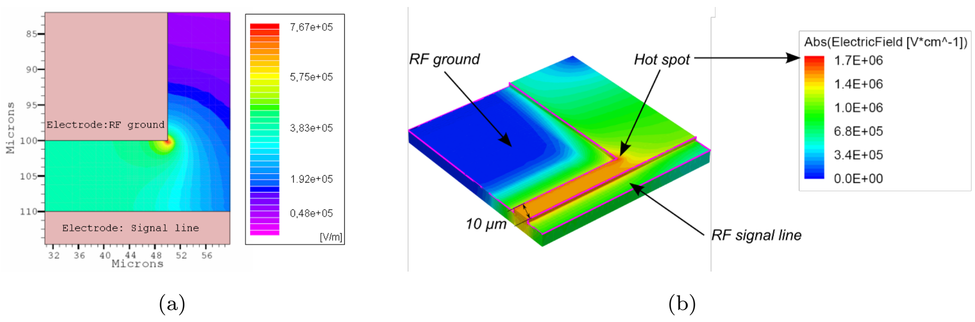

(a) (b)

FIGURE 3.28: Electric field distribution using static 2D and 3D simulation with a DC voltage of 420V at the CPW access.

Breakdown in HBM testing

The HBM-ESD tester works differently than the TLP one and as previously mentioned only current waveform are acquired during HBM discharges. The current transient waveforms were obtained using a $6GHz$, $20GS/s$ digital storage oscilloscope and a CT-1 Tektronix current probe. In the following experiment, one device receives cumulative HBM stress from $10V$ to $1kV$, using variable voltage steps. The results are shown in Fig.3.29. For HBM magnitudes below $250V_{HBM}$, a negative current transfer is measured after each stress. Despite of the effect

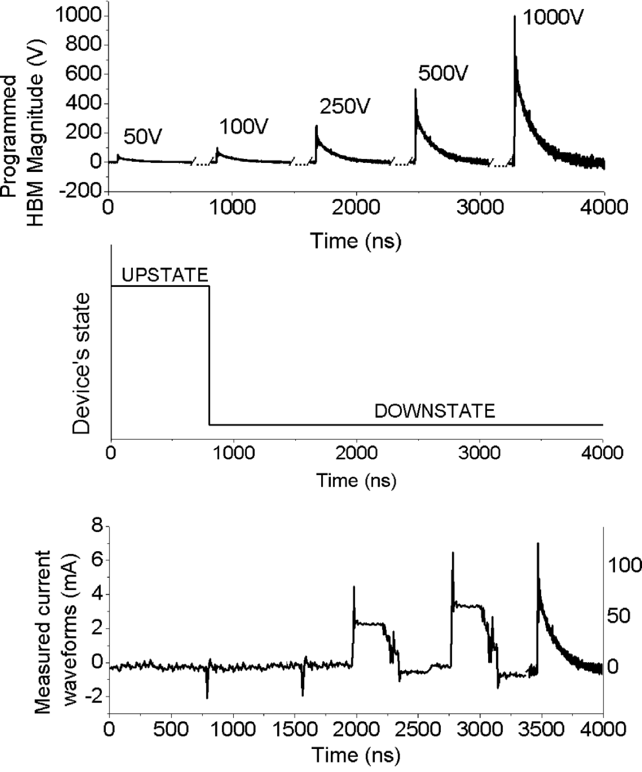

FIGURE 3.29: Current waveform responses in function of HBM failure signature.

induced by the voltage probe, we used it once to better understand this negative current transfer. The measured current signal corresponds to the signal shorted to ground after the discharge by the set-up ($20ms$), and not to a current path across the device. The current waveforms obtained in the soft failures region clearly show the current flowing through the device during the HBM pulse. Finally, the hard failures region appears when the magnitude reaches above $1kV_{HBM}$. The current waveform corresponds to a low-impedance-device one (short circuit).
An optical verification after the stress procedure does not shown any degradation (Fig.3.30(a)). We removed the membrane and then noticed that each spark creates a physical damage on the dielectric layer (circled in Fig.3.30(b)). Since the HBM system brings the membrane in the downstate configuration when applying stresses, the failure mechanism can probably be assimilate as a "tree growth" defects [97], where completed tree-like channels turn out to local fractures damaging the thin dielectric layer.

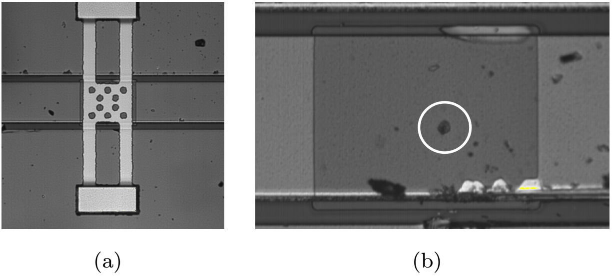

(a) (b)

FIGURE 3.30: Optical checking (a) after the total stress is applied, (b) a zoom of the dielectric area after removing the bridge.

3.2.3.2 Charging studies

In the previous subsection breakdown levels have been determined and it has shown that RF-MEMS switches are very sensitive devices (according to microelectronics system testing specifications). The following subsections will described the work that has been done concerning;

– charging mechanisms due to TLP and HBM stresses,
– discharging process after HBM stresses,
– inhomogeneous charging analysis
– and pulse induced accelerated charging.

TLP charging mechanisms in MEMS

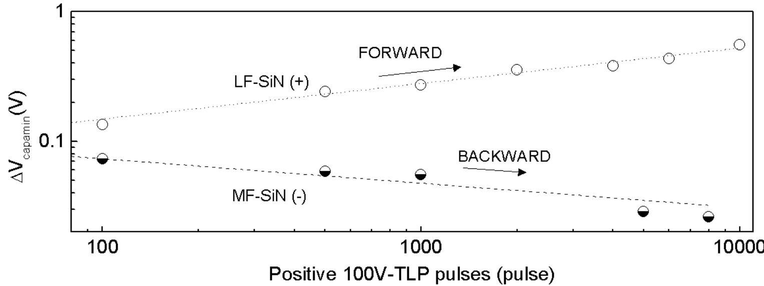

FIGURE 3.31: The shift of $V_{capamin}$ as a function of positive TLP pulses, for MF-SiN and LF-SiN structures.

Fig.3.31 indicates the series of experiments conducted using MF-SiN and LF-SiN devices, under TLP positive pulses. The same results were obtained for TLP negative pulses [98]. Both expected field-induced charging and charge injection phenomena are distinguished (positive and negative slope), with respect to the charging mechanisms hypothesis. As a result the slope constitutes an index of how vulnerable the dielectric material is to disruptive events. The log-log scale of Fig.3.31 indicates a power law dependence of the shift on the accumulated stress. A more detailed discussion on this dependence is reported in Section 3.2.3.4. It comes out that in contact-less charging, LF material is dominated by the injected charges while MF material is dominated by dipole orientation and intrinsic mobile charge displacement.

HBM charging mechanisms in MEMS

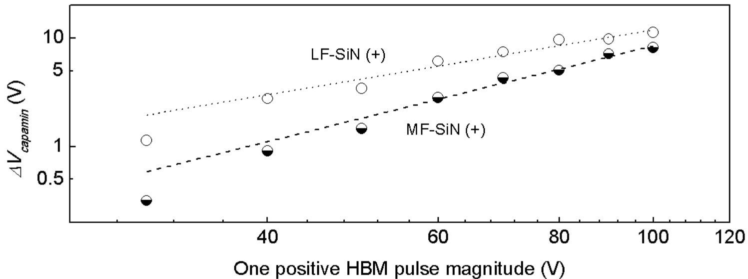

FIGURE 3.32: The shift of $V_{capamin}$ as a function of the magnitude of one positive HBM pulse.

Fig.3.32 presents the shift of $V_{capamin}$ vs. the magnitude of HBM pulses. The HBM magnitude is increased from $30V$ to $100V$. Each point corresponds to a single discharge on a fresh device, in order to avoid any trace left by previous charging phenomenon. A comparison between the TLP (Fig.3.31) and HBM (Fig.3.32)

ESD stressing methods reveals some common features and differences. As already mentioned, in Fig.3.31 we can distinguish the two charging mechanisms, namely injected charging and induced charging. In Fig.3.32, due to the fact that the bridge is actuated during the HBM pulse, only charge injection is observed and consequently the shift in $V_{capamin}$ is ten times larger than the one obtained for TLP testing. Concerning the slopes, it can be deduced that the charging in LF material builds-up faster than in the MF material, which was also the case for TLP. Both results indicate that LF-SiN is more sensitive to electrostatic discharges than MF-SiN.

In fact FTIR assessment has revealed that in MF-SiN the concentration of Si-H bonds is significantly larger than in LF-SiN [99] we conclude that the behaviour of MF-SiN material may arise from the large concentration of Si-H bonds and a possible hydrogen migration. So it depends on the properties of the different nitrides. Based on published data from MIM capacitor mentioned in the introduction, we can point out that; according to [56], transient leakage current analysis revealed that LF material is affected by the presence of defects due to high electric field injection. These defects are related to the presence of N-H bending bonds. The amount of hydrogen is lower in MF-SiN. It is correlated to the dielectric film macroscopic polarization, obtained from TSDC measurements [99], which shows the interaction from dipoles and also from free carriers. Another point is that the roughness of dielectric and bridge surfaces gives rise to a non uniform charge distribution. During an ESD event, competition between the two basic mechanisms mentioned in the section of charging mechanisms hypothesis, will take place and a charge distribution similar to the one shown in [91] cannot be overruled.

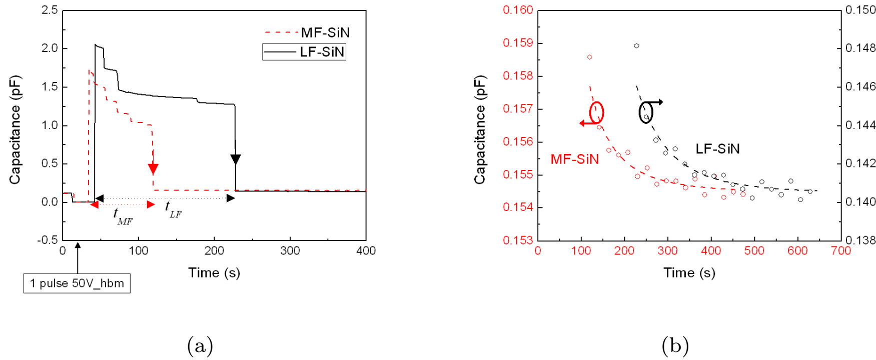

(a) (b)

FIGURE 3.33: Capacitance over time of devices submitted to one positive HBM pulse of $50V$, (a) complete and (b) right after pull-up state.

Discharging after HBM stresses

One single pulse of HBM provokes a much more pronounced shift compared to TLP. By comparing the time dynamic of the HBM stress and the mechanical response of the devices, it becomes evident that this latter is long enough to bring the membrane in the down-state position. Hence the strong charge injection process is the consequence of this contact. In fact the longer duration of HBM stress yields to the device actuation. Since the HBM charging is much larger than the TLP one, the electrostatic force at rest position (zero bias) is non negligible and allows us to monitor the discharge time constant through capacitance-time measurements, as presented in Fig.3.33. The discharging time constant can be calculated by assuming an exponential decay fitting law [89]:

$$C(t) = C_{\infty} - \Delta C_0 \cdot \exp\left[-\left(\frac{t}{\tau}\right)^{\beta}\right] \tag{3.24}$$

where C_{∞} is the deviation term and the capacitance transients are different in terms of amplitude ΔC_0, stretch coefficient β and process time constant τ.

It is observed that MF-SiN exhibits shorter discharging time constant compared to the LF-SiN one ($\tau_{MF} = 6.14s < \tau_{LF} = 7.0s$). This conclusion supports the aforementioned data on ESD experiments, i.e. the more sensitive the material is to charging the more time it will takes for its relaxation process.

3.2.3.3 Inhomogeneous dielectric charging

The previous data show that the dominant charging mechanism is translated into shifts of the C(V) characteristics. In this section we will discuss on the fact that inhomogeneous injected charges produce a narrowing effect in the C(V) characteristics, for instance under bipolar actuation. The recorded data using the PIC setup is shown in Fig.3.34. Two successive pulses are applied, one positive and then right after one negative. The first experimental observation is the shift yielded by the short pulse stress. The second observation is that there is a slight variation of the capacitance for both positive (1) and negative (2) stresses. In order to exploit both the information of the shift of bias for minimum capacitance and the minimum capacitance we adopt the model of non flat electrodes and non uniform distribution of charges at dielectric surface proposed in [52].

In parallel, another experiment done using the Kelvin Probe Force Microscopy (KPFM) technique described in [100] reinforce the interpretation of this model. In

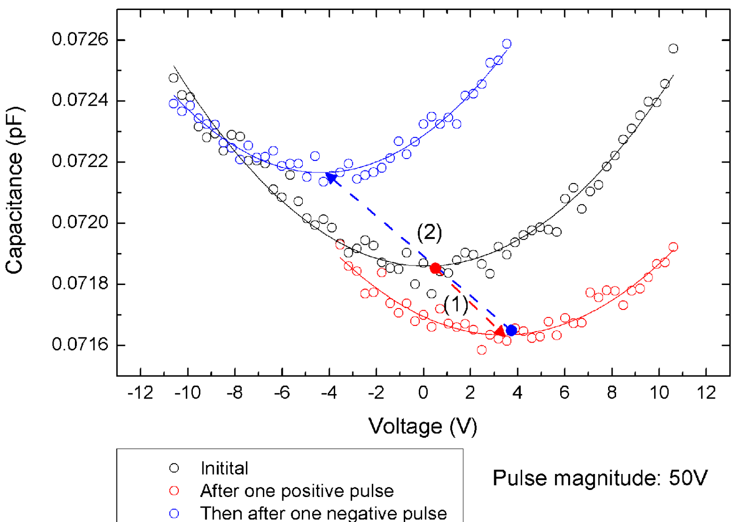

FIGURE 3.34: Non-contact C(V) curve before (black), after one positive pulse (red) and then after one negative pulse (blue) for the same device which has been stressed at 50V for short pulse of $10ms$.

fact the experiment starts with a calibration step which consists in using a simple dielectric layer deposited on the bottom electrode and fabricated on the same wafer than our MEMS structures. It is important to monitor these parameters in order to track their effect on topology and surface potential. Typically we will adjust the frequency and the area of scan, amplitude, phase and height of the tip. Once the adjusting is done, we applied a stress voltage to a switch (in this experiment $40V$ during $2min$) and we monitor the state of the device through a capacitance meter. After the DC stress we sacrificed the upper membrane by removing it and make sure that the bottom electrode is grounded to the KPFM system. The obtained results are shown in Fig.3.35. It is obvious that the charge distribution is laterally inhomogeneous as shown in [101].

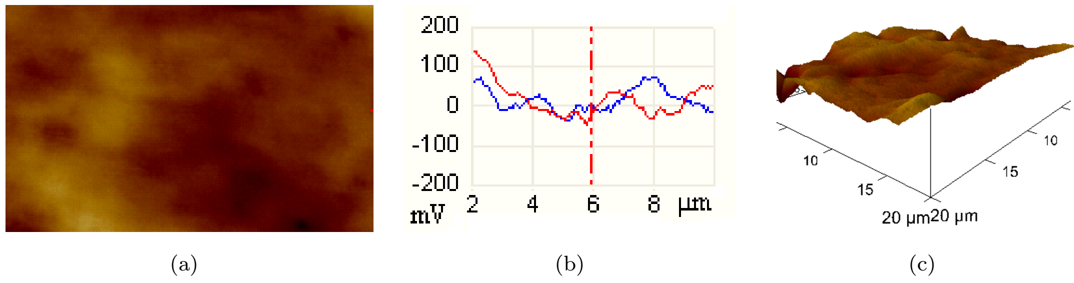

(a) (b) (c)

FIGURE 3.35: Surface potential distribution of a stressed device (a) the top view of the scanned area (b) the corresponding cross sections (c) and 3D map.

Therefore following this analytical model [52] the electrostatic force F_e can be

written in a compact form of:

$$F_e(z) = \frac{A}{2\varepsilon_0}\left[(V\mu_\alpha - \mu_\beta)^2 + V^2\sigma_\alpha^2 + \sigma_\beta^2 - 2V\mathrm{cov}_{\alpha,\beta}\right] \quad (3.25)$$

where μ, σ^2, and cov denote the mean, variance, and covariance respectively, of the $\alpha(x, y, z)$ and charge $\beta(x, y, z)$ distributions shown in Eq.3.13 and z is the displacement along z direction.
However, the experimental $C(V)$ characteristics were obtained below the pull-in of the structure, so $V_{capamin}$ is the parameter used for the analyses. In this configuration the electrostatic force is minimized independently of the charge and air gap distributions. Since this situation does not involved actuation characteristics, $V_{capamin}$ is obtained from Eq.3.13 as:

$$V_{capamin} = \frac{\mu_\alpha\mu_\beta + \mathrm{cov}_{(\alpha,\beta)}}{\mu_\alpha^2 + \sigma_\alpha^2} \quad (3.26)$$

At the point $V_{capamin}$ the electrostatic force expression can be simplified to:

$$F_{e-min}(z) = \frac{A}{2\varepsilon_0}\left[\mu_\beta^2 + \sigma_\beta^2 - (\mu_\alpha^2 + \sigma_\alpha^2)V_{capamin}^2\right] \quad (3.27)$$

Furthermore, if Hooke's law is applicable at this small scale, which states that strain is directly proportional to stress, the displacement at the minimum z_{min} is given by:

$$z_{min} = \frac{A}{2 \cdot \varepsilon_0 \cdot k}\left[\mu_\beta^2 + \sigma_\beta^2 - (\mu_\alpha^2 + \sigma_\alpha^2)V_{capamin}^2\right] \quad (3.28)$$

, where k is the spring constant.
From Eq.3.27, Eq.3.28 and data obtained in Fig.3.34, it is obvious that the mean value of background charge distribution μ_β or the variance σ_β affects the electrostatic force at the point $V_{capamin}$ and by the way the displacement. So it affects the minimum of capacitance, the linearity and also the curvature of the non-contact C(V) curves.

In low field (i.e. the applied voltage is lower that the pull-down voltage of the device, $\sim 15V$), we have observed an slight increase in capacitance which can be translated in an attraction between the two electrodes likely due to induced charges. So it is obvious that an increase of $V_{capamin}$ independently of polarity leads to a decrease of the minimum of capacitance $C_0(z)$(the vertex of the parabola) while an increase of μ_β and σ_β to a increase of the vertex. Unfortunately further investigation is needed to extract μ_β and σ_β because they depends mainly on the

mechanical properties such as spring constant and on parasitic charges affecting the background charge distribution.
In high field regime, we defined the applied pulse stress with an intensity and duration high and long enough to bring the membrane in the down-state. In this case, the charging mechanism is fully charge injection and the amount of trapped charges is comparable to the amount observed during cycling tests (cycling test is considered as one of the benchmarks for device lifetime estimation). This study is discussed in a more extended way in the next section.

3.2.3.4 Pulse induced accelerated stress test analyses

Definition
Accelerated lifetime test consists of experimental techniques in which a given DUT undergoes a specific stress protocol such to induce the same failures mechanisms which would appear in regular working conditions, but in a much shorter elapsed time. These techniques are typically based on overstressing the DUT without altering the underlying physics, i.e. introduce new failure mechanisms or mask the sought ones. By this means the assessment of reliability figures and test are much more robust and quick to be accomplished.

Interpretation
In a capacitive MEMS switch, charge may be trapped in areas like insulator surface, bulk or insulator-electrode interface. When charge is trapped in the dielectric, it will caused a voltage shift ΔV. The relation between the voltage shift and the trapped charge have been previously referred from the definition of the electrostatic force in Eq.3.27. In fact when there's no charge trapped, the electrostatic force is equally generated between charge on the membrane and charge on the electrode. If charge is trapped, the membrane will be attracted by the combination of the charge on the electrode plus the charge trapped in the material. This additional charge enhances or diminishes the electrostatic force with respect to the polarity of trapped charges and the polarity of the applied bias. Consequently the change in electrostatic force translates itself as a shift of the $V_{capamin}$ parameter in C(V) graphs performed below pull-in. Since the relation between the trapped charge and the shift of the C(V) signature is obvious from Eq.3.28, the following analyses are based on the observation of this particular parameter $V_{capamin}$.

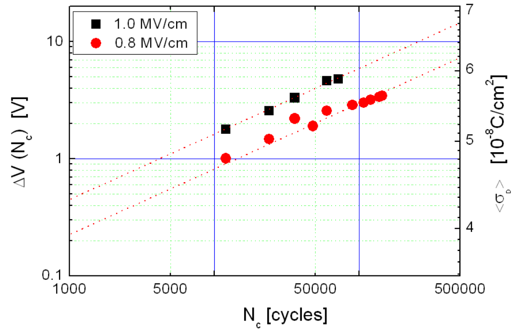

FIGURE 3.36: The shift of $V_{capamin}$ as a function of number of cycles (includes the equivalent surface charge density).

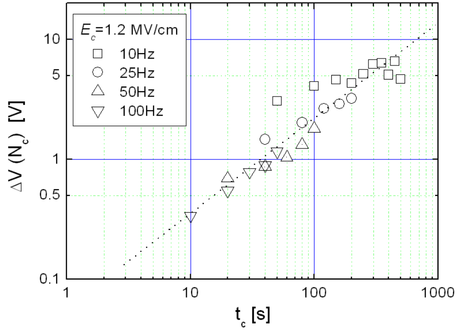

FIGURE 3.37: The shift of $V_{capamin}$ as a function of the down-state duration $t_{down,s}$.

Experimentation

Cycling measurements were done to illustrate normal stress lifetime. The devices were actuated under positive square signal, with frequency ranges from 10 to $100Hz$, a duty factor of 50% and at room temperature of $300K$. Cycling measurements are time consuming (including the data acquisition time) therefore it has been done only until 2×10^5 cycles in this work. The data acquisition time should be reduced and the test should be increased over 100 million cycles. Nevertheless the relation between the charging and the number of cycles is clearly power law and it is depicted in Fig.3.36. Since the charging depends on the time the switch last in the down-state, the power law dependence is also observed between the charging and the down-state duration (Fig.3.37). Those results allow us to write:

$$\boxed{\Delta V_c(t_c, N_c) = \Delta V_{0,c} \cdot \left(\frac{t_{down,c}}{\tau_c}\right)^{n_c} \cdot N_c^{n_c}} \quad (3.29)$$

where $\Delta V^*_{0,c}$ is the cycling amplitude factor that depends on the material, $t_{down,c}$ is the total down-state time of the cycling calculated from the frequency and the duty cycle, τ_c the charging process time constant (also material dependant), N_c is the number of cycles, and n_c is power law exponent/index.

Since Fig.3.36 and Fig.3.37 show that the downs-state time and number of cycles are linked, the fitting expression can be simplified to:

$$\Delta V_c(N_c) = \Delta V^*_{0,c} \cdot N_c^{n_c}$$

where $\Delta V_{0,c} = 0.018V$ and $n_c = 0.443$ at an electric field of $0.8MV/cm$. It has to be pointed out that $\Delta V^*_{0,c}$ is different from the aforementioned one $\Delta V_{0,c}$, because

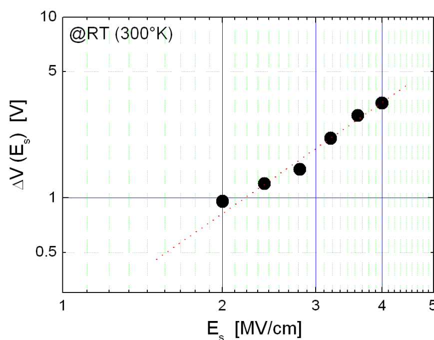

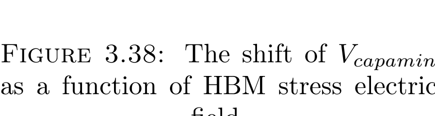

FIGURE 3.38: The shift of $V_{capamin}$ as a function of HBM stress electric field.

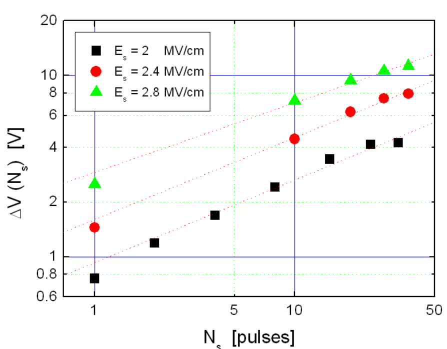

FIGURE 3.39: The shift of $V_{capamin}$ as a function number of HBM pulses at different electric-fields.

here it includes the time parameter. Furthermore, the experiment results show a sublinear relationship between the equivalent surface charge density and the number of cycles, so the stress time.

The pulse stress measurements were done using the HBM-ESD tester. The discharge remains for a few milliseconds before being switched to the ground by the test system. This is important for RF-MEMS testing, because the mechanical response for this kind of MEMS structure is around $10 - 20\mu s$. So if the electric field is high enough and the pulse last more than the switching time of the switch, the HBM discharge can induce displacement of the movable membrane. When the membrane is brought in contact with the dielectric, the high electric field induces a much higher stress than in normal cycling. A series of measurements were done for HBM stress ranging from 40 to $100V$ (which is higher than the actuation voltage of switch $\sim 20V$ and much lower than the breakdown voltage $\sim 380V$). The outcome shows that the charging has also a power law-“stress” dependence (Fig.3.38 and Fig.3.39). The stress parameters that have been varied in those experiments are the electric-field and the number of pulses which is related to the total time the switch last in the down-state position. Around 40 cumulative stresses were done at three different electric-field levels, and over 20 fresh devices were used to plot the experimental data in Fig.3.39. With respect to the applied electric field, and within the time scale of the charging procedure, the shift of the C(V) characteristics induced by the pulse stress can be written as (according to

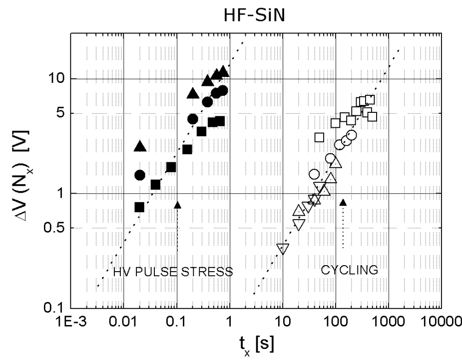

FIGURE 3.40: The shift of $V_{capamin}$ as a function of the down-state time.

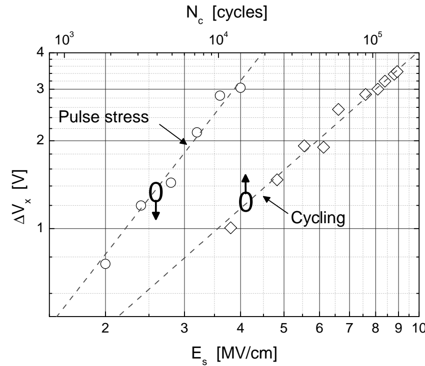

FIGURE 3.41: Comparison between $\Delta V_c(N_c)$ and $\Delta V_s(E_s)$.

Fig.3.38 and Fig.3.39):

$$\boxed{\Delta V_s(t_s, N_s, E_s) = \Delta V_{0,s} \cdot \left(\frac{t_{down,s}}{\tau_s}\right)^{n_s} \cdot N_s^{n_s} \cdot \left(\frac{E_s}{E_0}\right)^{m_s},} \tag{3.30}$$

where $\Delta V_{0,s}$ is the stress amplitude factor that depends on the material, $t_{down,s}$ is the total down-state time of the stress, τ_s the charging process time constant, N_s is the number of pulses, E_s is the electric field of the stress, E_0 is an equivalent factor and m_s, n_s are power law exponents.

Cycling vs. pulse stress:

In order to compare stress and cycling data, the shift of the C(V) graphs (ΔV) is considered as the comparison parameter. The results of cycling and HBM pulse stress tests are summarized in Fig.3.40 and Fig.3.41. The plots of the two experimental ageing methods clearly indicate the same magnitude of shift ΔV is obtained much faster using the HBM pulse setup. Thus the HBM-ESD setup or any other setup that can provide a similar waveform can be considered as a promising accelerated lifetime test method (although keeping in mind that EOS waveforms results in catastrophic damages). In order to make the correlation between the pulse stress method and cycling, it is necessary to examine the common relation between the calculated resulting shifts ΔV_c and ΔV_s. Taking into account the electric field intensity during cycling is $E_c = 0.8MV/cm$, assuming that we apply only one cycle/pulse under this electric field, and that the estimated total duration of the corresponding pulses are for cycling method $5ms$ and for the HBM method $\sim 25ms$, we obtain:

$\Delta V_c = 18mV$

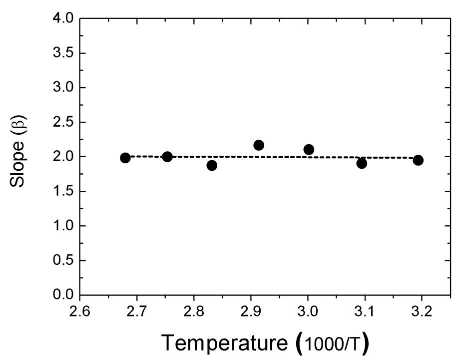

FIGURE 3.42: The slopes as a function of the temperature.

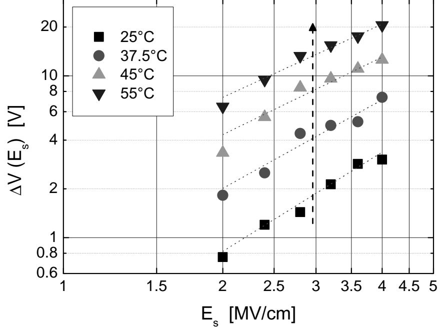

FIGURE 3.43: The shift of $V_{capamin}$ as a function of stress voltage from $25°C$ to $55°C$.

$\Delta V_s = 26mV$

The calculated values can be considered to be in good agreement since the calculated values correspond to extrapolation in Fig.3.41. These values and extrapolations make us assume with no significant error that we obtain the same shift ΔV from both methods. Then we are confident to use initial equations (Eq.3.29 and Eq.3.30) in order to define the relation between the pulse stress field and the corresponding number of cycles N, the latter performed under down state electric field E_c:

$$N = \left(\frac{E_s}{E_c}\right)^{\alpha}$$

, where $\alpha > 1$.

Finally, those results show that high-voltage impulse ageing stress works in the case of accelerated testing in capacitive RF-MEMS switches and the acceleration factor is shown above. Consequently, it will reduce significantly the testing time and reliability statistics may be obtain faster.

Temperature dependence

Temperature is often used as an acceleration factor to determine the mean time to failure (MTTF) parameter of a structure. Using an Arrhenius relation for this parameter, the operation time of the structure can be accurately calculated. Hence temperature experiments were completed to verify if pulse induced acceleration is thermal activated or not. One should first make sure that one work in the same failure mechanism conditions. Therefore in Fig.3.42, the slope m as a function of the temperature (1000/T) is observed to be a straight line. The fit indicates that in temperature accelerated conditions the failure mechanism does not vary. Since

there is no change in failure mechanism, it allows us to combine pulse stress and temperature increase. In Fig.3.43, measurements done at temperatures ranging from 300K to 330K are shown. It is read-out that as above mentioned the slope is not changing but the shift increase with temperature, which means that the charging process may be thermal activated. Therefore a practical definition to calculate the increase of the shift is by calculating the charging susceptibility of the dielectric using the following simplified expression at each temperature:

$$\Delta V(E_s) = K \cdot \left(\frac{E_s}{E_0}\right)^{\alpha}$$

$$K = \Delta V_{0,s} \cdot \left(\frac{t_{down,s}}{\tau_s}\right)^{n_s} \cdot N_s^{n_s}$$

where $\Delta V(E_s)$ is extracted from the experimentally obtained Fig.3.43 and K is the thermally activated coefficient which is related to electro-thermal behaviour of the material and α is the power law index.

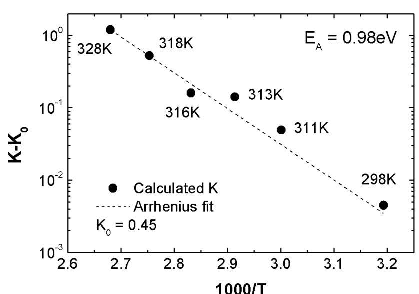

FIGURE 3.44: Arrhenius model fit.

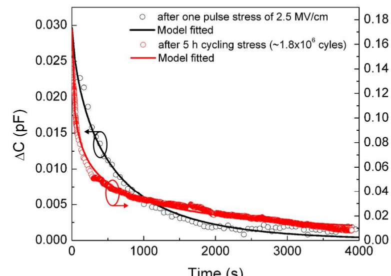

FIGURE 3.45: Capacitance transient response measured after the applied stresses during 1 hour.

A series of experiments using over 50 fresh devices were performed to cover the temperature range from $300K$ to $330K$ and the data is depicted in Fig.3.44. To extract the activation energy of those data the Arrhenius model is used.

The Arrhenius model used for acceleration of temperature related stress is described by the following expression:

$$K = K_0 + K_1 \cdot \exp\left(\frac{E_a}{k_B \cdot T}\right) \tag{3.31}$$

where K is the acceleration factor, E_a is the activation energy (eV), k_B is the Boltzmann's constant $8.6159 \times 10^5 eV/K$, T is the temperature in Kelvin, K_1 is the amplitude coefficient of the model (strongly dependent on the thermal properties

of the material) and K_0 is a constant.
Using this model the activation energy of a specific device can be extracted. In our case the activation energy was found to be around $0.98eV$ in 3 decay range.
The Arrhenius model described above shows the relationship between charging rate and temperature for capacitive RF-MEMS switches. In this manner, the charging of a device under normal usage conditions can be estimated from temperature accelerated test data.

Dielectric relaxation

In accelerated-stress-test, timed recovery is one of the main parameters to examine. Therefore we have used a model that evaluates the dielectric material as well as the material properties dispersion due to the method of deposition [89]. This model introduces the idea of macroscopic dipole moment per unit volume, observed and modeled using experimental results. The insulating material used here is rather a disordered material and the measured capacitance transient is proportional to the decrease of macroscopic polarization. Hence the stretched exponential law (Eq.3.24) is the most adequate equation that describes the relaxation mechanism observed here. To compare the capacitance transient responses, two experiments were performed; the first experiment consists in applying cycling stress during 5 hours and then measures the capacitance over 1 hour. The second experiment applies one pulse stress with a well known electric field to produce approximately the same shift in the $V_{capamin}$ value. Fig.3.45 shows that the two transients fit well with the model. As a result it makes us more confident about their recovery mechanism. However if we look at the extracted decay times ($\tau_{cycling} \approx 170s$ and $\tau_{pulse} \approx 500s$) we realize that the pulse-stress relaxation time takes 3 times longer than the cycling-stress one. Actually this deviation comes from a common fact that the more charge the material accumulate, more time it will takes to recover. In other words, there was a slight deviation on the $V_{capamin}$ shift estimation.

Note: Material properties

In capacitive switches, charge injection is a common cause that affects its reliability, because it is dielectric dependent. The material selection will solve the key issue in capacitive switches, keeping in mind that we want a low leakage material with a high dielectric constant for low RF losses and high capacitance ratio respectively. Another point is that the roughness of dielectric and bridge surfaces gives rise to a non uniform charge distribution. During an ESD event, competition between the two aforementioned basic charging mechanisms will take place and leads to a inhomogeneous charge distribution. Material selection remains a huge task, because information such as; the impact of the dielectric material, the effect of metal contacts, the chemical bonding of the material and the charging/conduction mechanisms in each material should be well known and demonstrated. An first example of the database that one should build is shown in Table 3.1 [102].

Material	ε_r	Chemical bonds	Charging Mechanisms			Conduction mechanisms (field dependent)	Ref.
			Ionic	Dipolar	Space charge		
SiO_2	3-4.5	Covalent	-	(x)	x	Fowler-Nordheim	*a*
Si_3N_4	6-7.5	Covalent	-	(x)	x	Poole-Frenkel	*b*
Al_2O_3	8-9	Iionic	x	x	x	Schottky/Tunneling/Space charge limited	*c*
AlN	10-12	Ionic/Spontaneous polarization and Piezoelectric	x		x	Space charge limited/Poole-Frenkel	*d*
HfO_2	11-12	Mainly ionic	x	x	x	Fowler-Nordheim	*e*
Ti_2O_5	$\sim$ 100	Mainly ionic, partially covalent	x	x	x	Poole-Frenkel/Schottky	*f*
BST	100-300	Covalent			x	Space charge limited/Poole-Frenkel	*g,h*

a S. Suyama, A. Okamoto and T. Serikawa, J. Appl. Phys. 65 (1),(1989)
b C.M. Svensson, J. Appl. Phys., Vol. 48, No. 1, (1977)
c V.K. Khanna and R.K. Nahar, Applied Surface Science 28, pp. 247-264, (1987)
d E. Papandreou, G. Papaioannou and T. Lisec, Intern. J. of Microw. Wirel. Tech., pp. 43-47, (2009)
e D. S. Jeong and C. S. Hwang, J. Appl. Phys. 98, 113701 (2005)
f A. Paskaleva et al, Vacuum 58, pp. 470-477, (2000)
g C.S. Hwang et al, J. Appl. Phys., Vol. 83, No. 7, (1998)
h A. Vorobiev et al, Mat. Res. Soc. Symp. Proc. Vol. 784, (2004)

Table 3.1: An overview of dielectric materials used in capacitive RF-MEMS.

3.3 RF power handling characterizations

Power handling characterizations measure the capability of switches to dissipate heat generated at the contacts or to resist RF-voltage induced actuation and latching. These tests are valuable in terms of reliability assessment of devices that will be used in power applications. In this respect, tests have been performed on switches from Imperial College London, United Kingdom [3][38] and for EADS Innovation works, Germany [37].

3.3.1 DUT

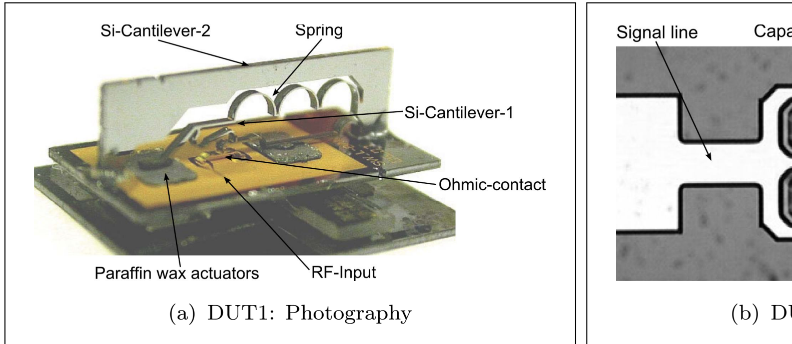

(a) DUT1: Photography

(b) DUT2: Top view

FIGURE 3.46: Devices for power applications.

DUT1 is a new and very interesting concept of a bistable 3-D RF-MEMS for power applications designed by J.-Y. Choi. Electrothermal hydraulic (Paraffin Wax) microactuators are used as switching elements, which control the silicon cantilevers with a blowing up system. The fabrication process, the measured RF performances and any mechanical considerations are detailed and reported in [38]. In this work, the discussion is focussed on its power handling characteristics and characterisation.

DUT2 is a advanced high power handling and low complexity capacitive RF-MEMS switch working in the Ku-band. The low complexity is based on a serial microstrip technology using only 3 masks [103]. During the test performed at LAAS, the switch has demonstrated to handle at least 6W under hot-switching conditions. Further testing has been performed at EADS showing an RF-power handling capability up to $9.8W$ in hot-switching mode at $14GHz$. No failures are detected after 10^5 cycles [72].

3. It was a close collaboration under the European Union's of Excellence AMICOM, contract FP6-507352.

3.3.2 Power handling setup

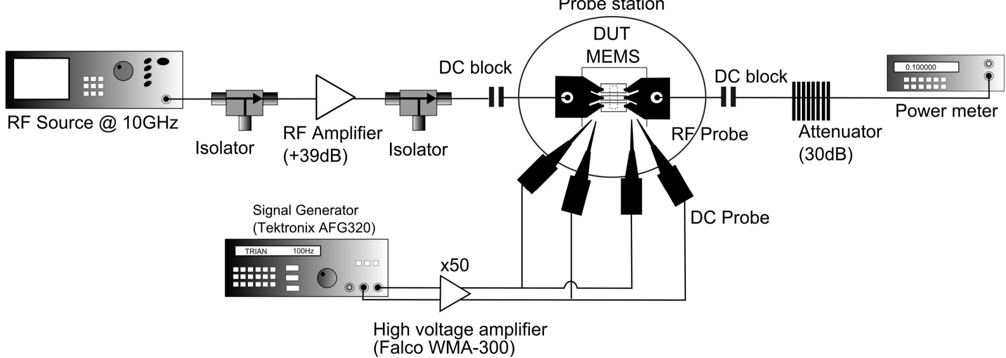

FIGURE 3.47: Measurement setup for high power testing at 10GHz.

The measurement setup is shown in Fig.3.47. From source to meter, the signal is supplied by a RF source (Anritsu MG3694B) at $10GHz$, followed by a solid state RF power amplifier with 39 dB of gain in the frequency range of $9.5 - 10.5GHz$. Despite of this gain, the input RF power to the amplifier was limited to $0dBm$, to avoid saturation. Isolators are used to protect the source and the amplifier in case of mismatching from spurious reflections along the signal line. The RF signal is applied and probed through dedicated RF probes. At the output, the signal is attenuated by an $30dB$ attenuator and readout by a power meter (Anritsu MA2474D), which sensitivity is $1pW - 100mW$. The setup was first calibrated using a "THRU" of $1200\mu m$ and the max power reach is $7.4W$. In order to perform hot-switching measurements of the DUTs, actuations are made by external DC probes and the signal is provided by a arbitrary signal generator connected to a high voltage amplifier.

3.3.3 Results

DUT1 has shown to work well at least upto $4.6W$, while we are quite confident that this unique and robust design can operate over $> 10W$ at higher frequencies. Unfortunately due to losses from cables, components or connections, it was the maximum RF power that could reach the device. Under this power at $10GHz$ hot switching tests using external DC probes have shown no degradation in performance (over 10 cycles with various down-state times). This switch is suitable for high RF power handling applications such as high-power redundancy amplifier or redundancy circuits for space applications.

RF Power	Frequency (GHz)	Switching mode	Reference
0.8	10	Hot & Cold	a
8	10	Cold	b
2.3	10	Cold	c
1	10	Hot & Cold	d
5	3	Hot & Cold	d
1.4	2	Cold	e
4.6	10	Hot & Cold	DUT1
9.8	14	Hot & Cold	DUT2

a D. Peroulis, S. P. Pachecco, and L.P.B. Katehi, IEEE Trans. MTT,52 (1),pp.5668,(2004)
b K. Grenier et al., in Proc. IEEE MEMS,pp. 155-158, (2004)
c E.P. McErlean et al., Proc. Inst. Elect. Eng. - Microw, Antennas Propag., vol 152, no. 6 , pp. 449-454, (2005)
d C. Palego et al., in IEEE MTT-S Int. Microw. Symp. Tech. Dig., vol.1, pp. 35-38, (2006)
e H. Kwon et al., in IEEE MTT-S Tech. Dig., vol.3,pp.1735-1738,(2005)

Table 3.2: Comparative summary of RF MEMS power switch performance.

DUT2 was loaded with different RF power levels at a frequency of $10GHz$, while a VNA was integrated into the reliability setup to monitor the S-parameters simultaneously. The results show that its RF properties are not affected by the hot-switching upto $6W$ and at least one hour switching was performed, showing that the switch can operate over $> 10^5$ cycles.
A comparative summary of RF-MEMS power switch performances is shown in Table 3.2.

3.4 Radiation effects in capacitive switches

3.4.1 Experiment

The investigation involved both MIM capacitors and MEMS switches (Fig.3.1 with SiN_x), fabricated on the same wafer. The dielectric material was SiN_x with a thickness of $300nm$. MIM capacitors is used to mimic a MEMS switch in the down-state and we also benefit from charging and discharging understanding assessed by monitoring:

• the charging and discharging current transients [56],

• the thermally-stimulated-depolarization-current (TSDC) method [99],

• the Time Dependent Dielectric Breakdown (TDDB) and leakage current [104],

• the charging mechanisms and charge kinetics with the aid of a Kelvin force microscopy (KFM) method [100, 101, 105].

The top and bottom electrode of MIM structures is composed of a Ti/Au layer ($0.1\mu m/1\mu m$). The top electrode, obtained by lift off, features a diameter of $500\mu m$. The silicon nitride layer was deposited by PECVD at $200°C$ with high frequency (HF, $13.56MHz$).

The TSDC current was measured through a Keithely 6487 voltage source - picoampere meter in the temperature range of $200K$ to $450K$. The bias was applied to the top electrode with respect to the bottom one; hence the polarity is in reference to the one of the top electrode.

The sacrificial layer of the MEMS capacitive switches features $2.5\mu m$ thickness. The dielectric charging before and after each successive irradiation was assessed through C(V) characteristics (using the accurate Boonton 7200 capacitance meter allowing a wide scanning range of $0.005 - 2000pF$). The C(V) below pull-down method described in Section 3.2.2.3 allows the determination of the magnitude of charge that is trapped in the dielectric after each positive or negative down state. The shift of pull-down and pull-up voltage was also monitored in order to determine the effect of charging under high electric field. Finally the irradiation experiments have been carried out at room temperature with $5MeV$ alpha particles provided by an Americium (Am) source. The alpha particle fluence was common for MIM and MEMS. Due to higher sensitivity of used experimental methods, fluence up to $10^{11}cm^{-2}$ were used for the MIM capacitors and up to $8 \times 10^{11}cm^{-2}$ for MEMS switches.

3.4.2 Results and discussion

The results shown here come from the collaboration between MINC group at LAAS-CNRS and the solid state physics section of National and Kapodistrian University of Athens (NKUA).

3.4.2.1 Radiation introduced vacancies

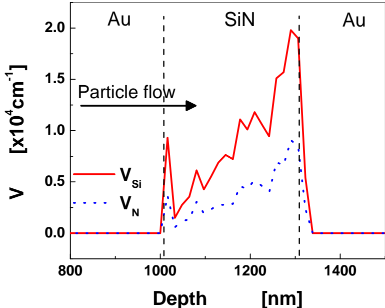

FIGURE 3.48: Distribution of Si and N vacancy introduction rates (V) for a MIM capacitor.

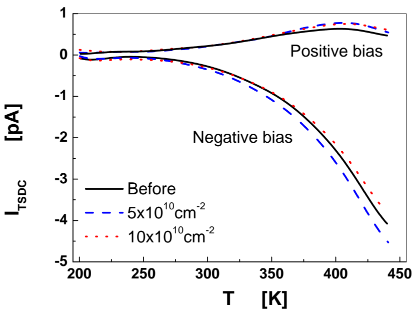

FIGURE 3.49: TSDC spectra and stored charge of MIM capacitor obtained before and after each successive irradiation experiment (biasing at $+20V$ and $-20V$).

The amorphous silicon nitride constitutes a disordered material which homogeneity and stoichiometry may vary significantly across the material. This variation leads to large potential fluctuations and consequently it will affects the charge trapping process. High energy particle radiation introduces defects due to lattice atom displacement (Section 2.3.4.2). This will generate vacancies and interstitials in the material, that induced atoms mixing (e.g. nitrogen with silicon). Determining the concentration of generated vacancies is a way to measure the atoms mixing. In this respect, simulations were performed assuming a homogeneous $SiN_{1.04}$ material and the MIM structures is considered as a stack of 500nm-Au/300nm-$SiN_{1.04}$ /1000nm-Au (bottom-up). The resulting distribution of Si and N vacancies are presented in Fig.3.48. A peak observed at the front interface and the increase of vacancy introduction rate with the film thickness caused by the recoiled heavy Au atoms and the cumulative process of recoiled Si and N atoms, respectively. The effect of backscattered Au atoms at the rear interface is negligible. Finally, the extension of Si and N vacancies beyond the SiN film has to be attributed to displaced atoms that are further displaced by knock-on process.

3.4.2.2 Effect in MIM capacitors

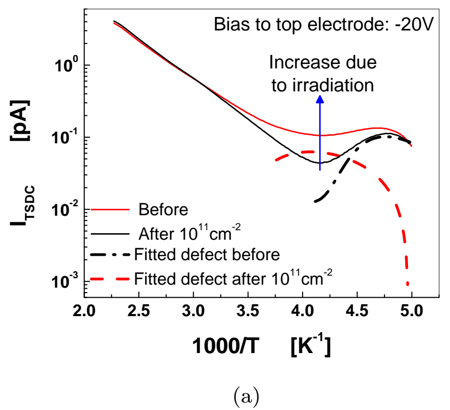

(a)

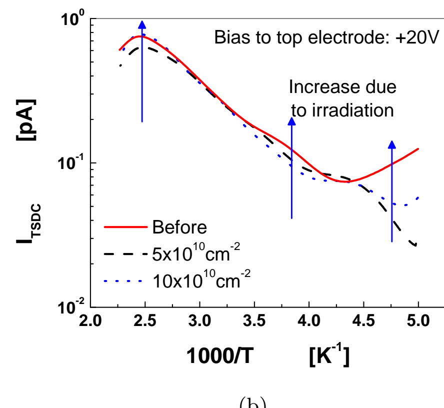

(b)

FIGURE 3.50: Arrhenius plots of TSDC currents obtained before and after each successive irradiation experiment for (a) $-20V$ and (b) $+20V$.

In insulators, the time and temperature dependence of polarization and depolarization processes are;

• in the case of dipolar polarization, driven by the competition, between the orienting action of the electric field and the randomizing action of thermal motion.

• in the case of space charge polarization the processes are much more complex because several mechanisms can be involved simultaneously and [106] and the the TSDC spectra may show the characteristic properties of distributed processes [79]. The TSDC spectra for radiation fluencies up to $10^{11}cm^{-2}$ as well as for positive and negative bias polarity applied to top electrode are plotted in Fig.3.49. The TSDC spectra are asymmetric and depend strongly on the sign of polarizing bias. The asymmetry was found to be generated when electrons are injected from the bottom electrode and attributed to the effects of impurities or the intrinsic differences in quality between first and last-grown material.

The analysis of the TSDC spectra indicates the presence of different defects which characteristics depend on the applied bias polarity (Fig.3.50). This has to be attributed to effects arising from the contact asymmetry, the defects introduced during irradiation and the interaction of injected holes, which interact with Si mid-gap and band tail defects. The importance of the contribution of Si defects is also supported by radiation simulations, which clearly show a larger introduction rate for Si vacancies (Fig.3.48). Since particle radiation contribution to dielectric charging arises from space charge polarization, the stored charge for radiation

fluencies can be calculated with:

$$Q = \frac{1}{\beta}\int_{T_1}^{T_2} I_{TSDC}(T)\mathrm{d}T \tag{3.32}$$

where β is the heating rate (K/s) and $T_2 - T_1$ the temperature range.

The stored charge for radiation fluencies up to $10^{11}cm^{-2}$ is presented in Fig.3.51. The dependence of stored charge on the radiation fluence seems to be linear. Radiation calculations have shown that the vacancy introduction rate is in the range of $8000cm^{-1}$ in SiN, which leads to a density of defects in the range of $10^{15}cm^{-3}$ for the used fluence. This value is very low compared to the reported density of defects of $10^{18}cm^{-2}$ [107]. Therefore, for a small perturbation caused by irradiation up to $10^{11}cm^{-2}$, we can assume a linear introduction or change in concentration of stored charge, a fact that is confirmed in Fig.3.51. Furthermore, since the injected charge is affected by the metal contact work function and the distribution of charged centers is not known we can calculate the degradation parameter defined from:

$$\sigma_\Sigma(F) = \sigma_{\Sigma,0} + r_q \cdot F \tag{3.33}$$

where $\sigma_{\Sigma,0}$ is the residual charge, r_q is a factor related to the charging introduction rate and F the radiation fluence. The obtained values for the charging introduction rate are about $0.28 \times 10^{-20}C \cdot cm^2$ and $2.3 \times 10^{-20}C \cdot cm^2$ for positive and negative bias respectively.

3.4.2.3 Effect in MEMS switches

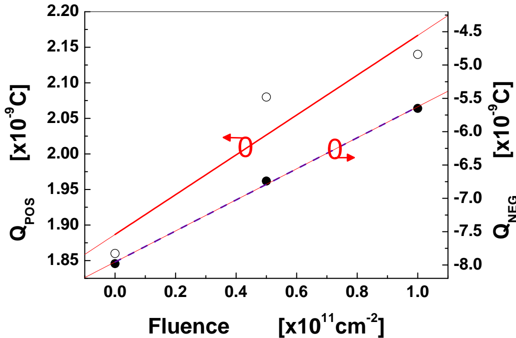

FIGURE 3.51: Dependence of stored charge on radiation fluence for (○) positive and (●) negative bias on top electrode.

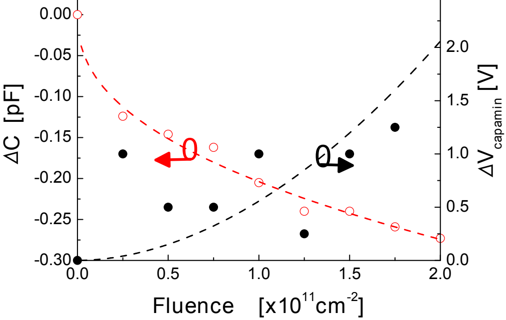

FIGURE 3.52: Dependence of (○) change capacitance at zero bias and (●) bias for capacitance minimum vs. radiation fluence.

In MEMS capacitive switches the built-in charges are monitor through the $V_{capamin}$ parameter (Eq.3.23), which is directly related to the charge density σ_Σ of the dielectric film. Besides the capacitance for zero bias gives information on the presence of opposite polarity charges [108].So, in the up-state and zero bias the switch bridge displacement, hence capacitance will be proportional to the electrostatic force. Now, if we assume that there is a proportionality of the additional charging caused by traps that have been introduced by radiation, the $V_{capamin}$ value is expected to vary following this proportionality with respect to the radiation fluence. Furthermore, if we assume that the bridge displacement at zero bias is much smaller than the bridge-dielectric gap we expect the capacitance to vary as:

$$\Delta C(0,F) \infty \left(\sigma_{\Sigma,0} + r_q \cdot F\right)^2 \tag{3.34}$$

The aforementioned hypothesis is verified by the plots of $\Delta C(F)$ and $\Delta V_{capamin}(F)$ vs. radiation fluence in Fig.3.52. The experimental data are fitted with a square and linear law, respectively. The degradation parameter extracted from the variation of $V_{capamin}$ on radiation fluence was found to range from $7 \times 10^{-20} C \cdot cm^2$ to $17 \times 10^{-20} C \cdot cm^2$, which is relatively in agreement with the TSDC ones.
Finally we can conclude that the device degradation arises from the primarily radiation introduced vacancies and the injected charge interaction/trapping during the switch down state. These effects enhance significantly the contribution of space charge polarization to the dielectric charging. In the case of capacitive switches where the dielectric and contact roughness affect the charging processes alpha particle radiation shifts the bias for minimum capacitance and varies the magnitude OFF-state capacitance.

To obtain knowledge travel into China if necessary

Arabic proverb

Muhammad Prophet of Islam

Conclusion

This thesis presents in-house performance characterization and reliability testing in RF MEMS switches. In particular, we have addressed its operation and specifications, as well as its electrostatic, microwave, power handling, radiation in order to target the component reliability. This study includes the relationship between charging, material and device physical structure. The resulting database of its failure mechanisms may contribute to the standardization of RF-MEMS testing procedures and hence to the industrial exploitation of this technology.

From a MEMS device perspective, the presented thesis adds knowledge in the fields of RF MEMS switches in terms of scientific insight into most significant development roadblock.

From a characterization point of view, the thesis provides a set of tools, methodologies and techniques with respect to demanding reliability needs and requirements.

For ESD inspection, test, and packaging of RF-MEMS should be carried out in a static-free environment. It should be packaged in conductive carriers, delivered in static-free bags and careful handling requirements should be take into account.

The purpose of this research was to investigate reliability issues in RF-MEMS switches. It required and involved the development and execution of several experiments and test plans;

- The first experiment tested AlN-based capacitive RF MEMS switches through a hold-down charging procedure. The testing principle consists in applying a constant bias across the structure and periodically performing C(V) measurements. Based on the voltage shift between the initial C(V) graph and the one performed after the stress, the amount of trapped charge was estimated. The rate of charging of the structures and the effective electric field, which takes into account the roughness and the asperities of the contact between the membrane and the dielectric layer, allow the estimation and comparison of the apparent conductance of different dielectrics.

- The second experiment deals with electrostatic discharge breakdown and charging analyses. Three different structures with different dielectric materials and two types of ESD tester (TLP and HBM) have been used for the experiments. The first results show electrical breakdown processes and failure analyses were conducted, showing how sensitive those air gap switches are face to disruptive discharges that can happen in any non-static free environment. The second part of the results shows the difference in charging process between MF and LF-SiN dielectric materials (under TLP and HBM). The third part involved only the HBM tester, because the pulse width is longer compare to TLP one and this latter can induced displacement of the membrane if the pulse stress magnitude is high enough (higher than the pull-down of the device). Using this method, pulse induced accelerated stress tests have been performed and correlation has been made with cycling tests. It shows that high voltage impulse ageing test works in the case of accelerated testing in capacitive RF-MEMS switches and the acceleration factor expression has been defined. Temperature acceleration tests have been also performed and the activation energy of the device has been determined. All the data show that testing time can be reduced significantly and thereby reliability statistics may be obtain faster.
- The third experiment consists in characterizing two original power switches (from Imperial College London, United Kingdom and EADS Innovation works, Germany) in terms of power handling and hot-switching behaviour. The results show that tests can be performed up to $6W$ at a frequency around $10GHz$. A comparative summary of RF-MEMS power switches has been reported.
- The last experiment investigates radiation effects in capacitive switches. It comes out that the device degradation arises from the primarily radiation introduced vacancies and the injected charge trapping during the switch down state. These effects enhance significantly the contribution of the total charge polarization to the dielectric charging. The voltage corresponding to the minimum of capacitance has shown to be affected by alpha particle radiation.

Finally, the scientific results obtained in the framework of this thesis have been the object of a several publications which list is given in the appendix. Moreover, design and simulation experiences acquired during this thesis is reported in appendix A.

For tomorrow belongs to the people who prepare for it today

African proverb

Outlook

The presented reliability experiments are well established and the characterizations are well control, however the tests were conducted in a ambient environmental conditions (i.e atmospheric pressure, room temperature $25°C$ and 30% of humidity). According to the high susceptibility of those micro- nano- items to this big big world, it is obvious that tests shall be done in a controlled environment. If one wants to study the influence of environmental parameters on the MEMS functioning, a dedicated instrumentation is required. Fortunately our laboratory acquired a new high-frequency manual cryogenic probe system PMC200 (SUSS MicroTec). It allows the testing of MEMS on wafer level, with DC and for RF signals applied, for different temperature, gasses and pressure. An optical system is mounted on top for optical monitoring.
The technology is already sufficiently mature on a device and system level according to the reliable devices shown worldwide, but it still need new impulses from material science.
In a more general concern, two concepts needs to be considered as well;
• Design for reliability, which is a huge task for MEMS engineers because they should take into account the knowledge from interdisciplinary experiences.
• Statistics database and models needs to be develop.

In the national context;
The continuous work on this field in our research group, through the ongoing projects;
• FAME, The French ANR project (PNANO-059)
• POLYNOE, A project funded by European Defence Agency (B-0035-IAP1-ERG)
• REDS, Reliability of redundancy MEMS switches project funded by European Space Agency, based in the Netherlands.
• FITMEMS, Regional project in collaboration with Laplace Laboratory and NovaMEMS.

is encouraging.
Xlim research institute from Limoges has make one's contribution to this field of research by presenting almost new concepts and new ideas.
The CEA-Leti from Grenoble has been active in mass producing RF-MEMS devices and has brought their valuation in characterization.

In the worldwide context;
DARPA has funded several programs such as "RF MEMS Improvement Program" and NASA/JPL, EADS and THALES have also ongoing programs on "RF-MEMS for space applications".
Finally there is around 40 companies and more than 150 research labs and universities worldwide dealing with RF-MEMS, in order to make the revolution in advanced telecommunication and switching technologies a reality.

Bibliography

[1] Robert Plana. What's Hot in RF Components and Systems. *Microwave Journal*, 49(2):22, February 2006.

[2] E.R. Brown. RF-MEMS switches for reconfigurable integrated circuits. *Microwave Theory and Techniques, IEEE Transactions on*, 46(11):1868–1880, 1998. ISSN 0018-9480.

[3] De Los Santos and R J Richards. MEMS for RF Microwave Wireless Applications - The Next Wave: Part II. *Microwave Journal*, July 2001.

[4] G. M. Rebeiz and J. B. Muldavin. RF MEMS switches and switch circuits. *IEEE M MW*, 2(4):59–71, 2001. ISSN 1527-3342. doi: 10.1109/6668.969936.

[5] Gabriel M. Rebeiz. *RF-MEMS Theory, Design, and Technology.* John Wiley & Sons, 2003.

[6] R.P. Feynman. There's plenty of room at the bottom [data storage]. *Microelectromechanical Systems, Journal of*, 1(1):60–66, 1992. ISSN 1057-7157.

[7] H. C. Nathanson, W. E. Newell, R. A. Wickstrom, and Jr. Davis, J. R. The resonant gate transistor. *Jour. IEEE Elec. Devic.*, 14(3):117–133, 1967. ISSN 0018-9383.

[8] Vijay K. Varadan, K.J. Vinoy, and K.A. Jose. *RF MEMS and Their Applications.* John Wiley & Sons Ltd., 2003.

[9] Sherif Sedky. *Post-Processing Techniques for Integrated MEMS.* ARTECH HOUSE, INC., 2006.

[10] K. E. Petersen. Micromechanical membrane switches on silicon. *IBM Journal of Research and Development*, 23:376–179, 1979.

[11] G.T.A. Kovacs, N.I. Maluf, and K.E. Petersen. Bulk micromachining of silicon. *Proceedings of the IEEE*, 86(8):1536–1551, 1998. ISSN 0018-9219.

[12] Mohamed Gad-El-Hak. *The MEMS Handbook 2nd edition*. CRC Press Taylor and Francis Group, 2006.

[13] E. J. Garcia and J. J. Sniegowski. Surface micromachined microengine. *Sensors and Actuators A: Physical*, 48(3):203–214, May 1995. ISSN 0924-4247.

[14] E. W. Backer, W. Ehrfeld, D. Munchmeyer, H. Betz, A. Heuberger, S. Pongratz, W. Glashauser, H. J. Michel, and R. Siemens. Production of separation-nozzle systems for uranium enrichment by a combination of x-ray lithography and galvanoplastics. *Naturwissenschaften*, 69(11):520–523, November 1982.

[15] M. McCormick, E. Chowanietz, and A. Lees. Microengineering design and manufacture using the liga process. *Engineering Science and Education Journal*, 3 (6):255–262, 1994. ISSN 0963-7346.

[16] K.A. Shaw, Z.L. Zhang, and N.C. MacDonald. SCREAM I: A single mask, single-crystal silicon process for microelectromechanical structures. In *Proc. IEEE-MEMS '93,*, pages 155–160, 1993.

[17] Noel C. MacDonald. SCREAM MicroElectroMechanical Systems. *Microelectronic Engineering*, 32(1-4):49–73, September 1996. ISSN 0167-9317.

[18] Heather Hanson. MEMS - A Small World with Big Opportunities. *Technology Today*, Winter 2004 issue, 2004.

[19] Héctor J. De Los Santos. *Introduction to Microelectromechanical Microwave Systems, 2nd edition*. ARTECH HOUSE, INC., 2004.

[20] L.E. Larson, R.H. Hackett, and R.F. Lohr. Microactuators for GaAs-based microwave integrated circuits. In *Proc. TRANSDUCERS '91*, pages 743–746, 1991.

[21] J. J. Yao and M. F. Chang. A Surface Micromachined Miniature Switch for Telecommunications Applications with Signal Frequencies from DC up to 4 GHz. In *Proc. and Eurosensors IX. Solid-State Sensors and Actuators Transducers '95*, volume 2, pages 384–387, 1995.

[22] C. Goldsmith, Tsen-Hwang Lin, B. Powers, Wen-Rong Wu, and B. Norvell. Micromechanical membrane switches for microwave applications. In *IEEE MTT-S 1995 Digest.*, pages 91–94 vol.1, 1995.

[23] C.T.-C. Nguyen, L.P.B. Katehi, and G.M. Rebeiz. Micromachined devices for wireless communications. In *Proceedings of the IEEE*, volume 86, pages 1756–1768, Au 1998. doi: 10.1109/5.704281.

[24] R. J. Richards and H. J. De Los Santos. MEMS for RF Microwave Wireless Applications - The Next Wave. *Microwave Journal*, March 2001.

[25] H A C Tilmans, W De Raedt, and E Beyne. MEMS for wireless communications: from RF-MEMS components to RF-MEMS-sip. *Journal of Micromechanics and Microengineering*, 13(4):S139–S163, 2003.

[26] C. T. C. Nguyen. Integrated micromechanical circuits for rf front ends. In *Proc. 32nd European Solid-State Circuits Conference ESSCIRC 2006*, pages 7–16, 2006. doi: 10.1109/ESSCIR.2006.307523.

[27] S.L. Miller, M.S. Rodgers, G. LaVigne, J.J. Sniegowski, P. Clews, D.M. Tanner, and K.A. Peterson. Failure modes in surface micromachined microelectromechanical actuators. In *In Proc. IEEE IRPS 1998*, pages 17–25, 1998. doi: 10.1109/RELPHY.1998.670437.

[28] S.T. Patton, W.D. Cowan, and J.S. Zabinski. Performance and reliability of a new MEMS electrostatic lateral output motor. In *Proc. IEEE-IRPS 1999*, pages 179–188, 1999.

[29] J. DeNatale, R. Mihailovich, and J. Waldrop. Techniques for reliability analysis of MEMS RF switch. In *Proc. 40th Annual Reliability Physics Symposium*, pages 116–117, 2002. doi: 10.1109/RELPHY.2002.996620.

[30] Chang L. Tien, Arunava Majumdar, and Frank M. Gerner. *Microscale energy transport*. 1997.

[31] Tauno Vaha-Heikkila and Marie Ylonen. CMOS Compatible Switched MEMS Capacitors up to 220 GHz Applications. In *Proc. of 36th European Microwave Conference*, pages 1060–1063, Sept. 2006. doi: 10.1109/EUMC.2006.281116.

[32] D. Mercier, K. Van Caekenberghe, and G. M. Rebeiz. Miniature rf mems switched capacitors. In *Proc. IEEE MTT-S 2005 Digest*, pages 4 pp.–, 2005. doi: 10.1109/MWSYM.2005.1516719.

[33] B. Lacroix, A. Pothier, A. Crunteanu, C. Cibert, F. Dumas-Bouchiat, C. Champeaux, A. Catherinot, and P. Blondy. Sub-Microsecond RF MEMS Switched Capacitors. *IEEE J-MTT*, 55(6):1314–1321, 2007. ISSN 0018-9480. doi: 10.1109/TMTT.2007.897760.

[34] K. Grenier, D. Dubuc, B. Ducarouge, V. Conedera, D. Bourrier, E. Ongareau, P. Derderian, and R. Plana. High power handling RF MEMS design and technology. In *Proc. 18th IEEE MEMS 2005*, pages 155–158, 2005. doi: 10.1109/MEMSYS.2005.1453890.

[35] C. Palego, A. Pothier, T. Gasseling, A. Crunteanu, C. Cibert, C. Champeaux, P. Tristant, A. Catherinot, and P. Blondy. Rf-mems switched varactor for high power applications. pages 35 –38, june 2006. doi: 10.1109/MWSYM.2006.249902.

[36] S. Balachandran, J. Kusterer, R. Connick, T.M. Weller, D. Maier, M. Dipalo, and E. Kohn. Thermally actuated nanocrystalline diamond micro-bridges for microwave and high power rf applications. pages 367 –370, june 2007. doi: 10.1109/MWSYM.2007.380447.

[37] A. Stehle, C. Siegel, V. Ziegler, B. Schonlinner, U. Prechtel, H. Seidel, and U. Schmid. High-power handling capability of low complexity RF-MEMS switch in Ku-band. *Electronics Letters*, 43(24):1367–1368, 2007. doi: 10.1049/el:20072827.

[38] Joo-Young Choi, Jinyu Ruan, F. Coccetti, and S. Lucyszyn. Three-Dimensional RF MEMS Switch for Power Applications. *IEEE Jour. IE*, 56(4):1031–1039, 2009. ISSN 0278-0046. doi: 10.1109/TIE.2008.2010087.

[39] J Jason Yao. RF MEMS from a device perspective. *Journal of Micromechanics and Microengineering*, 10(4):R9–R38, 2000.

[40] V. Puyal, D. Dragomirescu, C. Villeneuve, J. Ruan, P. Pons, and Robert Plana. Frequency scalable model for mems capacitive shunt switches at millimeter wave frequencies. *IEEE Transactions on Microwave Theory and Techniques*, 57(11): 2824–2833, 2009. doi: 10.1109/TMTT.2009.2032473.

[41] A. Takacs, D. Neculoiu, D. Vasilache, A. Muller, P. Pons, L. Bary, P. Calmon, H. Aubert, and R. Plana. Tunable bandstop and bandpass mems filters for millimeter wave applications. In *Proc. 38th European Microwave Conference*, pages 591–594, 2008.

[42] E. Rius, C. Quendo, A. Manchec, Y. Clavet, C. Person, J.F. Favennec, G. Jarthon, O. Bosch, J.C. Cayrou, P. Moroni, and J.L. Cazaux. Design of microstrip dual behavior resonator filters : A practical guide. *Microwave Journal*, 49:72–92, 2006.

[43] Gaetan Prigent, ThanhMai Vu, and Robert Plana. Synthesis for Tunable Dual Behavior Resonator. In *Proc. of APMC2009*, 2009.

[44] Jérémie Bouchaud and Bernado Knoblich. RF MEMS switches deliver on early promise. *Think Small !*, 2(4), Septembre 2007.

[45] Mathieu Potin. MEMS Switch and Varicap Market. Technical report, Yole Développement, 2009.

[46] G. Rebeiz, K. Entesari, I. Reines, S.-j. Park, M. El-tanani, A. Grichener, and A. Brown. Tuning in to RF MEMS. *Microwave Magazine, IEEE*, 10(6):55–72, 2009. ISSN 1527-3342.

[47] I. De Wolf. Reliability of MEMS. In *Proc. EuroSime 2006*, pages 1–6, 2006. doi: 10.1109/ESIME.2006.1644069.

[48] I. de Wolf. AMICOM public deliverable D241-1: Database on Failure modes. Technical report, IMEC, 2005. URL www.amicom.info.

[49] B. Bhushan. *Springer Handbook of Nanotechnology*. Springer, 2nd edition, 2007.

[50] J. Wibbeler, G. Pfeifer, and M. Hietschold. Parasitic charging of dielectric surfaces in capacitive microelectromechanical systems (MEMS). *Sensors and Actuators*, 71: 74–80, 1998. doi: 10.1016/S0924-4247(98)00155-1.

[51] W Merlijn van Spengen, Robert Puers, Robert Mertens, and Ingrid De Wolf. A comprehensive model to predict the charging and reliability of capacitive RF MEMS switches. *Journal of Micromechanics and Microengineering*, 14(4):514–521, 2004.

[52] X. Rottenberg, I. De Wolf, Nauwelaers, W. De Raedt, and Tilmans. Analytical Model of the DC Actuation of Electrostatic MEMS Devices with Distributed Dielectric Charging and Nonplanar Electrodes. *Jour. of MEMS*, 16(5):1243–1253, 2007. ISSN 1057-7157.

[53] G. J. Papaioannou and J. Papapolymerou. Dielectric charging mechanisms in RF-MEMS capacitive switches. In *Proc. EuMIC2007*, pages 359–362, 2007. doi: 10.1109/EMICC.2007.4412723.

[54] Kwan Chi Kao. *Dielectric Phenomena in Solids*. Elsevier Academic Press, 2004.

[55] R. Ramprasad. Phenomenological theory to model leakage currents in metal-insulator-metal capacitor systems. *Physica Status Solidi (b)*, 239(1):59–70, 2003.

[56] M. Lamhamdi, J. Guastavino, L. Boudou, Y. Segui, P. Pons, L. Bouscayrol, and R. Plana. Charging-Effects in RF capacitive switches influence of insulating layers composition. *Microelectronics and Reliability*, 46(9-11):1700 – 1704, 2006. ISSN 0026-2714. doi: DOI:10.1016/j.microrel.2006.07.046.

[57] U. Zaghloul, G. Papaioannou, F. Coccetti, P. Pons, and R. Plana. Dielectric charging in silicon nitride films for mems capacitive switches: Effect of film thickness and deposition conditions. *Microelectronics Reliability*, 49(9-11):1309 – 1314, 2009. ISSN 0026-2714. doi: DOI:10.1016/j.microrel.2009.07.006.

[58] G. Papaioannou, N. Tavassolian, M. Koutsoureli, E. Papandreou, and J. Papapolymerou. Investigation of charging mechanisms in RF-MEMS capacitive switches with silicon nitride: The effect of material stoichiometry. In *IEEE MTT-S 2009 Digest.*, pages 1653–1656, June 2009. doi: 10.1109/MWSYM.2009.5166031.

[59] J. Frenkel. On Pre-Breakdown Phenomena in Insulators and Electronic Semi-Conductors. *Phys. Rev.*, 54(8):647–648, Oct 1938. doi: 10.1103/PhysRev.54.647.

[60] S. Melle, D. De Conto, D. Dubuc, K. Grenier, O. Vendier, J. L. Muraro, J. L. Cazaux, and R. Plana. Reliability modeling of capacitive rf mems. *IEEE J-MTT*, 53(11):3482–3488, 2005. ISSN 0018-9480. doi: 10.1109/TMTT.2005.857109.

[61] Michael Douglass. DMD reliability: a MEMS success story. volume 4980, pages 1–11. SPIE, 2003. doi: 10.1117/12.478212.

[62] Jeremy A. Walraven, Jerry M. Soden, Danelle M. Tanner, Paiboon Tangyunyong, Jr. Edward I. Cole, Richard E. Anderson, and Lloyd W. Irwin. Electrostatic discharge/electrical overstress susceptibility in MEMS: a new failure mode. volume 4180, pages 30–39. SPIE, 2000. doi: 10.1117/12.395703.

[63] J. A. Walraven, E. I. Cole Jr., L. R. Sloan, S. Hietala, C. P. Tigges, and C. W. Dyck. Failure analysis of radio frequency RF microelectromechanical systems MEMS. In *Proceedings of SPIE Vol. 4558*, pages 254–259, 2001.

[64] A. Tazzoli, V. Peretti, R. Gaddi, A. Gnudi, E. Zanoni, and G. Meneghesso. Reliability Issues in RF-MEMS Switches Submitted to Cycling and ESD Test. In *Proc. 44th IEEE IRPS*, pages 410–415, 2006. doi: 10.1109/RELPHY.2006.251253.

[65] Sandeep Sangameswaran, Jeroen De Coster, Mirko Scholz, Dimitri Linten, Steven Thijs, Chris Van Hoof, Ingrid De Wolf, and Guido Groeseneken. A study of breakdown mechanisms in electrostatic actuators using mechanical response under EOS-ESD stress. In *EOS ESD Symposium proceedings 2009*, 2009.

[66] Jinyu Ruan, Nicolas Nolhier, David Trémouilles, George Papaioannou, and Robert Plana. ESD events in SiN RF-MEMS Capacitive Switches. In *EOS ESD Symposium proceedings 2009*, 2009.

[67] T Maloney and N Khurana. Transmission Line Pulsing Techniques for Circuit Modeling of ESD Phenomena. In *Proceedings of the EOS/ESD Symposium 7*, page 49Ũ54, 1985.

[68] J.R. Black. Electromigration : A brief survey and some recent results. *Electron Devices, IEEE Transactions on*, 16(4):338–347, 1969. ISSN 0018-9383.

[69] S. Cass. MEMS in space. *Spectrum, IEEE*, 38(7):56–61, Jul 2001. ISSN 0018-9235. doi: 10.1109/6.931884.

[70] J Jason Yao, Charles Chien, Robert Mihailovich, Viktor Panov, Jeffrey DeNatale, Judy Studer, Xiaobin Li, Anhua Wang, and Sangtae Park. Microelectromechanical system radio frequency switches in a picosatellite mission. *Smart Materials and Structures*, 10(6):1196–1203, 2001.

[71] R. Osiander, M. G. Darrin, and J. L. Champion. *MEMS and Microstructures in Aerospace Applications*. CRC Press Taylor and Francis Group, 2006.

[72] V. Ziegler, W. Gautier, A. Stehle, B. Schoenlinner, and U. Prechtel. Challenges and opportunities for RF-MEMS in aeronautics and space - the EADS perspective. In *Proc. of 10th Topical Meeting on Silicon Monolithic Integrated Circuits in RF Systems (SiRF2010)*, pages 200–203, 2010.

[73] S.S. McClure, L.D. Edmonds, R. Mihailovich, A.H. Johnston, P. Alonzo, J. DeNatale, J. Lehman, and C. Yui. Radiation effects in micro-electromechanical systems (MEMS): RF relays. *Nuclear Science, IEEE Transactions on*, 49(6):3197–3202, Dec 2002. ISSN 0018-9499. doi: 10.1109/TNS.2002.805406.

[74] A. Tazzoli, G. Cellere, E. Autizi, V. Peretti, A. Paccagnella, and G. Meneghesso. Radiation Sensitivity of Ohmic RF-MEMS Switches for Spatial Applications. In *Proc. IEEE MEMS 2009*, pages 634–637, Jan. 2009. doi: 10.1109/MEMSYS.2009.4805462.

[75] Herbert R. Shea. Radiation sensitivity of microelectromechanical system devices. *Journal of Micro/Nanolithography, MEMS and MOEMS*, 8(3):031303, 2009. doi: 10.1117/1.3152362.

[76] R. N. Schwartz and. Gamma-ray radiation effects on RF MEMS switches. In *Proc. of the 2000 IEEE Microelectronics Reliability and Qualification Workshop*, 2000.

[77] G.J. Papaioannou, V. Theonas, M. Exarchos, and G. Konstantinidis. RF MEMS sensitivity to radiations. In *Microwave Conference, 2004. 34th European*, volume 1, pages 65–68, Oct. 2004.

[78] V G Theonas, M Exarchos, G J Papaioannou, and G Konstantinidis. RF MEMS dielectric sensitivity to electromagnetic radiation. *Journal of Sensors and Actuators A*, 131:25–33, 2006.

[79] M. Exarchos, E. Papandreou, P. Pons, M. Lamhamdi, G.J. Papaioannou, and R. Plana. Charging of radiation induced defects in RF MEMS dielectric films. *Microelectronics and Reliability*, 46(9-11):1695–1699, 2006. ISSN 0026-2714.

[80] A. Crunteanu, A. Pothier, P. Blondy, F. Dumas-Bouchiat, C. Champeaux, A. Catherinot, P. Tristant, O. Vendier, C. Drevon, J.L. Cazaux, and L. Marchand. Gamma radiation effects on RF MEMS capacitive switches. *Microelectronics and Reliability*, 46:1741–1746, 2006.

[81] J. Ruan, E. Papandreou, M. Lamhamdi, M. Koutsoureli, G. Papaioannou F. Coccetti, P. Pons, and R. Plana. Alpha particle radiation effects in RF MEMS capacitive switches. *Microelectronics Reliability*, 48(8-9):1241–1244, September 2008.

[82] J. Muldavin, C.O. Bozler, S. Rabe, P.W. Wyatt, and C.L. Keast. Wafer-Scale Packaged RF Microelectromechanical Switches. *Microwave Theory and Techniques, IEEE Transactions on*, 56(2):522–529, Feb. 2008. ISSN 0018-9480. doi: 10.1109/TMTT.2007.914654.

[83] B. Ducarouge, D. Dubuc, S. Melle, L. Bary, P. Pons, and R. Plana. Efficient design methodology of polymer based RF MEMS switches. In *Proc. SiRF2004*, pages 298–301, Sept. 2004. doi: 10.1109/SMIC.2004.1398228.

[84] David M. Pozar. *Microwave Engineering 3rd Ed.* Wiley, 2005.

[85] Xiaobin Yuan, Zhen Peng, J. C. M. Hwang, D. Forehand, and C. L. Goldsmith. Acceleration of Dielectric Charging in RF MEMS Capacitive Switches. *Jour. IEEE TDMR*, 6(4):556–563, 2006. ISSN 1530-4388. doi: 10.1109/TDMR.2006.887417.

[86] T. Lisec, C. Huth, and B. Wagner. Dielectric material impact on capacitive RF MEMS reliability. In *Proc. 34th European Microwave Conference*, volume 1, pages 73–76, 2004.

[87] G. J. Papaioannou and T. Lisec. Dielectric charging process in AlN RF-MEMS capacitive switches. In *Proc. European Microwave Conference*, pages 1338–1341, 2007. doi: 10.1109/EUMC.2007.4405450.

[88] L. Kelvin, G. Fitzgerald, and W. Francis. Contact electricity of metals. *Phil. Mag.*, XLVI:96–98, 1898.

[89] G. J. Papaioannou, G. Wang, D. Bessas, and J. Papapolymerou. Contactless Dielectric Charging Mechanisms in RF-MEMS Capacitive Switches. In *Proc. 36th European Microwave Conference*, pages 1739–1742, 2006. doi: 10.1109/EUMC.2006.281478.

[90] Hiroaki Yamazaki, Tamio Ikehashi, Tatsuya Ohguro, Etsuji Ogawa, Kenji Kojima, Kazunari Ishimaru, and Hidemi Ishiuchi. An intelligent bipolar actuation method

with high stiction immunity for RF MEMS capacitive switches and variable capacitors. *Sensors and Actuators A: Physical*, 139(1-2):233 – 236, 2007. ISSN 0924-4247. doi: DOI:10.1016/j.sna.2007.03.014.

[91] R.W. Herfst, P.G. Steeneken, H.G.A. Huizing, and J. Schmitz. Center-Shift Method for the Characterization of Dielectric Charging in RF MEMS Capacitive Switches. *Semiconductor Manufacturing, IEEE Transactions on*, 21(2):148–153, May 2008. ISSN 0894-6507. doi: 10.1109/TSM.2008.2000285.

[92] Friedrich Paschen. Ueber die zum funkenübergang in luft, wasserstoff und kohlensäure bei verschiedenen drucken erforderliche potentialdifferenz. *Annalen der Physik*, 273(5):69–96, 1889.

[93] J. S. Townsend. Motion of electrons in gases. *Journal of the Franklin Institute*, 200 (5):563 – 590, 1925. ISSN 0016-0032. doi: DOI:10.1016/S0016-0032(25)90708-9.

[94] R. M. Schaffert. Electrophotography. *Wiley and Sons : New York*, pages 516–517, 1975.

[95] R.S. Dhariwal, J.-M. Torres, and M.P.Y. Desmulliez. Electric field breakdown at micrometre separations in air and nitrogen at atmospheric pressure. *IEE Proceedings - Science, Measurement and Technology*, 147(5):261–265, 2000. doi: 10.1049/ip-smt:20000506.

[96] P. Carazzetti, Ph. Renaud, and H. R. Shea. Experimental study of electrical breakdown in MEMS devices with micrometer scale gaps. In *SPIE Proceedings Vol. 6884*, 2008.

[97] P.P. Budenstein. On the mechanism of dielectric breakdown of solids. *Electrical Insulation, IEEE Transactions on*, EI-15(3):225 –240, June 1980. ISSN 0018-9367. doi: 10.1109/TEI.1980.298315.

[98] J. Ruan, G.J. Papaioannou, N. Nolhier, M. Bafleur, F. Coccetti, and R. Plana. ESD stress in RF-MEMS capacitive switches: The influence of dielectric material deposition method. In *Reliability Physics Symposium, 2009 IEEE International*, pages 568–572, 2009.

[99] E. Papandreou, M. Lamhamdi, C.M. Skoulikidou, P. Pons, G. Papaioannou, and R. Plana. Structure dependent charging process in rf mems capacitive switches. *Microelectronics Reliability*, 47(9-11):1812 – 1817, 2007. ISSN 0026-2714. doi: DOI:10.1016/j.microrel.2007.07.100.

[100] A. Belarni, M. Lamhamdi, P. Pons, L. Boudou, J. Guastavino, Y. Segui, G. Papaioannou, and R. Plana. Kelvin probe microscopy for reliability investigation of rf-mems capacitive switches. *Microelectronics Reliability*, 48(8-9): 1232 – 1236, 2008. ISSN 0026-2714. doi: DOI:10.1016/j.microrel.2008.07.046.

[101] R.W. Herfst, P.G. Steeneken, J. Schmitz, A.J.G. Mank, and M. van Gils. Kelvin probe study of laterally inhomogeneous dielectric charging and charge diffusion in RF MEMS capacitive switches. In *Reliability Physics Symposium, 2008. IRPS 2008. IEEE International*, pages 492–495, 27 2008-May 1 2008. doi: 10.1109/RELPHY.2008.4558935.

[102] G. Papaioannou and J. Papapolymerou. Dielectric Charging in MEMS by Material, Structure and Temperature. In *WWD Workshop International Microwave Symposium*, 2009.

[103] C. Siegel, V. Ziegler, B. Schonlinner, U. Prechtel, and H. Schumacher. Simplified RF-MEMS Switches Using Implanted Conductors and Thermal Oxide. In *European Microwave Integrated Circuits Conference, 2006. The 1st*, pages 509–512, Sept. 2006. doi: 10.1109/EMICC.2006.282695.

[104] J. Ackaert, R. Charavel, K. Dhondt, B. Vlachakis, L. De Schepper, M. Millecam, E. Vandevelde, P. Bogaert, A. Iline, E. De Backer, A. Vlad, and J.-P. Raskin. Mimc reliability and electrical behavior defined by a physical layer property of the dielectric. *Microelectronics Reliability*, 48(8-9):1553 – 1556, 2008. ISSN 0026-2714. doi: DOI:10.1016/j.microrel.2008.06.043.

[105] U. Zaghloul, A. Belarni, F. Coccetti, G. J. Papaioannou, L. Bouscayrol, P. Pons, and R. Plana. A comprehensive study for dielectric charging process in silicon nitride films for RF MEMS switches using kelvin probe microscopy. In *Proc. TRANSDUCERS 2009*, pages 789–793, 2009. doi: 10.1109/SENSOR.2009.5285667.

[106] J. Vandershueren and J. Casiot. *Thermally stimulated relaxation in solids*, volume 37, chapter 4, page 135. Springer-Verlag, 1979.

[107] D. T. Krick, P. M. Lenahan, and J. Kanicki. Electrically active point defects in amorphous silicon nitride: An illumination and charge injection study. *Journal of Applied Physics*, 64(7):3558–3563, 1988. doi: 10.1063/1.341499.

[108] X. Rottenberg, B. Nauwelaers, W. De Raedt, and H. A. C. Tilmans. Distributed dielectric charging and its impact on RF MEMS devices. In *Proc. 34th European Microwave Conference*, volume 1, pages 77–80, 2004.

[109] Castells Manuel. *L'Ere de l'information, tome 1 : La Société en réseaux*. Fayard.

[110] R. Fournié and R. Coelho. Diélectriques, bases théoriques. *Techniques de l'ingénieur, traité Génie électrique*, pages D2300–1–D2300–18, 2008.

List of Papers

Journals :

1. *Accelerated lifetime test of RF-MEMS switches under ESD stress*
   Jinyu Jason Ruan, Nicolas Nolhier, George J. Papaioannou, David Trémouilles, Vincent Puyal, Christina Villeneuve, Tonio Idda, Fabio Coccetti and Robert Plana.
   Microelectronics Reliability, Vol.49, No9-11, pp.1256-1259, September 2009.
2. *Alpha particle radiation effects in RF MEMS capacitive switches*
   J. Ruan, E. Papandreou, M. Lamhamdi, M. Koutsoureli, F. Coccetti, P. Pons, G.J. Papaioannou, R. Plana.
   Microelectronics Reliability, Vol.48, No8-9, pp.1241-1244, January 2009.
3. *ESD failure signature in capacitive RF MEMS switches*
   Jinyu Jason Ruan, George J. Papaioannou, Nicolas Nolhier, Nicolas Mauran, Marise Bafleur, Fabio Coccetti and Robert Plana.
   Microelectronics Reliability, Vol.48, No8-9, pp.1237-1240, November 2008
4. *Electrostatic discharge failure analysis of capacitive RF MEMS switches*
   Jinyu Jason Ruan, Nicolas Nolhier, Marise Bafleur, Laurent Bary, Fabio Coccetti, Thomas Lisec and Robert Plana.
   Microelectronics Reliability, Vol.47, No9-11, pp.1818-1822, November 2007

International Conferences :

5. *Pulse Induced Charging Tests in Capacitive RF-MEMS Switches*
   Jinyu J. Ruan, George Papaioannou, David Trémouilles, Nicolas Nolhier, Fabio Coccetti and Robert Plana.
   In Proc. EuMW 2010, October 2010, Paris.
6. *Push-Pull Seesaw Principle Capacitive RF-MEMS Shunt Switch*
   Jinyu J. Ruan, Christina Villeneuve, Fabio Coccetti, Patrick Pons, Nicolas Nolhier and Robert Plana.
   In Proc. MEMSWAVE 2010, June 2010, Otranto.

7. *Charging and discharging studies in microwave capacitive switches under high field pulse discharges*
   Jinyu J. Ruan, George Papaioannou, Nicolas Nolhier, David Trémouilles, Fabio Coccetti and Robert Plana.
   In Proc. SiRF 2010, January 2010, New Orleans.
8. *Temperature dependence of ESD charging in RF MEMS capacitive switch*
   Jinyu J. Ruan, George Papaioannou, Nicolas Nolhier, David Trémouilles, Fabio Coccetti and Robert Plana.
   In Proc. of 39th European Microwave Conference, October 2009, Rome.
9. *ESD events in SiN RF-MEMS Capacitive Switches*
   Jinyu J. Ruan, Nicolas Nolhier, David Trémouilles, George Papaioannou and Robert Plana.
   In Proc. of ESD/EOS Symposium 2009, September 2009, Anaheim.
10. *ESD stress in RF-MEMS capacitive switches: the influence of dielectric material deposition method*
    Jinyu J. Ruan, George Papaioannou, Nicolas Nolhier, Marise Bafleur, Fabio Coccetti and Robert Plana.
    In Proc. of IEEE-IRPS2009, Montréal.
11. *ESD effects in capacitive RF MEMS switches*
    Jinyu J. Ruan, George Papaioannou, Nicolas Nolhier, and Robert Plana.
    In Proc. of 8th WCCM8 and 5th ECCOMAS2008, July 2008, Venise.
12. *Dielectric material charging and ESD stress of AlN-based capacitive RF MEMS*
    Jinyu J. Ruan, Nicolas Nolhier, Marise Bafleur, Laurent Bary, Nicolas Mauran, Fabio Coccetti, Thomas Lisec and Robert Plana.
    In Proc. of MEMSWAVE 2007, June 2007, Barcelone.
13. *Failure mechanisms of AlN based RF-MEMS switches under DC and ESD stresses*
    Jinyu J. Ruan, Nicolas Nolhier, Marise Bafleur, Laurent Bary, Nicolas Mauran, Fabio Coccetti, Thomas Lisec and Robert Plana.
    In Proc. of 14th IEEE-IPFA 2007, July 2007, pp.120-123, 2007, Bangalore.

National Conferences :

14. *La fiabilité d'un MEMS-RF capacitif en bande W soumis à des décharges électrostatiques*
    J.Ruan, N.Nolhier, G.J.Papaioannou, D.Trémouilles, F.Coccetti, R.Plana.
    16èmes Journées Nationales Microondes (JNM 2009), Grenoble (France), 27-29 Mai 2009, 4p.
15. *Analyse de défaillance des MEMS RF capacitifs sous décharges électrostatiques*
    J.Ruan, N.Nolhier, F.Coccetti, G.J.Papaioannou, R.Plana.
    11e Journées Nationales du Réseau Doctoral en Microélectronique (JNRDM), Bordeaux (France), 14-16 Mai 2008, 3p.
16. *Analyse des propriétés électriques de MEMS RF sous contraintes DC et décharges électrostatiques*

J.Ruan, N. Nolhier, M. Bafleur, L. Bary, F. Coccetti, R. Plana.
15èmes Journées Nationales Micro-ondes (JNM'2007), Toulouse (France), 23-25 Mai 2007, 4p.

Co-authoring (Journals):

17. *Frequency scalable model for MEMS capacitive shunt switches at millimeter wave frequencies*
V.Puyal, D.Dragomirescu, C.Villeneuve, **J.Ruan**, P.Pons, R.Plana.
IEEE Transactions on Microwave Theory and Techniques, Vol.57, Nř11, pp.2824-2833,November 2009.
18. *Three-dimensional RF MEMS switch for power applications*
J.Y.Choi, **J.Ruan**, F.Coccetti, S.Lucyszyn. IEEE Transactions on Industrial Electronics, Vol.56, Nř4, pp.1031-1039, April 2009.

Co-authoring (International Conferences):

19. *Fabrication and characterization of RF-MEMS switch in V-band*
T.M.Vu, G.Prigent, **J.Ruan**, A.Rumeau, P.Pons, R.Plana.
In Proc. of APMC 2009, 7-10 December 2009, 4p, Singapore.
20. *RF MEMS design for phase shifters from K-band up to W-band*
V.Puyal, D.Dragomirescu, C.Villeneuve, J. Lattes, **J.Ruan**, P.Pons, R.Plana.
In Proc. of APMC 2008, 16-20 December 2008, 5p, Hong Kong.
21. *Dimensioning of the stoppers used to reduce the sticking effects in electrostatic capacitor switches*
H.Achkar, **J.Ruan**, C.Villeneuve, D.Peyrou, F.Pennec, M.Sartor, P.Pons, R.Plana.
In Proc. of MEMSWAVE 2008, 30 June - 3 July 2008, 4p, Heraklion.

Co-authoring (National Conferences):

22. *Modélisation d'une capacité variable à base de nanotubes de carbone verticaux*
T.Idda, N.Olofsson, J.Ek-Weis, **J.Ruan**, S.Pacchini, E.Campbell, R.Plana.
16èmes Journées Nationales Microondes (JNM 2009), 27-29 Mai 2009, 5p, Grenoble.

Appendices

Appendix A

Designs and Simulations

In the frame of high reliability MEMS redundancy switch for space applications and to be experienced in designing and simulating RF-MEMS switches, several single switching units have been evaluate during this thesis. The main purpose is to study some building blocks that will be used in more complex architectures or circuits. Therefore, within the time scale of this thesis only the "two ports - two states" unit, also named as Single Pole Single Thru (SPST) switch is developed. Furthermore, concerning ESD events protection of RF-MEMS switches, "a MEMS protecting a RF-MEMS" prototype is proposed.

A.1 MEMS designs for RF applications

The test vehicles designs performed during this thesis are shown in Fig.A.1. It consist of SPST-switches with difference in geometry (e.g. anchoring parts, configuration minimizing the dielectric charging). The devices will be used to evaluate the structural and functional failures modes in order to get better insight into the involved physic of failure effects.

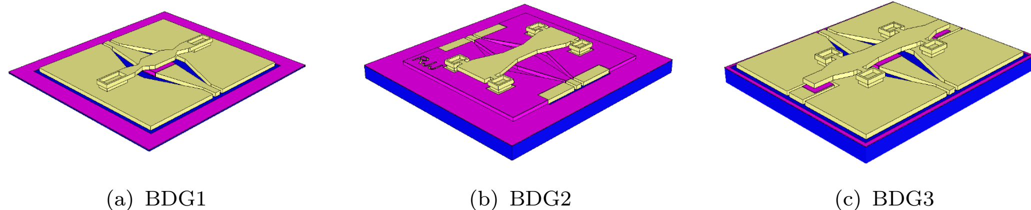

(a) BDG1 (b) BDG2 (c) BDG3

Figure A.1: Different topologies of SPST switches, (a) regular anchors, (b) lateral anchors and (c) push-pull capacitive.

Parameter	BDG1	BDG2	BDG3
Originality	Regular anchors	Lateral anchors	Push-Pull with lateral anchors
A	$140 \times 200\mu m$		
L_{beam}	$1040\mu m$	$990\mu m$	$1170\mu m$
W_{beam}	$140\mu m$	$280\mu m$	$180\mu m$
z_{beam}	$2.5\mu m$		
d	$2.4\mu m$		
z_d	$400nm$		
ε_r	$6.5 - 7$		
σ_r	$30 - 50MPa$		

Table A.1: Physical dimensions of SPST switches shown in Fig.A.1.

A.1.1 Electro-Mechanical considerations

In this work, we will focus on the shunt capacitive SPST switched, which consists of metal membrane bridge suspended over the center conductor of a coplanar waveguide and fixed on the ground parts. The physical dimensions and parameters used for the simulations are listed in Table A.1. The CPW access line has a pitch of $100\mu m$, so to keep the active area larger than the width of the line, tapers are used. Using analytical expressions from Section 2.2.1, the off-state and the on-state capacitances are calculated to be equal to $0.0719pF$ and $4.028pF$ respectively. This leads to a switching ratio of $C_{ratio} = 56.02$. The pull-down and pull-up voltages equal $15V$ and $5V$ for a spring constant of $k = 13N/m$.
Furthermore the mechanical resonance frequency associated with the given beam is equal to :

$$f_{mech} = \frac{1}{2\pi}\sqrt{\frac{13N \cdot m^{-1}}{9 \times 10^{-8}kg}} = 18878Hz,$$

So its switching time is calculated as [5]:

$$t_s \simeq 3.67\frac{V_{down}}{V_{applied} \cdot \omega_0} = 3.67\frac{15V}{20V \cdot 2\pi \cdot 18878.6Hz} \simeq 23\mu s$$

Finally in terms of microwave characteristics, the series resonant frequency is calculated to be:

$$f_0 = \frac{1}{2\pi\sqrt{L \cdot C}} = \frac{1}{2\pi \cdot \sqrt{\sim 4pH \cdot 4.028pF}} = 39.65GHz$$

The first electro-mechanical validation is done using FEM (CoventorWare) simulations. It allows us to couple electro-mechanics interaction so that a variety of design concepts can be explored along with parametric studies to carry out the design optimization. The process procedure (Fig.A.4) is imported to build a representative 3D model embedding the most significant technological parameters such as material properties (e.g. residual stress). Then an adequate fine meshing is chosen allowing the accurate simulation of mechanical contact between surfaces. The results obtained for the pull-in voltages is shown in Fig.A.2. It is observed that the simulation data fit well with the measured ones.
Due to parasitic capacitances, asperities and surfaces roughness, the measured capacitance ratio

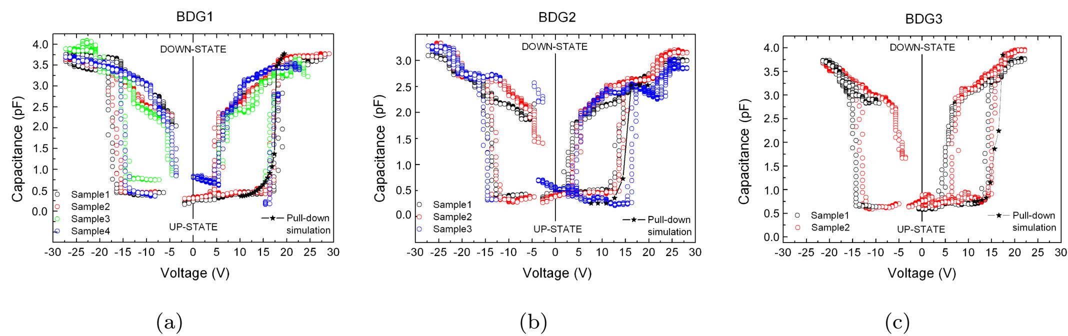

(a) (b) (c)

FIGURE A.2: Measured and simulated C(V) characteristics.

was only:

$$C_{ratio} = \frac{3.38pF}{0.61pF^*} = 5.54$$

* it corresponds to the up-state value in the initial position not in the pull-up position where it should be lower thanks to the shape (curvature) of the central part of the membrane.

This is well known to be mainly due to the non perfect mechanical contact of the membrane in the down state which lower the corresponding value of capacitance combined with the an extra parasitic capacitance in the up-state. In this case, the deviation of 16% is calculated between the expected C_{down} value and the measured one.

A.1.2 Electro-Magnetic analysis

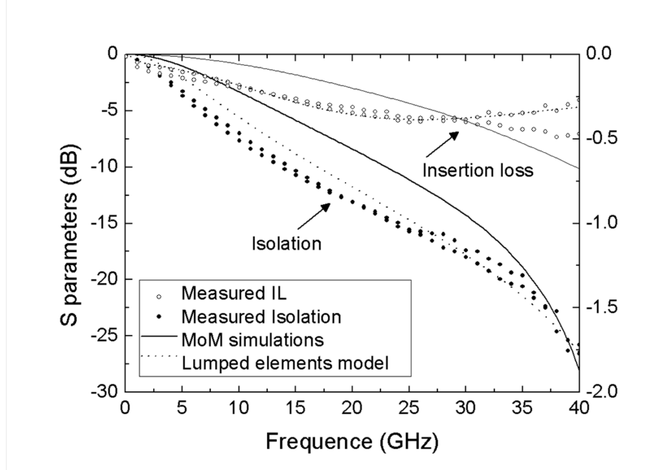

FIGURE A.3: Measured and simulated S parameters characteristics.

The switches have been simulated using a planar EM simulation tool based on the Method of Moments technique (Momentum from ADS), and the S-parameters have been extracted for the proposed geometrical dimensions (Table. A.1).

From bottom up, the substrate is first defined as high resistive with relative dielectric constant of 11.9 and thickness of $500\mu m$. The CPW line is defined as perfect conductors and the signal line is coated with silicon nitride having relative dielectric constant of 6.5 and thickness of

400nm. One air layer is used to defined the air-gap and via-holes are used to anchor the upper membrane to the ground planes. A lumped elements equivalent circuit of the switches has also been obtained through a network simulator (ADS). The measured and simulated results are presented together in Fig.A.3 and show good agreement between analytical model, the method of moment simulation, the lumped elements equivalent circuit and finally the measurements on the fabricated test structures.

A.1.3 Technology process

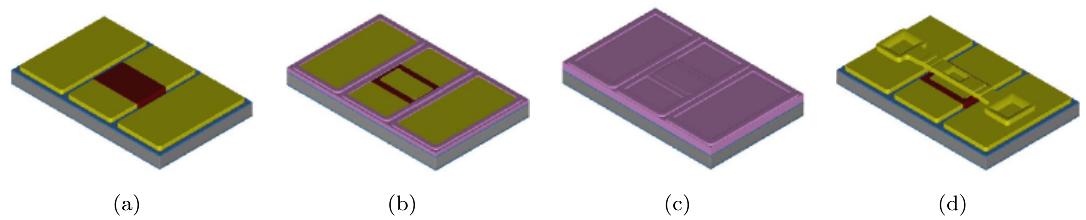

(a) (b) (c) (d)

FIGURE A.4: RF MEMS switch process flow at LAAS-CNRS.

The fabrication sequence of RF-MEMS capacitive micro-switches is depicted in Fig.A.4 and described below:

(a) Coplanar wave lines: High Resistivity Si is cleaned by RCA and a bilayer composed by 800nm thick dry-SiO_2 layer and 600nm thick SiN_x LPCVD layer is deposited. A 50nm thick Ti and Cu layers are evaporated and over this a 2.5μm thick electroplated gold is grown in photo-resist mould to form CPW lines. A 50nm thick Ti layer is evaporated over Au CPW before the patterning by chemical etching of Ti/Cu/Ti layers. A 250nm thick Si_3N_4 layer is deposited by PECVD and patterned using Reactive Ion Etching to form dielectric layer of down-state capacitance.

(b) Gap filling: A 2.5μm thick PMGI SF15 is spin coated and pre-baked at 170°C. After photo-lithography, this layer is etched and hard-baked at 230°C.

(c) Sacrificial layer: A 2.5μm thick PMGI is spin coated and pre-baked at 200°C. After photo-lithography this layer is etched and hard-baked at 210°C to improve planarization.

(d) Mobile membrane: A 100nm thick evaporated Au layer following by a 2.5μm thick electroplated Au layer are deposited on the sacrificial layer and patterned by chemical etching. The final step consists in sacrificial layer wet etching and drying with a CO_2 supercritical dryer.

The fabricated structures are illustrate in Fig.A.5. RF-MEMS switches with actuation voltage as $\sim 15V$ and good RF characteristics have been demonstrated. Measurements show an isolation of better than $-25dB$ at 40GHz. These structures are suitable for wireless and/or space systems where low power consumption is essential. Unfortunately due to the delayed fabrication process, reliability results are not shown for those devices. It will be interesting to test them under well controlled environment using the cryogenic test bench as mentioned in the outlook.

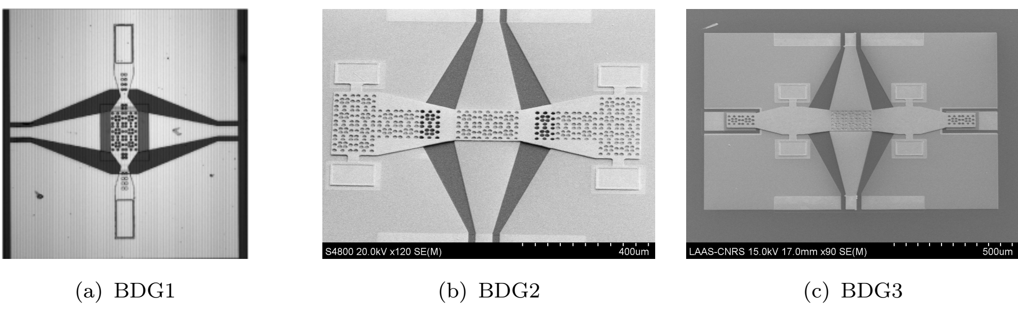

(a) BDG1 (b) BDG2 (c) BDG3

FIGURE A.5: Pictures of the fabricated structures.

A.1.4 Displacement characterizations

For the BDG3 design, the signal line is used as the push-down electrode while two additional lateral electrodes are used to implement the pull-up action. For the synchronisation of the biasing, two outputs (A and B) of a arbitrary signal generator are used by keeping (B) slightly delayed with respect to the other one (A). Bipolar actuation (which is used to reduce dielectric charging) may be also used with this design.
Mechanical characteristics of the fabricated BDG3 switch have been measured using FOGALE nanotech's optical profilometer (with a $6nm$ precision in the z direction). Displacement of the actuated membrane is measured as a function of the actuation area as shown in Fig.A.6. The actuated area is observed to be the brighter parts in the pictures. Fig.A.6(a) corresponds to the initial position when no bias is applied. The distance between the top central part of the membrane and the surface of the CPW line is measured to be $5.02\mu m$ (note that the air gap is $\sim 2.5\mu m$ according to the process flow). When the bias ($20V$) is applied through the signal line, this distance is measured to be $3.11\mu m$. Finally when the bias is applied to the lateral electrodes ($30V$) the distance between the top of the electrodes and the surface of the CPW line shows a value of $3.25\mu m$ and between the top central part and the surface of the CPW line it is $5.76\mu m$. Moreover the shape (curvature) of the membrane is made evident by the $5.76\mu m$ with $30V$ lateral actuation and $5.02\mu m$ no actuation. The proof of concept is validated by the reported results.

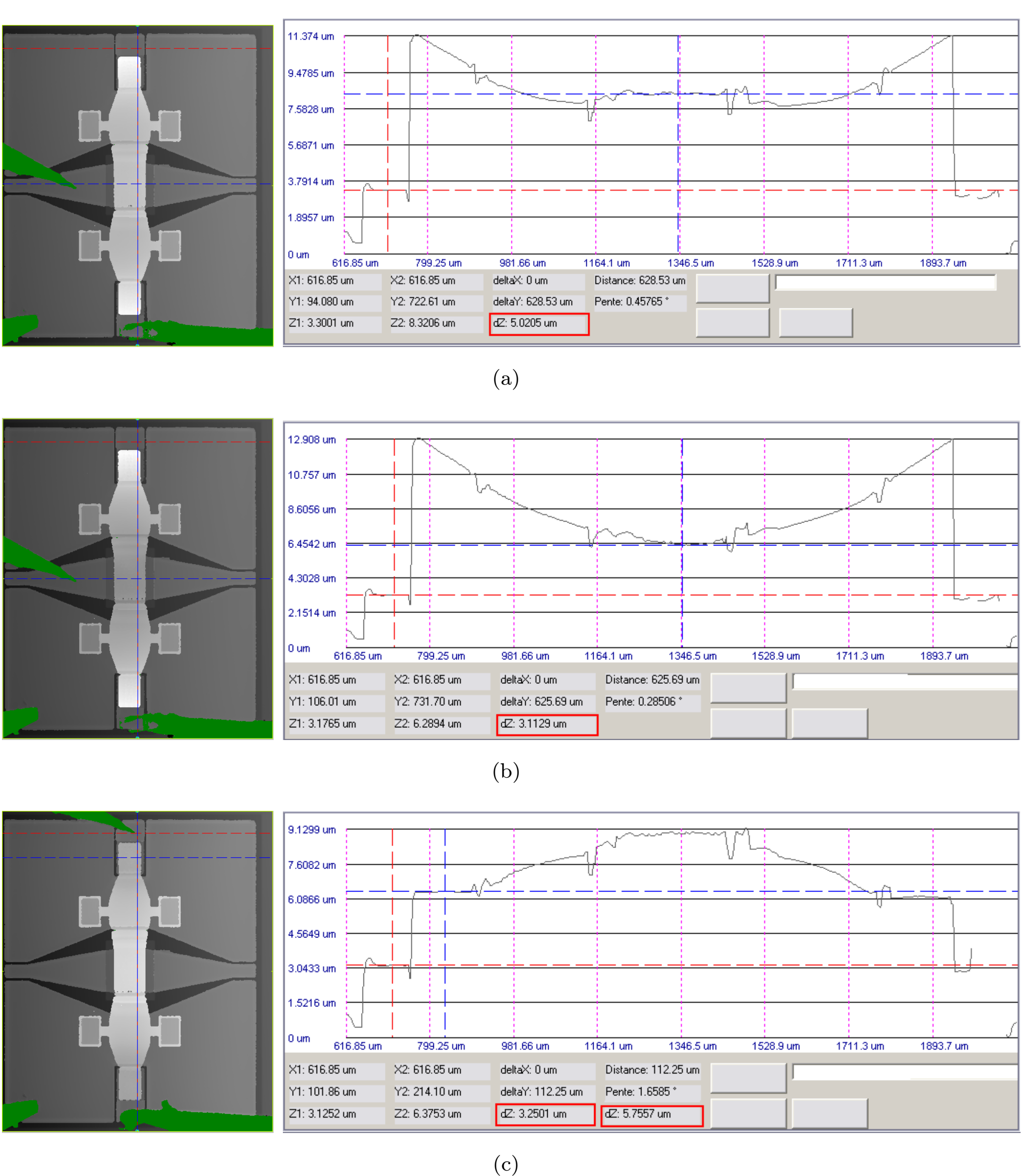

FIGURE A.6: Optical profilometer data of the fabricated BDG3 switch, (a) the initial position, (b) when actuated through the signal line and (c) when actuated by lateral electrodes.

A.2 MEMS protecting RF-MEMS

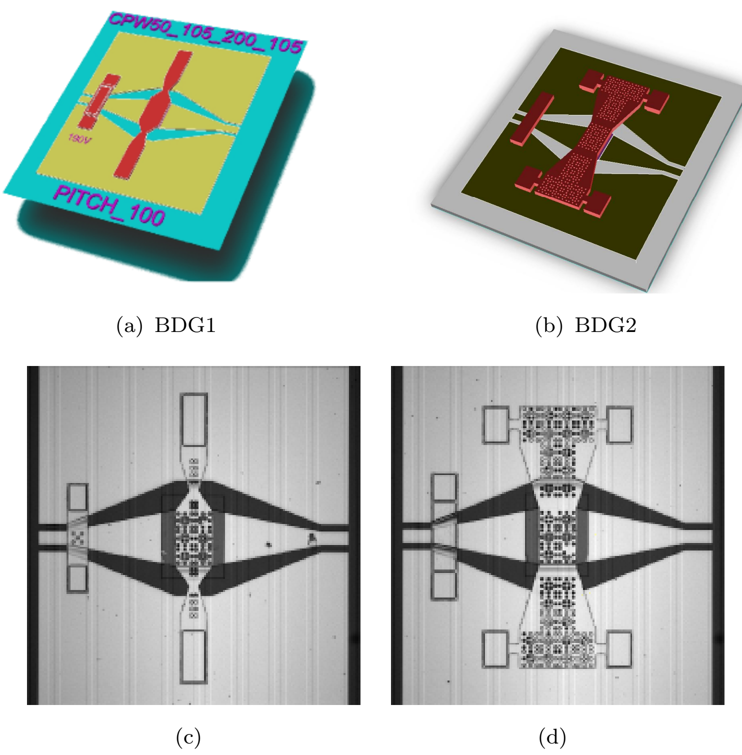

(a) BDG1 (b) BDG2

(c) (d)

FIGURE A.7: Prototypes including ESD protection.

According to the susceptibility of RF-MEMS structures discussed in Section 3.2.3.1. Prototypes including an ESD event protection is proposed. The concept deals with a "MEMS protecting a RF-MEMS". In fact the idea is to design a fast switching and high voltage metal-contact MEMS switch in parallel. When the ESD event happens in the signal line, the protection should actuated during this short time and the signal is then discharge to the ground planes whereas the RF-MEMS itself has no time to react. Three different protections were designed having actuation voltage of 120, 150 and 190V for BDG1 and BDG2 switches. Their geometry and dimensions take into account that we want a higher restoring force in order to make the fast switching. Moreover, the effect of the protection structure on the RF-MEMS S-parameters characteristics has been verified, by simulations and measurements, to be negligible and it is not impacting its microwave performances. The second verification consists in using a 3D non-contact profilometer (FOGALE nanotech) in order to analyse mechanical behaviour while applying an DC voltage up to 70V. In Fig.A.8, we can observed that as expected at 70V the RF-MEMS structure is actuated while the protection is still in the up-state. The difficulty now is to find a method to characterise the protection structure, because it should be fast and non-contacting, due to the ESD stress that we want to applied.

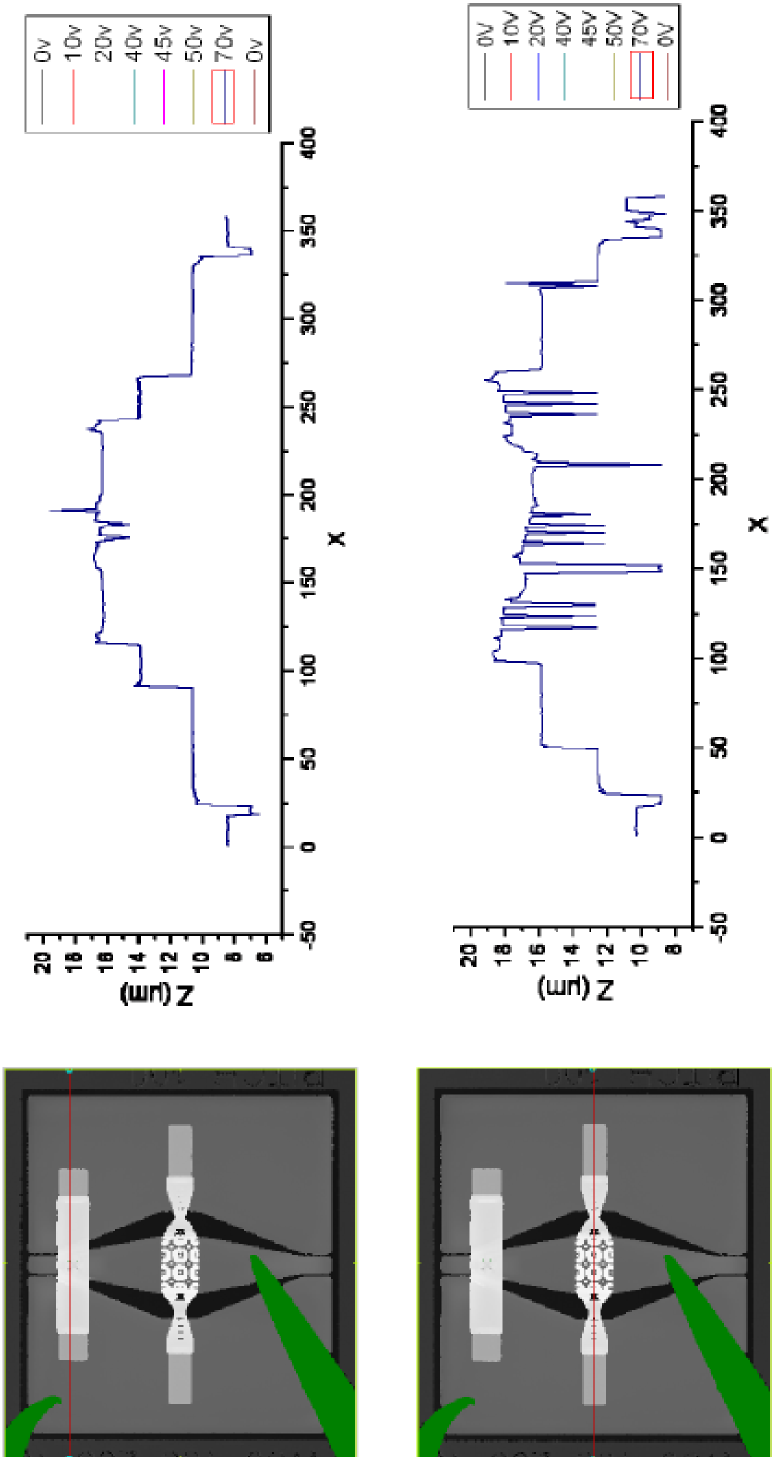

FIGURE A.8: Profilometer image and cross sections of BDG1 with the protection structure.

Appendix B

Accelerated Stress Test Circuit

According to results shown in Subsection 3.2.3.4, a circuit have been realised for the dedicated stress test. The circuit is miniaturized to be directly mounted on the RF-probe in order to have the shortest distance between the discharge and the DUT. Besides, as mentioned in Subsection 3.2.2.2, it is not possible to use a voltage probe due to its capacitance with respect to the one of the DUT. Therefore with this circuit, we will be able to assess the image of the applied voltage across the DUT by calculating:

$$V_{DUT} = V_{applied} - \frac{1}{C}\int_t I\mathrm{d}t$$

Principle of operation

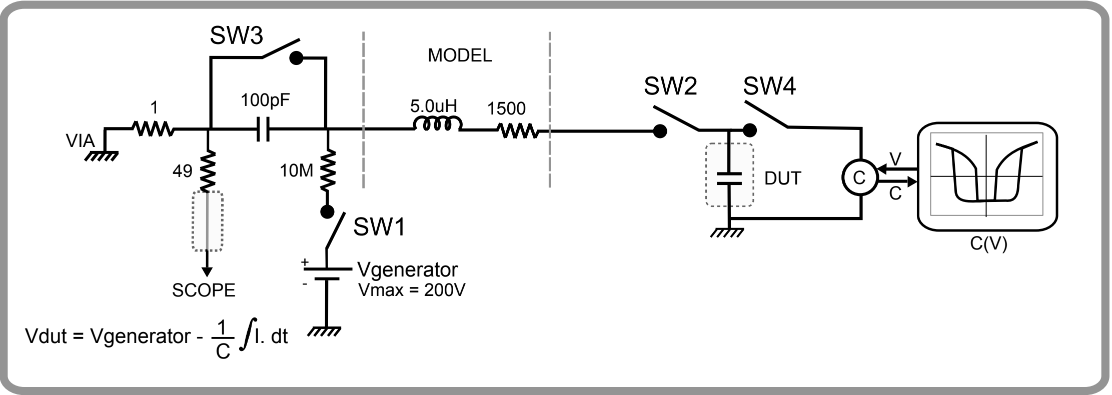

FIGURE B.1: Electrical schematic of the AST circuit for MEMS.

The approach consists in using the charge and discharge of a $100pF$ capacitor, by analogy to the HBM tester. This is necessary because if we simply use a signal generator to supply the pulse stress, it will impact as a EOS and not like an ESD. The whole procedure will be done in 4 steps:

– **SW1** is “on” and the capacitor is charged using a voltage generator through a resistance of $10M\Omega$,

– Then once SW1 is set "off", right after **SW2** is set "on" and the stress is then applied to the DUT. By controlling the duration of SW2, we can control the width of the pulse ($> 1ms$).
– By the way, when SW2 is still "on" we may set **SW3** "on" in order to see or simulate the effect of the charged DUT to the HBM model.
– Finally, we will set SW2 "off" and SW4 "on" in order to measure the C(V) characteristics.

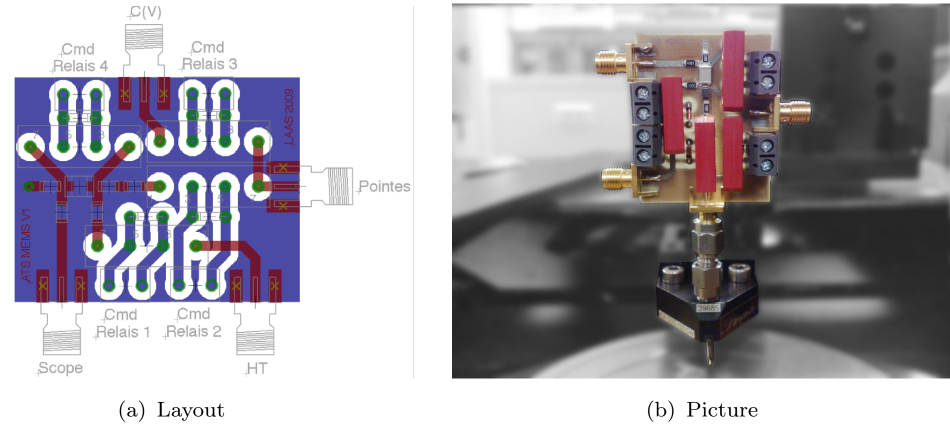

(a) Layout (b) Picture

Figure B.2: The AST-MEMS circuit.

Résumé (FR)

Titre : Analyse et modélisation de l'impact des décharges électrostatiques et des agressions électromagnétiques sur les MEMS RF : application à la conception d'un circuit d'adressage pour tête de réception reconfigurable.

Introduction

Depuis la deuxième moitié du 20e siècle, nos sociétés sont passées de l'ère énergétique à l'ère de l'information [109]. Dans cette nouvelle ère, nous assistions à une croissance exponentielle de l'émergence des applications sans fils. En effet depuis ces derniers 20 ans, nous sommes passés de la période où les communications étaient exclusivement réservées à l'armée ou pour une utilisation gouvernementale, à une explosion de ces hautes technologies vers un marché de grand public. Cette augmentation radicale du nombre d'utilisateurs a provoqué très vite des encombrements au niveau du spectre de fréquence alloué, obligeant les acteurs principaux des architectures et technologie de communication à constamment évoluer vers des modules électronique plus performants et plus reconfigurables. Cela met en évidence la nécessité de la recherche et le développement des nouveaux composants et circuits RF plus performants.

Dans ce contexte, les technologies de Micro Systèmes ElectroMécanique (MEMS) semblent pouvoir apporter les caractéristiques nécessaires, tels que la miniaturisation, la multitude des fonctions, la réduction de consommation et la linéarité de fonctionnement. Dans le domaine de la télécommunication, les micro-commutateurs RF (MEMS-RF) présentent d'excellentes performances électriques,

une très bonne linéarité, une faible consommation ainsi qu'un fort potentiel d'intégration [2–5]. Cependant leur industrialisation et commercialisation se font ralentir par leur maturité technologique ou par leur coût de fabrication, principalement dédiée à la résolution des problèmes de fiabilité et de la mise en boitier. Par conséquent, la fiabilité de ces MEMS RF reste un sujet de recherche très motivant et active partout dans le monde.

C'est dans ce cadre que s'inscrivent les travaux de recherche de cette thèse. Ils focalisent sur quatre principales problématiques liées au fonctionnement de ces structures MEMS RF, à savoir :

- Le chargement de l'isolant
- Les impacts des décharges électrostatiques
- Leur tenue en puissance
- L'effet du rayonnement

Il est bien évident que les aspects de fiabilité considérée dans ces travaux nécessitent des notions pluridisciplinaires (tels que la science des matériaux, les étapes de fabrication, la physique et la mécanique des structures, le design et modélisation et simulation). Les discussions avec de nombreuses personnes expérimentées et les enseignements acquises ont contribué à la rédaction de ce manuscrit.

Ces travaux de thèse s'articulent autour de trois chapitres ; Le premier est dédié à la vieille technologique à partir d'une vue d'ensemble des motivations jusqu'à l'étude de marché, de l'état de l'art vers une tendance future.
Le second chapitre présentera les bases fondamentales, la théorie des phénomènes physique lié aux différentes problématiques dont nous nous sommes fixés.
Enfin, le dernier chapitre présentera les principaux résultats de ces études et ces expériences, validant les hypothèses préablement définies sur les mécanismes de défaillances de ces structures.

Le manuscrit se clôturera par une conclusion sur l'ensemble des résultats et présentera les perspectives qui en découlent.

Chapitre 1

Introduction

Les micro-commutateurs MEMS RF sont utilisé pour créer un court-circuit ou bien un circuit-ouvert dans une ligne de transmission microonde. Ils se présentent généralement sous la forme d'une poutre ou d'un pont mobile qui à l'état initial ont une position haute, puis sous l'action d'une force physique (électrostatique, électrothermique, magnétostatiques ou piézoélectrique) les parties mobiles s'actionnent, c'est-à-dire qu'elles se mettront en état bas due à l'attraction issue de cette force.
Les deux topologies et types de contact : ohmique-série et capacitif-parallèle sont représenté sur le Tableau.4.1. A l'état haut, leur capacité sont de l'ordre de quelques fF alorqu'en état bas, le commutateur ohmique définit un court-circuit par un contact résistif. D'où l'importance d'avoir une valeur de la résistance de contact faible afin de minimiser les pertes d'insertion. Le commutateur capacitif à l'état bas court-circuite le signal RF grâce à la forte valeur de la capacité.
Ces structures peuvent être conçu pour fonctionner à des fréquences allant de quelques GHz à des fréquences supérieures à $200GHz$ [31].
Dans ce chapitre nous allons ; Comparer les performances de ces MEMS-RF aux performances des autres technologies de commutation microonde tels que les diodes PIN ou les switch FET. Donner des exemples d'applications nécessitant les caractéristiques de ces MEMS-RF. Présenter une étude de marché jusqu'en 2012 et évoquer l'état de la technologie ainsi que la fiabilité actuelle des MEMS RF.

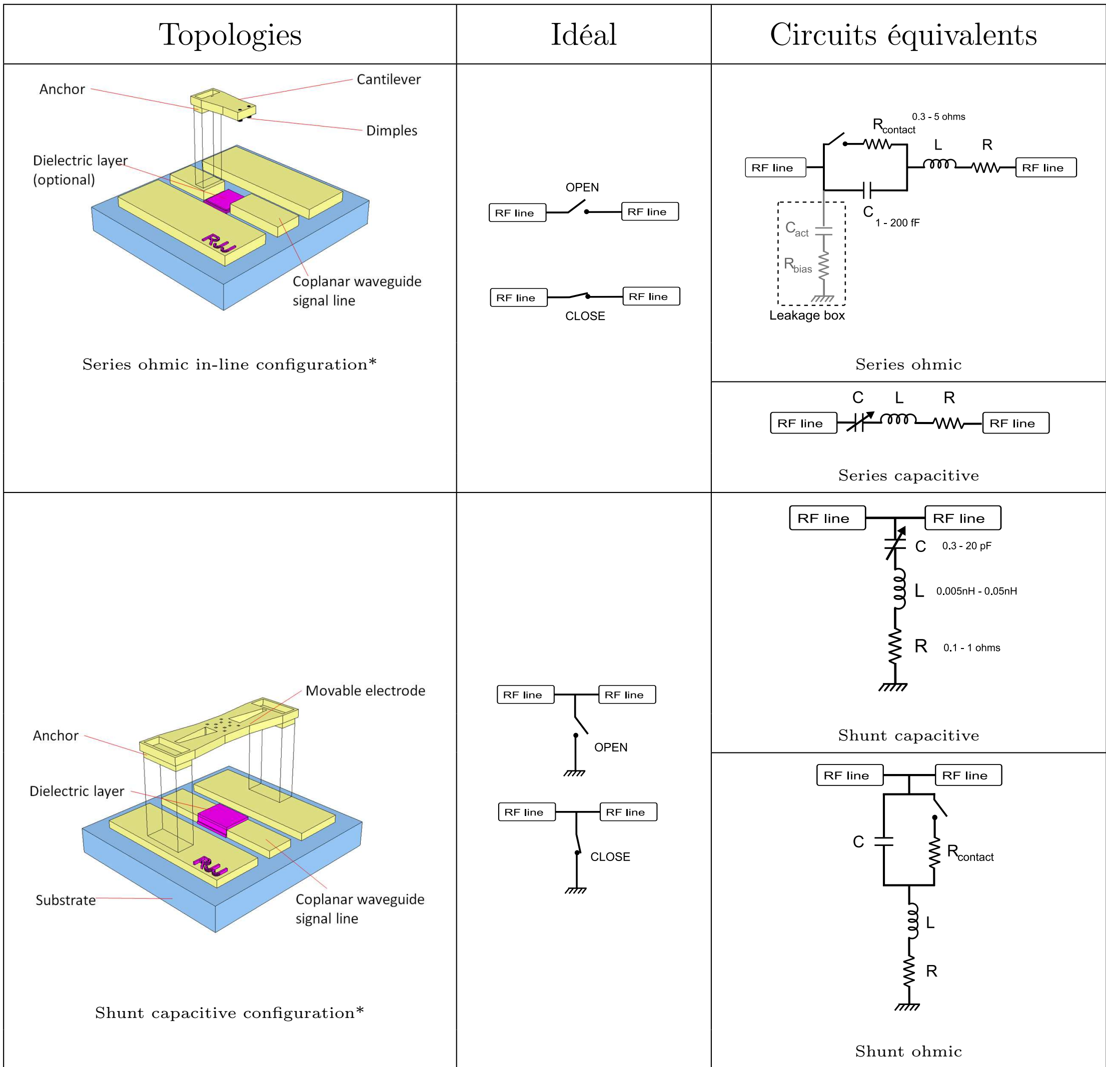

Topologies	Idéal	Circuits équivalents
Series ohmic in-line configuration*	OPEN / CLOSE	Series ohmic
		Series capacitive
Shunt capacitive configuration*	OPEN / CLOSE	Shunt capacitive
		Shunt ohmic

* topologies qui fonctionnent le mieux

TABLE 4.1: Principaux designs des micro-commutateurs MEMS RF

Les performances

Les hautes performances en termes de pertes, d'isolation et d'intermodulation, de consommation d'énergie et d'intégrabilité des MEMS RF augmenteraient efficacement les nouveaux systèmes et circuits microonde. Le Tableau.4.2 regroupe un ensemble de comparatifs. Les caractéristiques principales sont :

- L'actionnement électrostatique nécessite des tensions allant de 15 à 80V, mais la consommation en courant est très faible.
- Leur conception avec le pont ou bien la poutre suspendue permet une valeur faible de capacité à l'état ≪OFF≫, d'où une isolation important jusqu'à des fréquences supérieures à 40 GHz. De même, les pertes d'insertion sont moins que 0.1dB pour des fréquences supérieures à 40GHz.

Parameter	Unit	RF-MEMS	FET switch	PIN diode
Size	mm^2	<0.1	∼ 1	0.1
Control voltage	V	3 – 80	1 – 10	3 – 5
Control current	μA	<10	<10	3K – 10K
Current handling	mA	∼ 200	∼ 200	> 20
Power consumption	mW	∼ 0.001 – 0.05	1 – 5	1 – 5
Power handling	W	<4	<10	<10
Insertion loss	dB	0.1 up to 120 GHz	0.4 – 2 up to 10 GHz	0.3 – 1.0 up to 10 GHz
Isolation	dB	> 30 up to 100 GHz	15 – 25 up to 10 GHz	20 – 35 up to 10 GHz
Switching time	ns	> 300	1 – 100	1 – 100
Bandwidth	GHz	10 - 30*/ <100**	*n/a*	0.02–2
Cutoff frequency	THz	20 – 80	0.5 – 2	1 – 4
Third-order intercept point	dBm	> 60	40 – 60	30 – 45
Up-state capacitance	fF	1 – 10 fF**	70 – 140	18 – 80
Series resistance	Ω	<1	4 – 6	2 – 4
Capacitance ratio	–	40 – 500*	–	10
Lifetime	Cycles	$> {}^a10^{13}$ or $> {}^b10^7$	$> 10^9$	$> 10^9$
Final cost	$	8 – 20	0.3 – 6	0.9 – 8

* shunt capacitive
** series ohmic
[a] cold switching
[b] hot switching

Table 4.2: Tableau comparatif de performance RF entre commutateurs MEMS-RF, FET et diodes PIN [4, 5, 8, 24, 39].

- Leur linéarité est meilleure que celle des commutateurs à semi-conducteur, ainsi les produits d'intermodulation sont plus très faibles.
- La possibilité d'intégration est très intéressante grâce au processus de fabrication simple et leur support peut être un substrat de type silicium, GaAs, Pyrex, alumine.
- Leur temps de commutation est relativement long comparé à celui de leurs homologues. Néanmoins il a été démontré qu'il est possible de réaliser des structures MEMS-RF rapides, en contre partie d'une tension d'actionnement haute.

  Enfin il est important de rappeler que la mise en boitier et leur fiabilité nécessitent de forts développements pour satisfaire une reproductibilité des performances.

RF-MEMS circuits	Application fields				
	Phased array antennas*	Satellite transponders	Automatic Test Equipments	Base stations	Mobile telephony
Single and multi-throw switches	x	x	x	x	x
Phase shifters	x	-	-	-	-
Tunable filters	x	x	-	x	x
Tunable matching networks	x	x	-	x	x
Timing oscillators	-	-	-	-	x
Switch matrices	-	x	-	-	-

^{x} susceptible d'être intégré

* militaire, aeronautique, radars automobiles

Table 4.3: Les principaux champs d'application des micro-commutateurs MEMS RF.

Les applications

La technologie MEMS RF semble avoir trouvé ses intérêts dans la nouvelle génération d'applications sans fils et minuterie. Cette technologie apporte des solutions aux applications analogique et numérique, tels que les systèmes de communication satellitaire et fibre optique, les téléphones mobiles et bien d'autres équipements sans fils, les équipements de test automatique et notamment d'autres systèmes pour le grand public ou encore militaire. Le Tableau.4.3 regroupe les possibilités d'intégrer les circuits à base de MEMS-RF dans des niveaux supérieurs de système.

L'étude du marché

Cette section montre une vision global du marché d'aujourd'hui et de demain des micro-commutateurs MEMS RF. D'après les études économiques menées par WTC, Yole Development, ARRRO, iSuppli Corporation et Mancef, on aperçoit (Fig.4.3) que le marché ne cesse d'augmenter au moins jusqu'en 2012 avec une somme mise en jeu d'environ 500 millions de dollars. Ceci correspond en effet à la prévision du besoin total de volume, qui est engendré principalement par les applications de mobiles et d'infrastructure télécom.

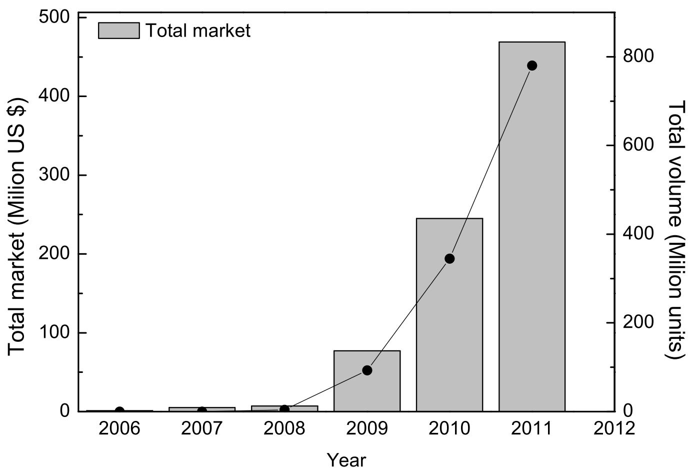

FIGURE 4.3: Le marché total du commutateur MEMS RF [45].

La fiabilité actuelle des MEMS RF

Depuis la fin des années 90s, les publications sur les microcommutateurs contiennent toutes une partie de discussion sur la fiabilité. En effet la fiabilité fut et ça l'est toujours un défi majeur pour la réussite, le succès et l'expansion de l'utilisation de ces microcommutateurs.
Cependant, des structures extrêmement fiable ont d'ors et déjà été démontré après une dizaine d'année de recherche [46], mais leur commercialisation reste encore problématique et nécessite encore un peu d'effort. Dans ce contexte, cette thèse tente d'analyser les aspects de fiabilités comme ; le chargement, les impacts des décharges électrostatiques, la tenue en puissance et les effets du rayonnement.

Chapitre 2

Principe de fonctionnement du μ-commutateur MEMS RF capacitif

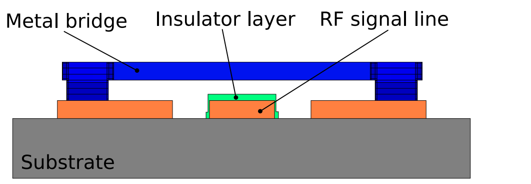

(a) Low capacitance value, RF signal passes.

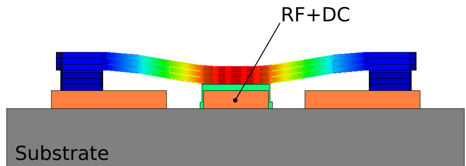

(b) High capacitance value, RF signal blocked.

FIGURE 4.4: Principle de fonctionnement d'un switch MEMS RF capacitif (a) à l'état haut (non actionné) et (b) à l'état bas (actionné).

La Figure.4.4 présente une topologie simple du micro-commutateur MEMS RF capacitif. Il est constitué d'une membrane métallique ancrée sur le plan de masse d'une ligne coplanaire de chaque coté. La ligne centrale peut être utilisée comme électrode d'actionnement et elle est recouverte d'une couche diélectrique pour éviter un court-circuit lorsque la membrane sera ramenée à l'état bas. La membrane est généralement suspendue à une hauteur d'environ 2.5μm au dessus de la couche diélectrique. Dans cette état haut la capacité est de l'ordre de quelques fF, ce qui correspond à l'état de fonctionnement $\ll$ passant $\gg$. Sous l'action d'une force électrostatique lorsqu'on vient appliquer une tension entre la masse et la ligne centrale, la membrane passe de l'état haut à l'état si cette force électrostatique est supérieure à la force de rappel. La tension correspondant à ce changement abrupt d'état est définie comme étant la tension d'actionnement (pull-down voltage) V_{down}. Cette action crée une capacité d'une valeur de quelques pF et elle est suffisamment grande pour bloquer le signal RF. Ceci corresponderai à l'état de fonctionnement $\ll$ bloqué $\gg$ du composant.

Ensuite si la force de rappel est supérieure à la force engendrée par la tension

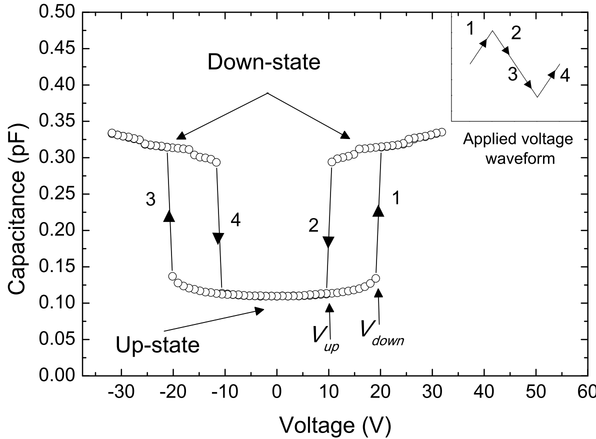

FIGURE 4.5: Courbe C(V) complète du μ-commutateur MEMS RF capacitif.

appliquée, la membrane revient à sa position initiale et ce changement est défini comme la tension de relâchement (pull-up voltage) V_{up}. En analysant finement les caractéristique capacité-tension C(V) de la structure, nous pouvons évaluer sa réponse électromécanique pour les études de fiabilité.

Bases théoriques sur le chargement du diélectrique

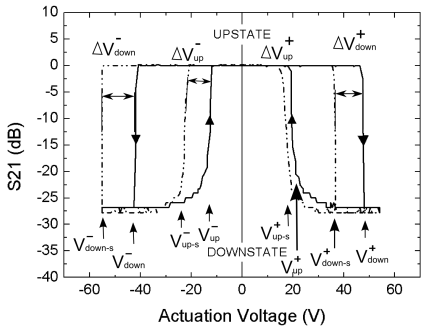

(a) Dans le cas où il y a chargement.

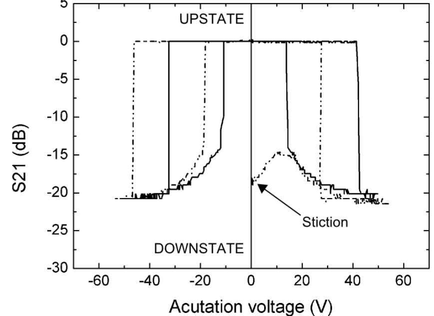

(b) Dans le cas où il y a défaillance (collage).

FIGURE 4.6: Caractéristiques typiques du chargement du diélectrique et de la défaillance.

La fiabilité des microcommutateurs MEMS RF est souvent cautionnée par la couche diélectrique utilisée. La problématique réside dans le changement du diélectrique en réponse de la tension appliquée au commutateur. Lorsque la membrane est en contact avec la fine couche de diélectrique, celle-ci est soumise à des forts champs électriques engendrant des courants de conduction et provoquant

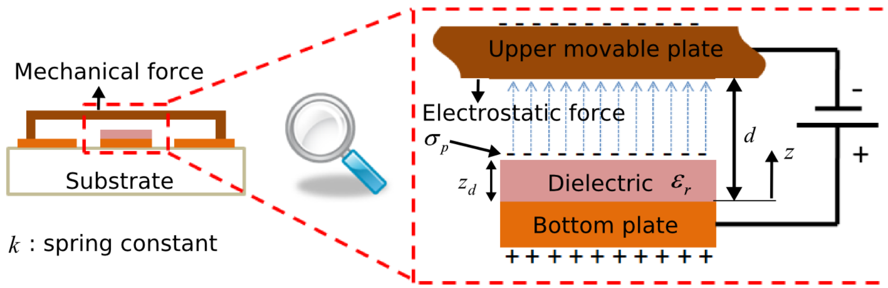

FIGURE 4.7: Modèle de chargement simplifié du μ-commutateur capacitf.

une accumulation de charges. Cette accumulation de charges est facilement détectable en analysant la superposition des réponses électromécanique C(V) ou S21(V), tel que le montre la Fig.4.6(a). Si l'accumulation de charges est trop importante, la force électrostatique généré (par les charges résiduelles et non pas par la tension appliquée) peut devenir plus forte que la force de rappel et cela se résulte à une défaillance, plus précisément un collage (Fig.4.6(b)).
Les phénomènes physiques de conduction et de piégeage de charges sont encore mal connus. Néanmoins l'exploration des propriétés diélectriques peut être appréhendée par des modèles empiriques et par des expérimentations.
Le modèle simplifié servant à interpréter nos résultats est présenté par la Fig.4.7. Il sert à définir l'influence de la densité de charge parasite en surface sur la force électrostatique. L'équation de la force électrostatique s'écrit de la manière suivante :

$$F_e = \int_{(A)} \mathrm{d}F = \frac{\mathrm{d}C}{\mathrm{d}z} \cdot \int_{(A)} \frac{(V - V_{shift})^2}{2} \mathrm{d}A \tag{4.1}$$

avec, la capacité par unité de surface:
$C = \dfrac{1}{\dfrac{d-z}{\varepsilon_0 \varepsilon_{air}} + \dfrac{z_d}{\varepsilon_0 \varepsilon_r}}$
et la tension résiduelle responsable du décalage des courves C(V):
$V_{shift} = -\sigma_p \cdot \dfrac{z_d}{\varepsilon_0 \varepsilon_r}$
Si la densité de flux électrique est constant sur la distance d, la densité de charge parasite est donnée par :

$$\sigma_p = -\frac{\varepsilon_0 \cdot V + z_d \cdot P}{\varepsilon_r \, (z - d)} \tag{4.2}$$

, avec P la polarization diélectrique.

L'origine des charges, induisant la défaillance chez les MEMS RF capacitifs peut être intrinsèque ou extrinsèque. Les charges intrinsèques sont des ions déjà présents dans le diélectrique lors de sa fabrication ou générés soit par

électrodissociation d'espèces neutres, soit par ionisation des constituants du solide dû à des interactions avec des rayonnements énergétiques ou des particules [110]. Les travaux du professeur G. Papaioannou et al. [53] montrent qu'à température ambiante le mécanisme dominant est la polarisation de charge d'espace d'origine extrinsèque et à des températures hautes ($\sim 380°K$) la polarisation dipolaire et charge d'espace d'origine intrinsèque domine. Dès lors que les résultats présents dans ce manuscrit sont obtenus à des températures inférieures à $330°K$, l'accumulation de charge lors du fonctionnement du composant est alors de nature extrinsèque.
Les courants de conduction liés à l'injection de charge dans les MEMS RF sont souvent de type Trap Assisted Tunneling (conduction par effect Tunnel assisté par piégeage) [55] ou Poole Frenkel [60].
Les défauts dans le diélectriques est à l'origine de l'effet tunnel du mouvement des électrons qui franchissent l'isolant. Ce mécanisme désigne la propriété que possède un objet quantique de franchir une barrière de potentiel en une ou plusieurs étapes. L'effet Poole Frenkel parle du porteur piégé dans le puits de potentiel coulombien dans le volume du diélectrique et qui sous l'effet d'un champ électrique et de la température franchit la barrière de potentiel et participe ainsi à la conduction dans l'isolant.

La compréhension de ces mécanismes et ces phénomènes est primordiale pour étudier les effets de chargement du diélectrique. Dans les MEMS capacitifs, ce chargement est accéléré par les fortes tensions utilisées pour l'actionnement et se traduit par une dérive de leur comportement électromécanique, donc de leur durée de vie. Le chapitre suivant présentera l'ensemble des résultats obtenus sur le chargement dû au contraints DC, cyclage et ESD (décharge électrostatique). Une attention particulière sera consacré aux tests de vieillissement en variation les paramètres tels que le niveau de la tension, la durée des impulsions et la temperature.

Chapitre 3

Les résultats expérimentaux et analyses

Ce chapitre détaillera les résultats expérimentaux obtenus durant cette thèse. Dans cette version courte, parmi les expérimentations sur le chargement, l'impact des décharge électrostatiques, la tenue en puissance et les effets dû au rayonnement, uniquement le chargement sous contraintes DC et sous ESD sera présenté.

Le chargement du diélectrique sous contraintes DC

La structure de test

La topologie des dispositifs utilisés pour le chargement du diélectrique est composée de:

- Une épaisseur de la membrane métallique de $0.9\mu m$ composée d'un empilement de $Au/Ni/Au$,
- Des lignes coplanaires de couches $Ta/Pt/Au/Pt$,
- Une couche diélectrique se trouvant sous la membrane de Nitrure d'Aluminium (AlN) d'une épaisseur de $0.3\mu m$,
- Une métallisation finale réalisée par une couche d'Au électrolytique de $2\mu m$ d'épaisseur

La procédure de test

La procédure de test sous contraintes DC consiste à évaluer la capacité de la structure d'être maintenue à l'état bas. Cette méthode et considérée comme étant un test accéléré de chargement [60, 85]. En effet il a déjà été démontré que la

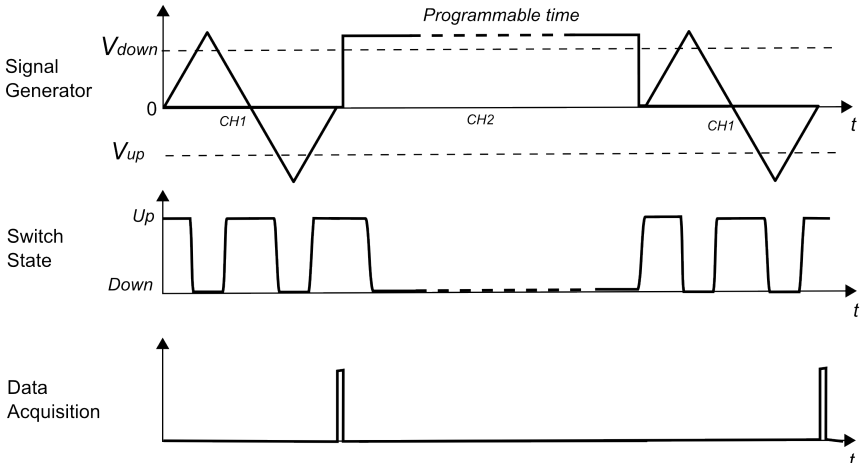

FIGURE 4.8: Chronogramme des signaux de commande et de la réponse du $\mu-$commutateur.

durée de vie du composant ne dépendait pas de la fréquence d'actionnement mais du temps total que la structure est resté à l'état bas [51].
La procédure commence avec une première mesure du paramètre de transmission ou bien de capacité en fonction de la tension (sa signature électromécanique). Ensuite on applique une tension de maintien dont la durée est facilement programmable. Une fois que le stress est appliqué, la signature électromécanique est à nouveau mesurée. Les chronogrammes des signaux de commande et de la réponse du commutateur sont illustré sur la Fig.4.8 A partir des résultats obtenus des microcommutateurs à base d'AlN (par exemple la Fig.4.6(a)), nous utilisons la superposition des courbes, initialement mesurée et celle mesurée après le stress, pour analyser la dérive ΔV de la signature électromécanique causée par le chargement.

Dans le cas d'une structure idéale, la dérive devrait être symétrique indépendamment de la polarité de la commande. En pratique c'est généralement impossible, car cela dépend beaucoup des propriétés structurales du diélectrique utilisé. En conséquence, afin de comparer différents dispositifs avec des matériaux diélectriques différents, la valeur moyenne de charge résiduelle accumulée est calculée en utilisant l'équation suivante :

$$\boxed{V_{off} = \frac{\langle \Delta V_{down} \rangle + \langle \Delta V_{up} \rangle}{2}} \tag{4.3}$$

, avec V_{off} la valeur moyenne, $\langle \Delta V_{down} \rangle$ la valeur moyenne calculée à partir de l'actionnement et $\langle \Delta V_{up} \rangle$ la valeur moyenne calculée à partir du relâchement.

Une fois que la valeur de la charge résiduelle a été déterminée, il est rigoureux de tenir compte de la cinétique de charge du matériau en calculant le ratio de chargement avec :

$$R_Q = \frac{\mathrm{d}V_{off}}{\mathrm{d}t_{down}} \tag{4.4}$$

, avec t_{down} le temps total dont le dispositif est resté à l'état bas.
Ce ratio est l'image de la réponse du matériau en conséquence du chargement, qui est dépendant du champ électrique. Or dans le cadre de ces structures, ce champ dépend énormément de la rugosité et des aspérités des surfaces de contact. De ce fait, le modèle du champ-électrique effectif proposé dans [60] semblent être cohérent :

$$E_{eff} = \left(\frac{V_{applied}}{z_d}\right) \times \left(\frac{C_{meas}}{C_{th}}\right) \tag{4.5}$$

, avec $V_{applied}$ la tension appliquée, C_{th} la capacité théorique à l'état bas et C_{meas} la capacité mesuré à l'état bas.
Implicitement ces deux expressions tiennent donc compte de tous les paramètres physiques et électriques tels que les propriétés diélectriques, le champ électrique effectif et la qualité du contact. En les rassemblant ensemble, nous obtenons la conductivité apparente du matériau par la formule :

$$\sigma_{eff} = \frac{R_Q}{E_{eff}} \frac{\varepsilon_0 \varepsilon_r}{z_d} \tag{4.6}$$

, avec z_d l'épaisseur du diélectrique.
La conductivité est une mesure de la capacité d'un matériau à conduire un courant électrique. En d'autres termes, il est donc possible de remonter aux mécanismes de conduction du dispositif en utilisant la formule fondamentale de :

$$J = \sigma \cdot E \tag{4.7}$$

Finalement, en utilisant ces formules et tous les résultats obtenus, la conductivité des différents matériaux sont calculés et affichés sur la Fig.4.9 (■). Tous les résultats de cette expérimentation sur les structures à base d'AlN y sont également tracé. En titre de comparaison, les résultats des travaux précédents du laboratoire sur les structures Si_3N_4 [60] et d'autre données extraites de la littérature sont tous résumé sur la figure.
Les résultats indiquent que les dispositifs a base d'AlN ont un meilleur comportement de charge que ceux à base de Si_3N_4. De plus ses performances équivalent à ceux à base de SiO_2, mais avec des niveaux d'isolation plus

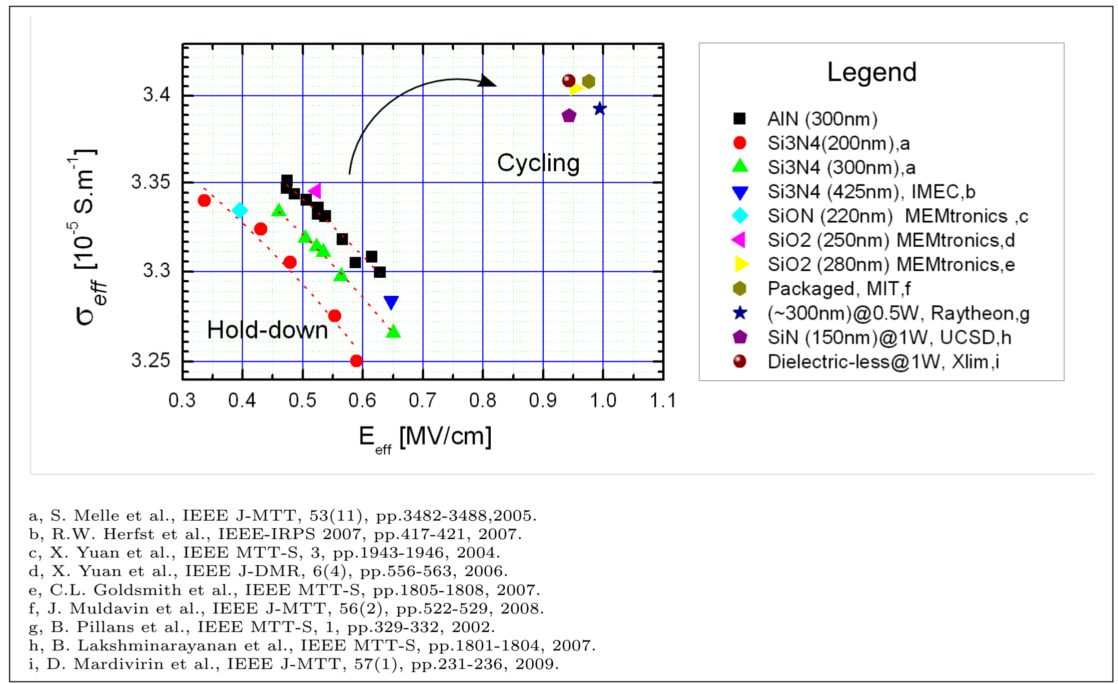

FIGURE 4.9: Comparaison empirique de différents matériaux diélectriques.

significatifs, ce qui pourraient être plus attractive en terme de circuit RF MEMS de haute fiabilité. Cela peut sans doute s'expliquer par la différence en propriétés structurales. En effet les nitrures utilisés sont en général de nature amorphe, qui favorise le piégeage des charges, alors que les couches AlN sont caractérisées par des grains denses et alignés donc d'une orientation excellente [86].

Le chargement du diélectrique sous ESD

Les deux normes de générateurs de décharges utilisés sont le ≪ Transmission Line Pulsing ≫ (TLP) et le ≪ Human Body Model ≫ (HBM). Ils diffèrent principalement au niveau de la forme d'onde (un signal carré de l'ordre de 100ns dans le cas du TLP et une double-exponentiel d'environ 500ns pour le HBM). Les résultats obtenus dans le cadre des expériences sous décharges électrostatiques se devisent en trois parties.

- Tout d'abord, les niveaux de tensions des impulsions sont appliqués de manière croissante jusqu'à ce qu'il y défaillance et une analyse de défaillance est alors effectuée.
- Ensuite pour les deux standards ESD, nous nous limitons à des niveaux de tensions inférieurs au niveau de claquage pour étudier les mécanismes de charge engendrés.

– Enfin, ces derniers résultats ont permit de comprendre qu'il était possible d'effectuer des tests pulsé pour réaliser des tests accélérés.

La défaillance sous test TLP et HBM

TLP:

Les stress sous décharges électrostatiques ont été conduits en utilisant une méthode dite TLP qui génère des impulsions par des charges et décharges d'une ligne de transmission. Ces décharges sont sous forme d'impulsions d'une durée de 100ns avec des temps montée et de descente de l'ordre d'une centaine de picosecondes. Nous avons tout d'abord fait des tests avec la membrane à l'état-haut. Cette configuration choisie se rapproche du cas réel, ou du moins le plus probable lors d'un phénomène de surtension. Des impulsions de 250V à 420V ont été générées sur l'accès RF et les défaillances observées à ces limites ont montré une destruction de la métallisation dans la majorité des cas et du diélectrique dans quelques cas. La mesure quasi-statique (Fig.4.10) indique la tenue en courant (I_{max}-TLP) de la structure jusqu'à ∼2A, ce qui correspond à un niveau de tension proche de 360V. Au-delà il y'aura destruction totale de la structure.
Pour des niveaux d'impulsions plus bas, quand il y a défaillance mineure, il est possible de vérifier le fonctionnement de la structure sur les mesures de l'évolution du paramètre de transmission en fonction de la tension d'actionnement S_{21}(V) (Fig.4.11). En effet, la différence de niveau d'isolation entre les deux courbes permet de dire que le contact capacitif du μ-commutateur a été endommagé par les agressions de décharges électrostatiques.

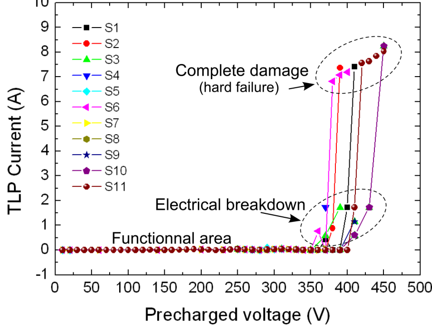

FIGURE 4.10: Courbes courant-tension TLP comme signature de défaillance.

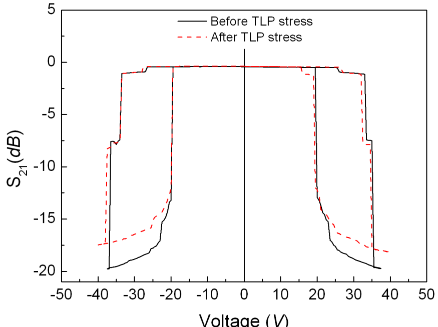

FIGURE 4.11: Une courbe typique de $S_{21}(V)$ dans le cas d'un commutateur affecté par des défaillances mineures.

***HBM*:**

Le générateur HBM diffère du TLP au niveau de la forme d'onde du signal. En effet, il permet une décharge d'une forme exponentielle d'une durée d'environ 500ns, mais la procédure de test fait que cette décharge reste sur le composant durant environ 10- 20 ms. Cette durée de stress suffise à amener la membrane à l'état bas, car le temps de commutation du dispositif est autour de $20\mu s$. Durant le déplacement, la distance entre-électrodes diminue et des micro- arcs électriques apparaissent pour des niveaux de tension plus bas (∼250V) comparés aux niveaux du test TLP (∼360V). Cependant, une fois que la membrane est à l'état bas, le niveau de destruction du composant est autour de 1kV, ce qui correspond à la tension de claquage du diélectrique.

Dans ce cas de test HBM, une première observation au microscope après une série de décharge n'a montré aucune défaillance apparente (Fig.4.12(a)). Mais en enlevant la membrane, l'analyse a pu montrer que chaque étincelle, ou micro arc électrique a crée une défaillance physique du diélectrique (encerclé dans la Fig.4.12(b))

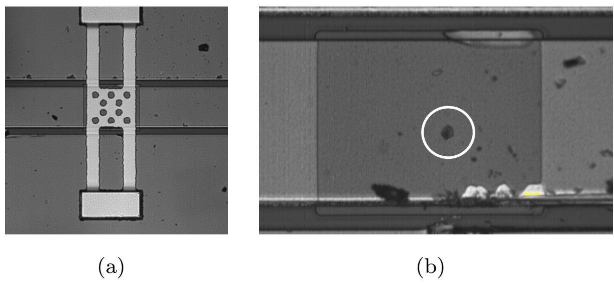

(a) (b)

FIGURE 4.12: Observations au microscope (a) après une série de décharge, (b) un agrandissement du diélectrique après avoir enlevé la membrane.

Les mécanismes de charge en TLP et HBM

Les paragraphes précédents ont montré les niveaux de défaillance pour des tests TLP et HBM. Pour approfondir cette étude et tenter de comprendre les mécanismes de charge dû aux décharges TLP et HBM, les résultats présentés dans ce paragraphe ont été obtenues pour des niveaux d'impulsions en dessous de 100V. Deux types de nitrure de silicium ont été utilisés pour réaliser les expérimentations, le MF-Si_3N_4 et le LF-Si_3N_4.

Les analyses ont été effectuées à l'aide des mesures de capacité en fonction de la tension. Lorsque la tension appliquée n'excède pas la tension d'actionnement du

μ-commutateur, les courbes C(V) sont généralement paraboliques. Ce principe de mesure est utilisé pour éviter tout chargement venant de la mesure elle-même. Pour observer les mécanismes de charge, nous allons analyser la dérive de la signature C(V) et plus précisément le point minimum de la parabole, noté $V_{capamin}$ la tension correspondant au minimum de capacité.
Lors d'une agression électrostatique (ESD) sur le dispositif la valeur moyenne des charges engendrées lors de ce stress se traduit par un décalage de la caractéristique C(V). Deux phénomènes de charge peuvent être à l'origine de ce décalage, à savoir l'induction de charge et l'injection de charge (Paragraphe.3.2.2.4). La direction vers laquelle la parabole de la caractéristique C(V) se décale indique le phénomène dominant (i.e. l'inclinaison de la droite, pente positive ou bien pente négative).

TLP:
La Fig.4.13 illustre les tests des impulsions TLP positives sur les composants ayant du MF-Si_3N_4 et LF-Si_3N_4. Le décalage en amont ou en aval de la mesure initiale confirme la présence des deux phénomènes précédemment mentionnés. L'échelle des coordonnées X-Y étant logarithmique et les courbes de tendance étant linéaires, montrent que le chargement induit par TLP suit une loi de puissance par rapport aux impulsions TLP.

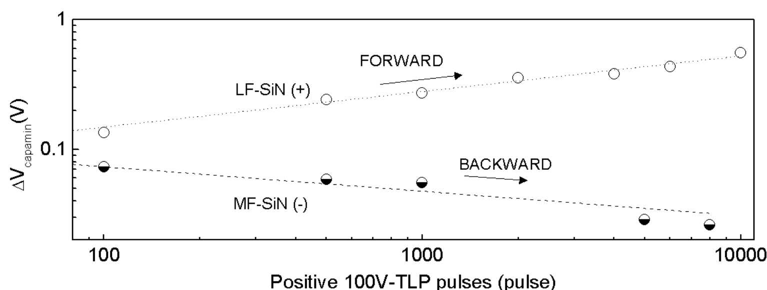

FIGURE 4.13: La dérive de $V_{capamin}$ en fonction d'impulsions positives TLP, pour les structures MF-SiN et LF-SiN.

Les résultats nous permettent de déduire que l'injection des charges est dominante sur le matériau LF-Si_3N_4 alors que l'induction de charge se manifeste sur l'isolant MF-Si_3N_4. En comparant l'intensité de l'ensemble des valeurs on en déduit que la dérive est moins prononcée pour le MF-Si_3N_4 que le LF-Si_3N_4, d'où l'affirmation que le MF-Si_3N_4 est moins sensible aux stress TLP. Ces comportements électriques sont directement liés aux propriétés diélectriques de l'isolant qui sont cautionnés par leur procédure d'élaboration (présence plus ou moins d'hydrogène, présence de défauts, la rugosité, la rigidité).

HBM:
La forme d'onde est différente entre les standards TLP et HBM. Malgré que le testeur HBM génère une impulsion d'environ 500ns, la procédure de stress de la station maintient la structure de test pendant environ 10 à 20 ms. Ceci peut ramener la membrane à l'état bas pour les deux types de structures. Contrairement à la Fig.4.13, sur la Fig.4.14 uniquement l'injection de charge est observée, indépendamment du type de diélectrique (pente positive des droites). De plus le décalage de $V_{capamin}$ est environ dix fois plus important, puisque le champ électrique appliqué lorsque la membrane est à l'état-bas est nettement plus intense. Mais si nous comparons les deux types de nitrure de silicium, nous apercevons que la sensibilité à la décharge HBM reste plus accrue chez le LF-Si_3N_4 que chez le MF-Si_3N_4.

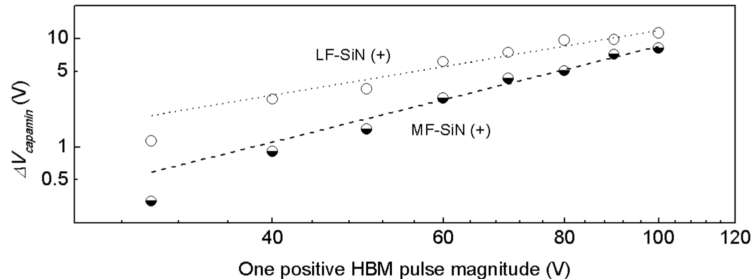

FIGURE 4.14: La dérive de $V_{capamin}$ en fonction d'une impulsion positive HBM pour des valeurs de tension allant de 30 à 100V, pour les structures MF-SiN et LF-SiN.

Les tests d'accélération en mode pulsée utilisant le generateur HBM

Définition:
Un test de vieillissement (appelé Accelerated Lifetime Test (ALT) en anglais) consiste à effectuer un protocole de test sur un dispositif au point d'induire les même mécanismes de défaillance qui apparaissent lors du fonctionnement normal, mais dans un laps de temps beaucoup plus court. Ces techniques sont souvent basées sur l'application d'un stress de type amplitude, température ou durée.

Expérimentations:
Dans ce contexte et suite aux résultats obtenus avec la station de test HBM (Fig.4.14), où l'application d'une impulsion suffise à créer une forte dérive de la signature C(V), nous avons effectué des tests de cyclage (souvent considéré comme étant une mesure de la durée de vie du μ-commutateur) et des tests sous décharge

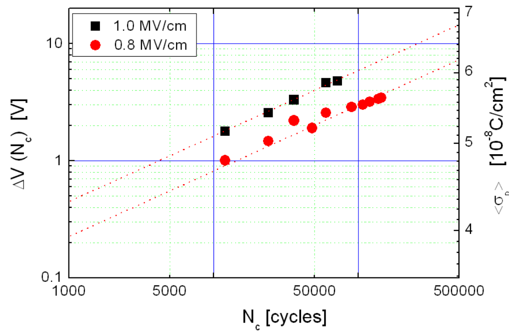

FIGURE 4.15: La dérive de $V_{capamin}$ en fonction du nombre de cycles (avec l'equivalence de la densité de charge en surface).

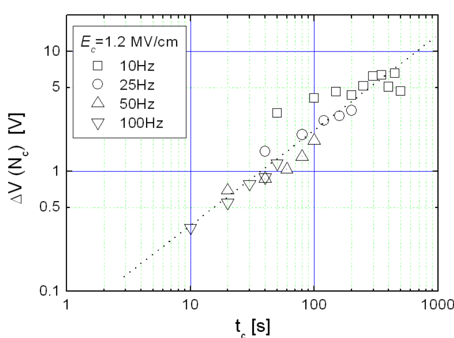

FIGURE 4.16: La dérive de $V_{capamin}$ en fonction du temps d'actionnement $t_{down,s}$.

HBM et la comparaison, ainsi que la corrélation seront présentées. Pour ce faire, nous nous basons toujours sur l'analyse du décalage du paramètre $V_{capamin}$, c'est-à-dire le ΔV.

Résultat de cyclage:

Les structures de test ont été actionné avec un signal unipolaire positif, à différentes fréquences, un rapport cyclique de 50% et à une température ambiante de 300K. Les résultats présentés sur la Fig.4.15 indique clairement une relation de puissance entre le chargement et le nombre de cycles (note : les figures sont en échelle log-log). Le chargement dépend aussi du temps d'actionnement (le temps durant lequel le commutateur reste à l'état bas). D'après ces deux figures, nous pouvons écrire :

$$\boxed{\Delta V_c(t_c, N_c) = \Delta V_{0,c} \cdot \left(\frac{t_{down,c}}{\tau_c}\right)^{n_c} \cdot N_c^{n_c}} \tag{4.8}$$

, où $\Delta V_{0,c}$ est une constante de proportionnalité, $t_{down,c}$ est le temps d'actionnement du cyclage, calculé à partir de la fréquence et du rapport cyclique, τ_c est la constante de temps lié au chargement, N_c est le nombre de cycles et n_c est la constante de puissance.

Résultat d'impulsion HBM:

Deux séries de mesure ont permit d'extraire les données présentées sur les figures (Fig.4.17 et Fig.4.18). Pour la première figure, nous avons varié le champ électrique du stress et gardé le nombre d'impulsion constant (une seule impulsion). Puis pour tracer la deuxième figure, nous incrémentons le nombre d'impulsions et nous

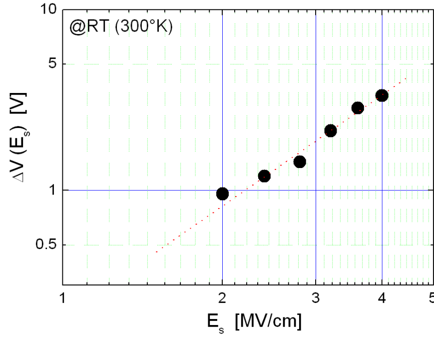

FIGURE 4.17: La dérive de $V_{capamin}$ en fonction du champ électrique du stress HBM.

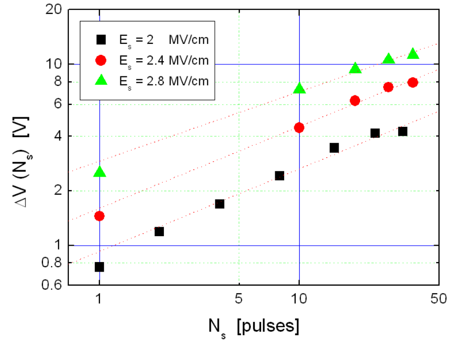

FIGURE 4.18: La dérive de $V_{capamin}$ en fonction du nombre d'impulsions HBM pour différents champs électriques.

avons répété l'expérimentation pour différents champs électriques. L'ensemble de ces deux figures nous permettent d'écrire l'équation suivante :

$$\boxed{\Delta V_s(t_s, N_s, E_s) = \Delta V_{0,s} \cdot \left(\frac{t_{down,s}}{\tau_s}\right)^{n_s} \cdot N_s^{n_s} \cdot \left(\frac{E_s}{E_0}\right)^{m_s},} \tag{4.9}$$

, où $\Delta V_{0,s}$ est la constante d'amplitude du stress, $t_{down,s}$ est le temps d'actionnement total du stress, τ_s la constante de temps du chargement, N_s est le nombre d'impulsions, E_s est le champ électrique du stress, E_0 est une constante d'équivalence et m_s, n_s sont des constantes de puissance.

Corrélation entre cyclage et stress HBM :

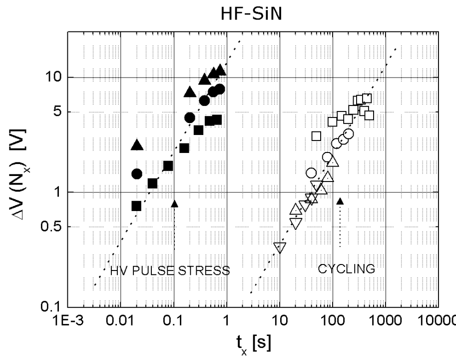

FIGURE 4.19: La dérive de $V_{capamin}$ en fonction du temps d'actionnement.

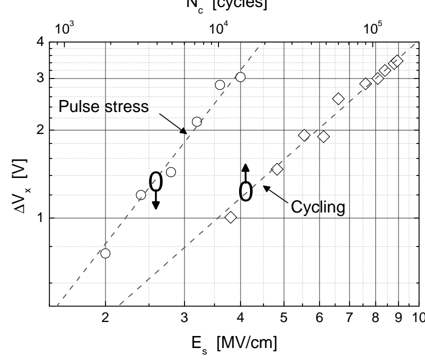

FIGURE 4.20: Comparaison entre $\Delta V_c(N_c)$ et $\Delta V_s(E_s)$.

La corrélation se base sur l'analyse de la dérive ΔV. Les résultats sont résumé sur la Fig.4.19 et Fig.4.20. Sur la Fig.4.19, il est clairement observé que la même dérive ΔV est obtenue beaucoup plus rapidement dans le cas du stress HBM que dans

le cas du cyclage. Pour que la comparaison de ces deux méthodes soie valable, on utilise les équations Eq.4.8 et Eq.4.9 pour calculer la dérive pour un champ électrique de $E_c = 0.8MV/cm$ et un nombre de cycle égal à un. Nous obtenons alors :
$\Delta V_c = 18mV$
$\Delta V_s = 26mV$
Ces calculs peuvent être considéré comme étant en accord et comparable l'un de l'autre, car ils correspondent notamment aux extrapolations de la Fig.4.20. Par conséquent, ces valeurs et ces extrapolations nous permettent de présumer que nous obtenons, sans erreur significative, la même dérive pour les deux méthodes. Somme toute, ces résultats montrent que le vieillissement utilisant de haute impulsion de tension est réalisable et très intéressant pour analyser la fiabilité des μ-commutateur capacitifs.

Variation en température:
Un autre facteur d'accélération souvent utilisé pour les tests de vieillissement est la température. Dans ce cas, nous avons mesuré les caractéristiques ΔV en fonction du champ électrique à différentes températures variant de $25°C$ à $55°C$. La première remarque c'est que la pente des droites sur la Fig.4.21 reste constante avec la temperature, ce qui signifie que le mécanisme de défaillance, à savoir le chargement reste le même. Cette remarque nous permet par la suite d'analyser la deuxième remarque qui montre que les courbes ont un décalage vertical vers le haut avec la montée en température, ce qui indiquerait que l'amplitude des droites (K) est le paramètre thérmiquement activable, si l'équation des droites

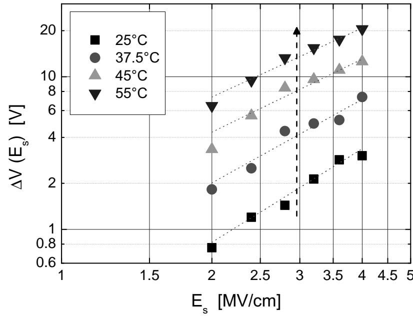

FIGURE 4.21: La dérive de $V_{capamin}$ en fonction du champ électrique à des températures de $25°C$ à $55°C$.

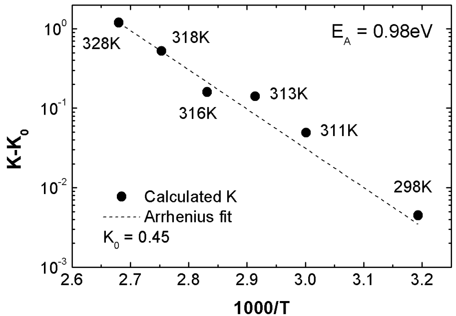

FIGURE 4.22: Le fit utilisant la loi d'Arrhenius.

s'écrit comme:

$$\Delta V(E_s) = K \cdot \left(\frac{E_s}{E_0}\right)^{\alpha}$$

, où $\Delta V(E_s)$ est extrait à partir de la Fig.4.21 et K est le coefficient thermiquement activable qui est lié au comportement électrothermique du diélectrique et α est le coefficient de puissance.

Utilisant cette équation et les données de la Fig.4.21, nous en extrairons le coefficient K en fonction de la température et les résultats obtenus sont tracés sur la Fig.4.22. Afin d'extraire l'énergie d'activation, on peut utiliser le modèle d'Arrhenius pour le fit. La Fig.4.22 met en évidence que les résultats suivent le modèle d'Arrhenius (représenté par la droite en pointillée). Finalement, l'énergie d'activation extrait est de $0.98eV$. Ces résultats montrent la relation entre le coefficient de chargement et la température des μ-commutateur MEMS RF capacitifs. En d'autres termes, le chargement du dispositif en condition normal d'utilisation peut être estimé beaucoup plus rapidement en utilisant les données du test accéléré par la variation de température.

Conclusion

Cette thèse présente les tests de fiabilité et les caractérisations de performance des μ-commutateurs MEMS RF. En particulier, nous avons regardé son fonctionnement et son respect du cahier de charge, ainsi que ses propriétés électrostatiques, microondes, sa tenue en puissance et sa réponse au rayonnement. Cette version substantielle en français propose l'étude de l'évolution des caractéristiques des MEMS RF capacitifs sous contrainte DC et ESD. La première partie des résultats montrent que les composants à base de nitrure d'aluminium présentent des cinétiques de chargement plus faible que les diélectriques à base de nitrure de silicium, avec des capacités relativement attractives pour des circuits MEMS RF de haute fiabilité. En ce qui concerne les tests de décharges électrostatiques, nous avons tout d'abord analysé la défaillance et la robustesse des structures. Puis leur mécanisme de chargement ont été affranchi en utilisant des hypothèses et des modèles dédiés, deux différents types de standard ESD et deux différents types de nitrure de silicium. Enfin les niveaux de tension élevés des décharges ont permis de développer des tests de vieillissement pour ces structures, en jouant sur l'amplitude, la durée de l'impulsion et la température. Les observations et les mesures effectués peuvent contribuer à la standardisation des procédures de test et par conséquent à l'exploitation industrielle de cette filaire technologique.

Université Paul Sabatier - Toulouse III

PROCES VERBAL DE SOUTENANCE DU 02/07/2010 A 10h00

ANNEE UNIVERSITAIRE 2009/2010

Etudiant	: M. JINYU RUAN	né le : 21/04/1982
Version de diplôme	: DOCT. UNIV. MICROONDES, ELECTROMAGNETISME ET OPTOELECTRONIQ.	
Titre des travaux	: Analyse et modélosation de l'impact des décharges électrostatiques et des agressions éléctromagnétiques sur les microcommutateurs.	
Ecole doctorale	: Ecole Doctorale Génie Electrique,Electronique, Télécommunications - UPS	
Directeur	: M. ROBERT PLANA	
Codirecteur	: M. NICOLAS NOLHIER	
Lieu de soutenance	: LAAS-CNRS 7 av du Colonel Roche 31077 Toulouse Cedex Salle EUROPE	

La soutenance est publique.

Résultat : Admis

Mention :

Membres du Jury

Nom	Qualité	Etablissement	Rôle	Signature
M. PIERRE BLONDY	PROFESSEUR DES UNIVERSITES	UNIVERSITE LIMOGES	Rapporteur	[signature]
Mme INGRID DE WOLF	PROFESSEUR DES UNIVERSITES	UNIVERSITE LOUVAIN	Rapporteur	[signature]
M. NICOLAS NOLHIER	PROFESSEUR DES UNIVERSITES	UNIVERSITE DE TOULOUSE III	Membre	[signature]
M. ROBERT PLANA	PROFESSEUR DES UNIVERSITES	UNIVERSITE DE TOULOUSE III	Membre	[signature]
M. MANOS TENTZERIS	PROFESSEUR DES UNIVERSITES	GEORGIA TECH. ATLANTA ETATS UNIS	Membre	[signature]
M. OLIVIER VENDIER	DOCTEUR	THALES ALENIA SPACE TOULOUSE	Membre	[signature]

Le jury propose à l'unanimité que le dossier de Jinyu RUAN soit présenté en vue de concourir au prix de l'Ecole Doctorale GEET.

AUTHOR : Jason Jinyu RUAN

TITLE : Investigation and modeling of the impact of electrostatic discharges on capacitive RF MEMS switches

SUPERVISORS : Robert PLANA et Nicolas NOLHIER

DATE AND PLACE OF THE DEFENSE : Salle des conférences, LAAS-CNRS, 2nd of July 2010

ABSTRACT :

Future architectures of communication systems will be more and more complex due to the need for reconfigurability in terms of frequency, emitted and received power, power consumption and reliability.

One interesting and very promising technology comes under the name of RF MEMS. In general MEMS component replaces and outperforms its counterparts. These structures will be yielded to electrostatic and/or electromagnetic strains that it is necessary to investigate and to understand the effects. Besides, power handling of those devices is one of the parameters that qualify its robustness. Since they have shown interesting functionalities for space applications, its sensitivity to radiation needs to be understood.

The motivation of the thesis aims at analysing the impact of those strains in the functional parameters (actuation voltages, switching times, insertion losses, isolation), using an appropriate reliability bench test. Clever analyses of the failure mechanisms that occur after stresses such as DC stress, ESD discharge, RF power qualification and radiation, have been performed.

The stresses will be applied on various structures with various architectures and designs, in order to determine the robustness and the reliability of each technology.

Finally, the validation and the new findings of these works present one design integrating ESD protection and an accelerated stress test circuit is also proposed.

This thesis was being part of the framework of the European Network of Excellence AMICOM on RF Micro-systems where reliability has been defined to be a major challenge to its integration and its commercialization.

KEYWORDS :

Microelectromechanical devices, RF-MEMS, Reliability testing, Electrostatic Discharge (ESD), Charging, Accelerated testing, Dielectric breakdown

---

DISCIPLINE

Microwave, Electromagnetism et Optoelectronics

LABORATORY'S ADDRESS

MIcro et Nanosystèmes pour les Communications sans fils (MINC) et
Intégration de Systèmes de Gestion de l'Energie (ISGE)

LAAS-CNRS
7, avenue du Colonel Roche,
31077, Toulouse Cedex 4

AUTEUR : Jason Jinyu RUAN

TITRE : Analyse et modélisation de l'impact des décharges électrostatiques et des agressions électromagnétiques sur les microcommutateurs microondes (MEMS RF)

DIRECTEURS DE THÈSE : Robert PLANA et Nicolas NOLHIER

LIEU ET DATE DE SOUTENANCE : Salle des conférences, LAAS-CNRS, 02 juillet 2010

RESUME :

Les futures architectures des systèmes de communication présenteront une forte complexité due à des besoins de reconfiguration à la fois en termes de fréquence, de puissance émise et/ou reçue, de puissance consommée et de fiabilité.

Une solution consiste à utiliser les MEMS RF pour obtenir ces fonctionnalités augmentées. Ces composants seront soumis à des agressions à la fois électrostatiques et/ou électromagnétiques dont il est important d'analyser et de comprendre leur impact. D'autre part la tenue en puissance de ces composants est un paramètre qualitatif de leur robustesse. Étant donné qu'ils présentent également des intérêts pour les applications spatiales, il est important de comprendre leur sensibilité face au rayonnement.

Le sujet de thèse vise à analyser l'impact de ces agressions sur les paramètres fonctionnels (tensions d'actionnements, vitesse de fonctionnement, pertes d'insertion et isolation) à partir du développement d'une plateforme appropriée ainsi qu'une analyse fine des mécanismes de dégradation apparaissant suite aux stress appliqués ; tension continu, décharges électrostatiques (de type HBM ou TLP), puissance RF et rayonnement.

Ces stress seront appliqués sur des composants aux architectures différentes (types de diélectrique différentes, épaisseur membrane, géométrie des dispositifs, topologie des zones d'actionnement) afin de déterminer si certaines architectures et ou filières technologiques sont plus résistantes que d'autres.

Enfin, afin de valider ces travaux, il sera conçu un design plus complexe présentant des résistances aux ESD/EMI améliorées et un circuit de vieillissement de ces composants sera également proposé.

Ce projet de thèse rentre dans le cadre d'un réseau d'excellence AMICOM sur les microsystèmes RF où la fiabilité a été identifiée comme étant un des enjeux majeurs pour leur intégration et commercialisation.

MOTS CLES :

Fiabilité, MEMS RF, décharges électrostatiques (ESD), chargement, isolants, diélectrique, défaillance, tests accélérés, vieillisement

---

DISCIPLINE ADMINISTRATIVE

Micro-ondes, Electromagnétisme et Optoélectronique

INTITULE ET ADRESSE DE L'U.F.R. OU DU LABORATOIRE :

MIcro et Nanosystèmes pour les Communications sans fils (MINC) et
Intégration de Systèmes de Gestion de l'Energie (ISGE)

LAAS-CNRS
7, avenue du Colonel Roche,
31077, Toulouse Cedex 4